TECHNOLOGY DRIVEN. WARFIGHTER FOCUSED.

FY17 PROCEEDINGS OF THE EDGEWOOD CHEMICAL BIOLOGICAL CENTER

IN-HOUSE LABORATORY INDEPENDENT RESEARCH AND SURFACE SCIENCE INITIATIVE PROGRAMS

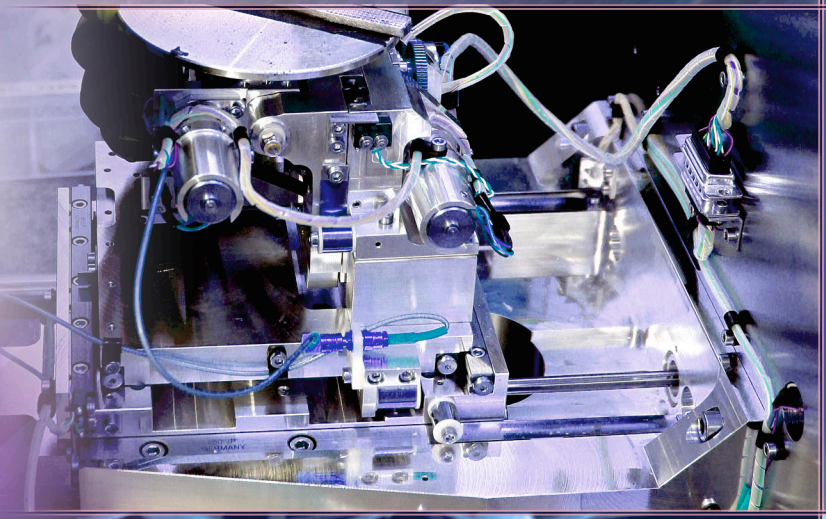

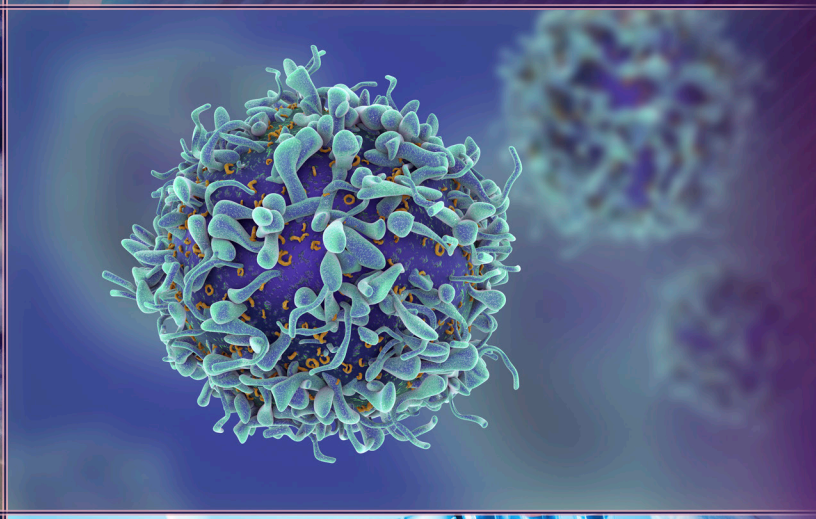

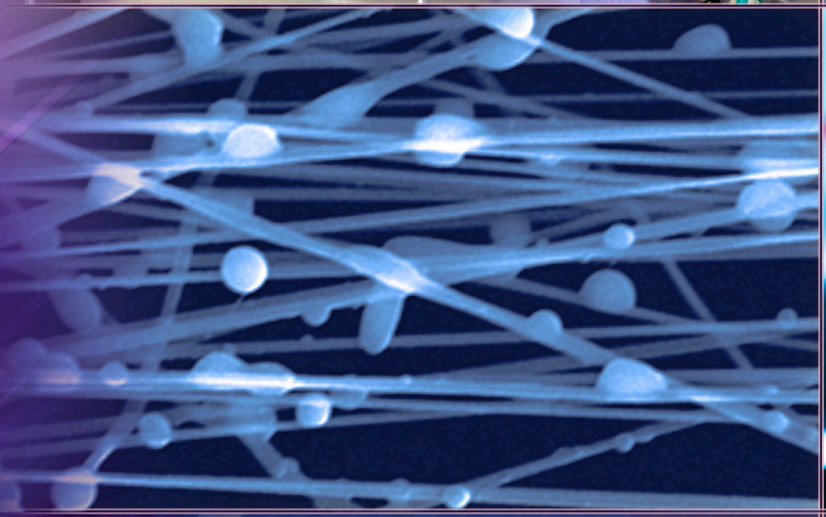

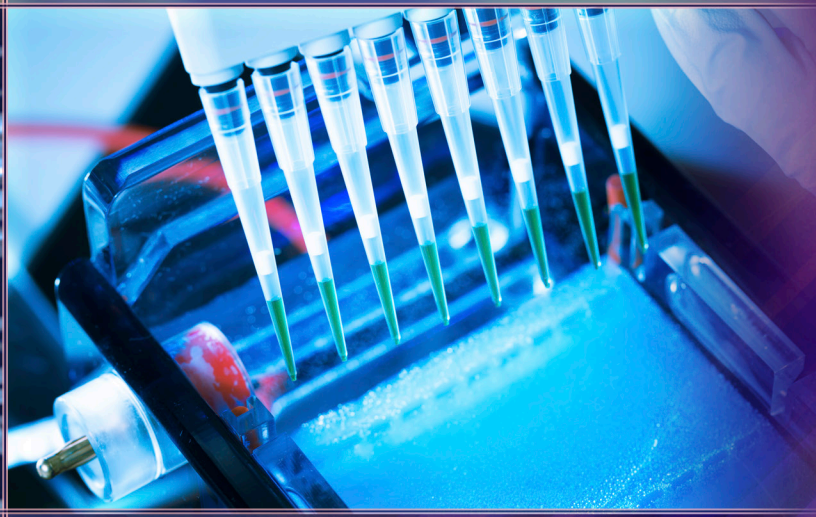

U.S. ARMY RDECOM®

Approved for public release; distribution unlimited.

Image credits, clockwise from top left: NASA/Dimitri Gerondidakis; stock image; stock image; Ross DeVolde and Hyunjoon Kong, Ph.D., M.S., National Cancer Institute, National Institutes of Health.

Message from the In-House Laboratory Independent Research Program Manager

It is my pleasure to present the ninth annual edition of the Proceedings of the Edgewood Chemical Biological Center's (ECBC) In-House Laboratory Independent Research (ILIR) and Surface Science Initiative (SSI) Programs. The ECBC ILIR program funds innovative fundamental research projects that are high-risk with high potential for fulfilling future Army capability needs. Specifically designed to foster increased innovation, the ILIR program also aims to mentor junior investigators in the art and practice of initiating technological innovations and pursuing phenomenology at the boundaries of chemistry, biology, mathematics, or physics to gain insight and advances in support of CBRNE defense missions.

As always, this report includes a description of the ILIR program's rigorous project selection and evaluation process. A critical component of our program is the peer review of project proposals by external senior scientists from across the government. These reviews ensure that we not only fund projects with the greatest potential for fulfilling future Army capability needs, but that we receive an honest and unbiased assessment of our research efforts to hone the Basic Research program year after year.

Feedback from recent reviews suggested that we provide continuous learning opportunities to the ECBC Research and Technology Directorate Workforce to enhance the proposal writing capabilities of principal investigators (PI). To that end, we reinvigorated our previous Proposal Writing Workshop, with the goal of making it an accessible forum for new and seasoned PIs to practice their proposal writing skills, in an informal venue. An overview of this workshop series is included within this report.

Finally, the report concludes with a technical manuscript from each of the five ILIR, seven SSI, and eight internally funded Seedling projects from FY17. Together, these projects covered areas of interest across the chemical, biological, and physical sciences, including: *Rational Molecular Synthesis and Novel Materials*, *Synthetic Biology*, *Nano Chemical and Biological Sensing*, *Panomics and Molecular Toxicology*, *Aerosol Sciences*, *Algorithm Design and Development*, and *Surface Science*.

If you have questions about the ILIR Program or this report, please do not hesitate to contact me or the ILIR Administrative Coordinator directly. I can be reached by telephone at (410) 436-0683, DSN 584-0683, or by email at augustus.w.fountain.civ@mail.mil. The ILIR Administrative Coordinator, Ms. Rebecca Braun, can be reached at (410) 417-4961 or by email at rebecca.m.braun.ctr@mail.mil.

Sincerely,

Augustus W. Fountain III, Ph.D.
Senior Research Scientist (ST) for Chemistry

Strategic Mission and Vision

The US Army Edgewood Chemical Biological Center (ECBC) is the nation's principal research and development resource for non-medical chemical-biological (CB) defense. ECBC's mission to be the Nation's premier provider of innovative CB solutions supports the Center's vision of being a Provider of world-class solutions. For more than 100 years, ECBC has been a unique national asset, providing innovative and cost-effective CB defense technology solutions through our scientific and engineering expertise, coupled with our unique facilities and collaboration with partners.

ECBC's mission and vision are supported by the Center's three Directorates: Research and Technology (R&T), Engineering, and Program Integration. The R&T Directorate provides integrated science and technology (S&T) solutions that address CB defense knowledge gaps and vulnerabilities. Basic science research at ECBC contributes valuable information to the fundamental science knowledgebase, enabling the development of technologies that directly benefit the Warfighter and further strengthen the Army's S&T mission. ECBC's unique set of core research and technology capabilities position it to be the Army's fundamental source of research in chemistry and biology.

ECBC scientist, Mike Feasel, Ph.D., performs research to learn more about opioids and generating metabolite libraries at ECBC. (US Army photo)

ECBC ILIR Project Selection and Evaluation Process

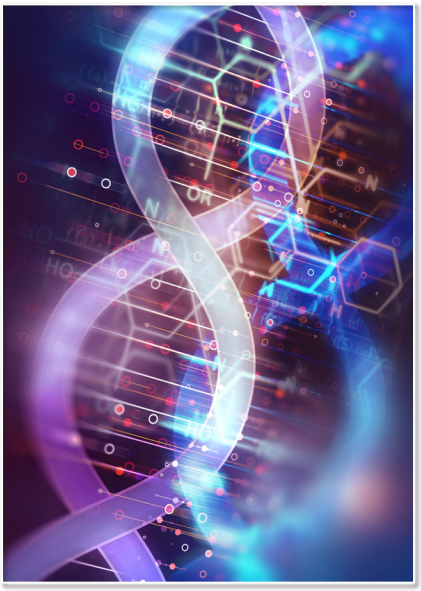

The purpose of the ILIR program is to fund innovative basic research projects that are high-risk but have high potential payoff for fulfilling future Army capability needs. The Department of Defense (DoD) defines basic research as "systematic study directed toward greater knowledge or understanding of the fundamental aspects of phenomena and of observable facts without specific applications toward processes or products in mind."[1] The ILIR program is also specifically designed to foster increased innovation within ECBC, where it is viewed as a critical part of the Center's efforts to ensure a high level of quality in basic science; to foster innovation in the areas of chemistry and biology; to mentor junior investigators in the art and practice of laboratory science; and to explore new technological innovations and phenomenology at the boundaries of chemistry, biology, mathematics, or physics to expand the state-of-the-possible in support of CBRNE defense missions.

The ILIR program solicits the Center's principal investigators for innovative proposals that correspond to topics highlighted in the ECBC R&T Directorate's Strategic Roadmap. The FY17 ILIR topics were: *Rational Molecular Synthesis and Novel Materials*, *Synthetic Biology*, *Nano Chemical and Biological Sensing*, *Panomics and Molecular Toxicology*, *Aerosol Sciences*, *Algorithm Design and Development*, and *Surface Science*. Proposals are first reviewed internally by Branch and Division Chiefs for their technical innovation, alignment to Army/ECBC S&T topic areas, and programmatic completeness. The proposals are then reviewed and critiqued by a panel comprised of resident and external Department of the Army Senior Research Scientists (ST), Senior Scientists from other DoD organizations, and civilian and military faculty members at the United States Military Academy.

The review panel evaluates each proposal on its scientific objective, the scientific methods proposed, the qualifications of the investigator, and the budget; with the scientific objective and methods weighted as the most important criteria. The proposals are then ranked according to merit. Only proposals deemed by the panel as basic research are considered for funding. Quality comments from the reviewers are compiled and used, along with the numerical score, as a critical assessment of the proposal. This written feedback is essential for ECBC's mentoring of researchers and for justifying the elimination of research programs that are not competitive. Quarterly reviews of project performance provide guidance to the program's participants, ensuring that projects meet significant milestones and that substantive new knowledge is being produced and transferred to ECBC and the broader scientific community. This cyclical review and assessment process was used to select and monitor the progress of five ILIR projects and seven basic research projects under the SSI program. Internal funds were also used to support eight Seedling projects, which are smaller-scale projects of high-risk, high-reward basic research.

Beginning in FY18, the US Army has mandated that independent annual reviews of all ILIR programs be conducted by a panel from the National Academies of Sciences, Engineering, and Medicine. This Review Panel will provide an overall assessment of the quality of ECBC's basic science research programs and be used as a guide for shaping the overall mission of the ILIR program in subsequent years.

This Proceedings Report contains the technical reports from all 20 ECBC-produced ILIR/SSI/Seedling-funded projects.

[1] *DoD Financial Management Regulation, DoD 7000.14-R, Vol. 2B, Ch. 5*

FY17 Innovation Program Highlights

In FY17, Dr. Fountain reinvigorated the ECBC Proposal Writing Workshop to help advance the R&T Workforce's skillset in the art of proposal writing. In previous years, a full-day workshop was offered to encourage attendees to participate in an active dialog surrounding the proposal process. Now a series of one-hour workshops, each session was guided by practical exercises drawn from previous winning and non-winning proposals from ECBC's Basic Research Programs, to identify strengths, weaknesses, and areas for improvement in each proposal.

"The first and last job of every scientist is communication. You must convince someone to fund your idea, and you must demonstrate how you delivered upon what they paid you to do," noted Dr. Fountain.

As the ECBC Innovation Goal Champion and the Director of the Center's ILIR and SSI Basic Research Programs, Dr. Fountain reviews upwards of 70 proposals annually within the ECBC portfolio alone. This Workshop Series provided an opportunity for personnel to actively practice their skills in an informal venue, in addition to gaining feedback from their peers and workshop facilitators.

The first workshop focused on strategies for formulating strong, testable hypotheses—a critical first step to developing a winning proposal. Having a strong and purposeful background section anchors the principal investigator's hypothesis, and sets the stage for the rest of the proposal—all subsequent sections, including methodology, risk mitigation plans, and milestones, must all tie back to this central hypothesis.

The second workshop focused on how to strategically design research methodology in order to test the hypothesis. This technical approach should be specific and inform proposal reviewers exactly how the research will be performed. It should also explain which experimental and control methods will be used and identify the time and resource limits of the approach. Establishing the potential impact of expected results shows reviewers that the approach is focused and purposeful.

The third workshop discussed the art of budget development. The proposal budget is used by a customer to evaluate return on investment of a proposed project—the budget can often identify weak areas in the proposal narrative. A carefully prepared budget can also improve the overall proposal. Dr. Fountain presented strategies on developing internal and external cost proposals, as well as how to avoid the pitfalls in underestimating and overestimating resource needs.

The final workshop focused on the peer/merit review process. This session explained to attendees what reviewers look for when they are evaluating proposals. This session allowed participants to "peek behind the curtain" of how the ILIR, SSI, and Seedling programs assess submitted proposals. In this session, participants evaluated and scored previously submitted proposals to the ILIR program, and then compared those evaluations with the scores given by the actual review panel from that year. This allowed attendees to see if they scored the proposals similarly or differently than the actual review panel. The participants then had an opportunity to discuss the results and why their reviews may have been similar or different.

Dr. Fountain will continue to identify potential topics for additional interactive workshops that would benefit the researchers of ECBC. Providing these continuous learning opportunities for the ECBC Workforce supports the ILIR program goal to mentor junior investigators in the art and practice of laboratory science.

Peer-reviewed Publications

- Debbrecht, B.; Mirotznik, M.; Zander, Z.; DeLacy, B.G. Cavity-based Aluminum Nanohole Arrays with Tunable Infrared Resonances, *Opt. Express*. **2017**, *25* (20), pp 24501–24511.
- Fang, H.; Xu, B.; Li, X.; Zander, Z.; Kuhn, D.; Tian, G.; Dai, H.L.; DeLacy, B.G.; Rao, Y. Effects of Molecular Structure and Solvent Polarity on Adsorption of Carboxylic Anchoring Dyes onto TiO_2 Particles in Aprotic Solvents. *Langmuir*. **2017**, *33* (28), pp 7036–7042.
- Guicheteau, J.; Tripathi, A.; Emmons, E.; Christesen, S.; Fountain A.W. Reassessing SERS Enhancement Factors: Using Thermodynamics to Drive Substrate Design. *Faraday Discuss*. **2017**, *205*, pp 547–560.
- Kesavan, J.S.; Humphreys, P.D.; Bottiger, J.R.; Valdes, E.R.; Rastogi, V.K.; Knox, C.K. Deposition method, relative humidity, and surface property effects of bacterial spore reaerosolization via pulsed air jet. *Aerosol Sci. Technol.* **2017**, *51* (9), pp 1027–1034.
- Kesavan, J.S.; Humphreys, P.D.; Nasr, B.; Ahmadi, G.; Knox, C.K.; Valdes, E.R.; Rastogi, V.K.; Dhaniyala, S. Experimental and computational study of reaerosolization of 1 to 5 μm PSL microspheres using jet impingement. *Aerosol Sci. Technol.* **2016**, *51* (3), pp 377–387.
- Nirujogi, R.S.; Muthusamy, B.; Kim, M.S.; Sathe, G.J.; Lakshmi, P.T.V.; Kovbasnjuk, O.N.; Prasad, T.S.K.; Wade, M.; Jabbour, R.E. Secretome analysis of diarrhea-inducing strains of Escherichia coli. *Proteomics*. **2017**, *17* (6) Special Issue: 1600299.
- Peterson, G.W.; Lu, A.X.; Epps III, T.H. Tuning the Morphology and Activity of Electrospun Polystyrene/UiO-66-NH_2 Metal-Organic Framework Composites to Enhance Chemical Warfare Agent Removal. *ACS Appl. Mater. Interfaces*. **2017**, *9* (37), pp 32248–32254.
- Prugh, A.M.; Cole, S.D.; Glaros, T.; Angelini, D.J. Effects of organophosphates on the regulation of mesenchymal stem cell proliferation and differentiation. *Chem. Biol. Interact.* **2017**, *266*, pp 38–46.

Basic Research Program Productivity

$1.1 M over **5** ILIR projects

$2.1 M over **7** SSI projects

$300 K over **6** Seedling projects

22 presentations and posters

8 peer-reviewed publications

2 technical reports

Technical Reports

- Angelini, D.; Phillips, C.; Prugh, A.; Glaros, T.; Tran, B. *Signaling Pathways Associated with VX Exposure in Mesenchymal Stem Cells*; ECBC-TR-1452. US Army Edgewood Chemical Biological Center: Aberdeen Proving Ground, MD, **2017;** UNCLASSIFIED Report.
- Feasel, M.G.; Moran, T.S.; Walz, A.J. *In Vitro Approach to Evaluating Opioid Receptor Subtype Specificity*; ECBC-TR-1440. US Army Edgewood Chemical Biological Center: Aberdeen Proving Ground, MD, **2017;** UNCLASSIFIED Report.

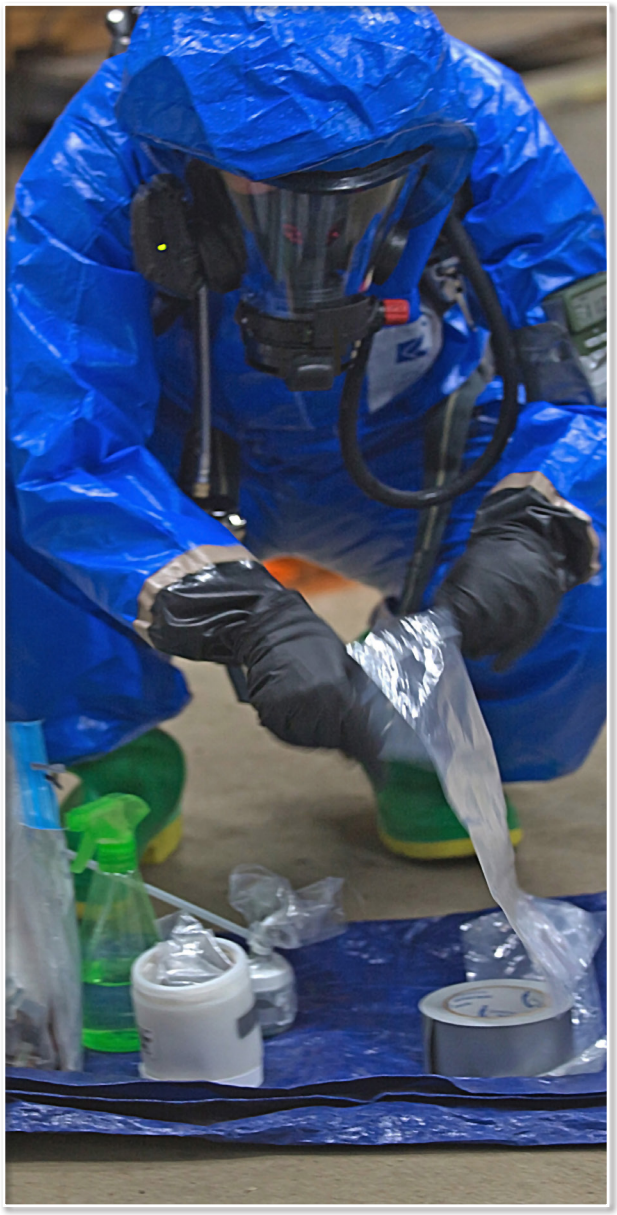

Presentations and Posters

- Abramson, A.; Boyd, G.; Stafford, K.; Calm, A.; Jabbour, R.; Cabalo, J.; Rebeil, R. Structure modeling and prediction of cystine knot miniproteins. *Presented at the 6th Annual ECBC Coffee with Colleagues Event*, Edgewood, MD, **11 January 2017**.
- DeCoste, J.B. Enhancing the uptake of oxygen in metal-organic frameworks. *Presented at the 253rd National American Chemical Society Meeting*, San Francisco, CA, **2–6 April 2017**.
- DeCoste, J.B. Synergistic effects of metal-organic framework containing polymer membranes for military applications. *Presented at the International Symposium on Composites of Metal and Covalent Organic Frameworks: Fundamental Design & Applications*, Granada, Spain, **12–13 October 2017**.
- DeCoste, J.B. Synergistic effects of metal-organic framework containing polymer membranes for military applications. *Presented at the 254th National American Chemical Society Meeting*, Washington, DC, **20–24 August 2017**.
- DeLacy, B.G. Fundamental research efforts in spectrally selective obscurants. *Presented at the Night Vision Labs Workshop on Degraded Visual Environments*, Fort Belvoir, VA, **7 March 2017**.
- DeLacy, B.G. Spectrally selective obscurants. *Presented at the 2016 Obscurants Symposium*, Charlottesville, VA, **29 November 2016**.
- DeLacy, B.G. The Impact of plasmon-exciton coupling on charge injection in semiconductors. *Presented at the 253rd National American Chemical Society Meeting*, San Francisco, CA, **2–6 April 2017**.
- Emmons, E.D.; Roese, E.; Hung, K.; Tripathi, A. Interaction of water with hygroscopic crystals studied by low-frequency Raman spectroscopy. *Presented at the 14th Confocal Raman Imaging Symposium*, Ulm, Germany, **25–27 September 2017**.

A US Soldier assigned to 22nd Battallion, 48th Chemical Biological Radiological Nuclear (CBRN) Brigade, secures hazardous materials during a training exercise. (US Army photo by Spc. Derrick Maragh)

Presentations and Posters (continued)

- Guicheteau, J.; Tripathi, A.; Emmons, E.; Christesen, S.; Fountain III, A. W. Reassessing SERS Enhancement Factors: Using Thermodynamics to Drive Substrate Design. *Presented at Surface Enhanced Raman Scattering - SERS: Faraday Discussions*, Glasgow, United Kingdom, **30 August–1 September 2017**.

- Jabbour, R.E.; Peterson, G.; DeCoste, J.; Wade, M. Metal organic frameworks as a new class of MALDI matrices, *Presented at the 65th American Society of Mass Spectrometry and Allied Topics*, Indianapolis, IN, **1–5 June 2017**.

- Kesavan, J.; Alstadt, V.; Bottiger, J.; Laube, B.; Total and regional particle deposition in various age, anatomically correct, and 3D printed human and animal respiratory system models. *Presented at the Edgewood Chemical Biological Center Aerosol Symposium*, Aberdeen Proving Ground, MD, **12–14 September 2017**.

- Kesavan, J.; Alstadt, V.; Bottiger, J.; Laube, B.; Particle deposition in anatomically correct human and animal respiratory system models. *Presented at the 6th Annual ECBC Coffee with Colleagues Event*, Edgewood, MD, **11 January 2017**.

- Kesavan, J.S.; Humphreys, P.D.; Nasr, B.; Ahmadi, G.; Knox, C.K.; Valdes, E.R.; Rastogi, V.K.; Dhaniyala, S. Experimental and computational study of reaerosolization of 1 to 5 µm PSL microspheres using jet impingement. *Presented at the American Association for Aerosol Research 35th Annual Conference*, Portland, OR. **17–21 October 2016**.

- Kuhn, D. Metal organic frameworks as pyrotechnically driven obscurants. *Presented at the Edgewood Chemical Biological Center Aerosol Symposium*, Aberdeen Proving Ground, MD, **12–14 September 2017**.

- Knox, C.; Cabalo, J.; Varady, M.; Bringuier, S.; Pearl, T.; Lambeth, R.; Mantooth, B. H-Bonding effects on multicomponent diffusion. *Presented at the 6th Annual ECBC Coffee with Colleagues Event*, Edgewood, MD, **11 January 2017**.

- Nasr, B.; Qiang, J.; He, M.; Kesavan, J.S.; Morgan, M.; Ferro, A.R.; Ahmadi, G.; Dhaniyala, S. Particle resuspension from substrates: analysis of time-dependence on removal rates. *Presented at the American Association for Aerosol Research 35th Annual Conference*, Portland, OR. **17–21 October 2016**.

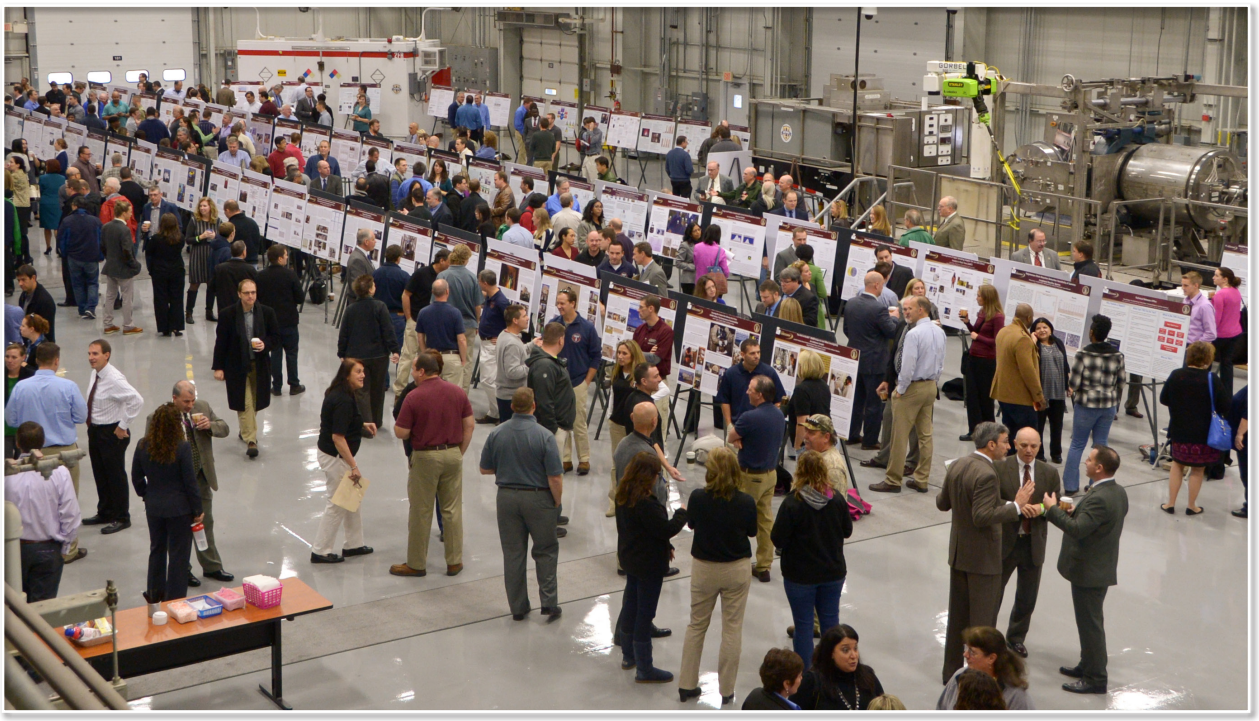

ECBC hosts a "Coffee With Colleagues" poster session. (US Army photo)

Presentations and Posters (continued)

- Peterson, G.W. Polymer/MOF composites for enhanced protection against chemical warfare agents. *Presented at the Composites of Metal and Covalent Organic Frameworks: Fundamental Design & Applications Symposium*, Granada, Spain, **14 September 2017**.
- Peterson, G.W.; Lu, A.X.; Epps, III, T.H. Tuning the morphology and activity of electrospun polystyrene/UiO-66-NH_2 metal-organic framework composites to enhance chemical warfare agent removal. *Presented at the 254th National American Chemical Society Meeting*, Washington, DC, **23 August 2017**.
- Tovar, T.; Iordanov, I.; Ploskonka, A.; DeCoste, J. Modifying MOFs for enhanced oxygen adsorption. *Presented at the 6th Annual ECBC Coffee with Colleagues Event*, Edgewood, MD, **11 January 2017**.
- Tovar, T.; Iordanov, I.; Ploskonka, A.; DeCoste, J. Modifying MOFs for enhanced oxygen adsorption. *Presented at the Surface Science and Multifunctional Materials for Force Protection Science Review*, Raleigh, NC, **6–7 September 2017**.
- Tripathi, A.; Emmons, E.D.; Fountain, A.W.; Guicheteau, J.A.; Christesen, S.D. Effect of Metal Types and Geometries on Planar Array Substrates Based Surface Enhanced Raman Spectroscopy. *Presented at the 2017 Pittsburgh Conference and Exposition*, Chicago, IL, **5–9 March 2017**.
- Tripathi, A.; Emmons, E.; Guicheteau, J.; Fountain III, A. W.; Christesen, S. Molecular Structure and Solvent Factors Influencing SERS on Planar Gold Substrates. *Presented at the 2016 SciX Conference: 43rd Annual North American Meeting of the Federation of Analytical Chemistry and Spectroscopy Societies*, Minneapolis, MN, **18–23 September 2016**.

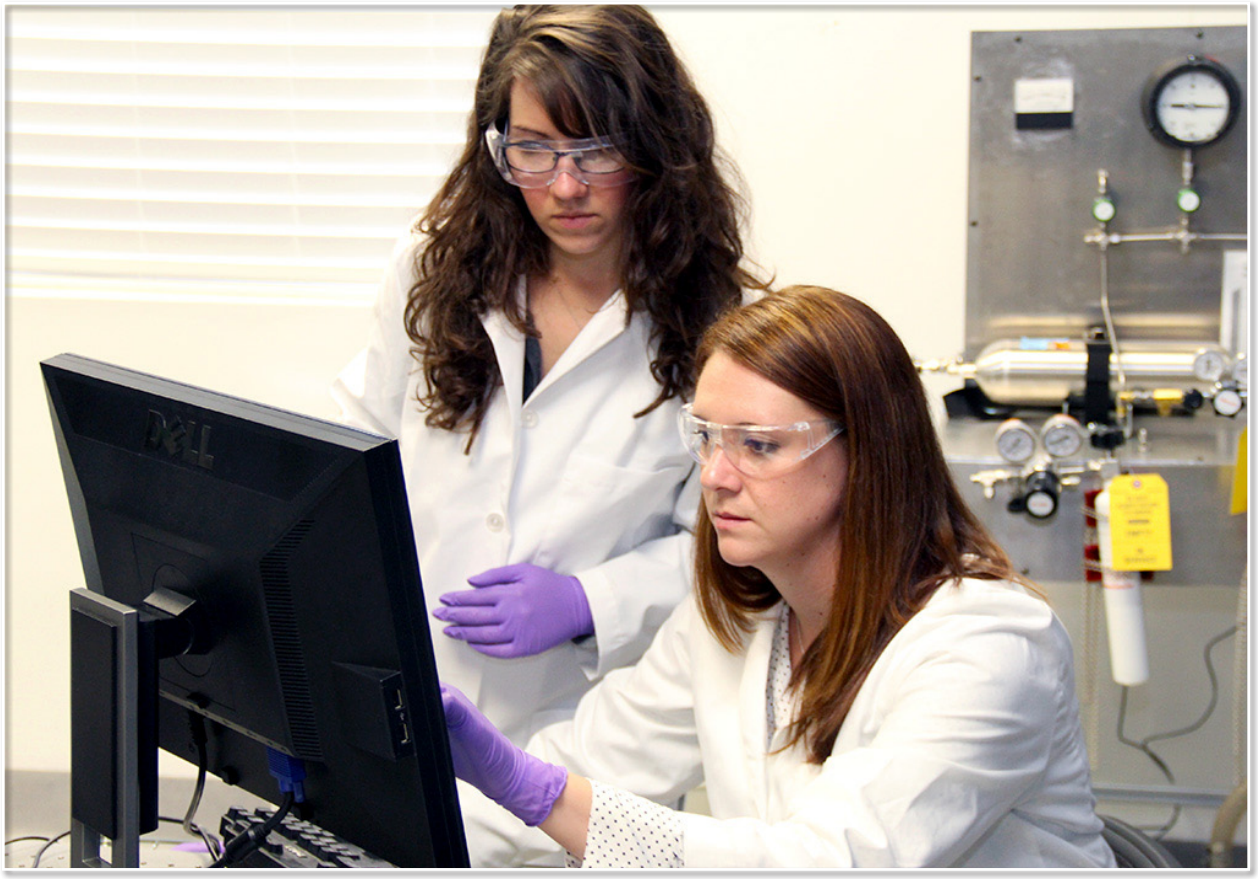

ECBC scientists, Dr. Angela Buonaugurio and Dr. Erin Durke, perform experiments focused on the characterization of agent aerosols using mid-infrared light to provide information about how aerosols transport, react, and persist in the atmosphere. (US Army photo)

Table of Contents

In-House Laboratory Independent Research (ILIR) Projects

1 Characterization of aerosol particle charge and the impact of a high degree of charge on the particle's physical and chemical properties
Erin M. Durke, Monica L. McEntee, Suresh Dhaniyala*
This first-year project aimed to quantitatively characterize the charge distribution for TiO_2 aerosols using transmission infrared spectroscopy, with the intent of correlating the resultant charge profile with other analytical outputs.

9 Comparative characterization of the host and viral proteome in Sindbis virus identifies sorting nexin 5 as critical host factor for alphavirus replication
*Andy Kilianski, Amanda Piper, Ryan Schuchman, Ricardo G. Vancini, Jose M.C. Ribeiro, Farooq Nasar, Raquel Hernandez, Thomas Sprague, Trevor G. Glaros**
In the final year of this study, highly purified Sindbis virus preparations were analyzed using liquid chromatography mass spectrometry to determine if previously undetected host proteins were packaged into virus particles in human, hamster, and mosquito cell lines. These identified proteins were analyzed to determine their role in the virus life cycle to see if they can serve as potential therapeutic targets.

21 Comparison of animal particle deposition data with physical and mathematical model data
Jana S. Kesavan, Valerie J. Alstadt, Jerold Bottiger, Beth L. Laube*
The final year of this project used anatomically correct 3D-printed respiratory tract models, created using CT scans from live animals, to collect particle deposition data within the models. The data obtained was compared to deposition data from *in vivo* animal testing and mathematical modeling to determine applicability to human data for exposure assessments.

29 Hierarchical systems through selective deposition and growth of metal-organic frameworks on block copolymers
*Gregory W. Peterson**
Current approaches to growing metal-organic frameworks lack the ability to systematically deposit these compounds in the form of arrays. This new effort used a bottom-up approach to precisely control the location of metal-organic frameworks nucleation to allow for systematic growth within both strands and bulk polymers.

38 Structure modeling and prediction of cystine knot miniproteins
*Caitlin E. Sharpes, Katelynn M. Stafford, Alena M. Calm, Rabih E. Jabbour, Jerry B. Cabalo, Roberto Rebeil**
This second-year project leveraged *in silico* protein folding and structure modeling tools with conventional protein biochemistry techniques to investigate how changes in primary amino acid sequence and spacing between cysteine residues can impact the ability of cystine knots to form.

Surface Science Initiative (SSI) Projects

46 Adsorption of non-polar adsorbates on the organic linker of metal-organic frameworks
Jared B. DeCoste, Trenton M. Tovar, Ivan O. Iordanov, Ann M. Ploskonka, Gregory W. Peterson*
The second year of this project employed post-synthetic surface modifications of metal-organic frameworks by selectively adding functional groups, particularly metal ions and highly polar groups, to enhance the adsorption of non-polar gases such as O_2 and CO_2.

56 A facile method for the growth of anisotropic silver nanoparticles on the surface of titania nanorods and nanofibers
*Danielle L. Kuhn, Zachary B. Zander, Shaun M. Debow, Hui Fang, Hai Lung Dai, Yi Rao, Brendan G. DeLacy**
The final year of this effort focused on interrogating the simultaneous use of plasmonic and excitonic structures to synergistically enhance the charge injection efficiency and rate from a given molecule into TiO_2 nanoparticles.

65 Cavity-based aluminum nanohole arrays with tunable infrared resonances
*Bryan Debbrecht, Morgan McElhiney, Victoria Carey, Chris Cullen, Mark S. Mirotznik, Brendan G. DeLacy**
This second-year effort completed the computational design, fabrication, and characterization of a cavity-based aluminum nanohole array that incorporates a metal-oxide sub layer, and explored the coupling of the localized resonances of aluminum-based structures with tunable resonances throughout the infrared region.

75 Understanding the effect of substrate material and solvation on surface-enhanced Raman spectroscopy enhancement
Jason A. Guicheteau, Ashish Tripathi, Erik D. Emmons, Augustus W. Fountain, III, Steven D. Christesen*
The final year of this project examined the effect of substrate geometry, deposited metals, and effect of solvation on surface-enhancement value. These results were used to advance SERS understanding to improve predictability of the SERS response.

83 Matrix-free assisted laser desorption ionization using metal-organic frameworks
Rabih E. Jabbour, Gregory W. Peterson, Jared B. DeCoste*
This second-year project utilized low frequency Raman spectroscopy to continue exploring the binding mechanisms of metal-organic frameworks with multifunctional groups and various pore structures in an attempt to develop a universal matrix for a new matrix-assisted laser desorption ionization mass spectrometry technique.

93 Probing the connection between low-frequency vibrational modes and macroscopic structural behavior of metal-organic frameworks
Neal D. Kline, Ann M. Ploskonka, Ivan O. Iordanov, Craig K. Knox, Gregory W. Peterson*
This first-year effort sought to understand how systematically varying the metal node and functionalization of linkers of the MIL-53 family of metal-organic frameworks affect the large scale structural flexibility of these compounds.

101 Determination of mechanisms and transport enhancement in liquid-phase extraction of penetrants from polymers
Brent A. Mantooth, Mark J. Varady, Thomas P. Pearl, Devon A. Boyne, Craig K. Knox, Jerry B. Cabalo, John A. Escarsega, Robert H. Lambeth*
The final year of this effort focused on studying the influence of solvents on the subsurface mass transport of molecular species in the bulk of polymer films with a multifaceted combination of computational and experimental approaches.

Seedling Projects

111 Effect of organophosphates on the regulation of endothelial barrier function
Daniel J. Angelini, Christopher S. Phillips, Jennifer R. Horsmon, Amber M. Prugh*
Non-lethal toxic effects of organophosphates are widely unexplored. This project examined the nonlethal effects of exposure to low levels of the organophosphate compound, malathion, and its metabolite, malaoxon, on human endothelial cells.

117 Interaction of water with hygroscopic crystals studied by low-frequency Raman spectroscopy
Erik D. Emmons, Ashish Tripathi*
This study used time-resolved Raman chemical imaging to examine the effects of humidity on the crystalline structure of ammonium nitrate and potassium. Measurements of low-frequency lattice modes and high-frequency internal modes were performed to spatially and temporally determine the distributions of crystalline and solution phases.

123 *In vitro* screening of opioid antagonist effectiveness
Michael G. Feasel, Theodore S. Moran*
This study assessed the ability of an *in vitro* method to assess the binding interactions of opioid compounds and to test whether reported irreversible opioid receptor binders were truly irreversible.

129 Mass spectrometric identification of *Yersinia pestis* antigens specific to the select agent polyclonal antibodies
*E. Randal Hofmann, Bao Q. Tran, Katherine A. Rhea, Gabrielle M. Boyd, Trevor G. Glaros**
This project integrated immunoprecipitation with liquid chromatography-mass spectrometry, to develop a method that resulted in new potential *Y. pestis* antigens to goat and rabbit anti-*Y. pestis* polyclonal antibodies. Determining antigen candidates is essential for developing monoclonal antibody replacements for *Y. pestis* detection assays.

134 Raman chemical imaging based cell cytometry: differentiation and quantification of viable and gamma-deactivated *B. anthracis* Sterne spore
Jason Guicheteau, Ashish Tripathi, Erik D. Emmons, Michael H. Kim, Jerry W. Pfarr*
This effort sought to analyze individual *B. anthracis* spores using Raman chemical imaging microscopy to determine the existence of unique spectral differences between viable and gamma-irradiated spores. This technique has potential to serve as a rapid means of discrimination between viable and gamma-irradiated spores.

140 Reducing false positives via capture/recapture modeling for early-warning
*Thomas E. Ingersoll**
This project compared the accuracy between occupancy modeling of threat alarm data to two other methods for estimating threats. A full model was fit, giving location-specific probability of contamination by agents, local probability of false-positives, and local probability of underreporting.

148 Oxidative decomposition of fentanyl by immobilized peroxide catalysts—a biomimetic perspective
*Li Kong, Jason K. Navin, Alex Balboa, John M. Landers, Monica L. McEntee, Christopher J. Karwacki**
This project investigated the oxidative decomposition of fentanyl using a solid form of oxy complexes on nanocrystalline metal substrates. The objective of this work is to develop a foundational understanding of surface interactions and possible decomposition mechanisms of fentanyl for protection applications.

156 Obscurant bispectral smoke
Danielle L. Kuhn, Amee L. Polk, Zach B. Zander*
This research evaluated metal-organic frameworks for their suitability for pyrotechnic or obscurant applications. Analysis of both solutions and aerosols were performed to determine if these compounds exhibit visual obscuring properties that can be exploited to create a composite material with higher performing bispectral properties.

ILIR PROJECTS

Characterization of aerosol particle charge and the impact of a high degree of charge on the particle's physical and chemical properties

Erin M. Durke[a*], Monica L. McEntee[b], Suresh Dhaniyala[c]
[a]U.S. Army Edgewood Chemical Biological Center, Research & Technology Directorate, 5183 Blackhawk Rd, Aberdeen Proving Ground, MD 21010
[b]Oak Ridge Institute for Science and Education, P.O. Box 117, Oak Ridge, TN 37831
[c]Clarkson University, 8 Clarkson Ave, Potsdam, NY 13699

ABSTRACT

Titanium dioxide, TiO_2, was aerosolized expulsively and then subsequently characterized using transmission infrared spectroscopy and electrical impedance spectroscopy. The successful generation of TiO_2 aerosols was confirmed using scanning electron microscopy with energy dispersive X-ray analysis. Aerosols were imaged on a tungsten mesh and ranged in size from ~0.5 µm to several µm in size. The transmission infrared spectroscopy data collected from the aerosolized TiO_2 was compared to data collected for TiO_2 powder. The transmission infrared spectroscopy spectra for the aerosols displayed features not observed in the spectra of the metal oxide powder. Various experiments were conducted to ensure the features were not attributable to artifacts of the system or test configuration. Thus far, all data suggests that the features observed in the TIR spectra for the aerosolized material are a function of the aerosolization process. Ongoing work will focus on a quantitative characterization of the charge distribution for TiO_2 aerosols, with the intent of correlating the resultant charge profile with other analytical outputs. Ideally, the charge measured via tandem differential mobility analyzers will be responsible for deviations in characteristic data, such as transmission infrared spectroscopy spectra.

Keywords: aerosol, particle, charge distribution, infrared, metal oxide, reactivity

1. INTRODUCTION

The existence of charge on aerosol particles, those generated both naturally and anthropogenically, is well known but the consequence of its presence is far from well understood. In both cases, the degree of charge exists in a rough distribution that is unpredictable and broadly generalized. The charge density of an aerosol particle has been shown to dominate over other forces associated with the particle by several orders of magnitude, dictating the behavior of the aerosol during various processes. In many laboratory setups, extensive measures are taken to minimize or neutralize charge on particles because of the impact on collected data. In fact, previous sampling studies have confirmed that the particle charge can be the main source of error with respect to measurements focused on the determination of concentration and particle size.[1] A detailed understanding of the impact of particle charge can be used for developments in the fields of detection/sensing, filtration/adsorption, and decontamination/reactivity. In the medical industry, aerosolized medicine is developed to maximize the charge per particle upon administration (e.g., inhalers are modified to create an aerosolized mist possessing highly charged particles). Highly charged particles have been shown to possess higher deposition fractions, especially in the deep lung, such as the alveolar region.[2,3] A study by Majid et al. showed that pulmonary deposition can be more than two times higher for charged particles.[2] Also impacting adsorption, charged particles have been known to experience a hundredfold decrease in filter penetration, the result of a stronger interaction between filter media and charged particle.[4] Preliminary data collected in our laboratory suggests that the aerosolization of materials may affect their physical or chemical properties. In this study, we were able to distinguish between TiO_2 powder and aerosolized TiO_2 powder via infrared spectroscopy; the variation between spectra is potentially due to the additional charge on the aerosolized material, see the example in Figure 1. The work described herein focuses on whether or not the spectral deviation is, in fact, a function of triboelectric charging of the material during the aerosolization process.

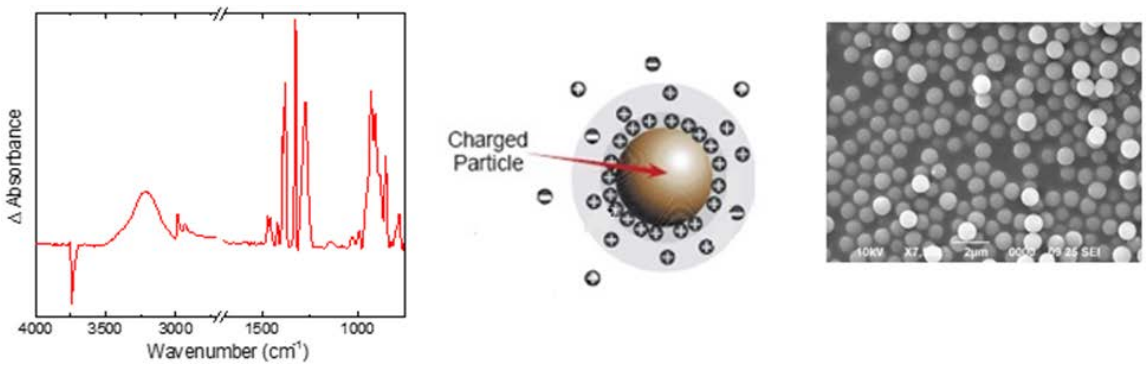

Figure 1. Charge present on a particle may have impact on the material's properties and therefore be observable in data collected, e.g., IR spectrum.

2. EXPERIMENTAL

2.1 Materials

Aeroxide® P25 TiO_2 was purchased from Sigma-Aldrich® and used without further purification.

2.2 Instrumentation

The TiO_2 was aerosolized onto the sample mounts (either W mesh for interrogation via infrared (IR) or glass slides for impedance) using the low volume powder disperser (LVPD), shown in Figure 2. The LVPD is comprised of two opposing sonic nozzles. Each nozzle exit faces the other, and the powder is suctioned into the nozzles via tubing[5] from small wells in a rotating disk. The wells provide a means for aerosolizing material for multiple runs or producing a prolonged aerosol challenge. Additionally, the position of the nozzle exits results in more of a "plume" of material, as opposed to significant impaction of aerosolized material on the side of the sample chamber. The aerosolized samples were interrogated with transmission infrared (TIR) spectroscopy inside of the custom Mid-infrared aerosol chemistry chamber (MIRACC); sample mount schematic and picture shown in Figure 3. The TIR spectroscopy was performed using a Thermo Scientific™ Nicolet™ 6700 Fourier transform infrared spectrometer equipped with a mid-IR source and MCT Type A detector, allowing for an observable range of 4000–650 cm^{-1}. Spectra are the sum of 1,024 scans acquired at a resolution of 2 cm^{-1}. Electrical impedance spectroscopy was conducted with a Solartron Analytical SI 1260 Impedance/Gain-Phase Analyzer using a parallel plate capacitor. Scanning electron microscopy (SEM) was performed using a Phenom GSR Desktop SEM with a backscatter electron detector in composition (full) mode.

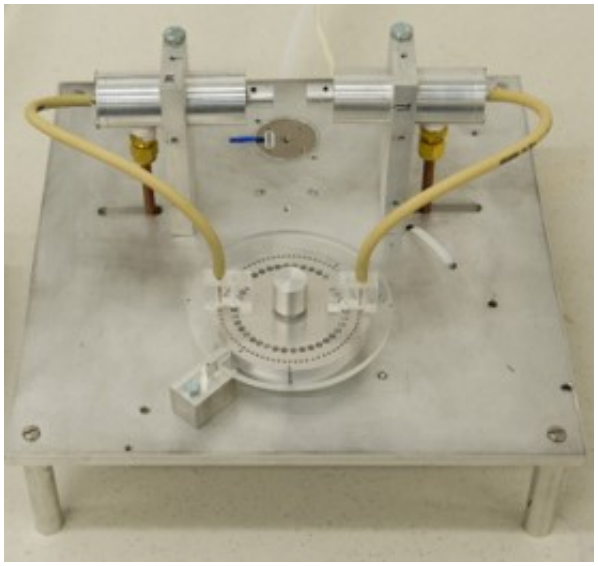

Figure 2. LVPD used to aerosolize TiO_2 for interrogation.

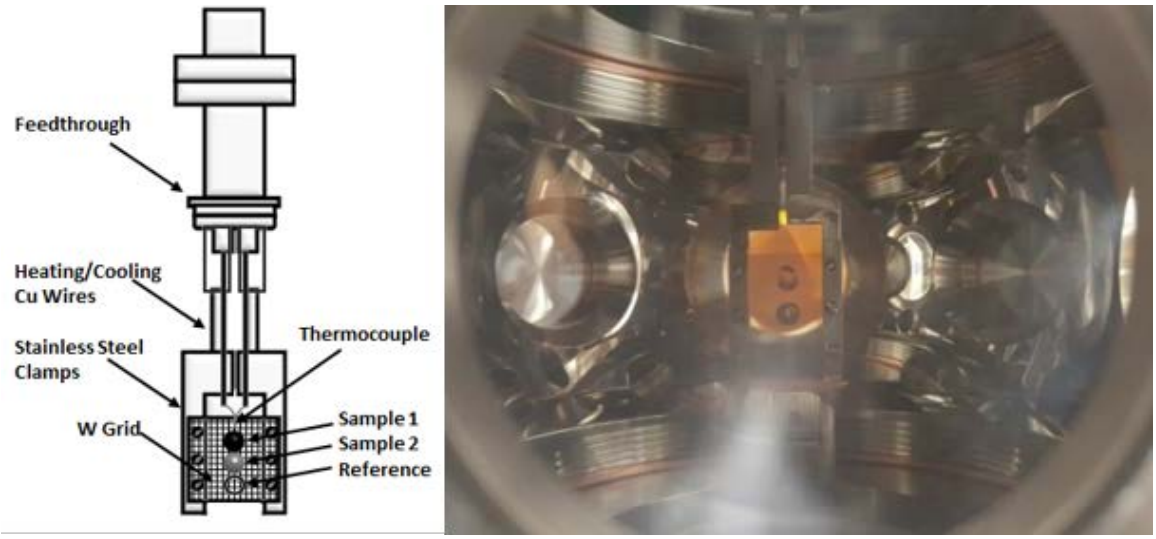

Figure 3. Schematic (left) and image (right) of the sample mount and W mesh used to perform TIR spectroscopy of the metal oxides (both powder and aerosols).

2.3 Aerosolization

The TiO_2 powder was aerosolized onto several samples using the LVPD. The LVPD was completely contained inside of a Lexan™ aerosol generation box. The samples (W mesh, 1-inch x 1-inch glass slides) were placed on the bottom of the box prior to aerosolization. Aerosols were generated for 10 seconds, then the particles were allowed to settle on the sample surfaces overnight.

2.4 Scanning electron microscopy

The presence of aerosolized TiO_2 on the W mesh was confirmed using SEM with EDX. The image and data displayed in Figure 4 confirm the presence of TiO_2 aerosols on the W mesh. TiO_2 aerosols were only detected on the side of the W mesh that was face-up during aerosol generation.

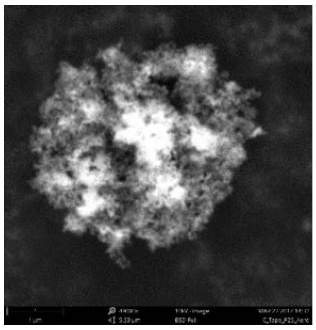

Element Number	Element Symbol	Element Name	Atomic Conc.	Weight Conc.
6	C	Carbon	73.42	65.06
8	O	Oxygen	25.06	29.58
22	Ti	Titanium	1.52	5.36

Figure 4. SEM image of TiO_2 aerosol deposited on W mesh (left). Table displaying the elemental composition of the aerosol imaged on the W mesh (right).

3. RESULTS AND DISCUSSION

One of the main goals of this work is to characterize the charge on aerosol particles and determine the impact on said particles' deposition, adsorption, or reactivity. Preliminary investigations utilizing IR spectroscopy revealed prominent differences in the spectra collected for the aerosolized TiO_2 and the unaltered powder sample of TiO_2. The neutral powder was placed into a KBr micro cup and analyzed with diffuse reflectance IR Fourier transform spectroscopy (DRIFTS). DRIFTS is an IR spectroscopic technique employed for the interrogation of powdered samples with no preparation required.[6] The top trace in Figure 5 represents the neutral, unaerosolized TiO_2 powder. The spectra displays typical features for the material, specifically peaks due to the Ti–O–Ti–O phonon modes. DRIFTS has also been utilized in various aerosol studies,[7–9] therefore it was reasonable to examine the aerosolized

sample in the same setup used for the powdered material. The bottom portion of the graph shows five separate spectra, all distinctly different from the spectrum collected for the neutral powder. Each spectrum was recorded after TiO_2 was aerosolized and allowed to deposit onto the sample cup. While each subsequent spectrum shows a growth of the individual features, characteristic of increasing concentration, the aerosol spectra possess unique features not observed in the powder's spectrum. While both samples do exhibit the peaks due to Ti–O phonon modes, the ratio of intensities is drastically different between the powder and aerosolized samples.

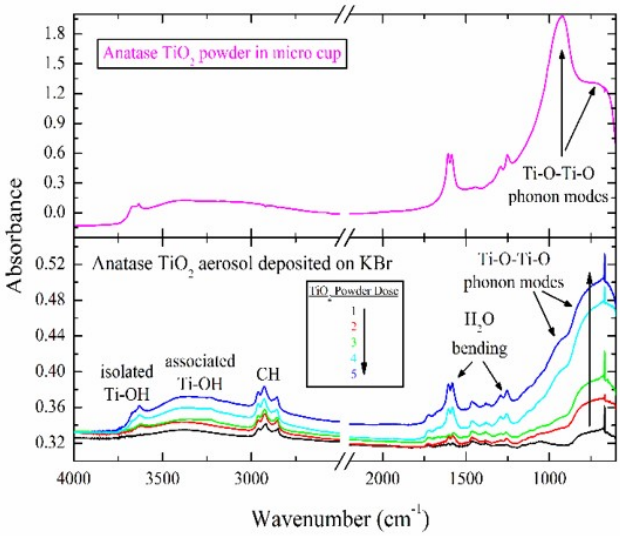

Figure 5. DRIFTS spectra of anatase TiO_2. Spectrum of neutral TiO_2 powder (top). Spectra for aerosolized TiO_2 (bottom).

In an effort to understand the noticeable differences between these two samples' IR spectra, a more conducive material was chosen for interrogation and the remainder of the studies were conducted in the MIRACC, utilizing the TIR setup. For all other studies performed, and discussed herein, Aeroxide® P25 TiO_2 was the material under test. Aeroxide® P25 TiO_2 is comprised of nanoparticles of TiO_2 with a primary particle size of 21 nm. Aeroxide® P25 TiO_2 is also a mixture of the anatase and rutile polymorphs. While it is unlikely that the bulk of the material will be aerosolized down to its primary particle size, it is likely to have a more narrow and reproducible particle size distribution than the previously used anatase TiO_2, which has a primary particle size closer to 40 µm.

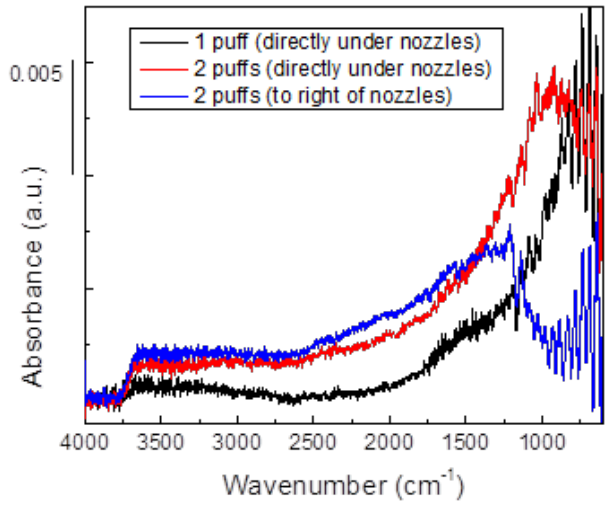

Figure 6. TIR spectra for aerosolized TiO_2.

The MIRACC was used to collect spectra for three different aerosol samples. Each sample was deposited onto a W mesh, which was placed within the aerosol generation box, and Aeroxide® P25 TiO_2 aerosols were generated and allowed to settle. One sample (blue trace in Figure 6) was placed several inches away from the point of generation.

All three samples have varying amounts of Aeroxide® P25 TiO_2 aerosols present on the surface, so it is reasonable to observe different intensities in the Ti–O region; however, each spectrum displays unique peaks, not typically seen in TiO_2 spectra, as shown in Figure 7. A series of experiments were performed in an effort to determine whether or not these peaks could be attributed to the aerosolization process, and therefore the presence of additional charge on the material.

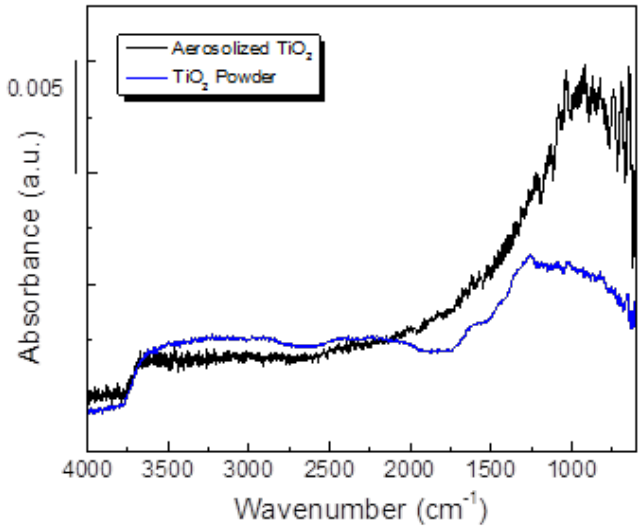

Figure 7. TIR spectra comparing aerosolized TiO_2 and neutral powder TiO_2.

Upon comparison of the powder spectrum and the aerosol spectrum, aside from the sharp peaks present below 2000 cm^{-1}, there is also a discernable rise in the overall spectrum background, again, below 2000 cm^{-1}. First, the sharp peaks are present in every TIR spectrum collected for aerosolized samples. Their existence in all acquired aerosol spectra suggests a potential experimental artifact. To determine if these peaks were in fact due to the experimental configuration, or instead, imparted by the aerosolized state itself, two tests were performed. The first investigation focused on varying the optical velocity of the spectrometer to see if a change in that variable of the experimental setup would cause a change in the spectra.[10]

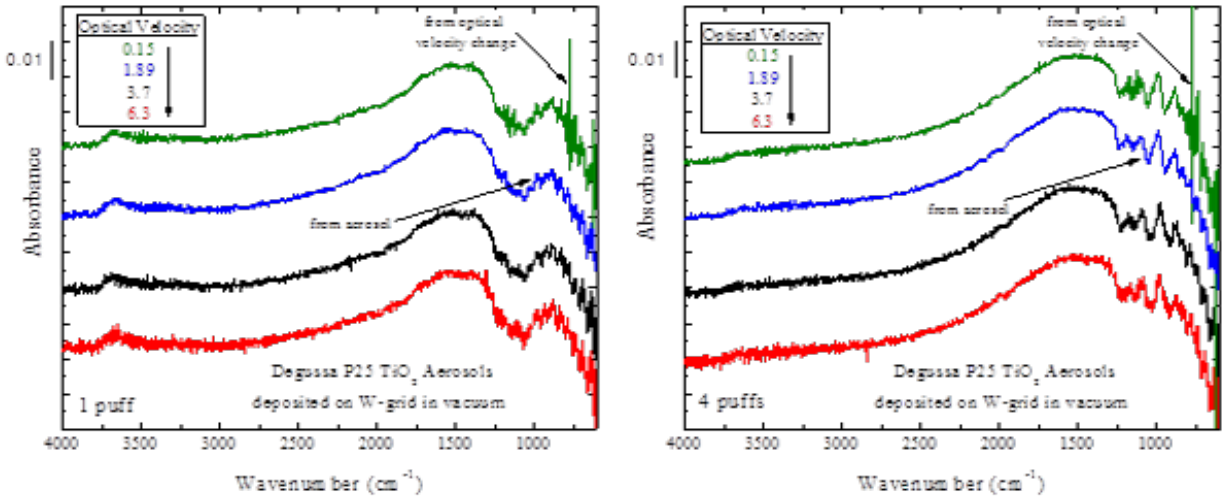

Figure 8. Data from the study of the effect of optical velocity variation. The spectra collected for a sample with only one deposition of aerosols is shown on the left. The spectra for a sample with four separate depositions of aerosolized material is shown on the right.

The spectra in Figure 8 were collected from two different aerosol samples. The left graph displays spectra recorded from a sample that was exposed to one aerosol deposition, while the graph on the right shows spectra from a sample with four subsequent aerosol exposures. The peaks due to the aerosolized TiO_2 are different between the two samples

because of the change in concentration of material on the sample. However, the optical velocity does not have a significant impact on the unique features observed in the aerosol spectra. The optical velocity does create some very sharp peaks at the lowest speed setting, but again, does not change the peaks observed throughout the rest of the spectra.

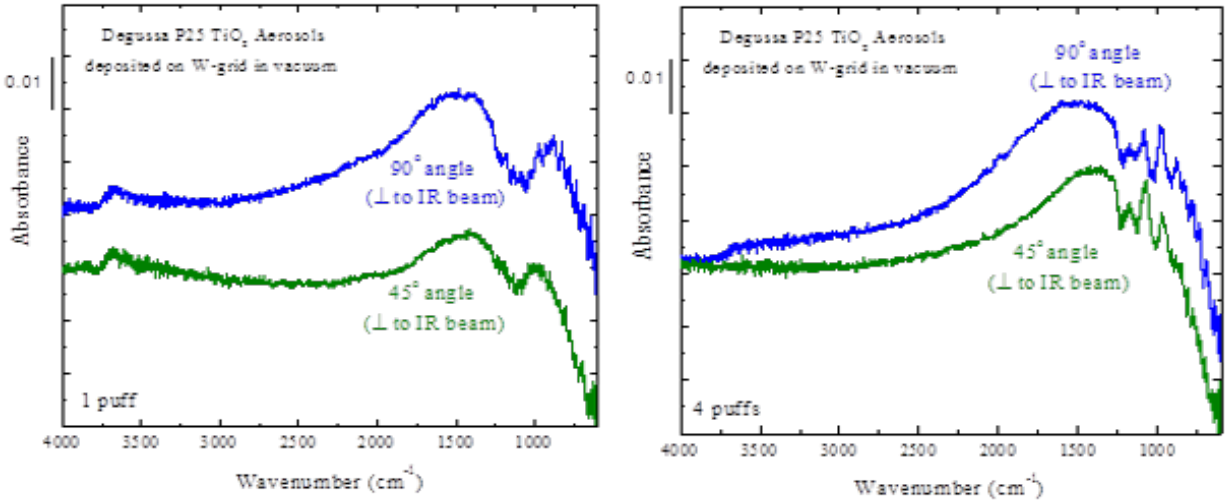

Figure 9. Data collected for samples interrogated at two different orientations relative to the incident IR beam.

The next experiment involved a change in orientation of the sample mount relative to the incident light. The same samples (one aerosol deposition versus four aerosol depositions), were oriented at a 90° angle and a 45° angle with respect to the IR beam. As with the optical velocity test, there was no impact on the presence of the peaks, as shown in Figure 9. The features do change in intensity; however, this is to be expected, as a change in sample orientation alters the effective path length and therefore the concentration of material interrogated. With no impact on the IR features, the peaks were believed to be a result of the aerosolization process. The shearing of material during aerosolization imparts charge onto the resultant aerosols, and said charge affects the observed IR spectrum. Another reason the selection of TiO_2 is advantageous is the detailed understanding of the electronics dictating its semiconductor behavior. This wide-band-gap semiconductor readily loses lattice oxygen, creating Ti^{3+} ions. A number of processes, both chemical and physical, can create these oxygen deficiencies.[11–18] It is possible that aerosolization of the material could be one such process. Upon aerosolization, lattice oxygen is lost, creating excess charge (i.e., two excess electrons per oxygen vacancy) which will occupy shallow trap states just below the conduction band minimum. Research has shown that IR illumination of this defect-rich TiO_2 can cause promotion of the electrons in the shallow traps into the conduction band. The newly promoted conduction band electrons (CBE) can be detected via IR spectroscopy and are characterized by a broad background increase the region below 2000 cm^{-1}, as seen in Figure 7 (black trace). To test whether or not the broad background absorption in the aerosolized sample is in fact due to CBEs, the sample was exposed to O_2(g). Exposure to O_2(g) will reduce the material (i.e., remove the excess charge), and the background should decrease as a result. The data shown in Figure 10 was collected before and after exposure to O_2(g). The blue and green traces represent aerosolized samples, at varying concentrations. The red spectrum was collected after the lower concentration sample (one aerosol deposition) was exposed to approximately one Torr of O_2(g). There is a noticeable decrease in the background following oxygen exposure, indicating the removal of excess charge.

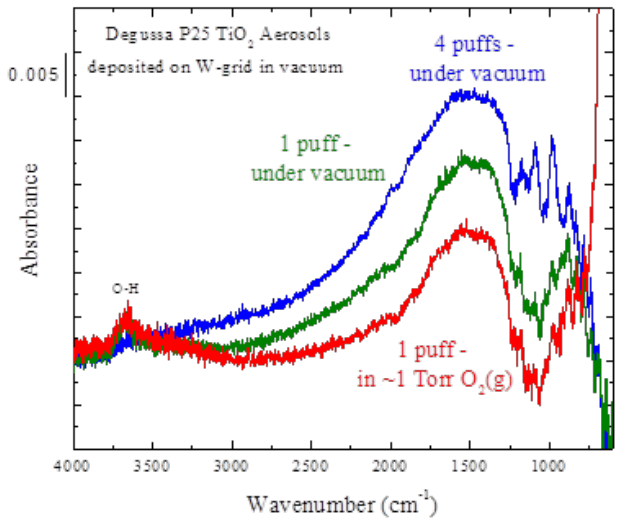

Figure 10. Spectra of aerosolized samples before and after exposure to molecular oxygen, O_2(g).

Based on the results of the oxygen exposure, an experiment was performed with electrochemical impedance spectroscopy (EIS), with the objective of distinguishing between the neutral powder TiO_2 and aerosolized TiO_2. Several samples were evaluated with EIS including aerosolized TiO_2, neutral powder at a weight of ~6 mg, a smaller amount weighing < 6 mg, and finally, clean glass slides. The glass slides were used to sandwich the other TiO_2 samples and place them into the parallel plate capacitor, therefore a baseline value was measured for this component of the setup. The data collected is shown in Figure 11, and preliminarily suggests that the aerosolized sample possesses more charge than the neutral powder; however, future testing is planned to obtain more quantitative results from this instrumentation.

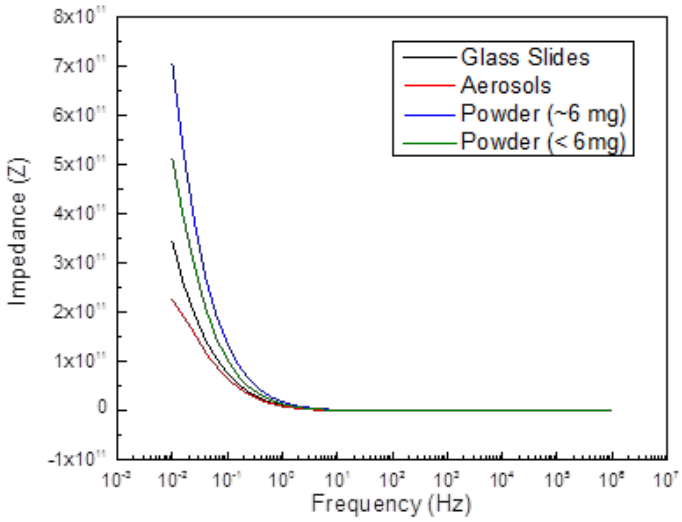

Figure 11. Data collected with EIS showing the impedance values for a sample of TiO_2 aerosols, two different TiO_2 powder samples, and clean glass slides.

4. CONCLUSIONS

The metal oxide, TiO_2, was interrogated before and after aerosolization, with the goal of evaluating the impact of the aerosolization process on said material's properties. Transmission IR spectroscopy data has shown, reproducibly, that the aerosolized material exhibits a distinctly different spectrum than that of the powder material. Initial studies performed focusing on the electronic properties of the aerosols suggest that the aerosol generation process may be

exploiting a particular feature of TiO_2—its readiness to lose lattice oxygen. Perhaps the more interesting aspect of these results is that, not only does aerosolization impart charge onto a material, but the TiO_2 may possess inherently more charge post-aerosolization because of its own unique property (i.e., final charge may be a combination of charge from material sheering as well as charge from production of oxygen vacancies). Future testing, focusing on a different metal oxide (SiO_2) will help to distinguish between these two components, as SiO_2 does not have a predisposition to oxygen loss, and therefore, will provide a more controlled sample for these investigations.

ACKNOWLEDGMENTS

The authors would like to acknowledge U.S. Army funding provided through the Edgewood Chemical Biological Center's In-House Laboratory Independent Research program. The authors would also like to thank Dr. Fountain for his support and feedback.

REFERENCES

[1] Bemer, D.; Chazelet, S.; Masson, A.; Subra, I.; Cadavid-Rodriguez, M. Measurement of the electrical charge of aerosol and its effects. *Hygiène et sécurité du travail.* **2011,** *225*, pp 3–15.

[2] Majid, H.; Madl, P.; Hofmann, W.; Khan, A. Implementation of Charged Particles Deposition in Stochastic Lung Model and Calculation of Enhanced Deposition. *Aerosol Sci. Tech.* **2012,** *46*, pp 547–554.

[3] Melandri, C.; Tarroni, G.; Prodi, V.; De Zaiacomo, T.; Formignani, M.; Lombardi, C.C. Deposition of charged particles in the human airways. *J. Aerosol Sci.* **1983,** *14* (5), pp 657–669.

[4] Lundgren, D.A.; Whitby, K.T. Effect of particle electrostatic charge on filtration by fibrous filters. *I&EC Proc. Des. Dev.* **1965,** *4* (4), pp 345–349.

[5] Calabrese, R.V.; Ranade, M.B. Pneumatic Nozzle Dissemination of Powders into Air; TCN 91291; U.S. Army Research Office: Research Triangle Park, NC, **1993;** UNCLASSIFIED Report.

[6] Sherman Hsu, C.-P. Infrared Spectroscopy. In *Handbook of Instrumental Techniques for Analytical Chemistry*; Settle, F.A., Ed.; Prentice-Hall: Upper Saddle River, NJ, **1997;** p 262.

[7] Tsai, Y.I.; Kuo, S.C. Development of diffuse reflectance infrared Fourier transform spectroscopy for the rapid characterization of aerosols. *Atmos. Environ.* **2006,** *40* (10), pp 1781–1793.

[8] Krivacsy, Z.; Hlavay, J. Method for the reliable quantitative analysis by diffuse reflectance infrared spectroscopy. *J. Mol. Struct.* **1995,** *349*, pp 289–292.

[9] Krivacsy, Z.; Hlavay, J. Comparison of calibration methods in quantitative diffuse reflectance infrared spectroscopy. *Talanta.* **1995,** *42* (4), pp 613–620.

[10] Chalmers, J.M. Mid-Infrared Spectroscopy: Anomalies, Artifacts and Common Errors in Using Vibrational Spectroscopy Techniques. In *Handbook of Vibrational Spectroscopy*; Chalmers, J.M., Griffiths, P.R., Eds.; John Wiley & Sons, Ltd: Chichester, UK, **2002;** Vol. 3; pp 2327–2347.

[11] Panayotov, D.A.; Burrows, S.P.; Yates, J.T.; Morris, J.R. Mechanistic Studies of Hydrogen Dissociation and Spillover on Au/TiO_2: IR Spectroscopy of Coadsorbed CO and H-Donated Electrons. *J. Phys. Chem. C.* **2012,** *116*, pp 4535–4544.

[12] Panayotov, D.A.; Morris, J.R. Thermal Decomposition of a Chemical Warfare Agent Simulant (DMMP) on TiO_2: Adsorbate Reactions with Lattice Oxygen as Studied by Infrared Spectroscopy. J. *Phys. Chem. C.* **2009,** *113* (35), pp 15684–15691.

[13] Diebold, U. The surface science of titanium dioxide. *Surf. Sci. Rep.* **2003,** *48* (5–8), pp 53–229.

[14] Pang, C.L.; Lindsay, R.; Thornton, G. Chemical reactions on rutile TiO_2(110). *Chem. Soc. Rev.* **2008,** *37*, pp 2328–2353.

[15] Linsebigler, A.L.; Lu, G.; Yates, J.T. Photocatalysis on TiO_2 Surfaces: Principles, Mechanisms, and Selected Results. *Chem. Rev.* **1995,** *95*, pp 735–758.

[16] Campbell, C.T. Ultrathin metal films and particles on oxide surfaces: structural, electronic and chemisorptive properties. *Surf. Sci. Rep.* **1997,** *27* (1–3), pp 1–111.

[17] Henrich, V.E.; Dresselhaus, G.; Zeiger, H.J. Observation of Two-Dimensional Phases Associated with Defect States on the Surface of TiO_2. *Phys. Rev. Lett.* **1976,** *36* (22), pp 1335.

[18] Fox, M.A.; Dulay, M.T. Heterogeneous photocatalysis. *Chem. Rev.* **1993,** *93* (1), pp 341–357.

Comparative characterization of the host and viral proteome in Sindbis virus identifies sorting nexin 5 as critical host factor for alphavirus replication

Andy Kilianski[a], Amanda Piper[b], Ryan Schuchman[b], Ricardo Vancini[b], Jose M.C. Ribeiro[c], Farooq Nasar[d], Thomas Sprague[d], Raquel Hernandez[b], Trevor Glaros[a*]
[a]U.S. Army Edgewood Chemical Biological Center, Research & Technology Directorate, 5183 Blackhawk Rd, Aberdeen Proving Ground, MD
[b]North Carolina State University, 346 Polk Hall, Raleigh, NC
[c]National Institute of Allergy and Infectious Diseases, Laboratory of Malaria and Vector Research, Rockville, MD
[d]U.S. Army Medical Research Institute of Infectious Disease, Department of Virology, Fort Detrick, MD

ABSTRACT

Alphaviruses, such as Chikungunya virus, continue to plague public health in developing and developed countries alike. Identifying effective antivirals is an important aspect of combating these diseases. Targeting host factors necessary for viral replication has become an attractive strategy for avoiding drug resistance mutations that are common in RNA viruses. Host factors have been observed in virus particles previously; however, recent advances in mass spectrometry methods and instrumentation now allow for the accurate identification of proteins in low quantity within virus particles. To determine if host proteins are specifically packaged in alphavirus virions, Sindbis virus was grown in multiple host backgrounds, and purified virions were interrogated for their total protein content by liquid chromatography mass spectrometry. This method was performed in vertebrate and invertebrate backgrounds and resulted in the identification of host factors not previously associated with alphavirus entry, replication, or egress. One of these host proteins, sorting nexin 5, was shown to be critical for the replications of both Sindbis virus and Mayaro virus. In addition to the host proteins identified, Sindbis virus nonstructural protein 2 was detected within virions grown in all backgrounds. The proviral and RNA interacting capabilities of nonstructural protein 2, coupled with its presence in the virion, support a role for nonstructural protein 2 during packaging and/or entry of progeny virus. Taken together, this novel strategy successfully identified at least one promising candidate for a host-based therapeutic and the other protein identifications provide insight into alphavirus-host interactions during viral replication in vertebrate and invertebrate backgrounds.

Keywords: proteomics, biomarkers, viral proteomics, host proteins, mass spectrometry

1. INTRODUCTION

The renewed emergence of viral diseases and the discovery of novel pathogenic viruses ensure constant risks to public health. The alphavirus family includes emerging and well characterized vector-borne diseases including Eastern, Western, and Venezuelan equine encephalitis viruses; Chikungunya virus; and Sindbis virus (SINV), which is nonpathogenic.[1] Many of these pathogens originate from zoonotic reservoirs, like mosquitoes, and lack effective vaccines or antivirals.[2] Host-based therapeutics are thought to be attractive avenues, but identifying targets for this approach requires a detailed understanding of how these viruses interact with host factors throughout the replication cycle.[3,4] To uncover these types of interactions, this research focused on the identification of host proteins within the virus particles, and future studies will address any functional relevance these specific proteins may have in the viral lifecycle.

To begin the viral replication cycle, SINV attaches to host cells using the E2 protein. Once the correct cell receptor has been identified, the positive sense, single-stranded viral RNA gains entry to the cell by direct penetration.[5] Several host receptor candidates exist, but there is no conclusive evidence that solely implicates a single one of these candidates in the replication cycle.[6–8] In the cytoplasm, the positive-sense RNA is then translated into four

nonstructural proteins—nsP1, nsP2, nsP3, and nsP4. nsP1 functions as a methyltransferase to add the methylguanosine cap to all newly synthesized viral RNA. nsP2 has two differing biological activities—it serves as the protease that cleaves the nonstructural polypeptide and also as a helicase. nsP3 is involved in the negative-sense RNA strand synthesis, while nsP4 is the RNA-dependent RNA polymerase.[9] Translation of subgenomic RNA produces the viral structural proteins (E1, E2, and capsid). The capsid protomers are assembled into viral nucleocapsids with RNA in the cytoplasm and are transported to the plasma membrane.[9] The virus fully matures at the plasma membrane by incorporation of the E1 and E2 proteins around the nucleocapsid core.[9] The assembly of the mature virus by the addition of the E proteins also adds a membrane between the capsid and E protein shell.[10,11] The composition of this membrane can vary between host organisms, mosquitoes and vertebrates, and even host cells due to the broad range of organs that are infected in the host. For this reason, we used cell lines of various tissue types and host backgrounds to characterize the complement of host cell-derived proteins. To determine the host protein content of the model alphavirus particle, SINV, a mass spectrometry-based approach was utilized to identify host proteins within virions that might not be resolvable using other methods. As mass spectrometry has evolved, the improved sensitivity of these techniques can answer questions regarding the composition of viral particles that have not been detected by conventional biochemical analysis.[12] Mass spectrometry (MS) can allow for the identification of proteins involved in virus replication and assembly that are specifically associated with the virus structure or alternatively have become trapped in the structure during the process of maturation. This data is important for the design of new diagnostics, prophylactics, treatments, and forensic techniques to combat virus infection.

In this study, highly purified SINV preparations were analyzed using liquid chromatography (LC) tandem mass spectrometry (LC-MS/MS) to determine if previously undetected host proteins were packaged into virus particles. When the virus is replicated in a human cell background in HEK293 or HepG2 cells, more than 124 unique host proteins were discovered. Functional analysis of these proteins revealed several unique molecular cellular roles including catalytic activity, receptor activity and binding. When the host background was changed to a different vertebrate species, hamster BHK21 cells, more than 38 host proteins were identified. When the host protein profiles between mammalian species were cross compared, 8 proteins were found in common. SINV was also prepared in a mosquito background using the C7-10 *Aedes albopictus* cell line. Although more than 50 host proteins were identified in the mosquito background, phospholipid scramblase was the most abundant and interestingly was the only protein found in both the invertebrate and vertebrate backgrounds. A detailed mapping of the viral proteome revealed a nearly 75 % coverage of SINV's structural polyprotein, containing peptides detected for capsid, E3, E2, and E1, but not 6K. An unexpected finding was that peptides from SINV's nonstructural polyprotein were also detected, but specifically only for nsP2, the viral protease.

We attempted to generate homozygous stable knockouts of each of the conserved host proteins (eight) in HEK293 cells. Several of the proteins proved to be lethal knockouts; however, we were able to obtain homozygous knockouts for sorting nexin 5 (SNX5) and RNA binding protein 3 (RBM3). Using these knockout cell lines, we observed a significant suppression in SINV production when compared to wild type HEK293s. To confirm this observation, we also performed phenotypic analysis using Mayaro virus (MAYV); a 'new-world' alphavirus. To our surprise, viral replication was also strongly inhibited. To the best of our knowledge, this is the first report that indicates SNX5 plays a critical role in the alphavirus's life cycle. Collectively, this novel LC-MS/MS approach has enhanced our understanding of the alphavirus replication while also identifying novel host targets with therapeutic promise.

2. METHODS

2.1 Virus preparation and purification

The heat resistant SINV (SVHR) used in this study was provided to Dr. Dennis Brown (North Carolina State University) in the late 1960s after being first isolated by Burge and Pfefferkorn in 1966.[13] SVHR was grown in experimental duplicates in BHK21 cells (hamster), HEK293 cells (human), HepG2 cells (human), and C7-10 cells (mosquito) as described.[14] All cells were obtained from American Tissue Culture Collection® (HEK-293: #CRL-1573, HepG2: #HB-8065, BHK21: #C-13) except for the C7-10, which is a laboratory cell line.[15] Culture medium from each uninfected cell culture were harvested and served as a negative control. Virus and negative controls were harvested from 10-T75 flasks (Corning®), which produced enough virus to form a visible band in a 30 mL potassium tartrate gradient. Cells were infected at a multiplicity of infection (MOI) of 100 PFU/mL and allowed to replicate for a single cycle. The resulting virus was twice purified in linear potassium tartrate gradients by isopycnic ultracentrifugation (Beckman Coulter®, Inc. SW 28 rotor, 18 hours at 24,000 rpm). The resulting band of purified

virus was collected and washed twice by pelleting the virus in 1X phosphate-buffered saline (PBS). A sample of the purified population was then visualized by transmission electron microscopy (TEM) as previously described.[16] Additionally, each preparation was resolved on a 4–12 % Bis-Tris SDS-PAGE gel (Invitrogen™) as described previously[17] and stained with SimplyBlue™ (Invitrogen™) according to the manufacturer's instructions. Visualized bands were excised and an in-gel digestion was performed as described previously,[18] prior to LC-MS/MS analysis for protein identification.

2.2 Protein extraction and digestion

Viral preparations and their respective negative controls were processed for LC-MS/MS analysis using the filter-aided sample preparation (FASP) method as previously described.[19] Briefly, following purification the total protein concentration was determined and all preparations were normalized to 0.5 µg/µL using sterile PBS, aliquoted in 10-µg fractions, and stored at -80 °C. A total of 10 µg of total protein (20 µL) was mixed 1:1 with M-PER™ mammalian protein extraction reagent (Thermo Scientific™) supplemented with 50 mM dithiothreitol and heated to 95 °C for 10 minutes. Once cooled to room temperature, the samples were mixed with 200 µL of urea buffer (8 M urea, 100 mM Tris-HCl, pH 8.5), placed over a 30-kDa filter spin column (Millipore® Ultracel™ YM-30), and centrifuged at 14,000 x g for 30 minutes at room temperature to collect all proteins on the filter membrane. Denatured and reduced proteins were then alkylated by adding 100 µL of indole-3-acetic acid solution (0.05 M iodoacetamide in urea buffer) to each filter and incubating at room temperature in the dark for 20 minutes. Following alkylation, the samples were centrifuged at 14,000 x g for 20 minutes to remove the alkylation solution. Next, each sample was washed three times with 100 µL of urea buffer, and then three times with 100 µL of 100 mM triethylammonium bicarbonate (TEAB). Centrifugation at 14,000 x g for 30 minutes was used to remove each wash including the final wash. To digest the captured protein, 100 µL of a trypsin digestion solution (10 µg/mL in 100 mM TEAB) was placed on each membrane and incubated in a sealed tube overnight at 37 °C with shaking. After incubation, the peptides were collected for LC-MS/MS analysis in a clean tube by centrifuging each tube for 30 minutes at 14,000 x g. The membrane was washed by centrifugation one time with 50 µL of 100 mM TEAB and once with 50 µL of 0.5 M NaCl. All washes were collected and pooled with the final peptide eluate. Each sample was then acidified using 10 % trifluoroacetic acid until the final pH reached roughly 2–3. Prior to MS analysis, each sample was desalted using Pierce™ C18 desalting columns (Thermo Scientific™) according to the manufacturer's directions.

2.3 LC-MS/MS analysis

Tryptic peptides were analyzed (technical triplicates) on an Orbitrap™ Elite™ MS coupled with the EASY-nLC™ II nano-flow LC pump system. Dried peptides were reconstituted in 3 % acetonitrile/0.1 % formic acid and resolved on virgin PicoFrit® 15 cm x 75 µm ID high-performance liquid chromatography columns packed with 5 µm BioBasic™ C18 particles 300 Å (New Objective™) using a 130-minute multistep gradient (0–5 minutes: 5–10 % B, 6–110 minutes: 10–35 % B, and 111–130 minutes: 35–95 % B). For the gradient, the A buffer is 3 % acetonitrile/0.1 % formic acid and the B buffer is 95 % acetonitrile/0.1 % formic acid. Orbitrap™ MS1 scans were performed at a resolution of 120,000 at 400 *m/z*, with a scan range of 110–2000 *m/z*. The top 20 precursors were selected for tandem MS (MS/MS) data-dependent fragmentation. An MS/MS spectrum was acquired using the ion trap scanning in normal mode (top20 method). The minimum signal required to trigger a data-dependent scan was 5,000. Collision-induced dissociation was used to generate MS/MS spectra with the following settings: normalized collision energy 35 %, default charge state 2, isolation width 2 *m/z*, and activation time 10 ms. The automatic gain control target was set to 1×10^6 for MS and 5×10^4 for MS/MS with a maximum accumulation time of 200 ms. Dynamic exclusion was set for 60 seconds for up to 500 targets with a 5-ppm mass window. A lock mass of 445.120025 was used for internal calibration to improve mass accuracy.

2.4 Mass spectrometry data processing

Spectra data was processed using Proteome Discoverer™ 1.4 (Thermo Scientific™) with the SEQUEST search algorithm against a SINV polyprotein database (Uniprot ID: P03317) merged with either *Homo sapiens* (RefSeq Tax ID: 9606) or *Cricetulus griseus* (RefSeq Tax ID: 10029). The *A. albopictus*-deducted proteome[20] data was downloaded from VectorBase.[21] Additional peptides were downloaded from the National Center for Biotechnology Information Transcriptome Shotgun Assembly sequence database. The non-redundant proteomes were organized in Microsoft® Excel® spreadsheets[22] and annotated as previously described.[23] The resulting FASTA file was merged with the SINV polyprotein and used to search against the SINV mosquito preparations. Dynamic modifications were set for carbamidomethylation of cysteine [+57.02 Da], oxidation of methionine [+15.99 Da], and N-terminal acetylation

[+42.011]. MS/MS spectra were searched with a precursor mass tolerance of 10 ppm and a fragment mass tolerance of 0.6 Da. Trypsin was specified as the protease with a maximum number of missed cleavages set to 2. A false discovery rate was calculated using PERCOLATOR and was set at < 1 % to score high confidence peptide identifications. Grouping and functional analysis was performed using the PANTHER classification system for the human background, using only each protein ID's accession number.[24]

2.5 Phenotypic studies with stable knockout HEK293 cells

HEK-293 knockout cell lines were purchased from Applied Biological Materials, Inc. (Richmond, BC, Canada). Cell lines were propagated at 37 °C with 5 % CO_2 in Dulbecco's modified Eagle's medium containing 10 % (v/v) fetal bovine serum (FBS), sodium pyruvate (1 mM), 1 % (v/v) non-essential amino acids, and 50 µg/mL gentamicin. cDNA clones of MAYV and Marburg virus (MARV) enhanced green fluorescent protein (GFP) were obtained from Dr. Scott Weaver at the University of Texas Medical Branch, and rescued as previously described.[25] MAYV and MAYV enhanced GFP were rescued in Vero cells. MAYV replication was assessed on HEK-293 wild type, RBM3$^{-/-}$, and SNX5$^{-/-}$ cell lines in triplicate on 50 % confluent monolayers in 6-well plates that were infected with MAYV enhanced GFP at an MOI of either 1.0 PFU/cell or 0.1 PFU/cell. Following infection, enhanced GFP expression was monitored at 1 and 2 days post-infection. Phase-contrast and fluorescent field photographs were taken at various time points post-infection.

SVHR replication was also assessed using HEK-293 wild type, RBM3$^{-/-}$, and SNX5$^{-/-}$ cell lines. Briefly, HEK293 monolayers were infected at equal MOIs (approximately 10 PFU/cell) and allowed to incubate for 20 hours. After infection, the media was removed, the cells were gently washed with PBS-D, and RNA was extracted from the monolayers with TRIzol™ Reagent, following manufacturer's instructions. After extraction, the RNA was normalized by total RNA concentration. Reverse transcription was done on the normalized RNA using a Maxima First Strand cDNA synthesis kit (Thermo Scientific™) and the following SINV-specific quantitative polymerase chain reaction (PCR) assay was used with an Applied Biosystems™ 7500 Fast Dx Real-Time PCR Instrument to quantify viral RNA. For SVHR, the following primers were used: SVHR Sense: 5'-TGTGTACACCATCTTAGC-3'; SVHR Antisense: 5'-CAAAGGTATGCACAACTG-3'; and SVHR Probe: 5'-FAM-AGTGCCTGACGCCATA -MGB-NFQ-3'.

3. RESULTS

3.1 Determination of viral purity

To effectively analyze the virus-associated host protein content, ultra-pure preparations of virions were prepared. Host background contamination from cellular vesicles or debris, not specifically incorporated, must be eliminated by the virus purification procedure prior to MS analysis. First, virus was grown and supernatant collected from infected and non-infected cells. Crude viral preparations were clarified by low speed centrifugation to remove large complexes and particulates. Negative control fractions were run through the same process as virus-containing fractions. The clarified material was then run through two serial potassium tartrate density gradients using isopycnic ultracentrifugation. Virus from the second purification was then pelleted through PBS as the final purification step. To determine if this purification scheme (Figure 1A) resulted in visually pure preparations of virus particles, fractions were visualized using TEM (Figure 1B). The electron micrographs of the three-step purified SINV preparations showed extremely pure virus preparations, with no cell debris or other cell-associated membrane-bound vesicles. To determine if there was any other unexpected protein contamination in the preparations, each purified prep was resolved on an SDS-PAGE gel and the proteins were stained with SimplyBlue™ (Invitrogen™). Like the TEM images, these gels also confirmed that the preparations were highly pure with no major protein contaminates (Figure 1C). As confirmed by LC-MS/MS, the only visible bands in the viral preps were from the virus' structural proteins—E1, E2, and capsid.

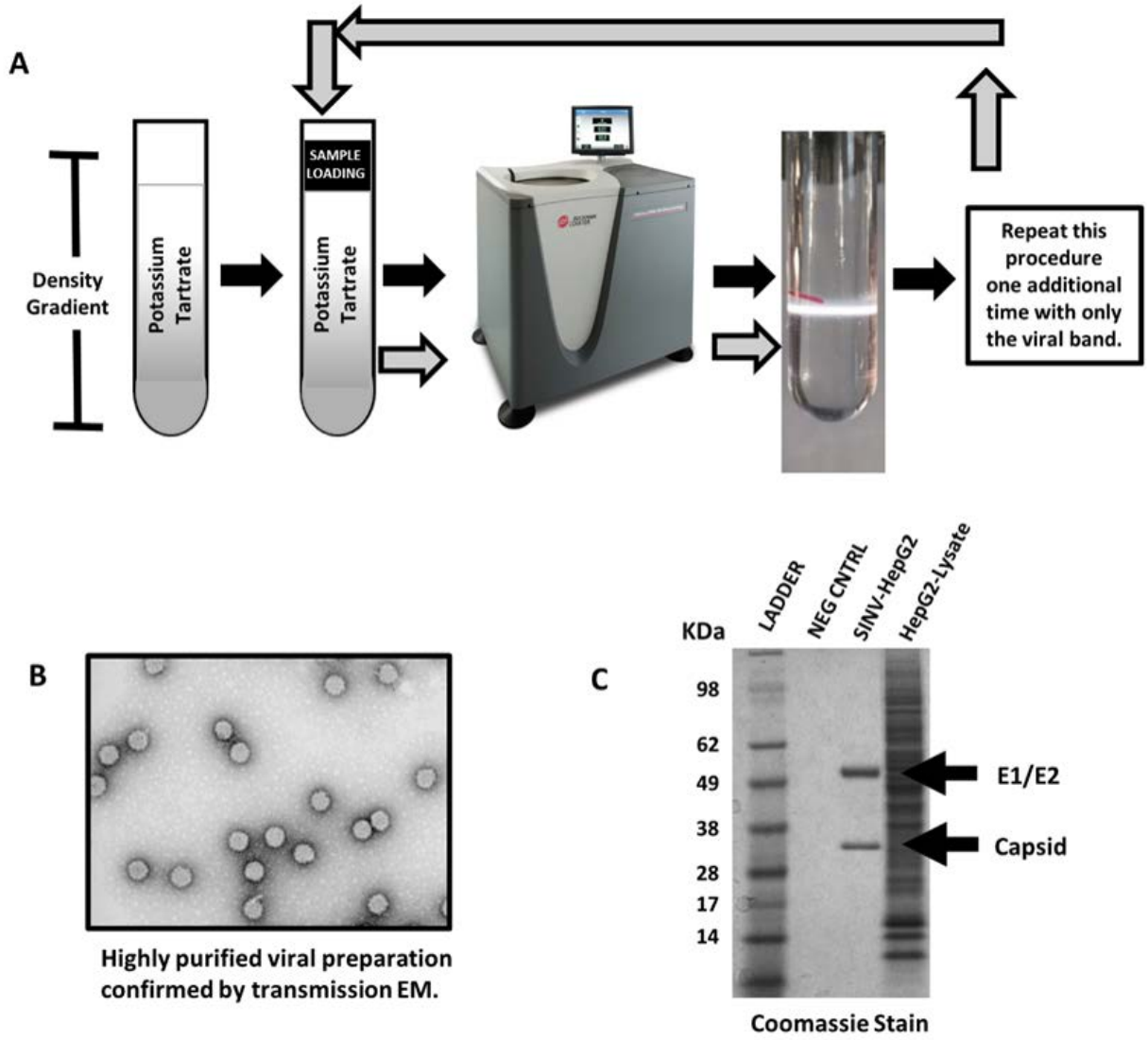

Figure 1. SINV virion purification strategy and production flowchart. A) Crude viral preparations were purified over two potassium tartrate density gradients done in series using isopycnic ultracentrifugation. Negative controls (uninfected cell culture supernatant) were processed in parallel with the virus preparations. B) TEM images were taken of the purified virions to confirm efficiency of this enrichment procedure. C) An SDS-PAGE gel was stained with SimplyBlue™ (Invitrogen™) for each of the viral preparations. HepG2 preparations are presented here, but this gel is representative of all the viral preparations regardless of the host cellular background.

3.2 Host protein identification and functional analysis of purified SINV virions

Visualization of the purified viral preparations indicated that no contaminating particles were present, so SINV preparations were analyzed, in parallel with negative control fractions, using LC-MS/MS. Viral preparations and negative controls from BHK21 (hamster, *C. griseus*), C7-10 (mosquito, *A. albopictus*), HEK293 (human), and HepG2 (human) cell backgrounds were analyzed to determine if any host proteins could be detected. Each sample was analyzed in technical triplicate on virgin C18 high-performance LC columns to ensure that carry over from sample to sample would not result in false host protein identifications. LC-MS/MS spectral data was searched using the SEQUEST algorithm in Proteome Discoverer™ 1.4 (Thermo Scientific™) to identify peptides and align them to known host proteins from each background. Each purified virus preparation yielded unique host protein identifications with only a limited number of host proteins being identified in the negative controls. Keratin was often identified in the negative control and was ignored for functional interpretation, since it was likely introduced during sample processing. In the human backgrounds, 124 host proteins were identified—91 in HepG2 cells and 58 in HEK293 cells.

Using the PANTHER classification to characterize these protein identifications, a significant portion of the proteins fell into three major molecular functional classes—binding, catalytic activity, and receptor activity. These host proteins cover a wide range of protein classes, such as nucleic acid binding and receptors.

While the human backgrounds are used as an example here, an additional 38 host proteins were identified from the BHK21 hamster background and 51 proteins from the C7-10 mosquito background. Both hamster and human genomes and proteomes are well characterized; however, the same level of characterization does not exist in the mosquito host *A. albopictus*, as the complete genome sequence was very recently published.[20] To analyze the raw data obtained from the C7-10 cell background, a curated draft proteome from *A. albopictus* was utilized (see section 2, Methods). Many of the proteins identified in the C7-10 background classify in similar functional categories and classes as the proteins identified in the mammalian backgrounds. Interestingly, for the mosquito background, phospholipid scramblase was overwhelmingly represented when compared to the other mosquito host proteins identified. Scramblase was detected as eight unique peptide sequences a total of 57 times (peptide-spectrum matches) for a total sequence coverage of 30 %.

3.3 Conserved host protein signatures between human, hamster, and mosquito backgrounds

When comparing replicate human virus preparations to each other (HEK293 versus HepG2), we observed a 36 % overlap, or identified 20 proteins, respectively (Figure 2). Given that the limiting factors that dictate detection by LC-MS/MS are dynamic range and instrument sensitivity, the host proteins which were commonly detected between each preparation were also in the highest abundance within these virus particles. In addition to comparing preparations within the same species, we also compared the host proteins identified across species. Using this strategy, we identified eight protein signatures that were conserved between hamster and human (Figure 2). Cellular nucleic acid binding protein 6 (CNBP6), RBM3, myosin (MYO), and claudin (CLDN) were present in all backgrounds. Interestingly, the exact peptide sequence was identified for CNBP6, RBM3, and SNX5 from all vertebrate-derived samples. When we compared the mammalian backgrounds to the mosquito background, we found that only phospholipid scramblase was conserved. Interestingly, we detected that the scramblase peptides overlapped, even though only 51 % of the amino acid sequence is conserved between the mosquito and humans (Figure 3).

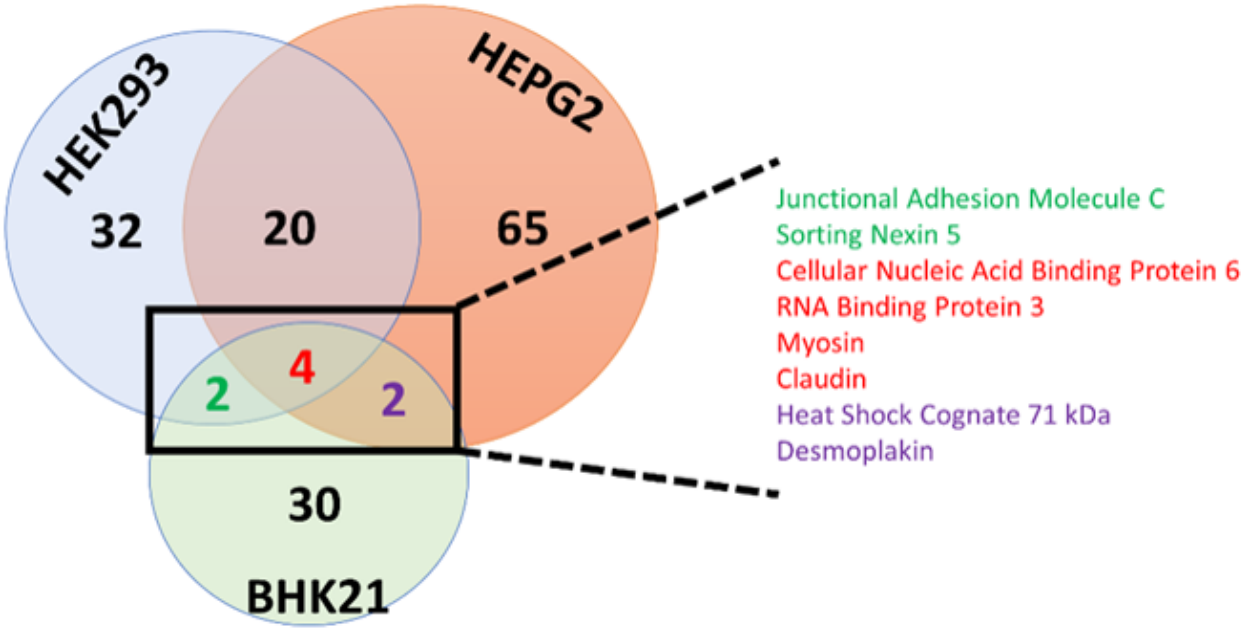

Figure 2. Comparison of the mammalian viral host proteomes.

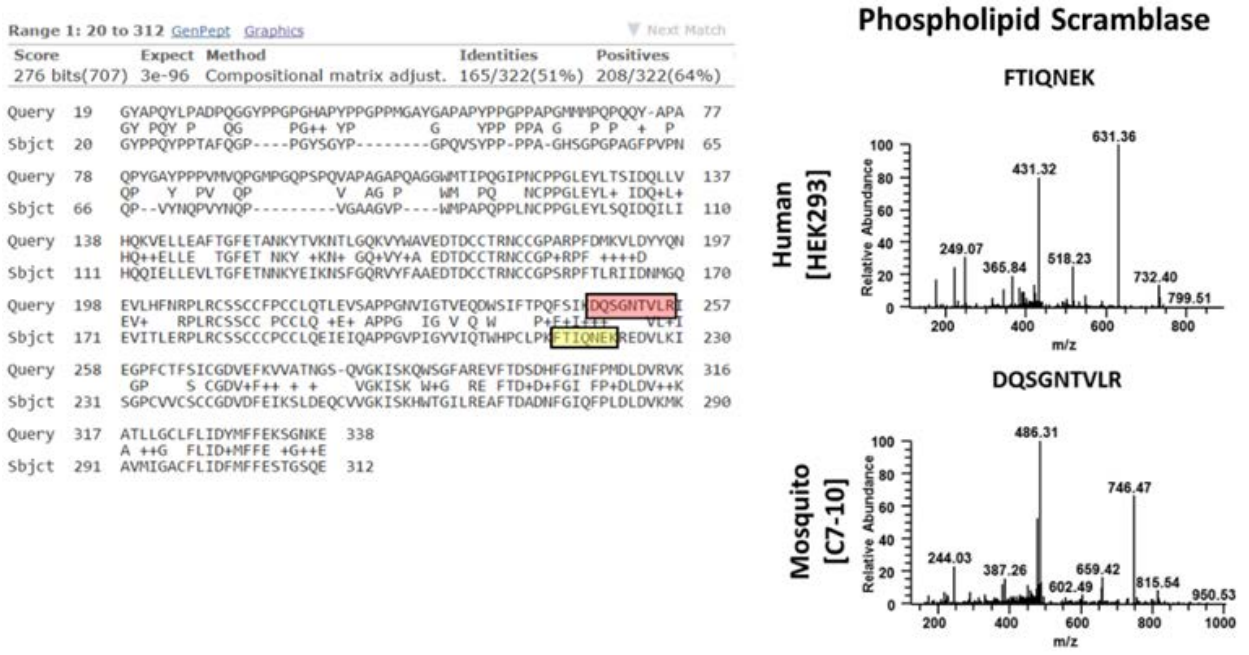

Figure 3. Mosquito phospholipid scramblase detection. The National Center for Biotechnology Information Basic Local Alignment Search Tool was used to align the protein sequence of phospholipid scramblase for *A. albopictus* and *H. sapiens*. The "Query" is the *A. albopictus* sequence (Accession #: 604777565) and the "Sbjct" is the *H. sapiens* sequence (Accession #: 10863877). MS/MS spectra were used to identify phospholipid scramblase in HEK293 and C7-10 cells. Peptide sequences presented below the alignment are highlighted—red (mosquito) and yellow (human).

3.4 Viral nonstructural proteins identified in purified SINV virions

In addition to the detailed analysis of the host proteome contained within the SINV virion, the viral proteome within SINV virions was also examined. Raw data gathered from each SINV preparation regardless of host background was pooled together to generate a comprehensive sequence map of SINV structural and nonstructural polyprotein coverage. For SINV's structural polyprotein, 91 unique peptide sequences were detected a total of 10,833 times. This resulted in a total sequence coverage of 74 %. Peptides from every processed structural protein were detected except 6K. In this study, we also searched our raw data against the SINV's nonstructural polyprotein. From this analysis, we only detected peptides from nsP2. No peptides from any other nonstructural protein were detected. For nsP2, we detected 20 unique peptide sequences at total of 121 times. When compared to the structural polyprotein, peptides corresponding to nsP2 were detected with a frequency of roughly 1 %. To confirm that nsP2 is not co-purifying with other structural proteins via protein-protein interactions, we performed an additional high-salt wash in 1M KCl on viral pellets prepared in the BHK background. LC-MS/MS analysis of these preparations still resulted in high sequence coverage of nsP2 and no other nonstructural protein.

3.5 Determining the importance of the conserved mammalian host proteins on the viral life cycle

Stable knockouts of each of the conserved host proteins were attempted in human HEK293 cells. Several of the proteins proved to be lethal knockouts; however, we were able to obtain homozygous knockouts for SNX5 and RBM3. Using these knockout cell lines, we observed a significant suppression in SINV production by real-time PCR, but only in the SNX5 knockout cell line when compared to wild type HEK293 (Figure 4).

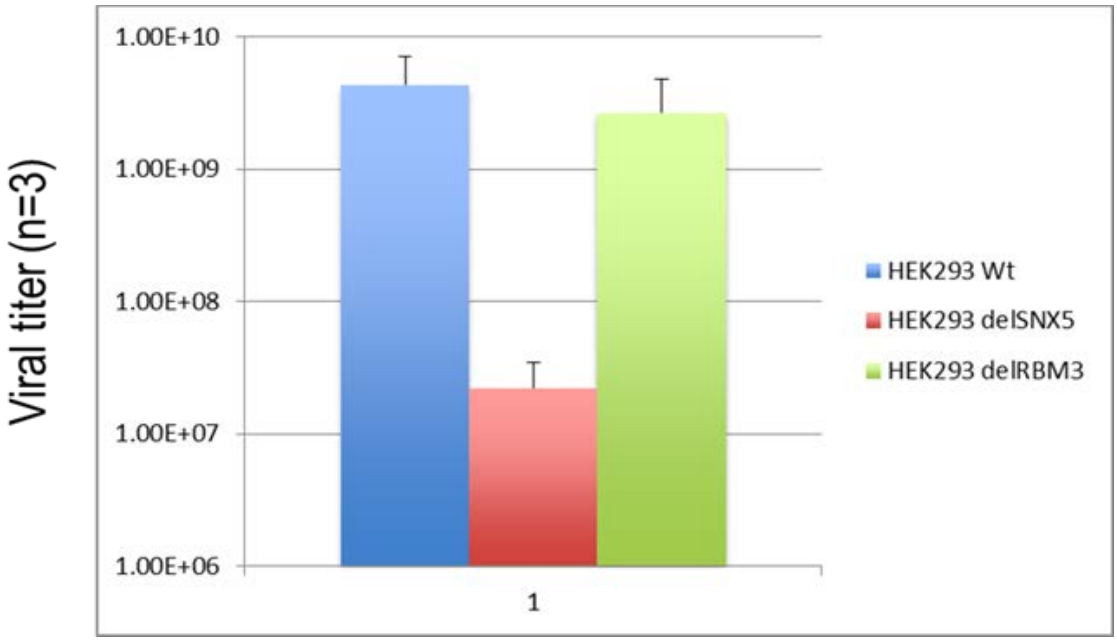

Figure 4. SVHR production determined by real-time PCR in HEK293 cells lacking RBM3 or SNX5.

Alphaviruses diverged in their evolution during the last few thousand years to two distinct groups—the old world and the new world. Although both groups share overall structure, recent evidence suggests that they have developed different mechanisms of host transcription inhibition.[26] Therefore, to establish that this observation is not specific just to SINV, but rather to alphaviruses, we repeated these studies using the 'new-world' MAYV. Using a microscopy-based approach with GFP-labeled MAYV, we were able to confirm our SINV observations. As shown in Figure 5, the production of MAYV was dramatically inhibited in only the SNX5 knockout cell lines at two different MOIs (0.1 PFU/cell and 1 PFU/cell) when visualized both 24 hours and 48 hours post-exposure.

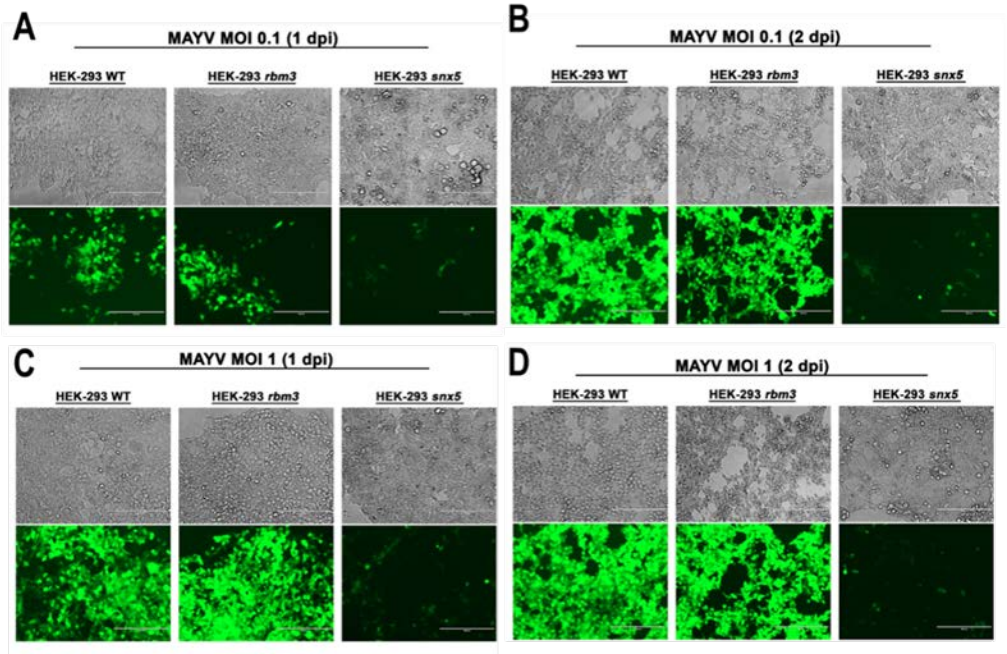

Figure 5. MAYV production in HEK293 cells lacking RBM3 or SNX5 visualized by confocal microscopy. Wild type, RBM3-/-, or SNX5-/- HEK293 cells were plated and infected with a MOI of either 0.1 PFU/cell (A & B) or 1.0 PFU/cell (C&D) for either one (A&C) or two (B & D) days post-infection.

4. DISCUSSION

The lack of a significant increase in the development of antivirals, vaccines, and investigative tools for the study of pathogenic viruses remains a major gap in the ability to protect susceptible populations from emerging diseases. Basic understanding of virus-host biology remains central to the development of these products, and new techniques must be harnessed to increase this basic scientific knowledge. Here, LC-MS/MS was utilized to determine if the prototypical alphavirus, SINV, specifically packaged host proteins into its virus particles. Using a two-stage purification process for SINV virions, followed by a FASP digestion procedure and MS analysis, revealed that a variety of host proteins were incorporated into SINV particles in each host background. Central to this approach was ensuring that the viral preparations were free of virion-associated impurities and cellular debris. TEM and a stained SDS-PAGE gel revealed that our approach yielded highly pure viral preparations that were not contaminated with other cellular debris, membrane fragments, or any significant protein contamination Figure 5 B & C). The observation that 6K was not found associated with the SINV particles is evidence of the purity of the virus preparations. This was expected since 6K is not a virion associated in SINR.[27] The mosquito proteome is not well annotated, and the characterization of MS data from the C7-10 background required our group to generate a manually curated mosquito proteome. Despite this limitation, the functional role of these proteins being associated with SINV replication will aid in experimental validation of their proteomic annotation. In the mammalian backgrounds, the identification of a core group of conserved host proteins creates strong leads for further antiviral potential (Figure 2). These proteins should serve as the first set of proteins interrogated for their functional relevance during the SINV life cycle.

In this study, SNX5 was found to be conserved within multiple different host cellular backgrounds. By generating a stable HEK293 SNX5 knockout cell line, we were able to show that SNX5 is essential for the growth of both SINV and MAYV. Without this host protein, the production of virions was found to be significantly inhibited both by real-time PCR and by microscopy. SNX5 has been shown to be critical in the replication of other intracellular pathogens as well. SNX5 forms part of the retromer complex within host cells, playing an important role in trafficking membranes between the plasma membrane and Golgi apparatus. These membrane movement events are required to recycle receptors and other plasma membrane components during normal cellular processes. Recently, a pair of studies has elucidated a role for SNX5 as a restriction factor for pathogen infection. The intracellular bacteria *Chlamydia trachomatis* requires membrane structures to replicate and produce infectious progeny within host cells. Both Aeberhard et al. and Mirrashidi et al. determined that SNX5 can negatively impact the membrane rearrangements required by *C. trachomatis* to replicate efficiently.[28,29] To counter this restrictive effect, *C. trachomatis* sequesters SNX5 in replicative bodies and prevents its action on membrane rearrangements. Although we have shown that SNX5 is essential for alphavirus replication, the exact mechanisms of action remains unknown. It is possible that SNX5 might be hijacked by SINV during particle assembly to induce events necessary for infectious particles to be formed. It is also possible that SNX5 can restrict SINV infection via a mechanism similar to *C. trachomatis*, so the sequestration of SNX5 at sites of SINV particle formation may be used as a virus-induced countermeasure. The retrograde pathway has not been implicated in alphavirus maturation, so the role of SNX5 in particle formation is especially of interest. Additionally, SNX5 has recently been found to co-localize with Ebola virus during the internalization process via micropinocytosis.[30] Therefore, it is possible that SNX5 provides fitness by helping to initiate viral internalization. SINV has been shown to enter host cells independent of clathrin- or caveloae-mediated endocytosis, so this finding may implicate SNX5 in host-pathogen processes that reach beyond micropinocytosis.[31] Further research to uncover the exact role of SNX5 in viral replication is warranted and needed to uncover potential host candidates for antiviral therapeutics.

While SNX5 has been definitively implicated in the pathogenesis of infectious agents, the other conserved proteins have a less-clear potential role in SINV replication. Junctional adhesion molecule C (JAMC) has roles in cancer biology and pathogenic immune responses related to cell adhesion and homing, but has no defined role in virus biology.[32,33] SINV has been shown to bud from localized regions of the plasma membrane, so it is possible that JAMC is enriched at this site and helps create a supportive environment for SINV budding.[34] CNBP6 and RBM3 both have the ability to bind single-stranded RNA—the species of RNA encoding the SINV genome.[35] These RNA-binding proteins could protect viral RNA from host cell antiviral sensors while also promoting translation of viral polyproteins upon progeny virus entry into the host cell cytoplasm. However, as shown in this study, RBM3 does not seem to have a direct effect on viral replication. HSP70/71 is important throughout the viral life cycle, although it remains unclear if these molecules play a role by incorporation into alphavirus and SINV virions.[36,37] However, HSP70 is known to be involved in the assembly of other RNA-containing viruses such as cucumber necrosis virus,[38] lentivirus,[39] and hepatitis C virus.[40] However, binding immunoglobulin protein (HSPA5), belonging to the HSP70 superfamily, has been shown to be required for the assembly of SINV.[41,42]

The identification of multiple host factors within SINV particles opens avenues for continued exploration into how these proteins influence the production of infectious virions by SINV. This novel characterization also included the conserved identification of SINV nonstructural proteins. Alphavirus nonstructural proteins are important for virus replication, but are not traditionally thought to form any structural components of the virus particle. In this study, LC-MS/MS data lead to the discovery that nsP2 is likely incorporated into SINV virus particles in each host background. This finding was confirmed by performing additional high-salt washes of the viral preps to eliminate the potential for nsP2 to co-purify with another structural protein such as the capsid protein via protein-protein interactions. Although this is a novel finding, there is recent supporting evidence that nsP2 plays a direct or indirect role in RNA encapsidation in Venezuelan equine encephalitis virus.[43] This discovery is significant, because nsP2 is a multifunctional enzyme previously thought only to function in RNA replication. nsP2 is a viral protease, with functions ranging from *trans*-cleavage of viral polyproteins to innate immune evasion early in viral replication.[44–49] The incorporation of an enzyme in a structural role is not novel among viruses. Thymidylate synthase and dihydrofolate reductase are DNA synthesis and replication enzymes encoded by the phage T4. However, they are also essential structural components of the phage baseplate and thus essential elements for phage infectivity.[50] By incorporating nsP2 into progeny virions, SINV may use its enzymatic and immune antagonist roles to facilitate the infection at the earliest stages of viral entry, before translation of the plus-stranded viral RNA occurs. This might be useful for viral evasion of host responses to viral replication and cellular immune responses.

Overall, this study has produced results that contribute to the understanding of alphavirus-host biology while identifying SNX5 as a potential target for antiviral therapy. LC-MS/MS analysis of highly pure viral particles determined that SINV likely specifically incorporates host proteins into progeny virus particles. These proteins have a variety of functions that can be investigated for a role in SINV replication, with a core group of proteins conserved in multiple host backgrounds serving as a logical starting point. Finally, the novel discovery of SINV nsP2 incorporation into virus particles suggests a specific interaction, and a possible structural role, for nsP2 during progeny infection. By interrogating SINV particles for the host background proteome, a better understanding of the virus-host interactions necessary for alphavirus entry, replication, protein assembly, and particle assembly prior to budding can be established.

ACKNOWLEDGMENTS

The authors would like to thank Dr. Fountain (ECBC), Dr. C. Nicole Rosenzweig (ECBC), Ms. Rebecca Braun (ECBC), and Dr. Eric Calvo (NIAID) for continued scientific and administrative support. The authors would like to acknowledge U.S. Army funding provided through the Edgewood Chemical Biological Center's In-House Laboratory Independent Research program.

REFERENCES

[1] Wilks, C. Alphaviruses: current biology [Book Review]. In *Australian Veterinary Journal*; Mahalingam, S., Herrero, L.J., Herring, B.L., Eds.; Caister Academic Press, Norfolk, UK. **2016;** *94* (3), p 59.

[2] Chattopadhyay, A.; Wang, E.; Seymour, R.; Weaver, S.C.; Rose, J.K. A chimeric vesiculo/alphavirus is an effective alphavirus vaccine. *J. Virol.* **2013,** *87* (1), pp 395–402.

[3] Fauci, A.S.; Challberg, M.D. Host-based antipoxvirus therapeutic strategies: turning the tables. *J. Clin. Invest.* **2005,** *115* (2), p 231.

[4] Lupberger, J.; Zeisel, M.B.; Xiao, F.; Thumann, C.; Fofana, I.; Zona, L.; Davis, C.; Mee, C.J.; Turek, M.; Gorke, S. EGFR and EphA2 are host factors for hepatitis C virus entry and possible targets for antiviral therapy. *Nat. Med.* **2011,** *17* (5), pp 589–595.

[5] Vancini, R.; Wang, G.; Ferreira, D.; Hernandez, R.; Brown, D.T. Alphavirus genome delivery occurs directly at the plasma membrane in a time-and temperature-dependent process. *J. Virol.* **2013,** *87* (8), pp 4352–4359.

[6] Oldstone, M.; Tishon, A.; Dutko, F.; Kennedy, S.; Holland, J.; Lampert, P. Does the major histocompatibility complex serve as a specific receptor for Semliki Forest virus? *J. Virol.* **1980,** *34* (1), pp 256–265.

[7] Maassen, J.; Terhorst, C. Identification of a Cell-Surface Protein Involved in the Binding Site of Sindbis Virus on Human Lymphoblastoic Cell Lines Using a Heterobifunctional Cross-Linker. *The FEBS Journal* **1981,** *115* (1), pp 153–158.

[8] Helenius, A.; Morein, B.; Fries, E.; Simons, K.; Robinson, P.; Schirrmacher, V.; Terhorst, C.; Strominger, J.L. Human (HLA-A and HLA-B) and murine (H-2K and H-2D) histocompatibility antigens are cell surface receptors for Semliki Forest virus. *P. Natl. Acad. Sci. USA.* **1978,** *75* (8), pp 3846–3850.
[9] Strauss, J.H.; Strauss, E.G. The alphaviruses: gene expression, replication, and evolution. *Microbiol. Rev.* **1994,** *58* (3), pp 491–562.
[10] Anthony, R.P.; Brown, D.T. Protein-protein interactions in an alphavirus membrane. *J. Virol.* **1991,** *65* (3), pp 1187–1194.
[11] Paredes, A.M.; Brown, D.T.; Rothnagel, R.; Chiu, W.; Schoepp, R.J.; Johnston, R.E.; Prasad, B. Three-dimensional structure of a membrane-containing virus. *P. Natl. Acad. Sci. USA.* **1993,** *90* (19), pp 9095–9099.
[12] Greco, T.M.; Diner, B.A.; Cristea, I.M. The impact of mass spectrometry–based proteomics on fundamental discoveries in virology. *Ann. Rev. Virol.* **2014,** *1*, pp 581–604.
[13] Burge, B.W.; Pfefferkorn, E. Complementation between temperature-sensitive mutants of Sindbis virus. *Virology* **1966,** *30* (2), pp 214–223.
[14] Hernandez, R.; Sinodis, C.; Brown, D.T. Sindbis virus: propagation, quantification, and storage. *Curr. Protoc. Microbiol.* **2005,** pp 15B. 1.1–15B. 1.41.
[15] Condreay, L.D.; Adams, R.H.; Edwards, J.; Brown, D.T. Effect of actinomycin D and cycloheximide on replication of Sindbis virus in Aedes albopictus (mosquito) cells. *J. Virol.* **1988,** *62* (8), pp 2629–2635.
[16] Magliocca, J.W. Alphavirus Entry, Assembly, and Egress. Ph.D. Dissertation, North Carolina State University, Raleigh, NC, 2016.
[17] Glaros, T.G.; Stockwin, L.H.; Mullendore, M.E.; Smith, B.; Morrison, B.L.; Newton, D.L. The "survivin suppressants" NSC 80467 and YM155 induce a DNA damage response. *Cancer. Chemoth. Pharm.* **2012,** *70* (1), pp 207–212.
[18] Wray, W.; Boulikas, T.; Wray, V.P.; Hancock, R. Silver staining of proteins in polyacrylamide gels. *Anal. Biochem.* **1981,** *118* (1), pp 197–203.
[19] Wiśniewski, J.R.; Zougman, A.; Nagaraj, N.; Mann, M. Universal sample preparation method for proteome analysis. *Nat. Methods.* **2009,** *6* (5), pp 359–362.
[20] Chen, X.-G.; Jiang, X.; Gu, J.; Xu, M.; Wu, Y.; Deng, Y.; Zhang, C.; Bonizzoni, M.; Dermauw, W.; Vontas, J. Genome sequence of the Asian Tiger mosquito, Aedes albopictus, reveals insights into its biology, genetics, and evolution. *P. Natl. Acad. Sci. USA.* **2015,** *112* (44), pp E5907–E5915.
[21] Giraldo-Calderón, G.I.; Emrich, S.J.; MacCallum, R.M.; Maslen, G.; Dialynas, E.; Topalis, P.; Ho, N.; Gesing, S.; Consortium, V.; Madey, G. VectorBase: an updated bioinformatics resource for invertebrate vectors and other organisms related with human diseases. *Nucleic Acids Res.* **2014,** *43* (D1), D707-D713.
[22] Ribeiro, J.; Topalis, P.; Louis, C. AnoXcel: an Anopheles gambiae protein database. *Insect Mol. Biol.* **2004,** *13* (5), pp 449–457.
[23] Karim, S.; Singh, P.; Ribeiro, J.M. A deep insight into the sialotranscriptome of the gulf coast tick, Amblyomma maculatum. *PLoS One.* **2011,** *6* (12), e28525.
[24] Mi, H.; Poudel, S.; Muruganujan, A.; Casagrande, J.T.; Thomas, P.D.,PANTHER version 10: expanded protein families and functions, and analysis tools. *Nucleic Acids Res.* **2016,** *44* (D1), D336-D342.
[25] Kautz, T.F.; Díaz-González, E.E.; Erasmus, J.H.; Malo-García, I.R.; Langsjoen, R.M.; Patterson, E.I.; Auguste, D.I.; Forrester, N.L.; Sanchez-Casas, R.M.; Hernández-Ávila, M. Chikungunya virus as cause of febrile illness outbreak, Chiapas, Mexico, 2014. *Emerg. Infect. Dis.* **2015,** *21* (11), pp 2070.
[26] Garmashova, N.; Gorchakov, R.; Volkova, E.; Paessler, S.; Frolova, E.; Frolov, I. The Old World and New World alphaviruses use different virus-specific proteins for induction of transcriptional shutoff. *J. Virol.* **2007,** *81* (5), pp 2472–2484.
[27] Sanz, M.A.; Madan, V.; Carrasco, L.; Nieva, J.L. Interfacial Domains in Sindbis Virus 6K Protein DETECTION AND FUNCTIONAL CHARACTERIZATION. *J. Biol. Chem.* **2003,** *278* (3), pp 2051–2057.
[28] Aeberhard, L.; Banhart, S.; Fischer, M.; Jehmlich, N.; Rose, L.; Koch, S.; Laue, M.; Renard, B.Y.; Schmidt, F.; Heuer, D. The proteome of the isolated Chlamydia trachomatis containing vacuole reveals a complex trafficking platform enriched for retromer components. *PLoS Pathog.* **2015,** *11* (6), e1004883.
[29] Mirrashidi, K.M.; Elwell, C.A.; Verschueren, E.; Johnson, J.R.; Frando, A.; Von Dollen, J.; Rosenberg, O.; Gulbahce, N.; Jang, G.; Johnson, T. Global mapping of the Inc-human interactome reveals that retromer restricts Chlamydia infection. *Cell Host Microbe.* **2015,** *18* (1), pp 109–121.
[30] Nanbo, A.; Imai, M.; Watanabe, S.; Noda, T.; Takahashi, K.; Neumann, G.; Halfmann, P.; Kawaoka, Y. Ebolavirus is internalized into host cells via macropinocytosis in a viral glycoprotein-dependent manner. *PLoS Pathog.* **2010,** *6* (9), e1001121.

[31] Wang, G.; Hernandez, R.; Weninger, K.; Brown, D.T. Infection of cells by Sindbis virus at low temperature. *Virology*. **2007,** *362* (2), pp 461–467.
[32] Langer, H.F.; Orlova, V.V.; Xie, C.; Kaul, S.; Schneider, D.; Lonsdorf, A.S.; Fahrleitner, M.; Choi, E.Y.; Dutoit, V.; Pellegrini, M. A novel function of junctional adhesion molecule-C in mediating melanoma cell metastasis. *Cancer Res.* **2011,** *71* (12), pp 4096–4105.
[33] Ballet, R.; Emre, Y.; Jemelin, S.; Charmoy, M.; Tacchini-Cottier, F.; Imhof, B.A. Blocking junctional adhesion molecule C enhances dendritic cell migration and boosts the immune responses against Leishmania major. *PLoS Pathog.* **2014,** *10* (12), e1004550.
[34] Martinez, M.G.; Snapp, E.-L.; Perumal, G.S.; Macaluso, F.P.; Kielian, M. Imaging the alphavirus exit pathway. *J. Virol.* **2014,** *88* (12), pp 6922–6933.
[35] Wright, C.F.; Oswald, B.W.; Dellis, S. Vaccinia virus late transcription is activated in vitro by cellular heterogeneous nuclear ribonucleoproteins. *J. Biol. Chem.* **2001,** *276* (44), pp 40680–40686.
[36] Jiang, X.; Chen, Z.J. The role of ubiquitylation in immune defence and pathogen evasion. *Nat. Rev. Immunol.* **2012,** *12* (1), pp 35–48.
[37] Nagy, P.; Wang, R.; Pogany, J.; Hafren, A.; Makinen, K. Emerging picture of host chaperone and cyclophilin roles in RNA virus replication. *Virology*. **2011,** *411* (2), pp 374–382.
[38] Alam, S.B.; Rochon, D.A. Cucumber necrosis virus recruits cellular heat shock protein 70 homologs at several stages of infection. *J. Virol.* **2016,** *90* (7), pp 3302–3317.
[39] Gurer, C.; Cimarelli, A.; Luban, J. Specific incorporation of heat shock protein 70 family members into primate lentiviral virions. *J. Virol.* **2002,** *76* (9), pp 4666–4670.
[40] Randall, G.; Panis, M.; Cooper, J.D.; Tellinghuisen, T.L.; Sukhodolets, K.E.; Pfeffer, S.; Landthaler, M.; Landgraf, P.; Kan, S.; Lindenbach, B.D. Cellular cofactors affecting hepatitis C virus infection and replication. *P. Natl. Acad. Sci. USA.* **2007,** *104* (31), pp 12884–12889.
[41] Mulvey, M.; Brown, D.T. Involvement of the molecular chaperone BiP in maturation of Sindbis virus envelope glycoproteins. *J. Virol.* **1995,** *69* (3), pp 1621–1627.
[42] Carleton, M.; Lee, H.; Mulvey, M.; Brown, D.T. Role of glycoprotein PE2 in formation and maturation of the Sindbis virus spike. *J. Virol.* **1997,** *71* (2), pp 1558–1566.
[43] Atasheva, S.; Frolova, E.I.; Frolov, I. Venezuelan equine encephalitis virus nsP2 protein regulates packaging of the viral genome into infectious virions. *J. Virol.* **2013,** *87* (8), pp 4202–4213.
[44] Shin, G.; Yost, S.A.; Miller, M.T.; Elrod, E.J.; Grakoui, A.; Marcotrigiano, J. Structural and functional insights into alphavirus polyprotein processing and pathogenesis. *P. Natl. Acad. Sci. USA.* **2012,** *109* (41), pp 16534–16539.
[45] Russo, A.T.; White, M.A.; Watowich, S.J. The crystal structure of the Venezuelan equine encephalitis alphavirus nsP2 protease. *Structure.* **2006,** *14* (9), pp 1449–1458.
[46] Akhrymuk, I.; Kulemzin, S.V.; Frolova, E.I. Evasion of the innate immune response: the Old World alphavirus nsP2 protein induces rapid degradation of Rpb1, a catalytic subunit of RNA polymerase II. *J. Virol.* **2012,** *86* (13), pp 7180–7191.
[47] Frolov, I.; Garmashova, N.; Atasheva, S.; Frolova, E.I. Random insertion mutagenesis of sindbis virus nonstructural protein 2 and selection of variants incapable of downregulating cellular transcription. *J. Virol.* **2009,** *83* (18), pp 9031–9044.
[48] Fros, J.J.; Liu, W.J.; Prow, N.A.; Geertsema, C.; Ligtenberg, M.; Vanlandingham, D.L.; Schnettler, E.; Vlak, J.M.; Suhrbier, A.; Khromykh, A.A. Chikungunya virus nonstructural protein 2 inhibits type I/II interferon-stimulated JAK-STAT signaling. *J. Virol.* **2010,** *84* (20), pp 10877–10887.
[49] Frolova, E.I.; Fayzulin, R.Z.; Cook, S.H.; Griffin, D.E.; Rice, C.M.; Frolov, I. Roles of nonstructural protein nsP2 and alpha/beta interferons in determining the outcome of Sindbis virus infection. *J. Virol.* **2002,** *76* (22), pp 11254–11264.
[50] Wang, Y.; Mathews, C.K. Analysis of T4 bacteriophage deletion mutants that lack td and frd genes. *J. Virol.* **1989,** *63* (11), pp 4736–4743.

Comparison of animal particle deposition data with physical and mathematical model data

Jana S. Kesavan[a*], Valerie J. Alstadt[a], Jerold Bottiger[b], Beth Laube[c]
[a]U.S. Army Edgewood Chemical Biological Center, Research & Technology Directorate, 5183 Blackhawk Rd, Aberdeen Proving Ground, MD 21010
[b]Excet, Inc., 6225 Brandon Ave #360, Springfield, VA 22150
[c]The Johns Hopkins University School of Medicine, 733 N Broadway, Baltimore, MD 21205

ABSTRACT

Particle deposition in the respiratory system has important implications for human health. The use of physical models to determine particle deposition is an easier method to assess the dangers facing the warfighter, compared to human testing. The aim of this project was to develop anatomically correct respiratory system physical models in order to quantify the amount and location of particle deposition in the upper airways of humans and in the upper airways/trachea of animals. Three human and five monkey models were created with 3D printing techniques from CT or MRI scans. The human models were based on an adult, a child, and a toddler. Deposition within the models was determined using Arizona Test Dust (Powder Technology, Inc.). Results from repeated experiments showed that the deposition fraction increased as the particle size and impaction parameter increased. The three human models had distinct deposition fraction curves, with the toddler having the highest and the adult the lowest deposition. The monkey models also had three distinct curves for deposition. Continuing work has focused on regional deposition within the models using radioactive Tc-99m particles to map deposition. The physical model deposition data will be compared to *in vivo* test and mathematical model results as they become available.

Keywords: physical respiratory system models, particle deposition, human models, monkey models

1. INTRODUCTION

Understanding particle deposition phenomenology within the human and animal respiratory tract is an important tool for the study of airborne hazards, as the location and quantity of particle deposition affect the response of humans and animals to hazardous aerosol exposures. Particle deposition phenomenology can be understood through a combination of *in vivo* testing, testing with anatomically correct physical models, and computational modeling. This project focused on the determination of the amount of particle deposition through the development and evaluation of anatomically correct animal models created with 3D printing techniques.

Previous studies have evaluated the effect of particle size on deposition site and disease development. Druett et al. evaluated the effect of particle size on the infectivity of bacteria on guinea pigs and concluded that larger particles deposit in the nasal passage while smaller particles deposit in the lower airways.[1] The LD_{50}, disease progression, and number of days alive after infection are highly dependent on the location of particle deposition, which is in turn dictated by particle size.[1]

Replicate models of the human respiratory system have been previously developed using MRI images and nasal casts from cadavers to conduct particle deposition studies.[2,3] Similarly, particle deposition studies have also been conducted in human subjects to determine the amount of deposition in the respiratory system.[4,5] In recent years, a small number of animal respiratory system models have been developed from animal cadavers. A study by Kelly et al. evaluated particle deposition in monkey and human respiratory systems with replicate models.[2] These models were made from postmortem casts, which may not be accurate representations of the animal respiratory tract, since cell structure changes after death could result in inaccuracies in such models. We believe that utilizing CT scans of live animals combined with 3D printing techniques can produce more accurate models of animal upper airway respiratory systems.

In addition to *in vivo* particle deposition studies in animals and physical models, mathematical models have been used to determine particle depositon and vapor uptake in the respiratory system. Corley et al. used computational fluid dynamics modeling to determine vapor uptake in the respiratory system of rats, rhesus monkeys, and humans; airway

geometry for each was determined using a combination of MRI, CT scans, and silicon solid casts.[6] However, this study was limited by the lack of comparison of the computational fluid dynamics predictions of absorption with actual animal/human vapor absorption. In addition, the human CT scan was of an 84-year-old female, who may not accurately represent the average person.

The use of physical models has many potential benefits over live animal testing, as models allow researchers to obtain multiple data points with ease and significantly reduce time and expense compared to similar live animal tests. The aim of this work was to use CT scans obtained from live animals to develop 3D-printed models of animal respiratory systems, and to determine particle deposition in the upper and lower airways of these models. Human and monkey deposition data were evaluated to determine if the monkey data can be interpreted to obtain human data for exposure assessment. Particle deposition data obtained from these anatomically correct models will be compared to deposition data obtained from *in vivo* animal testing and mathematical modeling results, as they become available.

2. METHODS

Human respiratory models of an adult (18 years old), child (5 years old), and toddler (2 years old) were used in these particle deposition studies to obtain data on a range of humans. Information regarding the parameters and details of these human models is found in Table 1. These models, shown in Figure 1, were created with stereolithography, a 3D printing technique, and included the upper airways (i.e., nasal regions, oral regions, and pharynx). Five rhesus macaque (*Macaca mulatta*) monkey models were produced via 3D printing, using CT scans obtained from live animals provided by the National Biodefense Analysis and Countermeasures Center (NBACC). These monkey models contained the upper airways and the tracheas as shown in Figure 2. Information about the five monkeys used in this test is shown in Table 2. The human and monkey models can be divided into several parts that are representative of various regions of the respiratory tract. The inside surfaces of these models were coated with oleic acid to simulate naturally-occurring airway mucus. An aerosol of oil droplets was generated using a nebulizer and drawn through the models using a pump to coat the inside surfaces of the models.

Table 1. Demographic data of the humans who provided the MRIs for the human models.

	Sex	Age	Ethnicity	Airflow rates (L/min)	Cross Sectional Area, A_{min}, (Left, Right), Total (cm^2)	Ellipticity (Length/Width)
Adult	M	18	Unknown	10, 15, 20, 25, 35	(0.606, 0.530), 1.136	1.63
Child	M	5	AA	4, 8, 9.5, 13,3	(1.127, 0.682), 1.809	1.93
Toddler	F	2	AA	2.5, 5, 7.3, 10.2	(0.517, 0.181), 0.698	1.25

*AA = African American

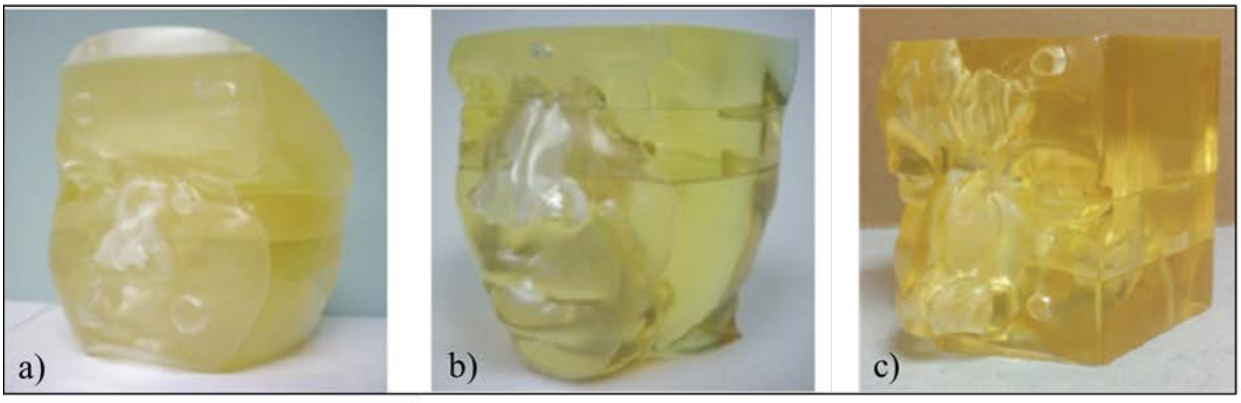

Figure 1. Human models of various ages a) 2-year-old toddler b) 5-year-old child c) 18-year-old adult. Models were manufactured using 3D printing techniques.

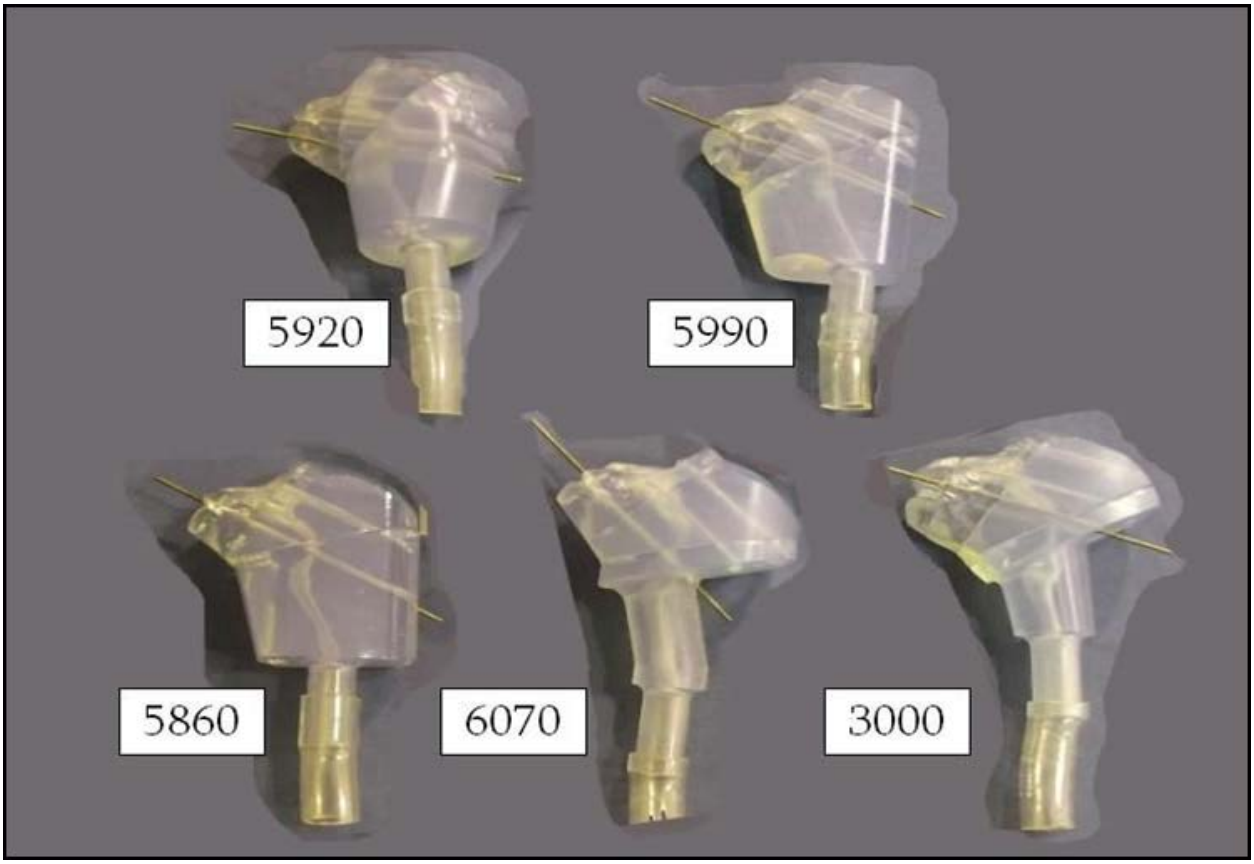

Figure 2. Five rhesus (*M. mulatta*) monkey models, each consisting of the upper airway and the trachea. Models were 3D printed from CT scans.

Table 2. Information about the monkeys corresponding to the models used. All models used flow rates of 2 L/min, 4 L/min, and 6 L/min.

Number	DOB	Sex	Age (years)*	Weight (kg)	Cross Sectional Area, A_{min}, (cm^2)
M5860	2012/03/20	F	3	4.22	0.342
M5920	2012/06/23	F	3	4.7	0.469
M5990	2012/02/19	F	3	4.8	0.548
M6070	2006/04/03	F	9	7.1	0.408
M3000	2012/02/08	M	4	6.04	0.666

*Age of monkey at time of CT scan.

Particle deposition testing was conducted in a large (60-inch x 36-inch x 48-inch) Plexiglas® chamber. Arizona Test Dust (0.06 g ± 0.003814 g) from Powder Technology, Inc. was aerosolized into the chamber using a two-fluid nozzle. An aerodynamic particle sizer (APS) was used to collect particle size and concentration data on both the reference inlet ("uptream") and model inlet ("downstream") aerosols for comparison. A solenoid switch enabled the operator to switch the APS sampling between "output of the model" and "reference" channels. In addition to the 1 L/min flow from the APS, an external pump was used to vary the flow through the physical model in order to mimic the proper respiratory rate of the mammal under study.

After the introduction of the Arizona Test Dust (Powder Technology, Inc.) into the chamber, mixing occurred via fan for 45 seconds. Sampling began 65 seconds after the aerosol was introduced into the chamber. Each APS sample measurement was 20 seconds in duration, and the number of particles at each size bin was recorded from

0.5–20 microns. There was a 10-second interval between measurements to accommodate the solenoid switching between channels. APS measurements were taken by alternating between the physical model output and reference channel. After sampling, the deposition at each size bin was determined using equation (1), where the reference counts used were the average of those taken immediately prior and after the output of the physical model measurement.

$$Deposition\ Fraction = 1 - \frac{Physical\ Model\ Channel\ Measurement}{Average\ of\ Reference\ Measurement\ Before\ and\ After} \quad (1)$$

Testing conditions were designed to evaluate particle deposition in the respiratory system during rest, light, moderate, and heavy activity conditions. The airflow of the human models were varied as shown in Table 1. Deposition occurred in all monkey models at airflow rates of 2 L/min, 4 L/min, and 6 L/min. The deposition fraction of the model was determined as a function of particle size and impaction parameter. The impaction parameter is the flow rate in cm^3/s multiplied by the squared particle size in micrometers. The particle deposition amount was determined using the average of three runs for each particle size. Collaborators at Stanford University have used mathematical modeling as a predictive particle deposition tool and are using these computational results to compare structure, model, and eventual subject data.

For regional deposition studies, a solution of radioactive Tc-99m diluted with water and Tween was made for deposition. Particles were aerosolized for deposition using an ink-jet aerosol generator (IJAG), which allows for the generation of particles with a narrow distribution. As depicted in Figure 3a, the model was held fixed over the IJAG opening during radioactive aerosol generation. After deposition, the model was brought to the Captus system for isotope detection, where the model was aligned in its holder for reproducible measurements. The Captus detector was blocked by lead panels with a 1-cm slit, allowing for measurement of a specific area, as depicted in Figure 3b.

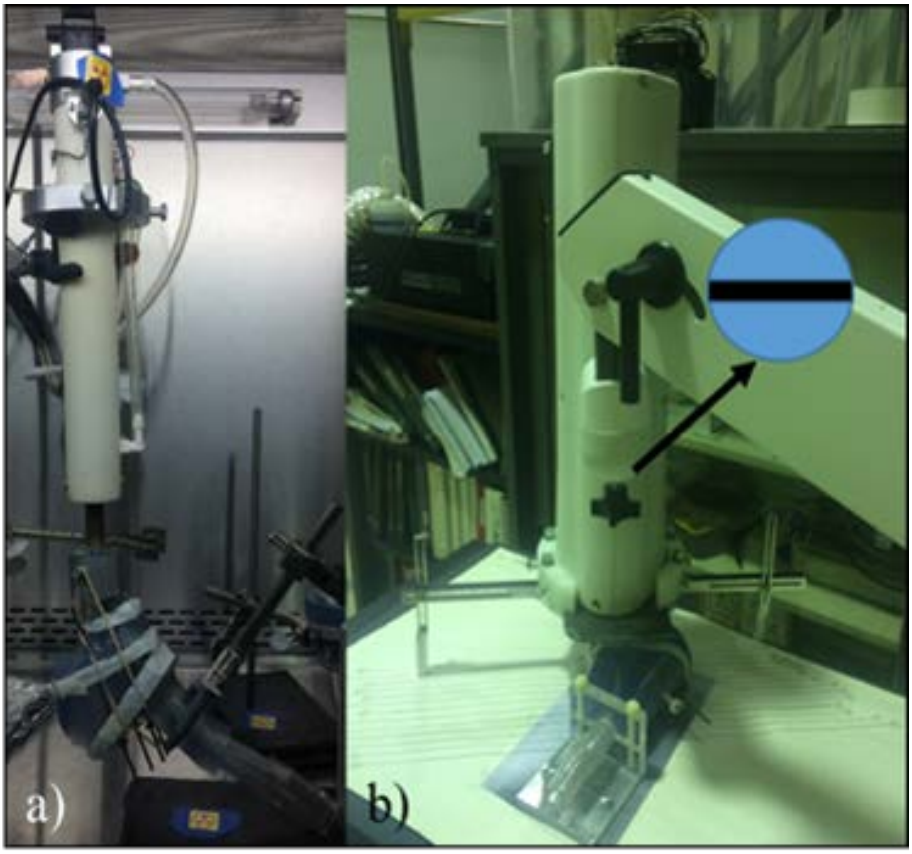

Figure 3. Regional deposition studies occured using a) the IJAG for aerosol generation and b) the Captus for isotope count by location. By using a small region for Captus measurements, regional deposition within the model was studied.

3. RESULTS AND DISCUSSION

Three human models and five monkey models were evaluated for overall depostion efficiency. Particle deposition fraction was determined in the human and monkey models at various airflow rates, representing rest to heavy activity conditions. The results showed that the deposition fraction increased as the airflow rate and particle size increased, which was also seen by Swift.[3] The observed separate deposition curves for each of the airflow rates collapsed into a single curve for each model when the depositon fraction was plotted as a function of impaction parameter, as shown in Figure 4.

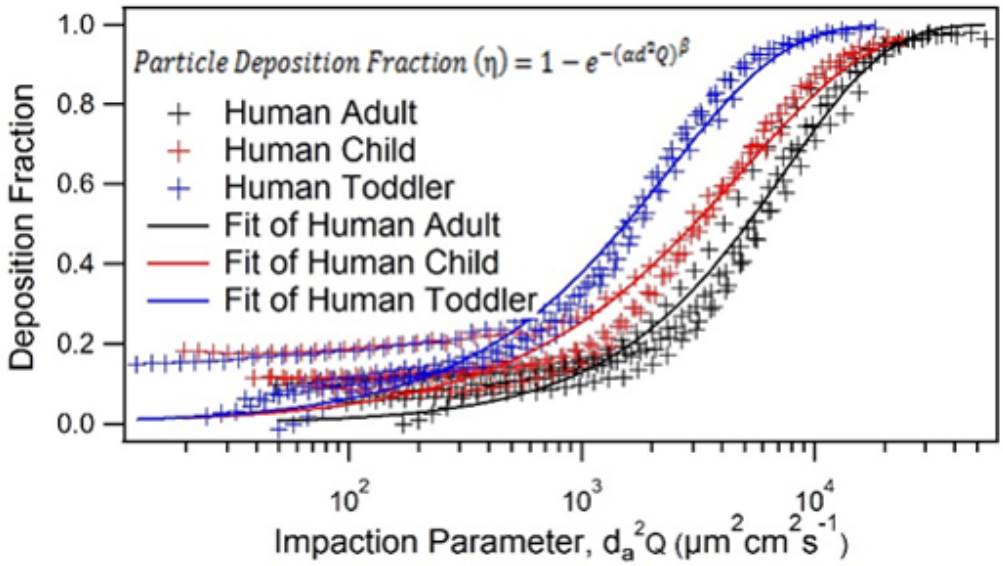

Figure 4. Particle deposition as a function of the impaction parameter for the three human models. Each model exhibits a different amount of deposition as the particle size varies.

In addition, the human models produced curves that were different from each other, a result due to age. For example, the toddler model typically showed greater deposition for a given impaction parameter value, compared to the child and adult models. Similarly, the child model showed a higher deposition fraction compared to the adult model. The deposition fraction for each model was fit to different equations to determine the best fit. The best fit lines are depicted in Figure 4, and the best fit line is of the form

$$Particle\ Deposition\ Fraction\ (\eta) = 1 - e^{-(\alpha d^2 Q)^{\beta}}, \quad (2)$$

where α and β are constants and d^2Q represents the impaction parameter. Analysis of Variance (ANOVA) was used to determine if the human models were statistically different from one another. This was done by comparing the α and β values, and by comparing the deposition fraction at a discrete particle size bin. It was determined that the human models had statistically significant differences with respect to α and β. For the ANOVA analysis by particle size, deposition fractions were grouped for each flow rate type (resting, light, moderate, and heavy) and 10 different-size bins for each rate were analyzed. We determined that the models exhibited statistically significant differences at all flow rates and at all particle sizes, except for the light flow rate for particles in the 2.5-μm sized bin. The deposition fraction observed in the adult human model in this study is similar to the results observed by Swift and Kelly et al. for the adult human models.[2,3] Furthermore, as depicted in Figure 5, the deposition fractions of the human models were compared to human subject data from previous works by Kesavan et al. and Kesavan and Swift.[4,5] The results from nine human subjects of varying ages (18–58 years old) are depicted in Figure 5 for three flow rates (15 L/min, 25 L/min, and 35 L/min). The results indicate that particle deposition in the human model is consistant with deposition in human subjects as the deposition fraction of particles within the human models falls in the center of the human subject data.

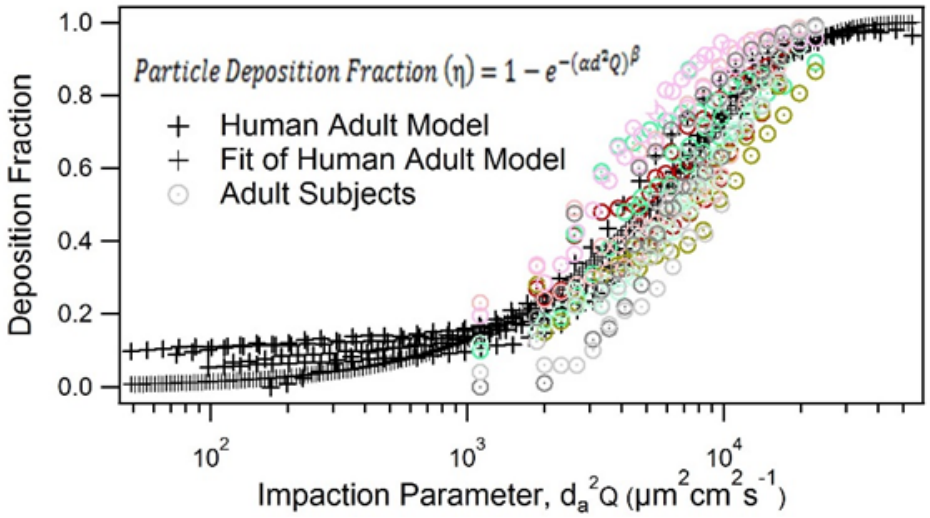

Figure 5. Particle deposition as a function of the impaction parameter for the adult human model with human subject data. Model data falls within the human subject data.

The deposition fraction as a function of impaction parameter for the five monkey models was measured using 2 L/min, 4 L/min, and 6 L/min airflow rates, and the results, which show three distinct deposition curves, are shown in Figure 6. Identical deposition was seen for models M5990, M6070, and M3000. Each model was fit using three different particle deposition fit equations, and the best fit was determined to be equation (2). ANOVA analysis of α and β for the five monkeys determined that the models exhibited a statistically significant difference for both α and β. ANOVA analysis by particle size resulted in the determination that the monkeys are statistically different at all particle sizes.

Kelly et al. conducted particle deposition studies on cast-models based on rhesus monkey postmortem casts.[2] Similar airflow rates (2–7 L/min) were used in that study, and particle depositon fraction data obtained in both studies are in general agreement. We are continuing to evaluate how the biological characteristics of these models affect particle deposition and could result in differing deposition fractions at the same particle size bins. Current work is focused on the regionl deposition studies as well as coordination with NBACC to obtain *in vivo* particle deposition results for the monkeys whose CT scans were used to make the models. The cross-sectional area of the nasal passage was determined for each human and monkey model, and deposition as function of the Stokes number was calculated for each model; however, little variation was seen between the plots of deposition fraction versus impaction parameter and deposition fraction versus Stokes number.

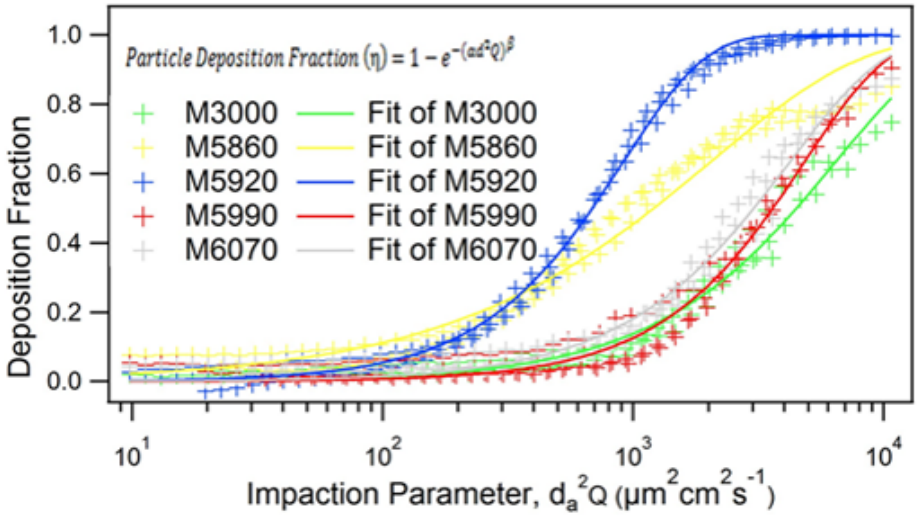

Figure 6. Particle deposition as a function of the impaction parameter for the five monkey models.

Work on regional particle deposition in all human and monkey models, and the new rabbit models, is progressing. The methodology has been finalized for particle deposition studies in the models, and preliminary studies have seen varying amounts of particle deposition in different regions depending on the model. New fixtures for holding the models will result in consistant, reproducible results. The upper airway of the human models and upper airway and trachea of the monkey models have been segmented in order to measure each section in 1-cm wide increments. Counts of the radioactive isotope Tc-99m will be determined for each region, and the total count in the model will be used to determine the percent deposition that occurred in each section. In this way, the extent of deposition in comparable model areas (nose, trachea, etc.) can be compared without having to correct for the decay of the radioactive isotope.

Initial comparison work to computational studies focused on comparing particle deposition in well-characterized shapes. A copper coil was constructed with known dimensions and placed on the apparatus in the position of a respiratory system model. The shape of the coil is depicted in Figure 7.

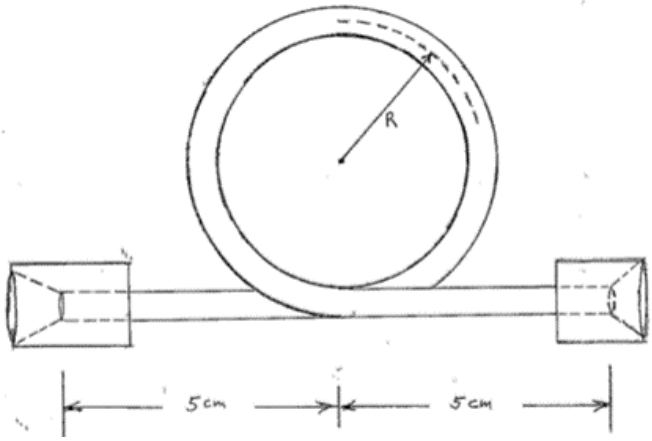

Figure 7. Diagram of copper coil used to compare a basic shape with a computational model for particle deposition.

Results of this work were compared to the computational modeling, and it was found that experimental results agree well with mathematical modeling results. In addition, more complex computational models were developed using the CT scans of the monkeys to determine the amount of particle deposition. Figure 8 illustrates the comparison of experimental and mathematical model data for monkey model M5920 at the three measured flow rates. There is good agreement between the experimental and computational data at the higher (4 L/min and 6 L/min) flow rates, but slight deviation at the lower (2 L/min) flow rate.

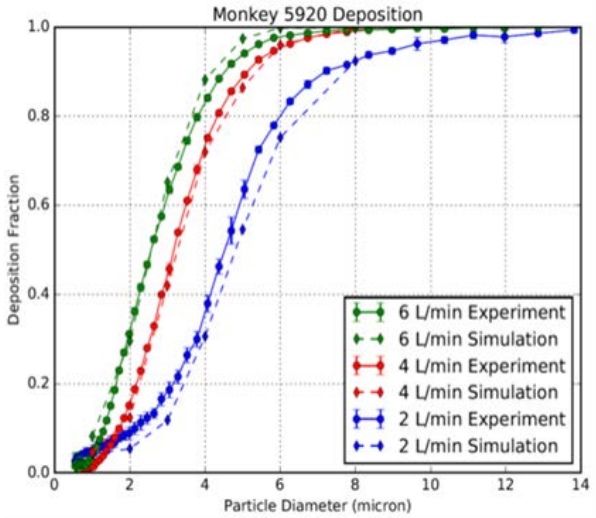

Figure 8. Comparison of particle deposition data in the model with computational results for monkey model M5920 with varying flow rates.

4. CONCLUSIONS

These results show that 3D-printed models based on CT scans obtained from live humans and monkeys can be created and evaluated for particle depostion efficiencies at various airflow conditions. The resulting human and animal model deposition data agree well with previous test results. Human model data agrees well with previous human subject data, while comparison of the monkey model data with monkey subject data is ongoing. Additional work will focus on determining how the monkey model data can be interpreted to obtain human particle deposition information for dose response studies. Additionally, the comparison of this data with data from computerized models is ongoing, as is work focusing on regional particle deposition.

ACKNOWLEDGMENTS

The authors would like to acknowledge U.S. Army funding provided through the Edgewood Chemical Biological Center's In-House Laboratory Independent Research program. The monkey CT scans were obtained from NBACC, and the 3D-printed monkey models were manufactured by the Edgewood Chemical and Biological Center Advanced Design and Manufacturing Division.

REFERENCES

[1] Druett, H.A.; Robinson, J.M.; Henderson, D.W.; Packman, L.; Peacock, S. Studies on Respiratory Infection: II. The Influence of Aerosol Particle Size on Infection of the Guinea-pig with Pasteurella pestis. *J. Hyg*. **1956,** *54* (1), pp 37–48.

[2] Kelly, J.T.; Asgharian, B.; Wong, B. Inertial Particle Deposition in a Monkey Nasal Mold Compared with that in Human Nasal Replicas. *Inhal. Toxicol*. **2005,** *17* (14), pp 823–830.

[3] Swift, D.L. Inspiratory Inertial Deposition of Aerosols in Human Nasal Airway Replicate Casts: Implication for the Proposed NCRP Lung Model. *Radiat. Prot. Dosim*. **1991,** *37* (8), pp 29–34.

[4] Kesavan, J.; Bascom, R.; Swift, D.L. The Effect of Nasal Passage Characteristics on Particle Deposition. *J. Aerosol Med*. **1998,** *11* (1), pp 27–39.

[5] Kesavan, J.; Swift, D.L. Human Nasal Passage Particle Deposition: The Effect of Particle Size, Flow Rate, and Anatomical Factors. *Aerosol Sci. Technol*. **1998,** *28* (5), pp 457–463.

[6] Corley, R.; Kabilan, S.; Kuprat, A.P.; Carson, J.P.; Minard, K.R.; Jacob, R.E.; Timchalk, C.; Glenny, R.; Pipavath, S.; Cox, T.; Wallis, C.D.; Larson, R.; Fanucchi, M.V.; Postlethwait, E.M.; Einstein, D.R. Comparative Computational Modeling of Airflows and Vapor Dosimetry in the Respiratory Tracts of Rat, Monkey and Human. *Toxicol. Sci.* **2012,** *128* (2), pp 500–516.

Hierarchical systems through selective deposition and growth of metal-organic frameworks on block copolymers

Gregory W. Peterson*
U.S. Army Edgewood Chemical Biological Center, Research & Technology Directorate,
5183 Blackhawk Rd, Aberdeen Proving Ground, MD 21010

ABSTRACT

The ability to grow metal-organic frameworks into systematic arrays and patterns has only briefly been explored to date. Typically, self-assembled monolayers are used to grow metal-organic frameworks on surfaces such as gold, or atomic layer deposition is used to nucleate crystal formation on relatively inert surfaces. Although both of these approaches have merit, they lack the ability to systematically deposit metal-organic frameworks in the form of arrays. Rather, the baseline substrate must be altered to selectively deposit, nucleate, and grow metal-organic frameworks. Herein, we take the first steps towards understanding the selective growth and deposition of metal-organic frameworks within polymer systems. We first studied the effects of solvent and electrospinning conditions on the deposition of UiO–66–NH_2 into polystyrene. Next, we investigated mixed-matrix membrane formation with selective layering of metal-organic frameworks. Finally, we began utilizing block copolymers to systematically grow HKUST-1 and ZIF-8 metal-organic frameworks.

Keywords: metal-organic framework, block copolymer, electrospinning, mixed-matrix membrane, *in situ* growth

1. INTRODUCTION

Metal-organic frameworks (MOF) are a relatively new class of highly porous materials that offer unprecedented control of porosity and chemistry.[1–3] By combining metal secondary building units with functionalized organic linkers, a wide variety of structures can be synthesized offering a wide range of properties. Over the past decade, the number of MOFs synthesized has grown, with well over 100,000 structures identified *in silico*.[4] Due to the ability to tune properties of MOFs, a wide range of potential applications have been identified, including gas storage,[5] catalysis,[6] toxic gas removal,[7] and sensing,[8] among others. However, although the chemistry of synthesis has been explored, tangible constructs other than crystalline powders have remained mostly unexplored.

Beyond simple growth of MOF crystallites, there have been some, albeit limited, investigations of hierarchical assembly of MOFs into thin films. MOFs are grown by connecting metal oxide secondary building units with organic linkers—by utilizing similar functional groups, such as oxygen centers, catechols, or carboxylic acids on polymer surfaces, nucleation and growth can occur. Layer-by-layer techniques using self-assembled monolayers have been investigated to create thin films, where MOFs are grown onto substrates, such as gold.[9] While thin films of MOFs are valuable in applications that require incorporating MOFs into devices, composite materials with MOFs on polymer substrates is far more advantageous for processability, flexibility, and reusability of the composite membrane. The two general approaches are the solution blending method (top-down approach), and *in situ* growth of MOFs in polymers (bottom-up approach). Various groups have employed the top-down approach of mixing different polymers with different MOFs. Specifically, the Cohen Group at the University of California has recently investigated using mixing of polyvinylidene fluoride (PVDF) to integrate MOFs into films.[10] The same group has also used polymerization techniques to create pure MOF films, called polyMOFs.[11] Although these techniques show promise, they do not offer the ability to deposit or grow MOFs into hierarchical or systematic patterns. Techniques that focus on nucleating MOF growth have also been investigated. For example, Parsons et al. have demonstrated the use of metal oxides (via atomic layer deposition) to nucleate the growth of MOFs on polypropylene fibers.[12] Polymers are a much older class of materials, but offer processability not enjoyed by MOFs. Several efforts have recently investigated using polymers as nucleation substrates for MOF growth. Li and coworkers amminated PVDF to form growth centers for MIL-53-type MOFs.[13] Zhou and coworkers doped "inert" polymers such as polystyrene (PS), polyethylene (PE), and polypropylene (PP) with polydopamine for use as a nucleation layer to grow MOFs such as HKUST-1, MOF-5, MIL-101, and others.[14]

To further enhance the possibility of MOF composites, it is desirable to use a bottom-up approach to precisely control the location of MOF nucleation. Such control would provide tailoring or arrangements of different types of MOFs on a single polymer strand. In the bulk membrane, alternating clusters of MOFs with different functionalities and reactivities would allow for systematic growth. To that end, we hypothesize that block copolymers (BCP) can be used to systematically build hierarchical MOF systems in structured arrays. Utilizing BCP systems allows for high tunability of polymers; by changing the types of polymers and controlling phase separation, we can systematically grow MOFs into a variety of patterns. Using a polymer, such as polyethylene oxide (PEO), within the block that possesses oxygen groups for MOF nucleation should allow for preferential growth on that block. Furthermore, by incorporating MOFs into the initial polymer solution, we can controllably phase separate the BCP, and therefore the MOF, into a variety of domains and morphologies. This BCP/MOF matrix can be investigated as-is, or further etched to produce a variety of chemical and physical properties. Figure 1A illustrates the potential morphologies that occur from phase separation of BCPs based on tuning the amount of polymer in each block. With these systems, the focus of this program is to systematically deposit or grow (Figure 1B) MOFs into select phases within the BCPs.

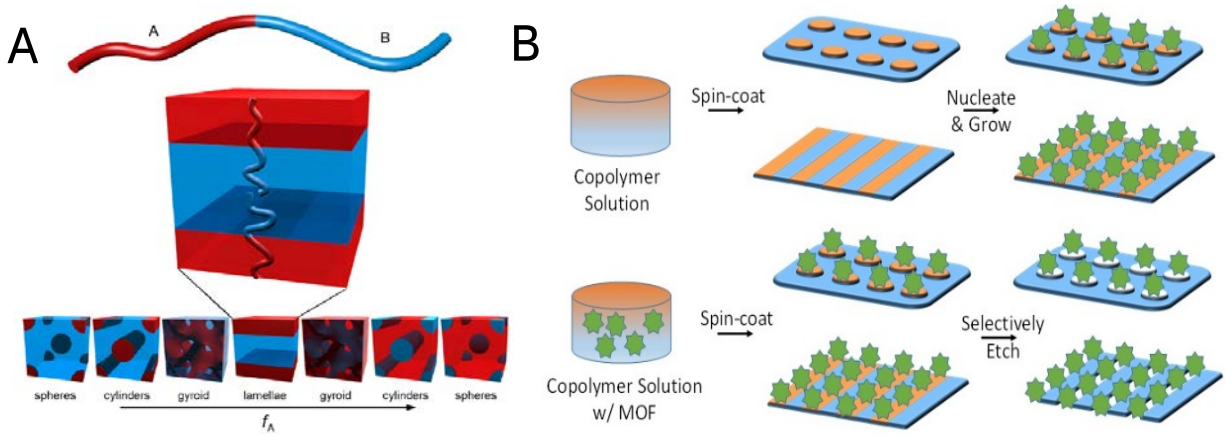

Figure 1. (A) BCP morphologies as a function of polymer content.[15] (B) Strategies for incorporating MOFs into BCPs using *in situ* growth or pre-synthesized particles.

Three efforts are highlighted in these proceedings, focused on the systematic deposition of MOFs within polymer systems: (1) electrospun MOF/fiber composites, (2) layered mixed-matrix membranes, and (3) *in situ* growth of MOFs in BCPs.

2. METHODOLOGY

2.1 Metal-organic framework synthesis

Three MOFs were investigated in these studies: UiO–66–NH_2, HKUST-1, and ZIF-8.

2.1.1 Procurement

Two samples of the MOF UiO–66–NH_2 were procured—one from TDA Research, Inc. through a Joint Science and Technology Office-sponsored Rapid Innovation Project, and the other from NuMat Technologies through a Small Business Technology Transfer program. HKUST-1 was also received through the Small Business Technology Transfer program, and ZIF-8 was purchased from Sigma-Aldrich®.

2.1.2 In situ *synthesis*

HKUST-1 and ZIF-8 were synthesized *in situ* in the presence of polymer films. Multiple strategies were used for each MOF, with the procedures from Azhar et al.[16] and Cravillon et al.[17] eventually being utilized for growth of HKUST-1 and ZIF-8, respectively. These general approaches are shown in Figure 2.

Solutions of ZIF-8 precursors were made according to a scaled procedure as detailed in Cravillon et al.[17] 0.073 g of zinc nitrate hexahydrate was dissolved in 5 mL of methanol (MeOH), and 0.081 g of 2-methylimidazole (HMIM) was dissolved in 5 mL of MeOH.

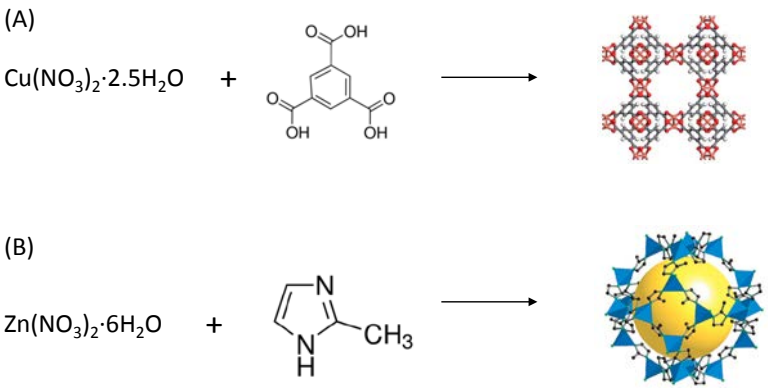

Figure 2. Synthesis of (A) HKUST-1 and (B) ZIF-8.

2.2 Polymer

Several polymers were investigated in this effort, including homopolymers and BCPs. Homopolymers were investigated initially to determine appropriate conditions for synthesis and processing as they are cheaper than BCPs.

2.2.1 Procurement

PS (350,000 g/mol), PEO (300,000 g/mol), polymethyl methacrylate (120,000 g/mol), and PS-*block*-polyisoprene-*block*-PS were purchased from Sigma-Aldrich® and used without purification. PS-*block*-PE-*ran*-polybutylene-*block*-PS (SEBS) was received gratis from Kraton™. PS-*block*-PEO (PS = 130,000 g/mol, PEO = 62,000 g/mol) was purchased from Polymer Source™, Inc.

2.2.2 Polymer-MOF solutions

Polymers were dissolved in a variety of solvents depending on the specific task. Initially, polymers were dissolved in appropriate solvents (e.g., dimethyl formamide (DMF), tetrahydrofuran (THF), etc.) in a 20-mL scintillation vial. After some experimentation, it was determined that adding MOF to the solvent first and then dissolving the polymer led to better dispersion of MOF throughout the solution. In the latter approach, the appropriate amount of MOF was added to the solvent and the suspension was tip sonicated for approximately 30–60 seconds. Next, polymers were added to the suspension and the resulting mixture was magnetically stirred until the polymer was completely dissolved, which generally took approximately 24 hours.

For *in situ* growth of MOFs in the presence of polymers, polymer solutions were first seeded using various MOF precursors. For example, PS-*b*-PEO and styrene-isoprene-styrene (SIS) were seeded with copper nitrate, copper acetate, zinc nitrate, benzenetricarboxylic acid (BTC), and HMIM, depending on the specific MOF to be grown. For PEO-*b*-PS samples, the amount of precursor seeded in the film was based on an approximate 1:1 molar ratio of metal or organic per mol PEO, and then systematically increased. After casting seeded polymer films, a swelling step incorporating precursors was generally conducted, followed by an annealing step. Specific procedures are described below.

2.3 Electrospinning

Electrospinning was conducted using a programmable floor-stand electrospinning unit (MSK NFES-4 by MTI Corporation). Solutions were loaded into 6-mL plastic syringes equipped with a 20-gauge needle. The solutions were pumped at a flow rate of 3 mL/hour onto a rotating mandrel operating at 300 rpm. The electric field was set at approximately 12 kV, but was modified, when necessary, according to perceived solution viscosity.

2.4 Materials characterization

A variety of techniques were used to characterize electrospun nanofibers and films developed. This section summarizes each technique.

2.4.1 Nitrogen isotherm

Nitrogen uptake was measured at 77 kelvin using a Micromeritics® ASAP™ 2040. Samples were off-gassed at 60 °C overnight under vacuum. Surface area measurements were calculated using the Brunauer-Emmett-Teller method, and total pore volumes were calculated at a relative pressure of 0.975 atm.

2.4.2 Powder X-ray diffraction

Powder X-ray diffraction (PXRD) measurements were conducted using a Rigaku Miniflex 600 X-ray powder diffractometer with a D/Tex detector. Samples were scanned at 40 kV and 15 mA using Cu Kα radiation, a scan rate of 5° min^{-1}, over a 2θ range of 3° to 50°. Data were plotted as absolute values and offset on the *y*-axis to show differences between each sample.

2.4.3 Scanning electron microscopy

Scanning electron microscopy (SEM) images were obtained using a Phenom GSR desktop SEM. Samples were supported on double-sided carbon tape and sputter-coated with gold prior to analysis. Typical settings for the instrument used an accelerating voltage of 5 kV at a nominal working distance of 10 mm. Specific operating conditions are listed with each image for clarity. Fiber diameters were automatically analyzed using the Phenom FiberMetric software package.

2.4.4 Thermogravimetric analysis

Thermogravimetric analysis (TGA) measurements were collected on a Netzsch TG 209 *F1 Libra*® analyzer to determine the mass of MOF deposited within the fiber mat. Measurements were obtained over a temperature range of 25 °C to 600 °C at a rate of 10 °C/min. Data were corrected for solvent as described in section 2.4, Materials characterization.

3. RESULTS AND DISCUSSION

3.1 Tuning the morphology and activity of electrospun PS/UiO–66–NH_2 composites

The effect of solvent on electrospinning PS/UiO–66–NH_2 MOF composites was studied to understand deposition strategies for MOFs. The objective of this work was to determine initial structure-activity-processing relationships using PS to inform subsequent work with BCP systems. Solutions containing DMF and THF were used to electrospin initial PS fibers. Both DMF and THF are good solvents for PS. DMF has a significantly higher dielectric constant (ε = 36.7) than THF (ε = 7.6), and is thus better for electrospinning, but is significantly less volatile. Furthermore, DMF is more difficult to remove from MOFs during activation due to hydrogen bonding and low volatility. Thus, an initial study was conducted on various ratios of DMF/THF to determine the highest ratio of THF that can be utilized while still maintaining high quality fibers. As shown in Figure 3, the highest amount of THF was found to be a 50/50 solution. Subsequent MOF/polymer composites were spun from both 50/50 DMF/THF and 100 DMF/THF solutions.

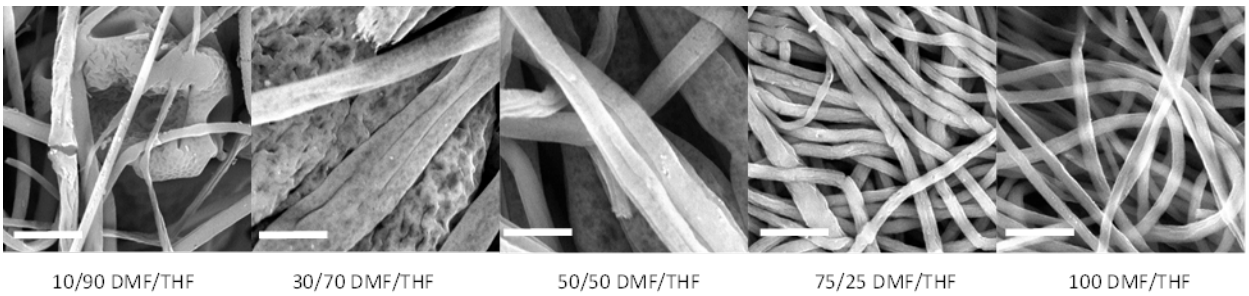

Figure 3. Effect of DMF/THF ratio on polystyrene fiber morphology.

Composites containing the MOF UiO–66–NH_2 were electrospun in both DMF and DMF/THF solutions using polystyrene contents of 10 % and 20 % (w/v) with respect to solvent and 10 wt%, 25 wt%, and 50 wt% MOF with respect to polystyrene. Nitrogen isotherms, PXRD data, and TGA data were collected on all composites and are summarized in an article published in ACS Applied Materials and Interfaces.[18] Figure 4 illustrates the major takeaways

from the study. First, increasing the amount of polystyrene in solution results in thicker fibers. Second, using a combination of DMF/THF to spin the composite results in MOFs intercalated within the fibers, whereas those spun from pure DMF result in MOFs deposited on the outside of the fiber. This behavior has important implications for future spinning of BCPs and deposition within specific phases.

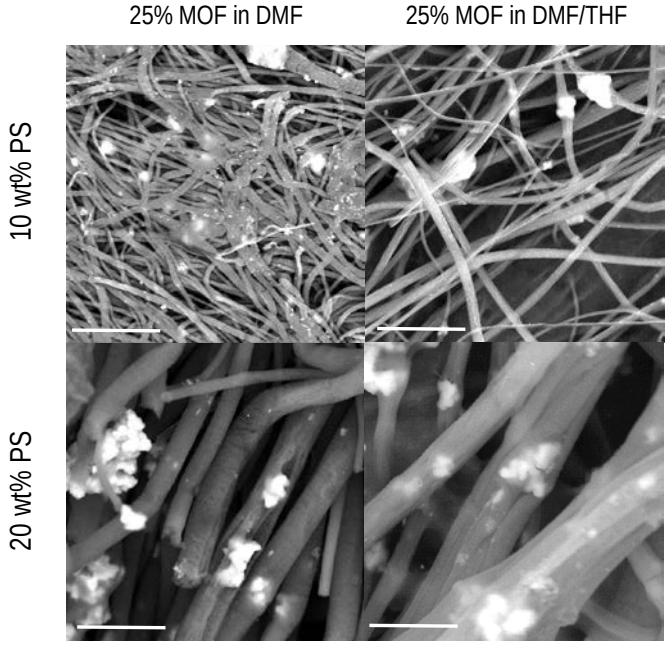

Figure 4. SEM images for fibers spun from varying wt% PS, and from DMF versus DMF/THF.

3.2 Selective deposition of MOFs using mixed-matrix membranes

Mixed-matrix membranes were developed as a means of incorporating MOFs into BCP films. The initial goal was to deposit MOFs selectively within specific phases of BCPs, yet it was quickly determined that preformed MOF crystals were much larger than BCP domains. Instead, an entirely new method of layering MOF/polymer films was developed and is illustrated in Figure 5—these composites are coined MOFwiches.

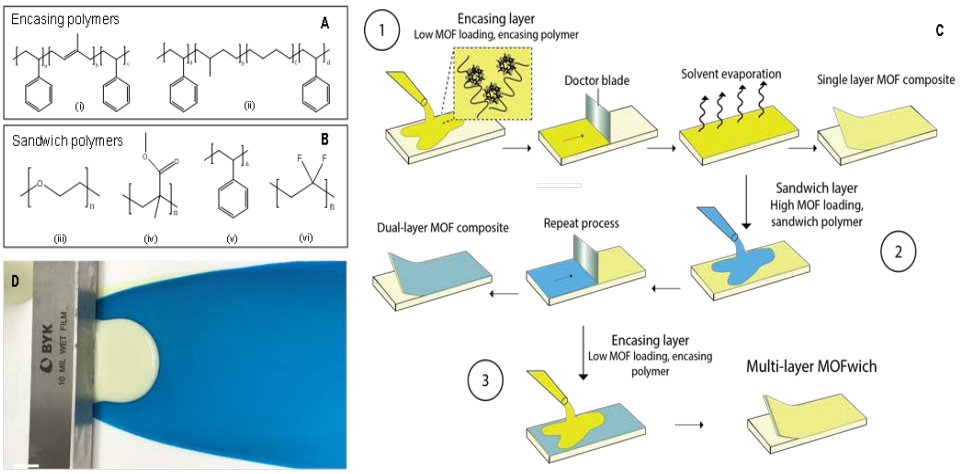

Figure 5. General concept of MOFwich formation.

The rubbery, elastomeric BCPs SIS and SEBS first were cast using traditional draw-down methods. Before the film completely dried, another polymer film was cast directly onto the first film. The process was repeated any number of times. The use of rubbery encasing layers allowed for a structurally robust composite. Figure 6 shows two archetypal MOFwiches. Both were made from three SIS layers. The first (Figure 6 A–C) was made from two encasing layers with 20 % UiO–66–NH_2 and a sandwich layer of 67 % HKUST-1. The second Figure 6 D–F) was made from two

encasing layers of 20 % HKUST-1 and a sandwich layer of 67 % UiO–66–NH_2. The novelty of the layered membranes is that, whereas a typical membrane containing 67 % MOF loading would fall apart, the tri-layer composite is structurally robust. Furthermore, each layer can be tuned with different polymer types, MOF types, and MOF loadings.

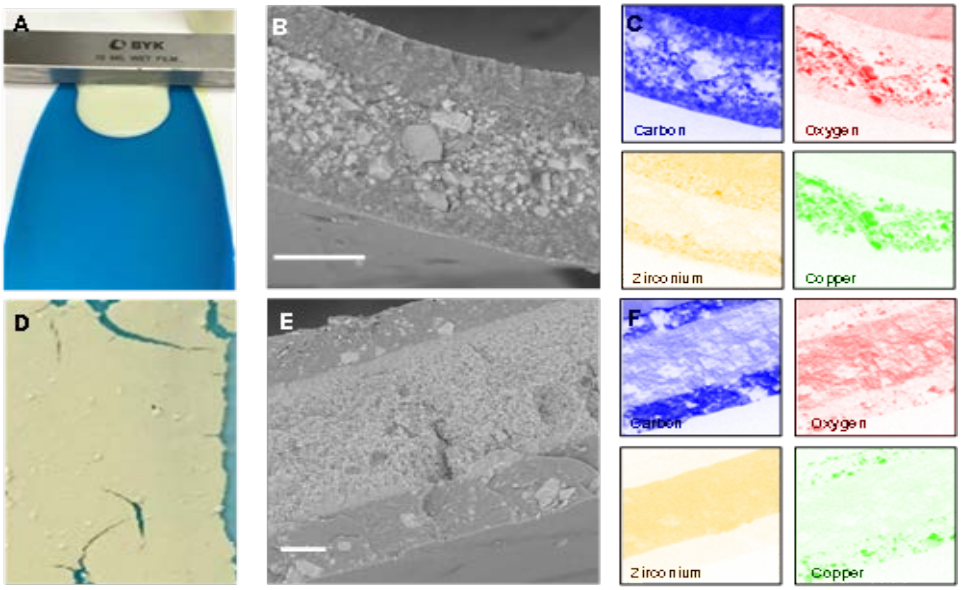

Figure 6. (A) Optical, (B) SEM, and (C) energy-dispersive X-ray spectroscopy (EDS) images of a MOFwich containing SIS/UiO–66–NH_2 (20 %) + SIS/HKUST-1 (67 %) + SIS/UiO–66–NH_2 (20 %). (D) Optical, (E) SEM, and (F) EDS images of a MOFwich containing SIS/HKUST-1 (20 %) + SIS/UiO–66–NH_2 (67 %) + SIS/HKUST-1 (20 %).

The novelty of the MOFwich concept was demonstrated on a material made from SEBS/UiO–66–NH_2 (50 %) + SEBS/HKUST-1 (50 %). A permeation test using 2-CEES was conducted (Figure 7A) and showed significantly better protection as compared to latex, while also maintaining an order of magnitude higher moisture vapor transport, essentially making the material a breathable rubber. The MOFwich also selectively absorbed carbon dioxide as compared to methane, nitrogen, and oxygen, making it applicable towards gas separations. The concept was also dosed with chlorine, and impedance measurements showed a change of six orders of magnitude, indicating the concept is useful for sensing as well. Finally, the structural robustness of a MOFwich is demonstrated in Figure 7 D–F. A composite containing PMMA was made, and where a pure PMMA film component easily broke, the composite was able to be folded. When stretched, cracks formed; however, the composite reformed once strain was removed. This has important implications for membranes and separations processes, but may also be useful for bendable electronics.

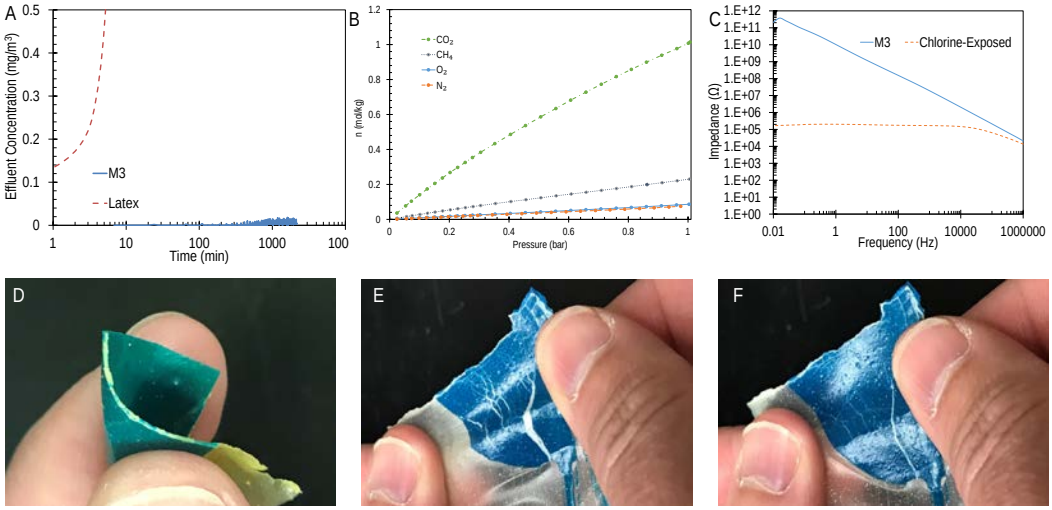

Figure 7. (A) 2-CEES permeation, (B) gas isotherms, and (C) impedance data after chlorine exposure to MOFwich M3. (D) Bending, (E) stretching, and (F) reforming of a MOFwich containing PMMA as a sandwiched layer.

3.3 *In situ* growth of ZIF-8 in PS-*b*-PEO

Initial films using SIS and PS-*b*-PEO were used to synthesize the MOF HKUST-1; however, there was not selective growth within the PEO phase as anticipated. This phenomenon was investigated through the analysis of Hansen Solubility Parameters, which can be used to determine solubility of polymers, solvents, and small molecules within mixtures.[19] The underlying equation is

$$\delta_t^2 = \delta_d^2 + \delta_p^2 + \delta_h^2 , \quad (1)$$

where δ_d = London dispersion parameter, δ_p = Polar interaction parameter, and δ_h = hydrogen bonding parameter. When considering the interaction of two bodies, the interaction radius is calculated according to

$$R^2 = 4 * (\delta_{d1} - \delta_{d2})^2 + \left(\delta_{p1} - \delta_{p2}\right)^2 + (\delta_{h1} - \delta_{h2})^2. \quad (2)$$

The interaction radii for the organic HKUST-1 and ZIF-8 precursors were calculated in PS and PEO. The results are summarized in Table 1.

Table 1. Interaction radii for HKUST-1 and ZIF-8 organic precursors.

Precursor/Linker	Interaction Radius	
	Polystyrene	Poly(ethylene oxide)
Benzenetricarboxylic acid (BTC)	13.8	10.5
2-methylimidazole (HMIM)	10.1	3.7

An interaction radius closer to zero indicates better dispersion and solubility of the precursor within a given polymer. Thus, when comparing BTC, there is seemingly little difference in solubility between PS and PEO, whereas HMIM is predicted to be significantly more soluble in PEO as compared to PS. Thus, ZIF-8 was further investigated for systematic growth in PS-*b*-PEO.

Two strategies were used for the *in situ* growth of ZIF-8 in the BCP PS-*b*-PEO:

1. Drop cast the BCP, infiltrate with solvent/precursor solutions, and grow ZIF-8.
2. Drop cast the BCP seeded with precursors for use as nucleation centers, infiltrate with solvent/precursor solutions, and grow ZIF-8.

Initial investigation using the first strategy was unsuccessful, and limited ZIF-8 was grown in or on the PS-*b*-PEO. Using the second strategy, PS-*b*-PEO (0.1 g) was dissolved a solution of HMIM (0.033 g) in 5 mL THF and then drop cast. The resulting films were then submerged into a solution of zinc nitrate hexahydrate (0.073 g) in 5 mL MeOH at either 25 °C or 70 °C for 1 hour or 24 hours. The resulting PXRD patterns are shown in Figure 8A, and an SEM image for the ZIF grown at 70 °C for 1 hour is shown in Figure 8D. Similar films were seeded with zinc nitrate hexahydrate (0.15 g), which was dissolved in 5 mL THF along with PS-*b*-PEO (0.1 g) and underwent similar annealing procedures. PXRD patterns are shown in Figure 8B, and an SEM image for the ZIF grown at 25 °C for 24 hours is shown in Figure 8E. Finally, the same solutions were mixed together, stirred for 5 minutes, and then drop cast followed by an annealing step. PXRD patterns are shown in Figure 8C, and an SEM image of the drop cast film is shown in Figure 8F.

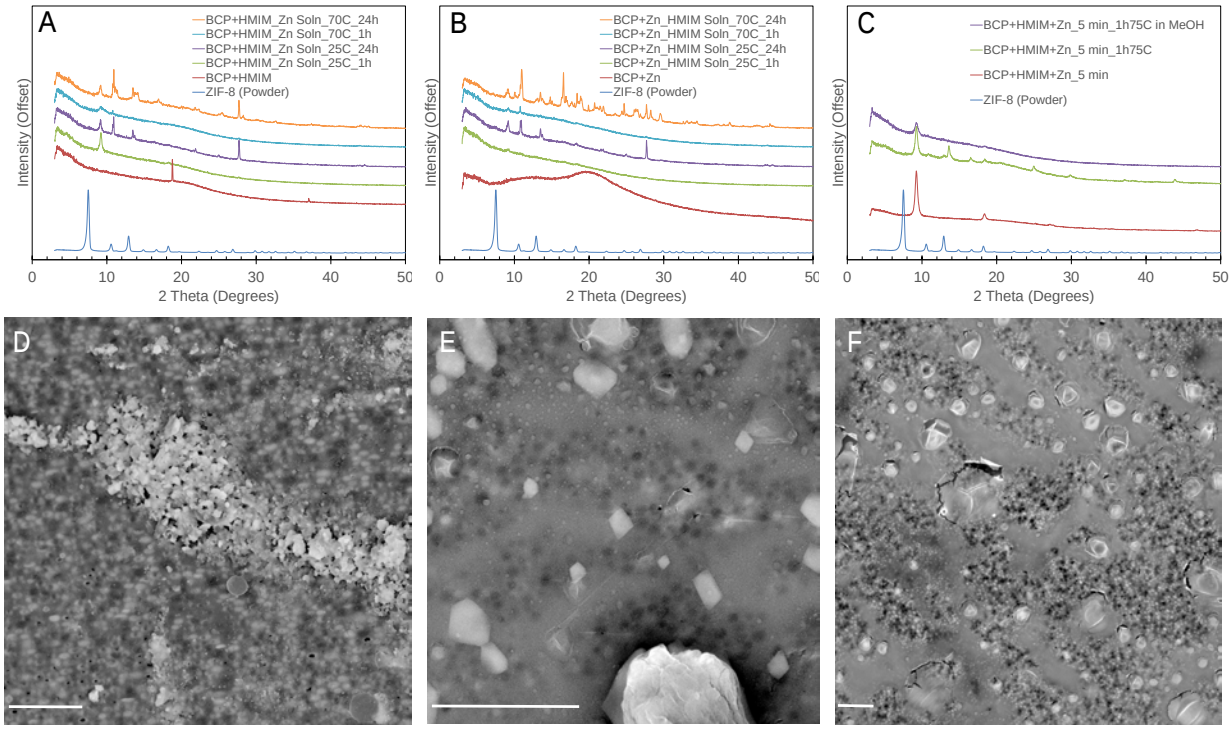

Figure 8. PXRD patterns for PS-*b*-PEO films seeded with ZIF-8 precursors. (A) PS-*b*-PEO seeded with HMIM, followed by casting and submerging in Zn/MeOH solution, followed by annealing. (B) PS-*b*-PEO seeded with zinc nitrate hexahydrate, followed by casting and submerging in HMIM/MeOH solution, followed by annealing. (C) PS-*b*-PEO seeded with HMIM and zinc nitrate in THF followed by casting and annealing. SEM imaging scale bar = 10 µm.

In all cases, PXRD patterns indicate the formation of crystalline materials; however, peaks are generally shifted as compared to known ZIF-8 samples. This behavior is under further investigation. Furthermore, although it appears that a crystalline material was indeed grown, in most cases there does not seem to be systematic growth in terms of a preferential phase of the BCP. Further imaging techniques will be used to determine if selective growth occurs at the nanoscale.

4. CONCLUSIONS

Several case studies have shown that MOFs are able to be incorporated systematically into various polymeric systems. In the first, choosing the appropriate solvent and electrospinning conditions allows for selective deposition of UiO–66–NH_2 into or onto polystyrene fibers. Next, a new method was developed for layered mixed-matrix membranes that shows promise in a wide range of potential applications. Finally, MOFs were grown in PS-*b*-PEO BCP with varying results. Especially in the latter, additional efforts will be made for better imaging of films and better systematic growth of MOFs within specific phases of the BCP.

ACKNOWLEDGMENTS

The author would like to acknowledge U.S. Army funding provided through the Edgewood Chemical Biological Center's In-House Laboratory Independent Research program. The author thanks Dr. Annie Lu for electrospinning and characterization support and discussion on membranes. The author thanks Prof. Thomas H. Epps, III from the University of Delaware for providing research guidance.

REFERENCES

[1] Eddaoudi, M.; Kim, J.; Rosi, N.; Vodak, D.; Wachter, J.; O'Keeffe, M.; Yaghi, O.M. Systematic design of pore size and functionality in isoreticular MOFs and their application in methane storage. *Science.* **2002,** *295* (5554), pp 469–472.

[2] Eddaoudi, M.; Li, H.L.; Yaghi, O.M. Highly porous and stable metal-organic frameworks: Structure design and sorption properties. *J. Amer. Chem. Soc.* **2000,** *122* (7), pp 1391–1397.

[3] Cavka, J.H.; Jakobsen, S.; Olsbye, U.; Guillou, N.; Lamberti, C.; Bordiga, S.; Lillerud, K.P.A New Zirconium Inorganic Building Brick Forming Metal Organic Frameworks with Exceptional Stability. *J. Amer. Chem. Soc.* **2008,** *130* (42), pp 13850–13851.

[4] Wilmer, C.E.; Leaf, M.; Lee, C.Y.; Farha, O.K.; Hauser, B.G.; Hupp, J.T.; Snurr, R.Q. Large-scale screening of hypothetical metal-organic frameworks. *Nat. Chem.* **2012,** *4* (2), pp 83–89.

[5] Suh, M.P.; Park, H.J.; Prasad, T.K.; Lim, D.-W. Hydrogen Storage in Metal-Organic Frameworks. *Chem. Rev.* **2012,** *112* (2), pp 782–835.

[6] Corma, A.; Garcia, H.; Llabres i Xamena, F.X.L.I. Engineering Metal Organic Frameworks for Heterogeneous Catalysis. *Chem. Rev.* **2010,** *110* (8), pp 4606–4655.

[7] DeCoste, J.B.; Peterson, G.W. Metal-Organic Frameworks for Air Purification of Toxic Chemicals. *Chem. Rev.* **2014,** *114* (11), pp 5695–5727.

[8] Kreno, L.E.; Leong, K.; Farha, O.K.; Allendorf, M.; Van Duyne, R.P.; Hupp, J.T. Metal-Organic Framework Materials as Chemical Sensors. *Chem. Rev.* **2011,** *112* (2), pp 1105–1125.

[9] Shekhah, O.; Wang, H.; Kowarik, S.; Schreiber, F.; Paulus, M.; Tolan, M.; Sternemann, C. Evers, F.; Zacher, D.; Fischer, R.A.; Wöll, C. Step-by-Step Route for the Synthesis of Metal−Organic Frameworks. *J. Am. Chem. Soc.* **2007,** *129* (49), pp 15118–15119.

[10] Denny, M.S., Jr.; Cohen, S.M. In Situ Modification of Metal-Organic Frameworks in Mixed-Matrix Membranes. *Angew. Chem., Int. Ed.* **2015,** *54* (31), pp 9029–9032.

[11] Zhang, Z.J.; Nguyen, H.T.H.; Miller, S.A.; Cohen, S.M. polyMOFs: A Class of Interconvertible Polymer-Metal-Organic-Framework Hybrid Materials. *Angew. Chem., Int. Ed.* **2015,** *54* (21), pp 6152–6157.

[12] Zhao, J.; Gong, B.; Nunn, W.T.; Lemaire, P.C.; Stevens, E.C.; Sidi, F.I.; Williams, P.S.; Oldham, C.J.; Walls, H.J.; Shepherd, S.D.; Browe, M.A.; Peterson, G.W.; Losego, M.D.; Parsons, G.N. Conformal and highly adsorptive metal-organic framework thin films via layer-by-layer growth on ALD-coated fiber mats. *J. Mater. Chem. A.* **2015,** *3* (4), pp 1458–1464.

[13] Li, W.B.; Meng, Q.; Zhang, C.Y.; Zhang, G.L. Metal-Organic Framework/PVDF Composite Membranes with High H-2 Permselectivity Synthesized by Ammoniation. *Chem. - Eur. J.* **2015,** *21* (19), pp 7224–7230.

[14] Zhou, M.M.; Li, J.; Zhang, M.; Wang, H.; Lan, Y.; Wu, Y.N.; Li, F.T.; Li, G.T. A polydopamine layer as the nucleation center of MOF deposition on "inert" polymer surfaces to fabricate hierarchically structured porous films. *Chem. Commun.* **2015,** *51* (13), pp 2706–2709.

[15] Darling, S.B. Directing the self-assembly of block copolymers. *Prog. in Polym. Sci.* **2007,** *32* (10), pp 1152–1204.

[16] Azhar, M.R.; Abid, H.R.; Sun, H.Q.; Periasamy, V.; Tade, M.O.; Wang, S.B. One-pot synthesis of binary metal organic frameworks (HKUST-1 and UiO-66) for enhanced adsorptive removal of water contaminants. *J. Colloid Interface Sci.* **2017,** *490*, pp 685–694.

[17] Cravillon, J.; Nayuk, R.; Springer, S.; Feldhoff, A.; Huber, K.; Wiebcke, M. Controlling Zeolitic Imidazolate Framework Nano- and Microcrystal Formation: Insight into Crystal Growth by Time-Resolved In Situ Static Light Scattering. *Chem. Mater.* **2011,** *23* (8), pp 2130–2141.

[18] Peterson, G.W.; Lu, A.X.; Epps, T.H. Tuning the Morphology and Activity of Electrospun Polystyrene/UiO–66–NH_2 Metal-Organic Framework Composites to Enhance Chemical Warfare Agent Removal. *ACS Appl. Mater. Interfaces.* **2017,** *9* (37), pp 32248–32254.

[19] Hansen, C.M. The Universality of the Solubility Parameter. *Ind. Eng. Chem. Prod. Res. Dev.* **1969,** *8* (1), pp 2–11.

777777fzfAAA

Structure modeling and prediction of cystine knot miniproteins

Caitlin E. Sharpes[a,b], Katelynn M. Stafford[a,b], Alena M. Calm[a], Rabih E. Jabbour[a], Jerry B. Cabalo[a], Roberto Rebeil[a]*
[a]U.S. Army Edgewood Chemical Biological Center, Research and Technology Directorate, 5183 Blackhawk Rd, Aberdeen Proving Ground, MD 21010
[b]Excet, Inc., 6225 Brandon Avenue, Suite 360, Springfield, VA 22150

ABSTRACT

Many organisms, including a diverse set of species across many genera, produce a large family of relatively short peptides collectively known as cystine knot proteins. Cystine knot proteins bind to a wide range of protein targets. These peptides, while largely divergent in primary amino acid sequence, share a similar six-cysteine residue motif which forms their characteristic structural feature termed the cystine knot. The cystine knot proteins' critical features are mainly formed and stabilized by three conserved tightly woven disulfide bonds formed by the cysteines and impart extraordinary thermal and proteolytic stability. The present study seeks to better understand how changes in primary amino acid sequence and spacing between cysteine residues can impact the ability of cystine knots to form. We hypothesize that the conserved cysteine spacing between cysteines III, IV, and V are important for generating a higher percentage of properly folded and linked peptides under oxidative conditions. Therefore, perturbations in the spacing pattern between cysteines III, IV, and V should result in slower folding dynamics or a lower percentage of properly folded peptides. Here, we leverage *in silico* protein folding and structure modeling tools with conventional protein biochemistry techniques in order to examine the impact that sequence modifications have on the ability of cystine knots to form.

Keywords: cystine knot, peptide, miniproteins, folding, *Ecballium elaterium* trypsin inhibitor-II, disulfide-rich

1. INTRODUCTION

Many chemical and biological defense applications rely heavily on chemically-selective binding. For sensing biological and some chemical threats, immunoassays depend on the high chemical specificity of immunoglobulins (Ig) to detect and identify both toxins and pathogenic organisms.[1,2] Finding acceptable alternatives to the current state-of-the-art use of proteins is highly desirable.[3] This is mainly because the chemical-specific binding of proteins, such as with Igs, suffers from a number of significant drawbacks: 1) they are large and expensive molecules to make, typically involving the use of animals for mass production, 2) Igs require precise environmental control to maintain the proper folded shape for the desired biological activity, and 3) when used as a therapeutic, Igs can trigger an immune response, especially if they were produced in an animal. DNA aptamers have been proposed to circumvent these drawbacks; however, DNA uses only four nucleotides as opposed to the 20 amino acids found in proteins, making it difficult to match the binding site diversity of the target protein when using aptamers.[4–6] Cystine knot proteins (CKP), a large family of short peptides produced by several organisms, can target a broad set of proteins, displaying a high degree of specificity and avidity to their respective targets (Figure 1).[7] Although CKPs consist of short peptides, 10–50 amino acids long, they can display remarkable variability in their 3D structure, target specificity, and affinity to various receptors.[7–10] It is reasonable to speculate that variant peptides based on CKPs may surmount the limitations known to affect conventional protein-based immunoassays and therapeutics. The objective of this project is to understand how the amino acid peptide sequence and length of the loop structures of the CKPs control the 3D structure of the molecules. While a significant amount of bioprospecting and comparisons of different structures from various CKPs are underway, few researchers are focusing on exploiting the potential use of this basic framework to target completely different ligands. The disulfide linkages between the cysteine residues are the key to their 3D structure (Figure 1). We hypothesize that the conserved cysteine spacing between cysteines III, IV, and V are important for generating a higher percentage of properly folded and linked peptides under oxidative conditions. Therefore, perturbations in the spacing pattern between cysteines III, IV, and V should result in slower folding dynamics or a lower percentage of properly folded peptides.

Of the different CKP types, the inhibitory CKPs (ICKP) have been the focus of many studies to better understand their structures and intrinsic properties.[7] For example, the 3D structure of several ICKPs has been determined using crystallography and nuclear magnetic resonance spectroscopy. This has required the generation of multiple *in vitro* reactions to help properly fold the CKPs into their native state and oxidation of all the cysteines to form the correct disulfide bonds. In the process, investigators have discovered that some ICKPs have a higher intrinsic capability to fold in the proper conformation under very simple oxidative conditions. The *Ecballium elaterium* (squirting cucumber) trypsin inhibitor II (EeTI-II) is one of the very well characterized ICKPs. The 3D structure of EeTI-II has already been elucidated, both by itself and while binding to trypsin.[11–13] Critical residues involved in binding and inhibition have also been identified via amino acid substitution and *in silico* modeling used to study these non-covalent bonds. Amino acids in loop #1 (L1) have been shown to interact directly with the trypsin proteolytic pocket. The bending of this loop is caused by the two adjacent cysteines forming the disulfide bridge, with L5 consisting of a single valine (Figure 1). At least two research groups have introduced alternative binding domains into the various loop regions of EeTI-II to generate molecular tools.[14,15] Hence, there is a wealth of background literature that can be exploited to help make progress towards testing the hypothesis.

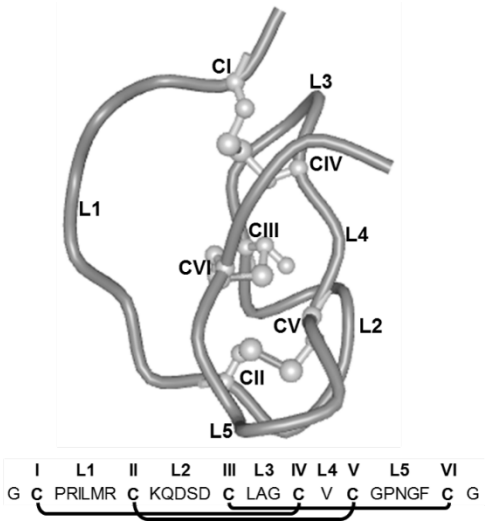

Figure 1. Primary amino acid sequence and 3D structure of EeTI-II. The diagram was obtained from the National Center of Biotechnology Information (U.S. National Library of Medicine, Bethesda, MD) structure database using the iCn3D web tool. Cysteines are designated with Latin numerals.

In order to tackle this problem, a combination of *in silico* and traditional laboratory bench research was performed in parallel to help explore how changes in loop length and primary amino acid sequence impact the intrinsic capability of the protein to fold properly. At least one research group has used this approach with significant success to help design and generate a synthetic peptide that contained alternative amino acids in place of two critical cysteines; the new peptide folded properly and showed similar physical properties to the wild type version, even though it lacked a major covalent bond.[16] In a similar manner, this study utilizes *in silico* folding and structure analysis *in silico* tools to review or screen effects that changes in amino acid sequence may cause to the intrinsic ability of EeTI-II to form the cystine knot under oxidative conditions. Synthetic versions of the peptide will be generated to study the ability of the peptides to fold and form the cystine knot appropriately under favorable oxidative conditions. The two approaches allow comparison of results and the ability to better understand the effects observed

2. MATERIALS AND METHODS

2.1 Protein sequence collection and analysis

Primary amino acid sequences for the various ICKPs were downloaded from the National Center of Biotechnology Information protein database (Bethesda, MD, https://www.ncbi.nlm.nih.gov/protein). The sequences were manually aligned using the six conserved cysteines involved in cystine knot formation to identify conserved loop features (data not shown).

2.2 Peptide variant design

The ICKP EETI-II was chosen as the primary backbone since there already is a wealth of information in regard to function and folding information. Previous research has demonstrated that the ability of a high percentage of EETI-II to fold properly *in vivo* and *in vitro* was associated with the GPNG amino acid sequence located between cysteines V and IV. This pattern and corresponding effect in helping to initiate proper folding and oxidation introduced a variable that could mask or enhance the effect of the cysteine spacing variation. Hence, the GPNG amino acid pattern was replaced with the NEDE amino acid pattern, which has been shown to still allow proper folding (Table 1). Peptides were purchased from Creative Peptides (Shirley, NY) and New England Peptide, Inc. (Gardner, MA) and were generated using standard fluorenylmethyloxycarbonyl protecting group (Fmoc) peptide synthesis chemistry.

Table 1. Amino acid sequence alignment of various EeTI-II variants designed for this study to study the impact of the cysteine spacing on *in vitro* folding dynamics. The EeTI-II native sequence is highlighted in gray; the amino acid changes are in bold.

Variant	*I*	*L1*	*II*	*L2*	*III*	*L3*	*IV*	*L4*	*V*	*L5*	*VI*	*#*
EETI-II	**C**	PRILMR	**C**	KQDSD	**C**	LAG	**C**	V	**C**	GPNGF	**C**	**26**
EETI-N1	**C**	PRILMR	**C**	KQDSD	**C**	LAG	**C**	V	**C**	**NEDE**F	**C**	**26**
EETI-N2	**C**	PRILMR	**C**	KQDSD	**C**	LAG	**C**	**SGA**	**C**	**NEDE**F	**C**	**28**
EETI-N3	**C**	PRILMR	**C**	KQDSD	**C**	LAG	**C**	**SGQGN**	**C**	**NEDEF**	**C**	**30**
EETI-N4	**C**	PRILMR	**C**	KQDSD	**C**	LAG	**C**	V	**C**	**NEDELRIFV**	**C**	**31**
EETI-N5	**C**	PRILMR	**C**	KQDSD	**C**	-	**C**	**LAG**V	**C**	NEDEF	**C**	**26**
EETI-N6	**C**	PRILMR	**C**	KQDSD	**C**	-	**C**	**KSSNL**V	**C**	NEDEF	**C**	**28**
EETI-N7	**C**	PRILMR	**C**	KQDSD	**C**	-	**C**	**LAG**V	**C**	**NEDELRIFV**	**C**	**30**
EETI-N8	**C**	PRILMR	**C**	**DNDRGPR**	**C**	-	**C**	**LAG**V	**C**	NEDEF	**C**	**29**
EETI-N9	**C**	PRILMR	**C**	KQDSD	**C**	-	**C**	V	**C**	NEDEF	**C**	**23**

2.3 *In silico* protein sequence folding and analysis

Several *in silico* tools were installed to perform protein folding and structure analysis: the Rosetta macromolecular modeling software suite; PSI-blast based secondary structure prediction (PSIPRED), a program for predicting protein secondary structure; Jufo 3D Server, a second/alternate program for predicting protein secondary structure; the National Center for Biotechnology Information Basic Local Alignment Search Tool searches and non-redundant peptide databases to help Rosetta find 3-mer and 9-mer peptide structures of known structure; and SPARKS, a program to account for solvent effects.[17,18] The PSIPRED program is used to determine the secondary structure—regions of α-helices and β-sheets. The next step was the alignment of 3-mer and 9-mer sequences to proteins of known structure using the National Center for Biotechnology Information Basic Local Alignment Search Tool database. The result was a set of structures corresponding to these fragments which were then used to build the set of output structures. Each structure was assigned an energy score and is in the protein data bank format.

For each peptide sequence, 6,000 folded structures were generated for clustering and analysis (Table 1). Based on the observation that the wild type sequence of the CKPs forms the correct disulfide linkages at room temperature, we filtered the possible structures for configurations that displayed a short distance (~ 4.5 Å) between the proper cysteine residues.[19] Peptide sequences that did not produce stable structures with the correct cysteines in proximity to each other were not counted. To calculate the *in silico* probability that a given sequence would form the CKP motif, the following simple formula was used: Probability (of proper folding) = N-structures with close S–S pairs divided by the N-total structures generated. Probability numbers for the synthetic peptides tested were compared to the probability score obtained for wild type EeTI-II. In addition to the probability score, the energy score (arbitrary units) will also be compared for each structure that has the proper CKP motif.

2.4 High-performance liquid chromatography analysis of folded proteins

Analysis of the incubated peptides was performed using high-performance liquid chromatography (HPLC). The system used was an Agilent Technologies 1200 Series system (Santa Clara, CA), fitted with a Vydac C18 analytical column (4.6 mm x 250 mm, 5 µm, 300 Å) and a Vydac C18 guard column (4.6 mm x 7.5 mm, 5 µm). The mobile phase used was of 0.1 % trifluoroacetic acid (TFA) in water (solution A) and 0.1 % TFA in acetonitrile (ACN), (solution B). Prior to starting, the column was first equilibrated by running two blank samples. For each sample, the column was first equilibrated using 20 % solution B for 3 minutes. After injection, the bound material was washed for 3 additional minutes in 20 % solution B. The toxin was eluted using a linear gradient of 20–70 % solution B, with a flow rate 1 mL/min, for 15 minutes. Eluted peaks were detected using a photodiode UV-vis detector with a channel

set to 214 nm. Peptide peaks typically eluted between 45 % and 65 % solution B; when needed, eluted peaks were manually collected and analyzed using mass spectrometry (MS). The column was then washed with 100 % solution B to clear the column of any remaining potential contaminants, before the column was reconditioned with 20 % solution B for the next sample injection.

2.5 MS analysis of CKP peptides

For structure analysis of peptides generated, a published liquid chromatography-mass spectrometry (LC-MS) approach was used since it potentially allowed a simple and more rapid analysis than other options.[20] An EeTI-II sample was custom-made by Creative Peptides (Shirley, NY) using Fmoc chemistry and the GCPRILMRCKQDSDCLAGCVCGPNGFCG primary amino acid sequence. The cysteines used in the peptide assembly process carried protective chemical groups so that the correct disulfide links could be generated in a series of deprotection and oxidation reactions. After generation, the folded peptide was purified to 95 % using HPLC. A 2.0 mg sample was dissolved in 95/5/0.1 % of water/ACN/fluoroacetic acid and allowed to dissolve for 30 minutes before MS analysis was performed. The system used for higher-energy collisional dissociation (HCD) fragmentation and MS analysis was a nanoflow liquid chromatography (nLC-1000) system and Q Exactive™ Hybrid Quadrupole-Orbitrap™ MS that is based on Fourier transformation-ion trap-MS configuration (Thermo Scientific™; Waltham, MA). The MS analyses were done in two different formats of HCD, a differential collision energy increase and a normalized collision energy approach—both were performed using direct infusion. The MS was operated in full mass scan between 100–2,000 amu, with data acquired in independent mode. The collision energy was varied after 30 seconds, and a gradual increase in collision energy from 10 % to 90 % was performed. Data was collected to show the effect of collision energy on different charge ions of the analyzed peptide chains; only ions with charge state (*z*) +2, +3, and +4 were observed.

3. RESULTS AND CONCLUSIONS

3.1 *In silico* analysis using Rosetta

The Rosetta suite of programs was chosen to perform structural predictions because of its performance under the critical assessment for protein structure prediction (CASP).[18] Rosetta utilizes a mixture of knowledge-based and physics-based structure search algorithms.[17] Knowledge based structure predictions rely on analogy to proteins of known structure.[21] Short sequences within the peptide of unknown structure are aligned with proteins of known structure, and the structure of the subsequences from the known proteins are assigned to the segments in the unknown peptide. A physics-based model performs a potential energy surface search given a description of the interatomic/intermolecular forces (e.g., a force field, such as AMBER or CHARMM).[22] The chief limitation of this approach is that the potential energy surface (PES) of any peptide is very large and complex. That is, the PES may contain multiple local minima, of which the native structure may only be one. Either long simulation times are necessary to sample enough of the PES to find the native structure, or the protein model may become stuck in the wrong local structure. The mixed approach utilized by Rosetta can bypass the difficulties encountered by using a single approach.

To determine its usefulness in folding prediction of CKPs, we exploited some of the numerical structure outputs of the program. 6,000 folded structure variants were generated; of these, the number of structures that displayed a low relative energy score and displayed correct cysteine pairs in a distance suitable for disulfide bridge formation were extracted. The total number of structures (6,000) and the subset number were used to calculate the “probability” (of proper folding). The native sequence of the EeTI-II protein was used to establish the baseline probability; this protein folds spontaneously in very simple oxidative conditions to form the appropriate disulfide bonds at a very high rate—more than 80 % properly folded/functional peptide. The various alternate sequences were likewise analyzed for comparison of their respective “probability” values (Table 2).

Table 2. Peptide variants, their respective primary amino acid sequences, and the probability calculated. Underlined amino acids are those changed compared to the native sequence

Peptide Variant	*Sequence*	*Probability*
EeTI-II (N0)	GCPRILMRCKQDSDCLAGCVCGPNGFC	0.00136
EeTI-N1	GCPRILMRCKQDSDCLAGCVCNEDEFC	0.000643
EeTI-N2	GCPRILMRCKQDSDCLAGCSGACNEDEFC	0.0145
EeTI-N3	GCPRILMRCKQDSDCLAGCSGQGNCNEDEFC	0.164
EeTI-N4	GCPRILMRCKQDSDCLAGCVCNEDELRIFVC	0.000466
EeTI-N5	GCPRILMRCKQDSDCCLAGVCNEDEFC	0.000000
EeTI-N6	GCPRILMRCKQDSDCCKSSNLVCNEDEFC	0.0225
EeTI-N7	GCPRILMRCKQDSDCCLAGVCNEDELRIFVC	0.000000
EeTI-N8	GCPRILMRCDNDRGPRCCLAGVCNEDEFC	0.000675
EeTI-N9	GCPRILMRCKQDSDCCVCNEDEFC	0.000338

An initial survey of the structures, ignoring energy score, was performed to score the different peptides. These resulted in the following ranking of likelihood for probability of generating correctly folded structures: N7∼N5<N9<N4<N1<N8<N0<N2<N6<N3. Currently, there is insufficient *in vitro* data for comparison; nevertheless, the results are surprising. The probability values support the hypothesis that variants N2, N6, and N3 should fold and form a cystine knot structure faster or at a higher percentage than that of the peptide with the wild type sequence. It will be important to determine the relative free-energy state of these alternate peptide folded structures to determine how those values impact probability. In addition, some sequences did not yield any structures with appropriate cysteine pairings. An effort will be made to try to "force" the proper conformation of the peptide to also determine the free-energy state of that structure, and to determine if any amino acid residues are impeding the knot formation.

3.2 *In vitro* folding reactions and analysis

The folding reaction required for this peptide is very simple and results in a very high percentage of properly folded peptides. Only two peptides were available at the time—EeTI-N1 with normal length Loop 4, and EeTI-N3 with four additional amino acids in Loop 4. The previously published report predicted that the NEDE substitution in Loop 4 would cause the folding efficiency of the peptide to decrease from 80–90 % properly folded peptide when the reaction was allowed to proceed to completion, to ∼ 60 % properly folded peptide. The synthetically generated EeTI-N1 peptide we obtained effectively reproduced the published results. Approximately 60 % of the linear peptide appears to have folded properly when allowed to incubate in folding buffer for 72 hours (Figure 2). Peaks observed with different retention times also point to several folding intermediate species being present in the reaction, consistent with previously published observations. The EeTI-N3 peptide also generated three folding intermediate species; however, the peak that potentially corresponds to the native (correctly folded) version of the peptide was much smaller (Figure 2). Correspondingly, the majority of the peptide appears to be distributed in several folding intermediates species; specifically, intermediates designated I2 and I3 were most abundant in the folding reaction. Additional MS analysis of these peaks may help to clarify if the putative intermediates observed are different from those generated by EeTI-N1.

While the above observations are consistent with the stated hypothesis, this is based on only a single point of comparison. MS analysis of the peptides present in the different reactions need to be performed to verify the identity of the peaks identified and to obtained collaboration of the percentages obtained using HPLC. Additional experiments performed showed that the folding reactions appear to reach completion between six and eight hours of incubation (data not shown). In addition, prolonged incubation sometimes resulted in the loss of the peak corresponding to the linear peptide with no corresponding increase in the intermediate or native peaks. It is possible that the disappearance of the linear peptide is due to lower stability than the folded peptide forms; however, this is only speculative, and MS analysis may help to shed some light on this observation as well.

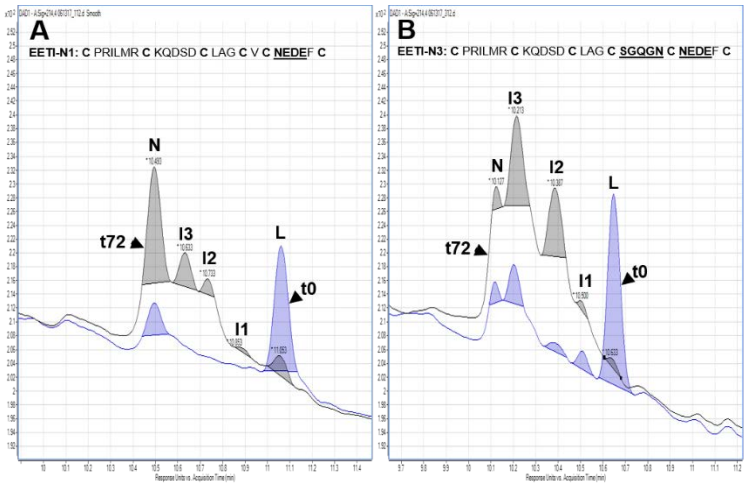

Figure 2. Comparison of the folding dynamics observed for EeTI-N1 (A) and EeTI-N3 (B) before and after incubation in folding buffer. Blue traces are for peptides harvested at time (*t*) 0 and the black traces are for *t* 72 hours incubation time. The corresponding peptide peaks for the linear (L), folding intermediate 1 (I1), folding intermediate 2 (I2), folding intermediate 3 (I3) and fully folded or native (N) peptide species are designated in each trace.

3.3 MS analysis

For disulfide link status or structure determination for generated peptides, several options are available. Most commonly, the structure of this type of peptide has been determined using nuclear magnetic resonance imaging.[23–25] However, this approach requires a significant amount of peptide and is relatively difficult to perform compared to other approaches. Recently, LC-MS approaches have been used with increasing frequency to determine the state of disulfide linkage for CKPs. This analytical approach requires less peptide, and determination of essential parameters, such as percent of correctly folded peptide, occurs more rapidly. In particular, a research group generated an LC-MS approach that allows the determination of the state of disulfide connectivity in peptides or proteins.[26] The researchers showed that, instead of performing peptide cleavage using a proteolytic method before analysis, the target peptide could be fragmented using the MS directly. The fragments generated by colliding the peptide into an ion trap were reanalyzed to obtain the atomic mass of the fragments. This allowed for very rapid determination of the folding/disulfide-link state with no need for preliminary treatment/preparation.

To determine if this approach would be suitable in this study, a custom synthetic peptide was acquired using the wild type primary amino acid sequence of EeTI-II. This peptide, 95 % pure and properly folded/linked, was used to establish the published approach in-house. The single-charge peptide was not observed due to its higher molar mass than the mass range set for the MS system. The +2 charge state parental ion appeared at m/z = 1440.10, the +3 charge state parental ion appeared at m/z = 962.40, and the +4 charge state parental ion appeared at m/z = 722.05 (Figure 3). This is consistent with the calculated molecular weight of 2885.44 Da for the synthetic peptide. The absence of any prominent peaks in the spectrogram was consistent with the highly pure state of the properly folded peptide. Initial HCD applied an increase in energy from 10–90 % over time; however, the +2 charge parental peptide was particularly resistant to dissasociation. An HCD energy strength of 95 % yielded multiple peptide fragments (z = +1) that can be used to derive the original peptide structure (Figure 3). Fragmentation performed on the +3 charge parental ion provided very different results. An HCD energy level of 45 % produced some fragmentation and a corresponding decrease in the parental ion peak (Figure 3). An increase in energy to 50 % resulted in a marked reduction of the parental peak and most other peaks present in the 45 % energy spectrum. The information provided is potentially useful, but further tuning of the HCD energy level between 45–50 % may need to be performed in order to obtain better results.

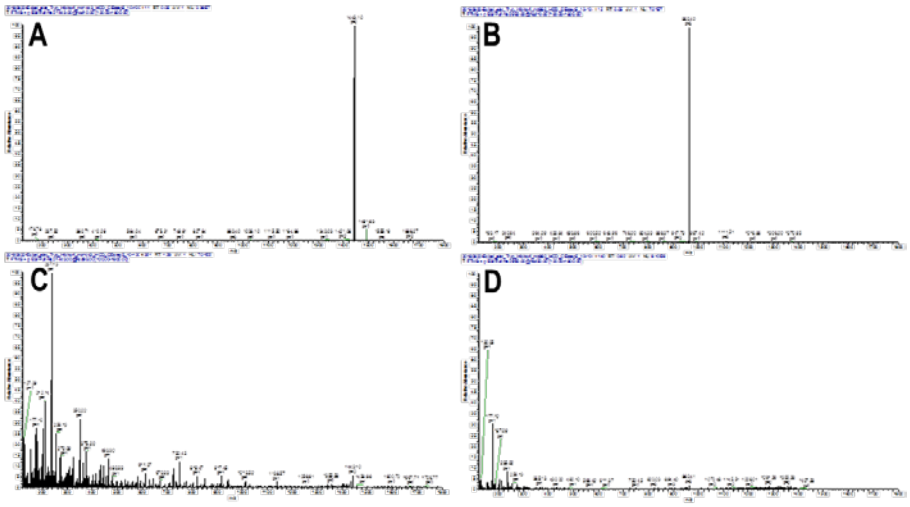

Figure 3. Sample MS spectra for the +2 charge state (A and C) and the +3 charge state (B and D) of the folded peptide ion. For the +2 charge state peptide ion at collision energy of 10 % (A) and 95 % (C), the various fragment peaks obtained from the native peptide are displayed. For the +3 charge state peptide ion at collision energy of 10 % (B) and 50 % (D), the various fragment peaks obtained from the native peptide are displayed.

Fragmentation performed on the +4 charge parental ion provided slightly different results to those shown in Figure 3. An HCD energy level of 20 % produced some fragmentation and a corresponding decrease in the parental ion peak in a similar manner to the +3 charge parental peak (data not shown). Fragment peaks possesing a +3 charge were primarily present in the spectrum with a few peaks similar to those identified earlier in the 100–300 *m/z* range possesing a +1 charge. As seen with the +3 charge parental ion, an increase in energy to 30 % resulted in a marked reduction of the parental peak and most other peaks present in the 20 % energy spectrum. As with the +3 charge parental ion, the information provided is potentially useful, but further tuning of the HCD energy level between 20–30 % may need to be performed in order to obtain better results. While further refinement is required, analysis can begin on the nature of the small ions identified in the 100–400 *m/z* range. Depending on information obtained expansion of analysis to peaks in the higher (400–800 *m/z*) range may be desirable. Now that some soluble product is being obtained, even if it is from one of the amino acid variants, an effort can start in cleaving and repurifying final product for similar MS analysis.

ACKNOWLEDGMENTS

The authors would like to acknowledge U.S. Army funding provided through the Edgewood Chemical Biological Center's In-House Laboratory Independent Research program.

REFERENCES

[1] Sesardic, D.; Jones, R.G.; Leung, T.; Alsop, T.; Tierney, R. Detection of Antibodies against Botulinum Toxins. *Mov. Disord.* **2004,** *19* (Suppl 8), pp S85–91.

[2] Tamborrini, M.; Holzer, M.; Seeberger, P.H.; Schurch, N.; Pluschke, G. Anthrax Spore Detection by a Luminex Assay Based on Monoclonal Antibodies That Recognize Anthrose-Containing Oligosaccharides. *Clin. Vaccine. Immunol.* **2010,** *17* (9), pp 1446–1451.

[3] Kolmar, H. Natural and Engineered Cystine Knot Miniproteins for Diagnostic and Therapeutic Applications. *Curr. Pharm. Des.* **2011,** *17* (38), pp 4329–4336.

[4] Ouyang, W.; Yu, Z.; Zhao, X.; Lu, S.; Wang, Z. Aptamers in Hematological Malignancies and Their Potential Therapeutic Implications. *Crit. Rev. Oncol. Hematol.* **2016,** *106*, pp 108–117.

[5] Hu, P.P. Recent Advances in Aptamers Targeting Immune System. *Inflammation.* **2017,** *40* (1), pp 295–302.

[6] Chandola, C.; Kalme, S.; Casteleijn, M.G.; Urtti, A.; Neerathilingam, M. Application of Aptamers in Diagnostics, Drug-Delivery and Imaging. *J. Biosci.* **2016,** *41* (3), pp 535–561.

[7] Daly, N.L.; Craik, D.J. Bioactive Cystine Knot Proteins. *Curr. Opin. Chem. Biol.* **2011,** *15* (3), pp 362–368.

[8] Kolmar, H. Biological Diversity and Therapeutic Potential of Natural and Engineered Cystine Knot Miniproteins. *Curr. Opin. Pharmacol.* **2009,** *9* (5), pp 608–614.
[9] Reinwarth, M.; Nasu, D.; Kolmar, H.; Avrutina, O. Chemical Synthesis, Backbone Cyclization and Oxidative Folding of Cystine-Knot Peptides: Promising Scaffolds for Applications in Drug Design. *Molecules.* **2012,** *17* (11), pp 12533–12552.
[10] Isaacs, N.W. Cystine Knots. *Curr. Opin. Struct. Biol.* **1995,** *5* (3), pp 391–395.
[11] Chiche, L.; Gaboriaud, C.; Heitz, A.; Mornon, J.P.; Castro, B.; Kollman, P.A. Use of Restrained Molecular Dynamics in Water to Determine Three-Dimensional Protein Structure: Prediction of the Three-Dimensional Structure of Ecballium Elaterium Trypsin Inhibitor II. *Proteins.* **1989,** *6*, pp 405–417.
[12] Gaboriaud, C.; Vaney, M.C.; Bachet, B.; Le-Nguyen, D.; Castro, B.; Mornon, J.P. Crystallization and Preliminary X-Ray Study of Porcine Trypsin, Free and Complexed with Ecballium Elaterium Trypsin Inhibitor, a Member of the Squash Inhibitors Family. *J. Mol. Biol.* **1989,** *210* (4), pp 883–884.
[13] Heitz, A.; Chiche, L.; Le-Nguyen, D.; Castro, B. 1H 2D NMR and Distance Geometry Study of the Folding of Ecballium Elaterium Trypsin Inhibitor, a Member of the Squash Inhibitors Family. *Biochemistry.* **1989,** *28* (6), pp 2392–2398.
[14] Kimura, R.H.; Jones, D.S.; Jiang, L.; Miao, Z.; Cheng, Z.; Cochran, J.R. Functional Mutation of Multiple Solvent-Exposed Loops in the Ecballium Elaterium Trypsin Inhibitor-II Cystine Knot Miniprotein. *PLoS One.* **2011,** *6* (2), p e16112.
[15] Lahti, J.L.; Silverman, A.P.; Cochran, J.R. Interrogating and Predicting Tolerated Sequence Diversity in Protein Folds: Application to E. elaterium Trypsin Inhibitor-II Cystine-Knot Miniprotein. *PLoS Comput. Biol.* **2009,** *5* (9), p e1000499.
[16] Yu, R.; Seymour, V.A.; Berecki, G.; Jia, X.; Akcan, M.; Adams, D.J.; Kaas, Q.; Craik, D.J. Less Is More: Design of a Highly Stable Disulfide-Deleted Mutant of Analgesic Cyclic α-Conotoxin Vc1.1. *Sci. Rep.* **2015,** *5*, p 13264.
[17] Bonneau, R.; Strauss, C.E.; Baker, D. Improving the Performance of Rosetta Using Multiple Sequence Alignment Information and Global Measures of Hydrophobic Core Formation. *Proteins.* **2001,** *43* (1), pp 1–11.
[18] Bonneau, R.; Tsai, J.; Ruczinski, I.; Chivian, D.; Rohl, C.; Strauss, C.E.; Baker, D. Rosetta in Casp4: Progress in Ab Initio Protein Structure Prediction. *Proteins.* **2001,** *45* (S5), pp 119–126.
[19] Le-Nguyen, D.; Mattras, H.; Coletti-Previero, M.A.; Castro, B. Design and Chemical Synthesis of a 32 Residues Chimeric Microprotein Inhibiting Both Trypsin and Carboxypeptidase A. *Biochem. Biophys. Res. Commun.* **1989,** *162* (3), pp 1425–1430.
[20] Bhattacharyya, M.; Gupta, K.; Gowd, K.H.; Balaram, P. Rapid Mass Spectrometric Determination of Disulfide Connectivity in Peptides and Proteins. *Mol. BioSyst.* **2013,** *9* (6), pp 1340–1350.
[21] Wu, S.; Skolnick, J.; Zhang, Y. Ab Initio Modeling of Small Proteins by Iterative Tasser Simulations. *BMC. Biol.* **2007,** *5*, p 17.
[22] Lee, M.S.; Olson, M.A. Assessment of Detection and Refinement Strategies for De Novo Protein Structures Using Force Field and Statistical Potentials. *J. Chem. Theory. Comput.* **2007,** *3* (1), pp 312–324.
[23] Jackson, P.J.; McNulty, J.C.; Yang, Y.K.; Thompson, D.A.; Chai, B.; Gantz, I.; Barsh, G.S.; Millhauser, G.L. Design, Pharmacology, and NMR Structure of a Minimized Cystine Knot with Agouti-Related Protein Activity. *Biochemistry.* **2002,** *41* (24), pp 7565–7572.
[24] McNulty, J.C.; Thompson, D.A.; Bolin, K.A.; Wilken, J.; Barsh, G.S.; Millhauser, G.L. High-Resolution NMR Structure of the Chemically-Synthesized Melanocortin Receptor Binding Domain Agrp(87-132) of the Agouti-Related Protein. *Biochemistry.* **2001,** *40* (51), pp 15520–15527.
[25] Daly, N.L.; Koltay, A.; Gustafson, K.R.; Boyd, M.R.; Casas-Finet, J.R.; Craik, D.J. Solution Structure by NMR of Circulin A: A Macrocyclic Knotted Peptide Having Anti-HIV Activity. *J. Biol. Chem.* **1999,** *285* (1), pp 333–345.

SSI PROJECTS

Adsorption of non-polar adsorbates on the organic linker of metal-organic frameworks

Trenton M. Tovar, Ivan O. Iordanov, Jared B. DeCoste*
U.S. Army Edgewood Chemical Biological Center, Research & Technology Directorate,
5183 Blackhawk Rd, Aberdeen Proving Ground, MD 21010

ABSTRACT

UiO–66 is a highly stable metal-organic framework that has garnered interest for many adsorption applications. For small, nonpolar adsorbates, physisorption is dominated by weak Van der Waals interactions limiting the adsorption capacity. A common strategy to enhance the adsorption properties of isoreticular metal-organic frameworks, such as UiO–66, is to add functional groups to the organic linker. Low- and high-pressure O_2 isotherms were measured on UiO–66 metal-organic frameworks functionalized with electron-donating and withdrawing groups. It was found that the electron-donating effects of $–NH_2$, –OH, and $–OCF_3$ groups enhance the uptake of O_2. Interestingly, a significant enhancement in both the binding energy and adsorption capacity of O_2 was observed for UiO–66–$(OH)_2$–*p*, which has two –OH groups *para* from one another. Density functional theory simulations were used to calculate the binding energy of oxygen to each metal-organic framework, which trended with the adsorption capacity and agreed well with the heats of adsorption calculated from the Toth model fit to multi-temperature isotherms. Density functional theory simulations also determined the highest energy binding site to be on top of the electron π-cloud of the aromatic ring of the ligand, with a direct trend of the binding energy with low-pressure adsorption capacity. Uniquely, density functional theory found that oxygen molecules adsorbed to UiO–66–$(OH)_2$–*p* prefer to align parallel to the –OH groups on the aromatic ring. Similar effects for the electron-donation of the functional groups were observed for the low-pressure adsorption of N_2, CH_4, and CO_2.

Keywords: metal-organic frameworks, oxygen adsorption, density functional theory

1. INTRODUCTION

Metal-organic frameworks (MOF) are promising materials for use as next-generation adsorbents. They consist of highly porous crystalline networks of metal nodes connected by organic linkers.[1] Due to the variability of both the metal centers and the organic linkers, the physical and chemical properties of MOFs can be tuned for specific applications such as gas storage,[2] catalysis,[3] separations,[4] and sensing.[5] Given the large number of potential MOFs,[6] it is highly desirable to develop rational design rules to guide the synthesis of MOFs with optimal properties. However, this is a complex task that requires detailed knowledge of atomistic interactions, specifically at adsorption sites.

Determining preferential adsorption sites in MOFs is complicated by the presence of multiple sites and intermolecular interactions that vary based on the desired adsorbate. Recently, experimental studies have used neutron scattering or X-ray crystallography to directly observe adsorption sites;[7–10] however, the most widely used tool to study preferential adsorption sites is molecular modeling.[11] Typical MOF adsorption sites include open-metal sites,[12–14] hydrogen bonding sites,[15,16] pore confinement sites,[17,18] and acid-base interactions.[19,20]

Physisorption of small non-polar gases, such as oxygen and nitrogen, has been sparsely studied at ambient temperature and pressures, due to the inherent lack of intermolecular forces for adsorption. Previous studies on oxygen adsorption have primarily focused on high-pressure adsorption,[21,22] which is driven by large pore volumes, or strong interactions with metals,[23–28] which typically require a hard vacuum or heating to deliver the adsorbate. Enhancement of the weak Van der Waals forces within the confined space of microporous material, such as a MOF, has the potential to increase the adsorption capacity of the material at ambient pressure, while allowing the adsorbate to be delivered on demand without the addition of energy.

Although many MOFs have significantly better adsorption properties than current industrial adsorbents, stability issues have limited their application. UiO–66 (Figure 1) is a MOF of interest due to its thermal, water, and acidic stability.[29–31] While UiO–66 lacks open-metal sites, the organic ligands are amenable to functionalization for improvement of adsorption properties.[33–37] The enhanced adsorption characteristics in functionalized UiO MOFs are

attributed to either the polarity of the functional group,[33] or a confinement effect due to a reduction in pore size;[34] however, a specific preferential adsorption site has yet to be defined.

A joint experimental and theoretical method is presented here to explore the adsorption enhancement of nonpolar adsorbates on functionalized UiO–66 and to determine the preferential adsorption sites. Room temperature O_2 adsorption isotherms were measured on various functionalized UiO MOFs. Density functional theory (DFT) simulations were used to calculate binding energies inside a unit cell to find the optimal adsorption site. Heat of adsorption measurements were compared to the DFT results. Isotherms were then measured for N_2, CH_4, and CO_2 to show similar trends across each of the nonpolar adsorbates.

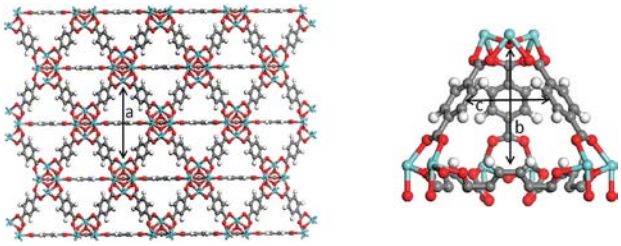

Figure 1. UiO–66 (zirconium: blue, oxygen: red, carbon: grey, and hydrogen: white) depicted along its axis (left) exhibiting its larger octahedral cages (a) with a diameter of ~ 1.6 nm. The smaller tetrahedral cage of UiO–66 is depicted (right), showing the bisection of the window (b) measuring ~ 1.0 nm and the distance between the benzene rings (c) measuring 0.6 nm. Pendant functional groups are incorporated into the UiO structure by using an organic linker with the appropriate functional group to replace the hydrogen atom(s).

2. METHODOLOGY

2.1 Metal-organic framework synthesis

The synthesis procedure of all UiO–66 analogs was adapted from Biswas et al.[38] Approximately 0.64 mmol of $ZrCl_4$ was mixed with 0.72 mmol of linker in 6 mL of N,N–Dimethylformamide (DMF) and 2 mL of formic acid in a 20-mL scintillation vial. The vial was sonicated for 1 hour to dissolve the precursors. The solution was transferred to a Teflon™-lined Parr™ bomb and placed in an oven at room temperature. The oven temperature was ramped at 5 °C/min to 150 °C and held for 24 hours. Once cooled, the solids were filtered and washed 3 times with 10 mL of DMF. The samples were then dried at 90 °C. After drying, the samples were solvent exchanged with 10 mL of methanol for 24 hours. The samples were centrifuged at 6,000 rpm for 5 minutes, decanted, and the exchange procedure was repeated 2 more times. The samples were then dried at 90 °C. Before all measurements, the samples were activated at 90 °C under high vacuum.

2.2 Metal-organic framework characterization

Nitrogen gas sorption measurements were performed on a Micromeritics® 3Flex 3500 instrument at 77 kelvin (K). Each sample was off-gassed overnight under vacuum at 90 °C. The Brunauer-Emmett-Teller (BET) model was applied over the pressure range, as described by Walton and Snurr,[39] to obtain the specific surface area (m^2/g).

Powder X-ray diffraction (PXRD) was measured using a Rigaku MiniFlex™ 600 X-ray diffractometer with a D/Tex detector. Samples were scanned at 40 kV and 15 mA with a scan rate of 2°/minute over a 2θ range of 3° to 50°. Zero-background discs were used, and a background correction was performed in the Rigaku PDXL software (version 2.1.3.6).

Low-pressure isotherms for O_2, N_2, CH_4, and CO_2 were measured on a Micromeritics® 3Flex 3500 instrument. Samples were immersed in a temperature controlled water bath at the desired temperature during the measurement.

High-pressure isotherms were measured on a home-built apparatus similar to the design in Wang et al.[40] The adsorbent bed was placed in a TestEquity Model 115 temperature chamber and degassed *in situ* at 90 °C with a Pfeiffer Vacuum HiCube 80 Eco pumping station. Pressures were measured using a Paroscientific Model 745 Digiquartz® transducer. Helium expansions were performed to calculate free volume. To measure isotherms, O_2 was dosed to a reference cell of known volume, the pressure was allowed to equilibrate, then a valve to the adsorbent bed was opened and pressure was allowed to equilibrate again. This process was repeated for each data point. Loading was calculated based on the

difference between the measured pressure and the expected pressure for the known free volume. For high-pressures, a compressibility factor based on virial coefficients was used to correct for non-ideal gas behavior.

2.3 Computational modeling

Calculations were performed using DFT, as implemented in the Gaussian and Quantum Espresso software packages. In order to model the paramagnetism of molecular oxygen correctly, all cluster calculations were done in the unrestricted Hartree-Fock (UHF) formalism, with a triplet state for oxygen. For the periodic calculations of UiO–66, a 14.6 Å x 14.6 Å x 20.7Å supercell with 228 atoms was used. The density functional used was PBE,[41] with projector-augmented wave (PAW) pseudopotentials and an energy wavefunction cutoff of 40 Ry. Dispersion interactions were included under Grimme's DFT-D2 scheme.[42] The calculations were spin-polarized to account for oxygen, and correctly converged to a net magnetic moment of 2 bohr magneton per unit cell containing oxygen.

3. RESULTS AND DISCUSSION

3.1 Effect of functional group on O_2 adsorption

UiO–66 and UiO–66 functionalized with an amine, hydroxy, nitro, trifluoromethoxy, or 2 *para* hydroxy groups were synthesized and are referred to as UiO–66–NH_2, UiO–66–OH, UiO–66–NO_2, UiO–66–OCF_3, and UiO–66–$(OH)_2$–*p*, respectively. N_2 isotherms at 77 K (Figure 2a) and XRD patterns (Figure 2b) of the MOFs show highly porous, crystalline materials with isoreticular structures. As expected, the surface area scales inversely to the mass of the linker (Table 1).[43]

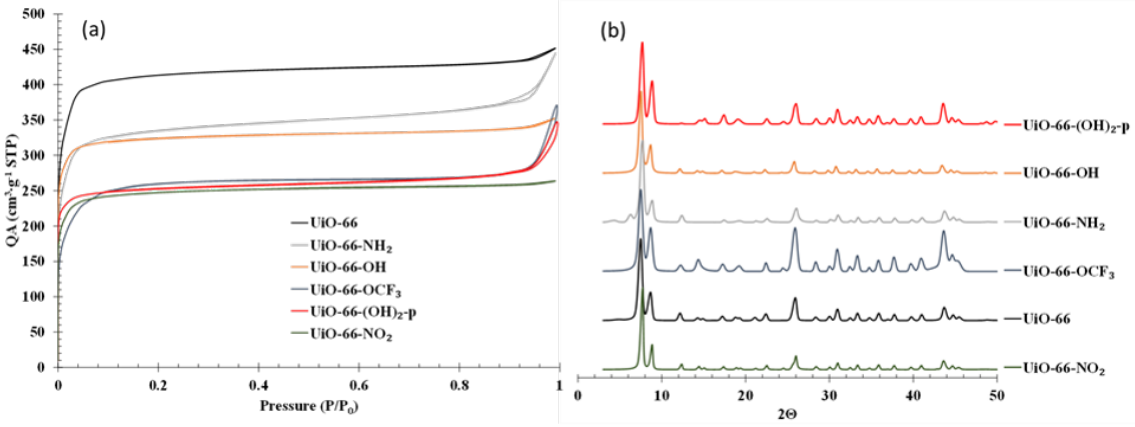

Figure 2. (a) PXRD patterns confirming the crystallinity for the UiO–66 analogs studied. (b) Nitrogen isotherms at 77 K used to determine the surface area of each MOF.

Table 1. Simulated binding energies for O_2 adsorption on the aromatic ring of the ligand, volumetric O_2 adsorption capacity at 0.5 bar, and BET surface area for UiO–66 analogs.

MOF	Binding Energy (kJ mol^{-1})	O_2 Adsorbed @ 0.5 bar × 10^{-4} (mol cm^{-1})	BET Surface Area (m^2 g^{-1})
UiO–66	-10.9	0.95	1710
UiO–66–NO_2	-11.1	1.04	1010
UiO–66–NH_2	-12.0	1.22	1360
UiO–66–OH	-11.5	1.27	1330
UiO–66–OCF_3	-11.7	1.28	1060
UiO–66–$(OH)_2$–*p*	-13.5	1.84	1030

Figure 3 shows excess O_2 isotherms at room temperature. On a gravimetric basis, the materials with the lowest uptake are UiO–66, UiO–66–OCF_3, and UiO–66–NO_2. This is interesting as both the –OCF_3 and –NO_2 groups are polar, bulky functional groups that would be expected to increase adsorption if the adsorption mechanism were based on pore confinement or an induced dipole interaction of the adsorbate with the functional group. An increase in adsorption capacity was observed for the –NH_2 and –OH groups. Both of these functional groups are polar and weigh significantly less than the –OCF_3 and –NO_2 groups. To take the effect of the mass of the functional group into account, the loading was normalized to volume (Figure 1, Table 1). When compared to UiO–66, UiO–66–NO_2 shows a slight enhancement in O_2 capacity, while UiO–66–NH_2, UiO–66–OH, and UiO–66–OCF_3 exhibit greater than a 25 % enhancement in O_2 capacity. It should be noted that the weight normalization was calculated using the skeletal density of an ideal UiO–66 crystal.[34]

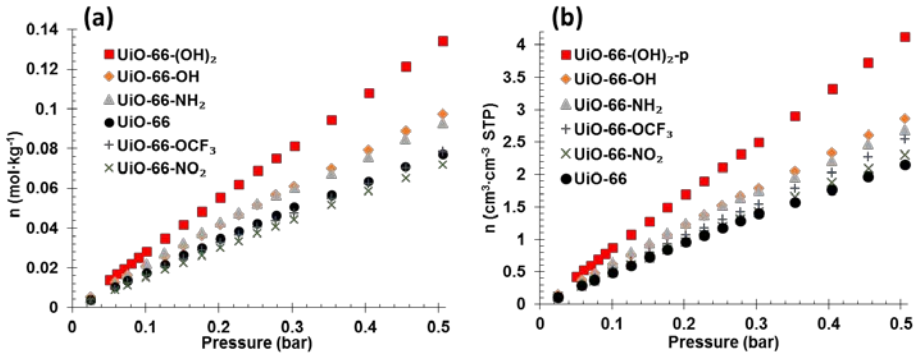

Figure 3. Room temperature excess O_2 isotherms measured on various functionalized UiO–66 analogs, presented on (a) a gravimetric basis and (b) a volumetric basis.

When UiO–66 functionalized with two –OH groups in the *para* positions to one another (UiO–66–$(OH)_2$–*p*) was examined, it was observed that it adsorbs significantly more oxygen than any other UiO analog tested. Even though UiO–66–$(OH)_2$–*p* has one of the smallest BET surface areas of the MOFs studied, there was a > 90 % enhancement in the adsorption of oxygen compared to UiO–66 on a normalized volume basis. From these results, it can be concluded that the adsorption of oxygen is not purely a surface area effect, leading to the hypothesis that the variation in low-pressure oxygen adsorption is driven by the effect the functional group has on the adsorption site.

3.2 DFT simulations of O_2 binding

To determine the effect various functional groups have on the adsorption of O_2, DFT was used to determine the optimal binding sites, orientations, and energies. The interaction between the O_2 molecule and the MOF linker is dominated by weak Van der Waals interactions, and therefore the optimization gradient could find many local minima in the potential energy surface, depending on the initial placement. It was found that the optimal binding configuration for the O_2 molecule near the MOF linker was with its bonds parallel to the face of the aromatic ring of the ligand, likely due to its interaction with the π-cloud. This was repeated with various UiO analogs, and a similar configuration for the energy minimum was observed.

With the knowledge that the optimal adsorption site for O_2 is on the aromatic ring, regardless of the attached functional group, we hypothesized that the increase in adsorption is due to an electronic effect from electron-donation from the functional group to the aromatic ring. The binding energies at this site are listed in Table 1 for each of the functionalized MOFs and agree with the increase in oxygen adsorption. The sole electron-withdrawing group studied, UiO–66–NO_2, shows the lowest O_2 adsorption and binding energy of the functionalized UiO–66 analogs. The electron-donating amino, hydroxy, and trifluoromethoxy groups exhibit significant enhancement to the binding energy and adsorption. Furthermore, UiO–66–$(OH)_2$–*p*, due to the two electron-donating groups, exhibits an even greater enhancement in adsorption capacity and DFT binding energy.

To further explore the idea of electron-donation from the functional groups to the aromatic ring being the driving factor for increased adsorption, several hypothetical UiO MOFs with different or additional hydroxy positions were simulated. Figure 4 shows the hypothetical linkers and binding energies for O_2. As expected, when the number of hydroxy groups increases to three and four, the binding energy increases as well. On the other hand, for the isomers with two hydroxy groups, the effect on the binding energy depends on the hydroxy orientation. For hydroxy groups *para* to one another, a significant increase in binding energy occurs. However, for hydroxy groups *ortho* or *meta* to one another, there is no increase in the binding energy compared to UiO–66–OH.

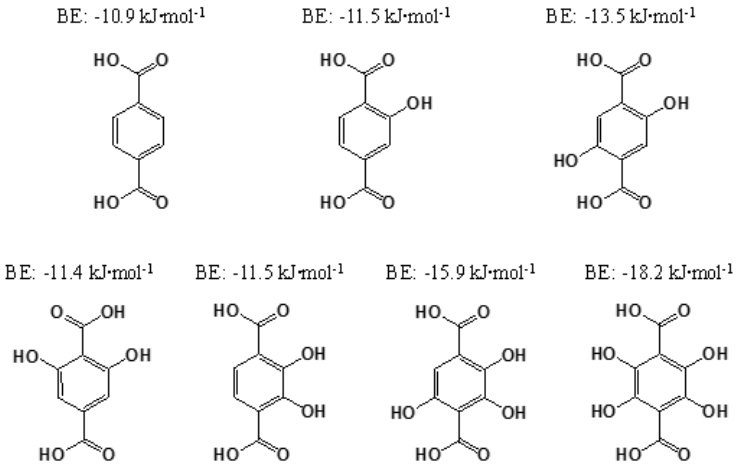

Figure 4. Calculated O_2 binding energies of terepthalic acid linkers containing hydroxyl groups.

Interestingly, when allowed to optimize, O_2 adsorbed on the ligand of UiO–66–$(OH)_2$–*p* aligns parallel to the two hydroxy groups, as shown in Figure 5, suggesting that the alignment of the O_2 molecule to the two hydroxy groups has a significant effect on the binding energy. To further demonstrate this effect, a series of calculations in which the O_2 molecule was fixed above the center of the benzene ring and rotated 180° within the plane parallel to the benzene ring were performed. In Figure 5, the Δ binding energy, relative to the weakest observed binding energy, is plotted as a function of the angle of the O_2 molecular alignment to the carboxylic acid groups for the *para*, *ortho*, and *meta* dihydroxy linkers. The plot shows that as the O_2 molecule is rotated counter-clockwise from the carboxylate groups, the binding energy of the O_2 molecule changes for each of the UiO–66–$(OH)_2$ isomers. For UiO–66–$(OH)_2$–*p*, the binding energy weakens slightly as the O_2 molecule is rotated toward the carbons with no functional groups, but then strengthens at 120° when aligned parallel to the hydroxy ligands. For UiO–66–$(OH)_2$–*o* and UiO–66–$(OH)_2$–*m*, the alignment effect is significantly weaker, with the preferred O_2 alignment perpendicular to the carboxylate groups in both cases.

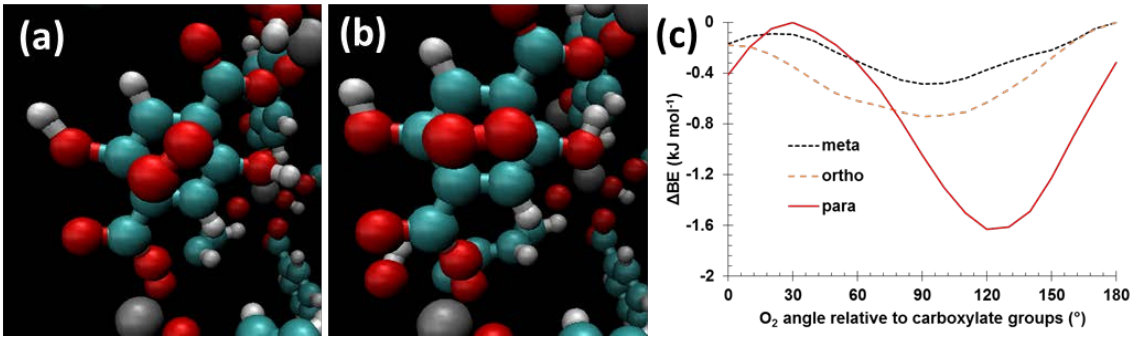

Figure 5. Oxygen adsorption on engineered forms of MOFs. Snap shots of DFT simulations (a) before and (b) after geometry optimization of O_2 on UiO–66–$(OH)_2$–*p*. (c) The change in binding energy as the O_2 molecule is rotated counter-clockwise from alignment with the carboxylic acid groups.

3.3 O_2 heats of adsorption

While adsorption energy is integral to the shape of the adsorption isotherm, simply trying to relate capacity to calculated binding energies is not an ideal comparison. To better support the binding energy calculations for this specific adsorption site, isosteric heats of adsorption were calculated from oxygen isotherms taken at multiple temperatures. Due to the limited pressure range and the linear nature of the O_2 isotherms when measured at low pressures, accurate heats of adsorption are difficult to obtain from isotherm model fitting due to too many degrees of freedom in the regression; therefore, high-pressure O_2 isotherms were used to calculate the heats of adsorption. Figure 6 shows high-pressure oxygen isotherms measured at 25 °C, 50 °C, and 75 °C for UiO–66, UiO–66–OH, and UiO–66–$(OH)_2$–*p*. At pressures below 20 bar, UiO–66–$(OH)_2$–*p* and UiO–66–OH adsorb more O_2 than UiO–66, which is consistent with the low-pressure measurements and the higher adsorption affinity predicted by DFT. However, at higher pressures, UiO–66 has the highest capacity due to its larger surface area and pore volume.

In Figure 6, the fits based on the multi-temperature Toth isotherm model are also shown. The Toth isotherm model was chosen as it correctly models linearity in the Henry's law regime and saturation at infinite pressure. It also has the advantage of the regressed parameter *Q* representing the heat of adsorption at zero loading, which can be directly compared to the calculated binding energy.[44]

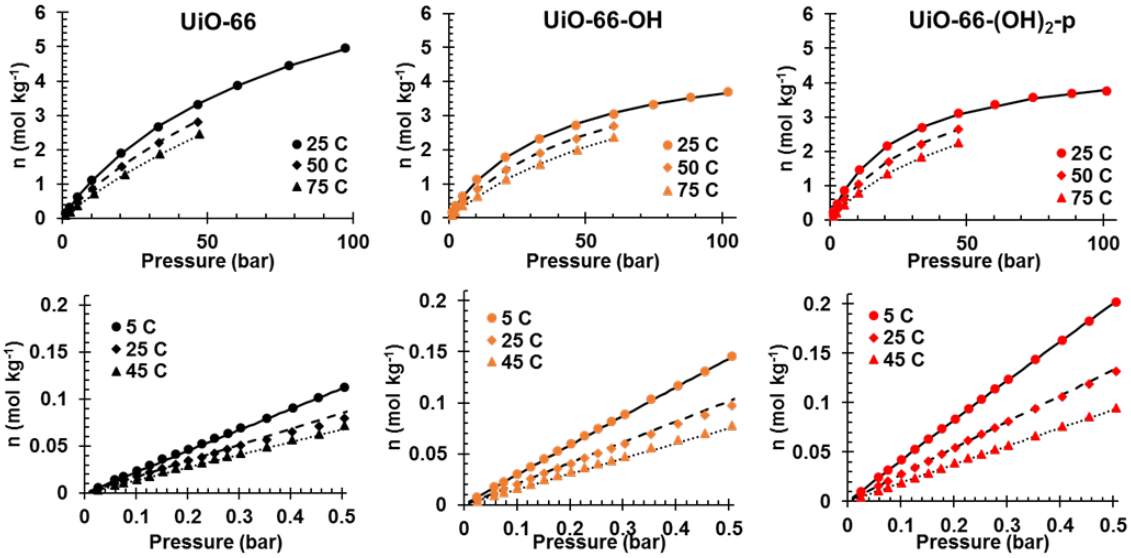

Figure 6. O_2 adsorption isotherms at multiple temperatures from the high (top) and low (bottom) pressure apparatuses on UiO–66, UiO–66–OH, and UiO–66–$(OH)_2$–*p*.

By using the regressed saturation loading from the high-pressure data, a multi-temperature Langmuir model was used to fit low-pressure isotherms measured at 5 °C, 25 °C, and 45 °C (data and fits are also shown in Figure 6). Table 2 lists the measured O_2 heats of adsorption using both the low- and high-pressure isotherm models and compares them to the calculated DFT binding energy for each MOF. The value for UiO–66 agrees well with previously reported O_2 heats of adsorption.[21] For each method, the values agree very well with each other, exhibiting the same trend that adding hydroxy groups increases the heat of adsorption. Furthermore, the agreement with the binding energies determined from the DFT simulations is remarkable.

Table 2. Heat of adsorption at zero loading measured from low- and high-pressure O_2 isotherms on UiO–66, UiO–66–OH, and UiO–66–$(OH)_2$–*p* fit by a Langmuir and Toth model respectively. The binding energy calculated from DFT is also given.

MOF	LP Q (kJ mol^{-1})	HP Q (kJ mol^{-1})	BE (kJ mol^{-1})
UiO–66	9.2	10.8	10.9
UiO–66–OH	12.1	12.8	11.5
UiO–66–$(OH)_2$–*p*	14.6	14.4	13.5

3.4 Effect of metal node variation on O_2 adsorption

To further support the positive effect of the 2,5–dihydroxyterephthalate (dobdc) linker on O_2 adsorption, another series of isoreticular MOFs was made using the dobdc linker with several rare-earth metals. The synthesis and characterization of these analogs was recently reported elsewhere.[45] The XRD patterns exhibit a related structure as the Zr based UiO–66 MOFs. Figure 7 shows the O_2 adsorption for UiO–66, UiO–66–$(OH)_2$–*p*, and three UiO–66–$(OH)_2$–*p* analogs made with Y, Eu, and Yb, referred to as Y–dobdc, Eu–dobdc, and Yb–dobdc, respectively. To account for the mass difference of the metals, an ideal crystal density was used to convert the isotherms from a mass basis to a volumetric uptake. While not as effective as UiO–66–$(OH)_2$–*p*, each of the MOFs with the dobdc linker adsorb significantly more O_2 than UiO–66. The isotherms for the Y–dobdc, Eu–dobdc, and Yb–dobdc MOFs are very similar, indicating that the metal does not play a significant role in O_2 adsorption. However, Y–dobdc, Eu–dobdc, and Yb–dobdc have much lower surface areas of 600 m^2/g, 510 m^2/g, and 490 m^2/g, respectively (compared to 1,030 m^2/g for UiO–66–$(OH)_2$–*p*), indicating that the morphology and subsequent surface area does play a role in the oxygen adsorption.

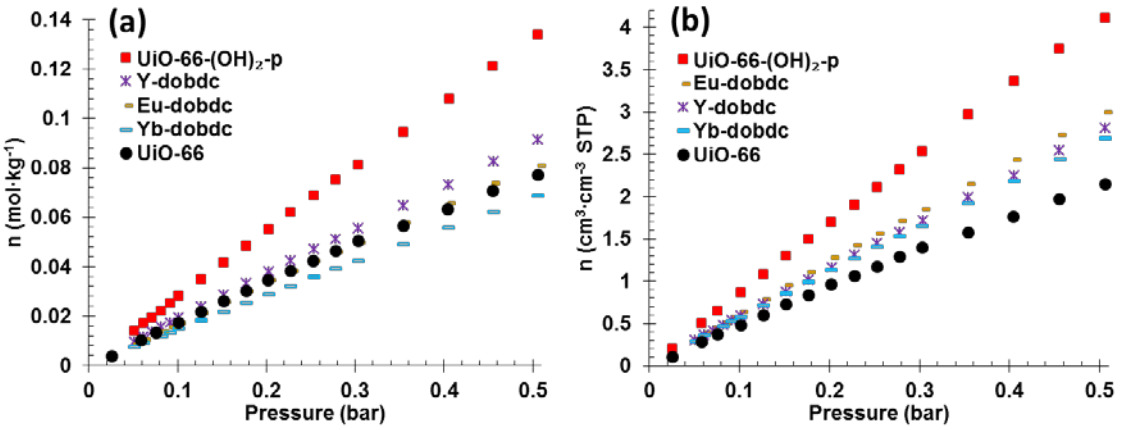

Figure 7. O_2 isotherms on three isoreticular MOFs made from Y, Eu, and Yb compared with UiO–66 and UiO–66–$(OH)_2$–*p* on (a) a gravimetric and (b) a volumetric basis.

3.5 N_2, CH_4, and CO_2 isotherms

To determine if the effect of electron donation is observed for other small non-polar gases, low-pressure isotherms were performed at room temperature for N_2, CH_4, and CO_2, as shown in Figure 8. The N_2 isotherms are very similar to O_2 in terms of loading, and the electron-donating functional groups have a significant increase on adsorption. CO_2 has significantly stronger intermolecular interactions than O_2, resulting in significantly higher loadings on each of the MOFs and a nonlinear isotherm shape. Despite the large increase in loadings, the same trend of enhanced adsorption from electron-donating functional groups was observed. While CH_4 is nonpolar, the molecular symmetry is different as it is not a linear molecule and does not have π-electrons like the other adsorbates examined. This possibly leads to a different mechanism of adsorption than interaction with the aromatic π-cloud. For the bulky functional groups of $–NO_2$ and $–OCF_3$, CH_4 adsorption is enhanced significantly above the baseline UiO–66. This may be due to another adsorption site that relies on a confinement effect that is not as strong for the linear adsorbates. UiO– 66–$(OH)_2$–*p* still has the highest adsorption indicating the electron-donating effect has an impact on adsorption independent of the adsorbate.

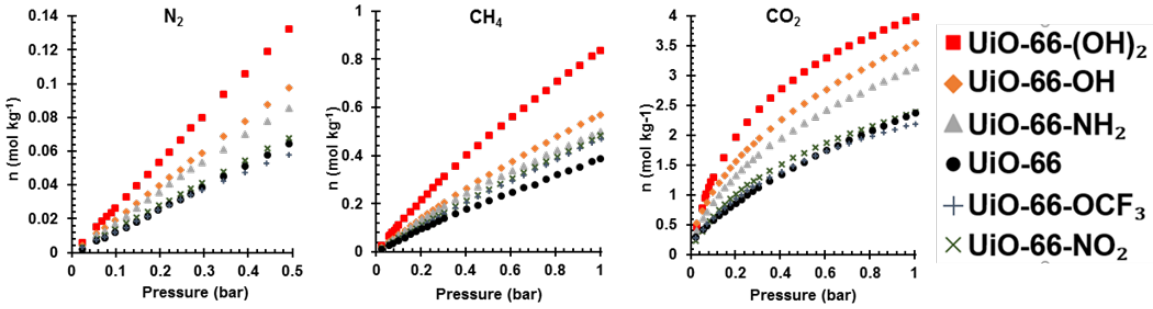

Figure 8. Room temperature N_2, CH_4, and CO_2 isotherms on functionalized UiO–66.

4. CONCLUSIONS

Experiments and simulations were used to explore the adsorption sites and impact of functionalization on a series of isoreticular UiO–66 MOFs for the adsorption of nonpolar adsorbates. DFT simulations found that the optimal binding site is on the face of the aromatic ring of the benzenedicarboxylic acid ligand. When functional groups are added, isotherms show that electron-donating groups significantly enhance the adsorption. The addition of a second hydroxy group in the *para* position to the first has a significant enhancement on the adsorption with the optimal binding site on the aromatic π-cloud parallel to the functional groups. The isosteric heats of adsorption agree well with the simulated DFT binding energies for O_2 on UiO–66, UiO–66–OH, and UiO–66–$(OH)_2$–*p*.

ACKNOWLEDGMENTS

The authors thank The U.S. Assistant Secretary of the Army for Acquisitions, Logistics, and Technology (ASA(ALT)) for supporting the Edgewood Chemical Biological Center's Surface Science Initiative program. This research was performed while Trenton Tovar held a National Research Council Postdoctoral Research Associateship Program position at the Edgewood Chemical Biological Center.

REFERENCES

[1] Kim, J.; Chen, B.; Reinike, T.M.; Li, H.; Eddaoudi, M.; Moler, D.B.; O'Keefe, M; Yaghi, O.M. Assembly of Metal−Organic Frameworks from Large Organic and Inorganic Secondary Building Units: New Examples and Simplifying Principles for Complex Structures. *J. Am. Chem. Soc.* **2001,** *123* (34), pp 8239–8247.

[2] Sumida, K.; Rogow, D.L.; Mason, J.A.; McDonald, T.M.; Bloch, E.D.; Herm, Z.R.; Bae, T.-H.; Long, J.R. Carbon Dioxide Capture in Metal–Organic Frameworks. *Chem. Rev.* **2012,** *112* (2), pp 724–781.

[3] Lee, J.Y.; Farha, O.K.; Roberts, J.; Scheidt, K.A.; Nguyen S.T.; Hupp, J.T. Metal-Organic Framework Materials as Catalysts. *Chem. Soc. Rev.* **2009,** *38* (5), pp 1450–1459.

[4] Li, J.R.; Sculley J.; Zhou, H.-C. Metal–Organic Frameworks for Separations. *Chem. Rev.* **2012,** *112* (2), pp 869–932.

[5] Kreno, L.E.; Leong, K.; Farha, O.K.; Allendorf, M.; Van Duyne, R.P.; Hupp, J.T. Metal–Organic Framework Materials as Chemical Sensors. *Chem. Rev.* **2012,** *112* (2), pp 1105–1125.

[6] Wilmer, C.E.; Leaf, M.; Lee, C.Y.; Farha, O.K.; Hauser, B.G.; Hupp, J.T.; Snurr, R.Q. Large-scale screening of hypothetical metal-organic frameworks. *Nat. Chem.* **2012,** *4* (2), pp 83–89.

[7] Wu, H.; Simmons, J.M.; Srinivas, G.; Zhou, W.; Yildirim, T.J. Adsorption Sites and Binding Nature of CO_2 in Prototypical Metal−Organic Frameworks: A Combined Neutron Diffraction and First-Principles Study. *Phys. Chem. Lett.* **2010,** *1* (13), pp 1946–1951.

[8] Mulder, F.M.; Dingemans, T.J.; Schimmel, H.G.; Ramirez-Cuesta, A.J.; Kearley, G.J. Hydrogen adsorption strength and sites in the metal organic framework MOF5: Comparing experiment and model calculations. *Chem. Phys.* **2008,** *351* (1-3), pp 72–76.

[9] Rowsell, J.L.C.; Spencer, E.C.; Eckert, J.; Howard J.A.K.; Yaghi, O.M. Gas Adsorption Sites in a Large-Pore Metal-Organic Framework. *Science*. **2005,** *309* (5739), pp 1350–1354.

[10] Yang, C.; Yang, X.; Omary, M.A. Crystallographic Observation of Dynamic Gas Adsorption Sites and Thermal Expansion in a Breathable Fluorous Metal-Organic Framework. *Agnew. Chem. Int. Ed.* **2009,** *48* (14), pp 2500–2505.

[11] Düren, T.; Bae, Y.-S.; Snurr, R.Q. Using molecular simulation to characterise metal–organic frameworks for adsorption applications. *Chem. Soc. Rev.* **2009,** *38* (5), pp 1237–1247.

[12] Yang, Q.; Zhong, C. Understanding Hydrogen Adsorption in Metal−Organic Frameworks with Open Metal Sites: A Computational Study. *J. Phys. Chem. B.* **2006,** *110* (2), pp 655–658.

[13] Mallick, A.; Saha, S.; Pachfule, P.; Roy, S.; Banerjee, R.J. Selective CO_2 and H_2 adsorption in a chiral magnesium-based metal organic framework (Mg-MOF) with open metal sites. *J. Mat. Chem.* **2010,** *20* (41), pp 9073–9080.

[14] Vishnyakov, A.; Ravikovitch, P.I.; Neimark, A.V.; Bulow, M.; Wang, Q.M. Nanopore Structure and Sorption Properties of Cu−BTC Metal−Organic Framework. *Nano. Lett.* **2003,** *3* (6), pp 713–718.

[15] Hamon, L.; Leclerc, H.; Ghoufi, A.; Oliviero, L.; Travert, A.; Lavalley, J.-C.; Devic, T.; Serre, C.; Ferey, G.; Weireld, G.D.; Vimont, A.; Maurin, G. Molecular Insight into the Adsorption of H_2S in the Flexible MIL-53(Cr) and Rigid MIL-47(V) MOFs: Infrared Spectroscopy Combined to Molecular Simulations. *J. Phys. Chem. C.* **2011,** *115* (5), pp 2047–2056.

[16] Glover, T.G.; Peterson, G.W.; Schindler, B.J.; Yaghi, O.M. MOF-74 building unit has a direct impact on toxic gas adsorption. *Chem. Eng. Sci.* **2011,** *66* (2), pp 163–170.

[17] Valenzano, L.; Civalleri, B.; Chavan, S.; Palomino, G.T.; Arean C.O.; Bordiga, S. Computational and Experimental Studies on the Adsorption of CO, N_2, and CO_2 on Mg-MOF-74. *J. Phys. Chem. C.* **2010,** *114* (25), pp 11185–11191.

[18] Atci, E.; Erucar, I.; Keskin, S. Adsorption and Transport of CH_4, CO_2, H_2 Mixtures in a Bio-MOF Material from Molecular Simulations. *J. Phys. Chem. C.* **2011,** *115* (14), pp 6833–6840.

[19] Couck, S.; Denayer, J.F.M.; Baron, G.V.; Remy, T.; Gascon, J.; Kapteijn, F. An Amine-Functionalized MIL-53 Metal−Organic Framework with Large Separation Power for CO_2 and CH_4. *J. Am. Chem. Soc.* **2009,** *131* (18), pp 6326–6327.

[20] McDonald, T.M.; D'Alessandro, D.M.; Krishna, R.; Long, J.R. Enhanced carbon dioxide capture upon incorporation of N,N′-dimethylethylenediamine in the metal–organic framework CuBTTri. *Chem. Sci.* **2011**, *2* (10), pp 2022–2028.

[21] DeCoste, J.B.; Weston, M.H.; Fuller, P.E.; Tovar, T.M.; Peterson, G.,W.; LeVan, M.D.; Farha, O.K. Metal-Organic Frameworks for Oxygen Storage. *Agnew. Chem. Int. Ed.* **2014,** *53* (51), pp 14092–14095.

[22] Alezi, D.; Belmakbkhout, Y.; Suyetin, M.; Bhatt, P.M.; Weselinski, L.J.; Solovyeva, V.; Adil, K.; Spanopoulos, I.; Trikalitis, P.N.; Emwas A.-H.; Eddaoudi, M. MOF Crystal Chemistry Paving the Way to Gas Storage Needs: Aluminum-Based soc-MOF for CH_4, O_2, and CO_2 Storage. *J. Am. Chem. Soc.* **2015,** *137* (41), pp 13308–13318.

[23] Sava Gallis, D.F.; Parkes, M.V.; Greathouse, J.A.; Zhang, X.; Nenoff, T.M. Enhanced O_2 Selectivity versus N_2 by Partial Metal Substitution in Cu-BTC. *Chem. Mater.* **2015,** *27* (6), pp 2018–2025.

[24] Wang, Y.; Yang, J.; Li, Z.; Zhang, Z.; Li, J.; Yang, Q.; Zhong, C. Computational study of oxygen adsorption in metal–organic frameworks with exposed cation sites: effect of framework metal ions. *RSC Adv.* **2015,** *5* (42), pp 33432–33437.

[25] Parkes, M.V.; Greathouse, J.A.; Hart, D.B.; Sava Gallis D.F.; Nenoff, T.M. Ab initio molecular dynamics determination of competitive O_2 vs. N_2 adsorption at open metal sites of M_2(dobdc). *Phys. Chem. Chem. Phys.* **2016,** *18* (16), pp 11528–11538.

[26] Zhang, W.; Banerjee, D.; Liu, J.; Schaef, H.T.; Crum, J.V.; Fernandez, C.A.; Kukkadapu, R.K.; Nie, Z.; Nune, S.K.; Motkuri, R.K.; Chapman, K.W.; Engelhard, M.H.; Hayes, J.C.; Silvers, K.L.; Krishna, R.; McGrail, B.P.; Liu, J.; Thallapally, P.K. Redox-Active Metal–Organic Composites for Highly Selective Oxygen Separation Applications. *Adv. Mater.* **2016,** *28* (18), pp 3572–3577.

[27] Bloch, E.D.; Murray, L.J.; Queen, W.L.; Chavan, S.; Maximoff, S.N.; Bigi, J.P.; Krishna, R.; Peterson, V.K.; Grandjean, F.; Long, G.J.; Smit, B.; Bordiga, S.; Brown C.M.; Long, J.R. Selective Binding of O_2 over N_2 in a Redox–Active Metal–Organic Framework with Open Iron(II) Coordination Sites. *J. Am. Chem. Soc.*, **2011**, *133* (37), pp 14814–14822.

[28] Murray, L.J.; Dinca, M.; Yano, J.; Chavan, S.; Bordiga, S.; Brown C.M.; Long, J.R. Highly-Selective and Reversible O_2 Binding in Cr_3(1,3,5-benzenetricarboxylate)$_2$. *J. Am. Chem. Soc.* **2010,** *132* (23), pp 7856–7857.

[29] Cavka, J.H.; Jakobsen, S.; Olsbye, U.; Guillou, N.; Lamberti, C.; Bordiga S.; Lillerud, K.P. A New Zirconium Inorganic Building Brick Forming Metal Organic Frameworks with Exceptional Stability. *J. Am. Chem. Soc.* **2008,** *130* (42), pp 13850–13851.

[30] DeCoste, J.B.; Peterson, G.W.; Schindler, B.J.; Killops, K.L.; Browe, M.A.; Mahle, J.J. The effect of water adsorption on the structure of the carboxylate containing metal–organic frameworks Cu-BTC, Mg-MOF-74, and UiO-66. *J. Mater. Chem. A.* **2013,** *1* (38), pp 11922–11932.

[31] DeCoste, J.B.; Peterson, G.W.; Jasuja, H.; Glover, T.G.; Huang, Y.; Walton, K.S. Stability and degradation mechanisms of metal–organic frameworks containing the $Zr_6O_4(OH)_4$ secondary building unit *J. Mater. Chem. A.* **2013,** *1* (18), pp 5642–5650.

[32] Garibay, S.J.; Cohen, S.M.; Walton, K.S. Isoreticular synthesis and modification of frameworks with the UiO-66 topology. *Chem. Commun.* **2010,** *46* (41), pp 7700–7702.

[33] Cmarik, G.E.; Kim, M.; Cohen, S.M.; Walton, K.S. Tuning the Adsorption Properties of UiO-66 via Ligand Functionalization. *Langmuir.* **2012,** *28* (44), pp 15606–15613.

[34] Yang, Q.; Wiersum, A.D.; Llewellyn, P.L.; Guillerm, V.; Serre, C.; Maurin, G. Functionalizing porous zirconium terephthalate UiO-66(Zr) for natural gas upgrading: a computational exploration. *Chem. Commun.* **2011,** 47 (34), pp 9603–9605.

[35] Biswas, S.; Zhang, J.; Li, Z.; Liu, Y.-Y.; Grzywa, M.; Sun, L.; Volkmer, D.; Van Der Voort, P. Enhanced selectivity of CO_2 over CH_4 in sulphonate-, carboxylate- and iodo-functionalized UiO-66 frameworks. *Dalton Trans.* **2013,** *42* (13), pp 4730–4737.

[36] Jasuja, H.; Walton, K.S. Experimental Study of CO_2, CH_4, and Water Vapor Adsorption on a Dimethyl-Functionalized UiO-66 Framework. *J. Phys. Chem. C.* **2013,** *117* (14), pp 7062–7068.

[37] Zlotea, C.; Phanon, D.; Mazaj, M.; Heurtaux, D.; Guillerm, V.; Serre, C.; Horcajada, P.; Devic, T.; Magnier, E.; Cuevas, F.; Ferey, G.; Llewellyn, P.L.; Latroche, M. Effect of NH_2 and CF_3 functionalization on the hydrogen sorption properties of MOFs. *Dalton Trans.* **2011,** *40* (18), pp 4879–4881.

[38] Biswas, S.; Van Der Voort, P.A. General Strategy for the Synthesis of Functionalised UiO-66 Frameworks: Characterisation, Stability and CO_2 Adsorption Properties. *Eur. J. Inorg. Chem.* **2013**, *2013* (12), pp 2154–2160.

[39] Walton, K.S.; Snurr, R.Q. Applicability of the BET Method for Determining Surface Areas of Microporous Metal−Organic Frameworks. *J. Am. Chem. Soc.* **2007,** *129* (27), pp 8552–8556.
[40] Wang, Y.; Helvensteijn, B.; Nizamidin, N.; Erion, A.M.; Seiner, L.A.; Mulloth, L.M.; Luna, B.; LeVan, M.D. High Pressure Excess Isotherms for Adsorption of Oxygen and Nitrogen in Zeolites. *Langmuir.* **2011,** *27* (17), pp 10648–10656.
[41] Grimme, S. Semiempirical GGA-type density functional constructed with a long-range dispersion correction. *J. Comput. Chem.* **2006,** *27* (15), pp 1787–1799.
[42] Barone, V.; Casarin, M.; Forrer, D.; Pavone, M.; Sambi, M.; Vittadini, A. Role and effective treatment of dispersive forces in materials: Polyethylene and graphite crystals as test cases. *J. Comput. Chem.* **2009,** *30* (6), pp 934–939.
[43] Wu, H.; Chua, Y.S.; Krungleviciute, V.; Tyagi, M.; Chen, P.; Yildirim, T.; Zhou, W. Unusual and Highly Tunable Missing-Linker Defects in Zirconium Metal–Organic Framework UiO-66 and Their Important Effects on Gas Adsorption. *J. Am. Chem. Soc.* **2013,** *135* (28), pp 10525–10532.
[44] Do, D.D. In *Adsorption Analysis: Equilibria and Kinetics*; Yang, R.T., Ed.; Series on Chemcal Engineering, Vol. 2; Imperial College Press: London, 1998.
[45] Sava Gallis, D.F.; Rohwer, L.E.S.; Rodriguez, M.A.; Barnhart-Dailey, M.C.; Butler, K.S.; Luk, T.S.; Timlin, J.A.; Chapman, K.A. Multifunctional, Tunable Metal–Organic Framework Materials Platform for Bioimaging Applications. *ACS Appl. Mater. Interfaces.* **2017,** *9* (27), pp 22268–22277.

A facile method for the growth of anisotropic silver nanoparticles on the surface of titania nanorods and nanofibers

Danielle L. Kuhn[a], Zachary Zander[a], Shaun M. Debow[a], Hui Fang[b], Hai-Lung Dai[b], Yi Rao[b], Brendan G. DeLacy[a*]
[a]U.S. Army Edgewood Chemical Biological Center, Research & Technology Directorate, 5183 Blackhawk Rd, Aberdeen Proving Ground, MD 21010
[b]Temple University, Department of Chemistry, 1901 N. 13th St., Philadelphia, PA 19122

ABSTRACT

We report the growth of anisotropic silver nanoparticles on the surface of titanium dioxide nanorods and nanofibers using a simple solvothermal method. Titanium dioxide nanorods and nanofibers were first fabricated using previously reported hydrothermal and electrospinning methods, respectively. The nanorods and nanofibers were then exposed to silver nitrate in the presence of: 1) dimethyl formamide, which served as the solvent and reducing agent, and 2) polyvinylpyrollidone, which served as a capping agent in the formation of non-spherical particles. Hydrogen peroxide, typically a vital ingredient for the formation of anisotropic silver nanoparticles, such as platelets, was purposely omitted in the reaction. Zeta potential measurements of the titanium dioxide nanorods and fibers, both prior to and after the growth of silver particles, confirmed that a base-treated titanium dioxide surface was critical in the formation of anisotropic silver nanoparticles. The base treatment of the titanium dioxide provided a "peroxide-like" surface which served as a basis for the omission of hydrogen peroxide in the reaction. UV-vis spectroscopy, X-ray powder diffraction, and transmission electron microscopy were used to confirm the presence of anisotropic silver particle formation on the surface of the titanium dioxide nanorods and fibers.

Keywords: plasmonics, nanoplatelets, silver, titania, anisotropy, semiconductor

1. INTRODUCTION

Sensitizing the surface of metal oxide semiconductors with plasmonic metal nanoparticles has been a prominent area of research in recent years.[1,2] Several research groups have explored the use of gold or silver nanoparticles on the surface of metal oxides, such as titanium dioxide (TiO_2) and zinc oxide (ZnO), as a means of enhancing photo-catalysis and solar energy conversion.[3,4] The presence of plasmonic nanoparticles on the surface of metal oxides provides several advantages. First, metal oxides such as TiO_2 and ZnO have wide bandgap energies which generate absorption primarily in the UV region. The inclusion of plasmonic nanoparticles on the surface of these metal oxides provides a means of extending the absorption of the plasmonic/metal-oxide nanocomposite from the UV into the visible region. The tunable nature of the surface plasmon resonance (SPR) in the visible region, via changes in the particle size and shape of the metal nanoparticle, is the driving force behind its use in improving visible light harvesting in the plasmonic/metal-oxide nanocomposites.[5] A second distinct advantage of functionalizing metal-oxide semiconductors with plasmonic nanoparticles is the enhancement of photo-generated charge separation across the metal-semiconductor interface. This so-called hot-electron injection process is one in which the photo-excited plasmon first decays into a hot electron-hole pair within the metal. The hot electron from the metal then decays into the conduction band of an adjacent semiconductor, providing charge separation at the Schottky barrier, which is formed at the metal-semiconductor interface. [6,7]

Many efforts to functionalize the surface of metal oxides with plasmonic nanoparticles has involved the growth of gold or silver nanoparticles on the surface of the semiconductor. The growth of gold or silver nanoparticles typically involves exposing the semiconductor to a gold ($HAuCl_4$) or a silver ($AgNO_3$) salt in solution, respectively.[8–11] A reducing agent (e.g., $NaBH_4$) is subsequently used to convert the cationic form of the metal to its solid state. In contrast to the nanoparticle growth approach, pre-made gold or silver nanoparticles may be covalently attached to the surface of semiconductor materials using coupling agents such as silanes, thiols, or ss-DNA.[12–18] Regardless of how the plasmonic particles are deposited onto the surface of the semiconductor (i.e., via growth or covalent attachment), a

spherical shape has been the primary nanoparticle geometry that has been explored in the deposition of metal nanoparticles on the surface of semiconductor materials.

In this study, we report a facile approach for growing anisotropic silver nanoparticles on the surface of TiO_2. Anisotropic shapes of silver are particularly attractive for tuning and maximizing absorption in the visible region, due to the exceedingly high extinctions that are predicted in the literature.[19] Synthetic approaches for fabricating silver in solution typically involve a silver salt ($AgNO_3$), a capping agent for inducing a non-spherical geometry (e.g., polyvinylpyrollidone (PVP)), a reducing agent (e.g., sodium citrate) for converting silver cations to solid silver, and hydrogen peroxide (H_2O_2). H_2O_2 has been shown to play a crucial role as an oxidative etchant in the formation of anisotropic silver particle geometries, such as platelets.[20,21] It was concluded from these previous studies that, in order to form an anisotropic geometry such as a platelet, a sufficient amount of H_2O_2 was required to ensure that the cationic form of silver was prevalent prior to its reduction.[22] In our study, we purposely omitted the use of H_2O_2 to grow anisotropic silver particles on the surface of TiO_2 nanorods and nanofibers. We hypothesized that a "peroxide-like" TiO_2 surface is generated at high pH, negating the need for H_2O_2 during the growth of silver nanoparticles. This hypothesis was also based on previous studies that explored the impact of pH on the chemical composition of TiO_2 surfaces.[23–25]

The impact of nanoparticle geometry on plasmonic resonance and extinction has been, and continues to be, a well-studied area of research.[26–28] However, the impact of plasmonic nanoparticle geometry and anisotropy, and the associated plasmonic resonance, on the injection of hot electrons into an adjacent semiconductor has not been a focal point of research studies to date. We anticipate that this simple approach of fabricating a silver platelet/TiO_2 nanocomposite will provide a basis for exploring alternative plasmonic-semiconductor nanocomposites in future photocatalytic and charge injection studies. Hence, our goal in this study was to merely demonstrate a simple approach for generating anisotropic plasmonic nanoparticles on the surface of a metal-oxide material such as TiO_2.

2. MATERIALS

Polyvinylpyrrolidone (M_w = 29,000), polymethyl methacrylate (M_w = 996,000), chloroform ($CHCl_3$), silver nitrate ($AgNO_3$), N,N–dimethylformamide (DMF), oxalic acid, titanium isopropoxide (TTiP), and sodium hydroxide (NaOH) pellets were purchased from Sigma-Aldrich®, Alfa Aesar, and Fisher Scientific™, and used without any further purification. 18.2 MΩ deionized water, obtained from a Millipore® Direct-Q® 5 water purification system, was used in all experiments.

3. EXPERIMENTAL

3.1 Synthesis of TiO_2 nanorods

The synthesis of titania nanorods was reproduced from Zander et al.,[29] in which titanium oxalate was prepared by reacting TTiP with 0.364 M oxalic acid (aq) in a 1:2 M ratio. While magnetically stirring, 16 g of NaOH pellets were added slowly to a 125-mL Teflon™-lined stainless-steel autoclave containing 40 mL of the titanium oxalate solution. Once the NaOH was fully dissolved, the reaction vessel was tightly sealed and placed in an oven for 48 hours at 150 °C. The product was cooled and rinsed with 1.0 L of deionized water. The final rinsed product was allowed to dry at 100 °C for 12 hours.[29] The resulting titanate rods were then annealed at 700 °C for 3 hours in atmospheric conditions, resulting in primarily anatase TiO_2 nanorods.

3.2 Synthesis of TiO_2 nanofibers

Electropsun TiO_2 nanofibers were fabricated by using the sol–gel process and electrospinning followed by a thermal treatment. Procedures were reproduced from Liu et al.[30] 320 mg of polymethyl methacrylate (PMMA) were dissolved in 2 mL of chloroform and allowed to stir until the polymer was dissolved. 0.67 mL of TTiP were added dropwise to the polymer solution and allowed to stir for an additional 30 minutes. Then, 2 mL of DMF were added to the solution to increase the dielectric constant and stirred for an additional 2 hours prior to electrospinning. Electrospinning was performed using a Holmarc HO-NFES-040B compact electrospinning and electrospraying unit (MTI Corporation). The sol–gel solution was added to a syringe, and the needle was placed 8 cm from the collector. The rotating mandrel collector was allowed to spin at 400 rpm. The syringe pump was set to 0.15 mL/min and 8 kV was applied to the

needle. The resulting composite nanofibers were allowed to stand at room temperature under ambient conditions for 24 hours. This allowed for the hydrolysis of TTiP to $Ti(OH)_4$ and then further condensation to amorphous TiO_2 prior to thermal treatment.[31] These fibers were then collected and calcined in a Thermo Scientific™ Lindberg/Blue M™ Mini-Mite™ 16 Pt: 120V tube furnace at 400 °C for 4 hours under atmospheric conditions.

3.3 Synthesis of silver nanoplatelet suspensions

As a control in this study, silver nanoplatelets were synthesized using a method similar to Mirkin et al.[21] Briefly, 25 mL of a 0.11 mM $AgNO_3$ solution was placed in a 2-oz Wheaton® glass jar. While magnetically stirring at ambient temperature, 1.5 mL of a 30-mM sodium citrate solution in water, 1.5 mL of a 10 mg/mL PVP (M_w = 29,000) solution in water, and a variable amount (20–40 µL) of 30 % (w/w) H_2O_2 were added. The mixtures were stirred for 15 minutes, after which 100 µL of 100 mM $NaBH_4$ was added to each solution. The solutions were stirred for 24 hours. The variable amount of H_2O_2 produced silver platelets with varying sizes, with major dimensions ranging from 34.5 nm to 58.2 nm.

3.4 Base treatment of electrospun TiO_2 nanofibers

To promote non-spherical growth of silver on the surface of the electropsun nanofibers, 100 mg of TiO_2 was suspended in a 0.05 M NaOH solution and stirred continuously for 3 hours. The resulting mixture was centrifuged and washed with deionized water three times, and then dried overnight in an oven at 100 °C.

3.5 Growth of silver on TiO_2 nanorods and electrospun nanofibers

Ag–TiO2 nanocomposites were synthesized using a modified method from Su et al.[32] The solvothermal synthesis included 200 mg of PVP, 17 mg AgNO3, and 15 mg TiO_2 nanorods or nanofibers dissolved in 20 mL of DMF. The solution was placed into a three-neck round-bottom flask and stirred continuously. The flask containing the reactants was refluxed at 160 °C for 2 hours. The DMF played a dual role of solvent and reducing agent for the Ag^+ ions to Ag. The hydroxylated surface of the titania was pertinent to the non-spherical silver growth at the surface, and the PVP was used as a stabilizing agent. The resulting solution was washed with deionized water and centrifuged, this was repeated three times until the decant solution was clear in color. The remaining solid was dried overnight at 100 °C. As a control, the acid-washed TiO_2 nanorods were used in the synthesis of silver to confirm the theory that the hydroxylated surface is necessary in forming anisotropic silver on the surface of the nanorods.

3.6 Characterization

Powder X-ray diffraction (XRD) patterns of the nanorods were recorded on a PANalytical X'Pert Pro diffractometer with X'Celerator, using Cu Kα radiation (λ = 1.5406 Å) at 45 kV and 40 mA. Scanning electron microscopy images were obtained using a JEOL JCM-5700 scanning electron microscope. All UV-vis absorption spectra were measured in a quartz cuvette (10 mm optical path length) using a V-670 spectrophotometer (JASCO Co.). Spectra were measured from 190 nm to 800 nm. Transmission electron microscopy (TEM) images of the Ag–TiO_2 nanorods were obtained using a JEOL JEM-1400 microscope operating at 120 kV. One drop of the Ag–TiO_2 nanorods aqueous colloid solution was dried overnight on the surface of a Cu grid covered with a PELCO® TEM grid support film of Formvar/Carbon (300 mesh Cu, TED PELLA, Inc.). For the determination of zeta potential, a Zetasizer Nano ZS (Malvern Instruments) was used.

4. RESULTS AND DISCUSSION

Figure 1 provides scanning electron microscopy images of the as-synthesized TiO_2 nanorods and TiO_2 nanofibers.

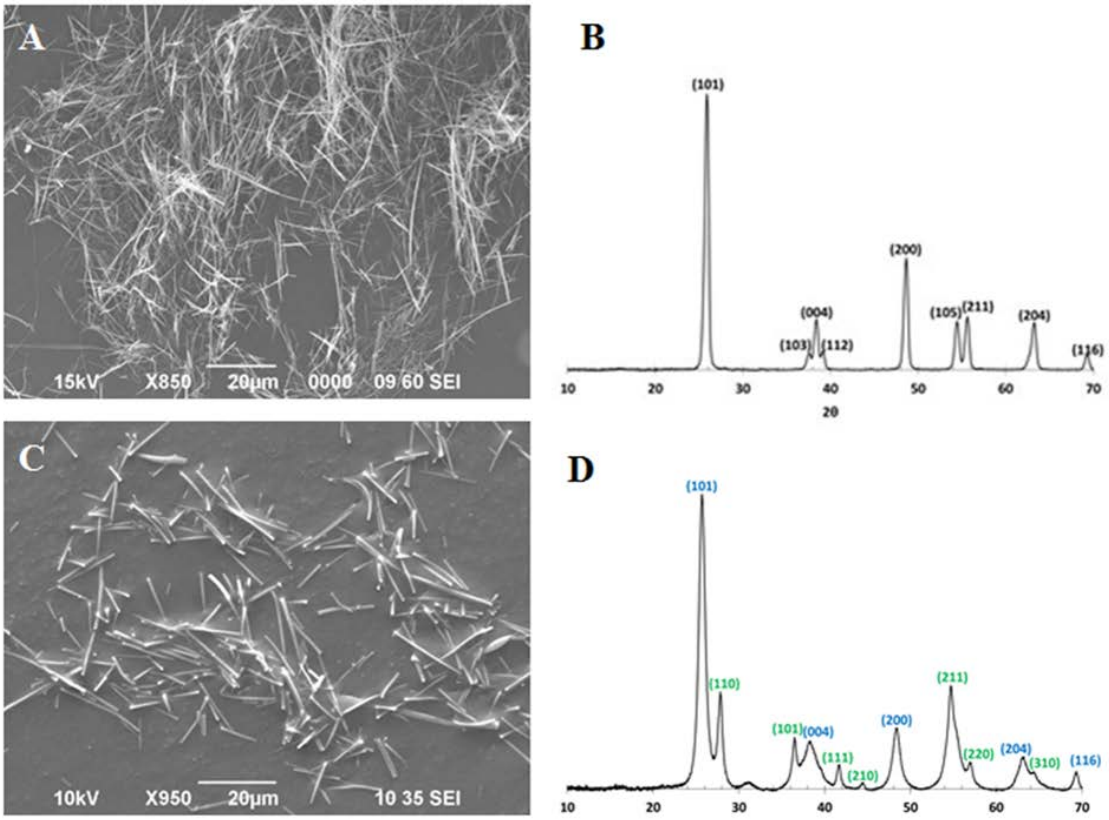

Figure 1. A) Hydrothermally fabricated TiO_2 nanorods with an average diameter of 160 nm. B) XRD patterns of anatase TiO_2 rods. C) Electrospun TiO_2 nanofibers with an average diameter of 680 nm. D) XRD patterns of anatase/rutile TiO_2 nanofibers (blue represents anatase and green represents rutile crystal structure).

The hydrothermal process used to fabricate TiO_2 yielded nanorods with an average diameter of 160 nm, and major dimensions on the order of tens of microns (Figure 1A). The electrospinning process used to fabricate TiO_2 yielded nanofibers with an average diameter of 680 nm, and major dimensions on the order of tens of microns and greater (Figure 1B).

In order to confirm the crystal form of the TiO_2 nanorods and nanofibers, powder XRD was performed on all samples. For the TiO_2 nanorods, this analysis revealed that titanate rods were initially produced by the hydrothermal process. Upon calcination of the titanate rods at 700 °C under atmospheric conditions for 3 hours, the crystal structure rearranged to a mostly anatase TiO_2 with well-defined diffraction peaks as shown in Figure 1B. For the anatase phase, the major peaks were obtained at 2θ values of 25.88°, 37.68°, 38.48°, 39.18°, 48.66°, 54.46°, 55.68°, 63.32°, and 69.36°, representing the Miller indices of (101), (103), (004), (112), (200), (105), (211), (204), and (116) planes respectively. For the rutile phase, a small peak was observed at 27.72°, representing the (110) Miller index. The weight fraction of the rutile phase was then calculated to be 10 % from the Scherrer equation,

$$\mathrm{WR} = 1/[1 + 0.8(\mathrm{IA}/\mathrm{IR})], \quad (1)$$

where IA is the X-ray integrated intensity of the (101) reflection of anatase at 2θ of 25.88°, and IR is that of the (110) reflection of rutile at 2θ 27.72°.[33]

The electrospun nanofibers underwent XRD characterization under the same conditions as the nanorods. The diffraction pattern showed a mixes phase of anatase and rutile, and can be seen in Figure 1D. The results display a well-defined diffraction pattern, indicating the presence of the rutile crystal formation. For the anatase phase, peaks were observed at 2θ values of 25.7°, 38.36°, 48.42°, 63.16°, and 69.34°, respectively, representing the Miller indices

of (101), (004), (200), (204), and (116) planes, respectively. For the rutile phase, peaks were observed at 2θ values of 27.82°, 36.52°, 41.60°, 44.40°, 54.76°, 57.06°, and 64.47°, representing the Miller indices of (110), (101), (111), (210), (211), (220), and (310) planes respectively. The weight fraction of the rutile phase was calculated to be 29.2 % and anatase phase to be 70.8 %, using equation (1).

Nanorod and nanofiber geometries were chosen as substrates for this study since their respective dimensions were large enough to accommodate the growth of anisotropic silver nanoparticles. Typical anistropic silver nanoparticles, such as silver nanoplatelets, can have major dimensions of near 40 nm. In order to demonstrate the spectral features and color of these silver nanoplatelets, an aqueous-based reduction method was used to fabricate colloidal suspensions of silver nanoplatelets. This process yielded silver nanoplatelets with maximum absorptions that range from 550 nm to 650 nm, as demonstrated in the visible spectra that is shown in Figure 2A.

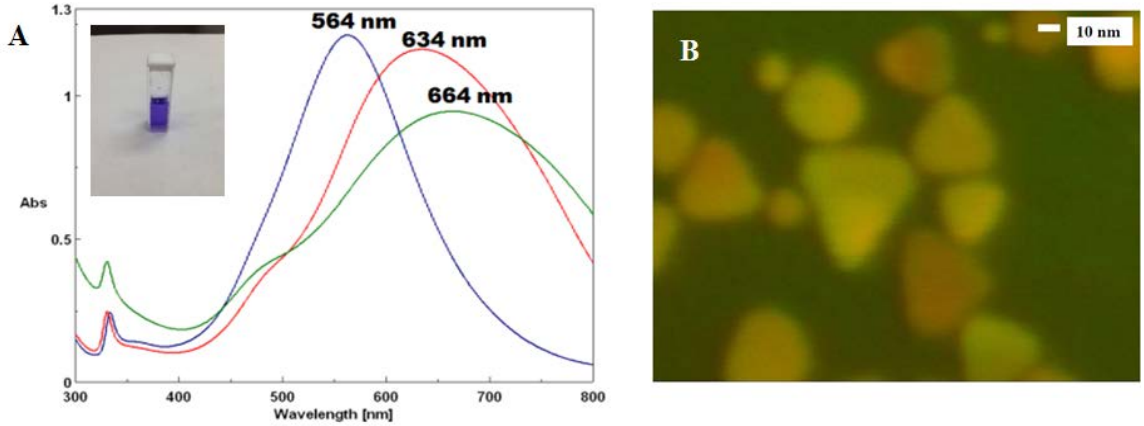

Figure 2. A) Visible spectra of silver nanoplatelets with variable major dimensions, producing resonances that range from from 564 nm to 664 nm. The inset provides an image of the blue color that is characteristic of these silver nanoplatelet suspensions. B) TEM image of the silver nanoplatelets; the average major dimension of the platelets was approximately 40 nm.

Colloidal suspensions containing silver nanoplatelets with absorptions in these spectral ranges generate a bluish color, as demonstrated by the image in the inset of Figure 2A. Figure 2B provides a TEM image of the silver nanoplatelets.

Once the size, geometry, and chemical composition of the TiO_2 nanorods/nanofibers and silver nanoplatelets were understood, the growth of anisotropic silver nanoparticles on the surface of the TiO_2 nanorods and nanofibers was subsequently explored. Using the approach described in section 3., Experimental, silver nanoparticles were grown on the surface of titania by exposing titania nanorods/nanofibers to aqueous silver cations and a reducing agent, in the presence a capping agent. As previously discussed, H_2O_2 is typically used as an oxidative etchant and plays a vital role in the colloidal synthesis of anisotropic silver nanoplatelets. However, we purposely omitted the use of H_2O_2 in our study. Since the titania nanorods and nanofibers were exposed to a highly basic environment (pH > 11) during the synthesis, we hypothesized that a highly negative titania surface would produce a "peroxide-like" oxidizing surface.[23–25] Hence, we chose to omit the use of H_2O_2 in our study.

Upon completion of the deposition of silver particles on the surface of the TiO_2 nanorods/nanofibers, XRD was used to characterize the phase of the Ag and TiO_2 crystal structure as shown in Figure 3A. The TiO_2 diffraction lines correlated well with the anatase phase, producing major 2θ peaks at 25.54°, 48.34°, 55.36°, 62.94°, and 69.04° representing the Miller indices (101), (200), (211), (204), and (116) planes respectively. The (111) phase of silver is present on the nanorods with major 2θ peaks at 38.32°, 44.58°, 54.20°, 64.72°, representing the Miller indices (111), (200), (105), and (220) planes respectively. These results confirmed that the TiO_2 nanorods maintained their crystal structure during the anisotropic growth of (111) Ag.

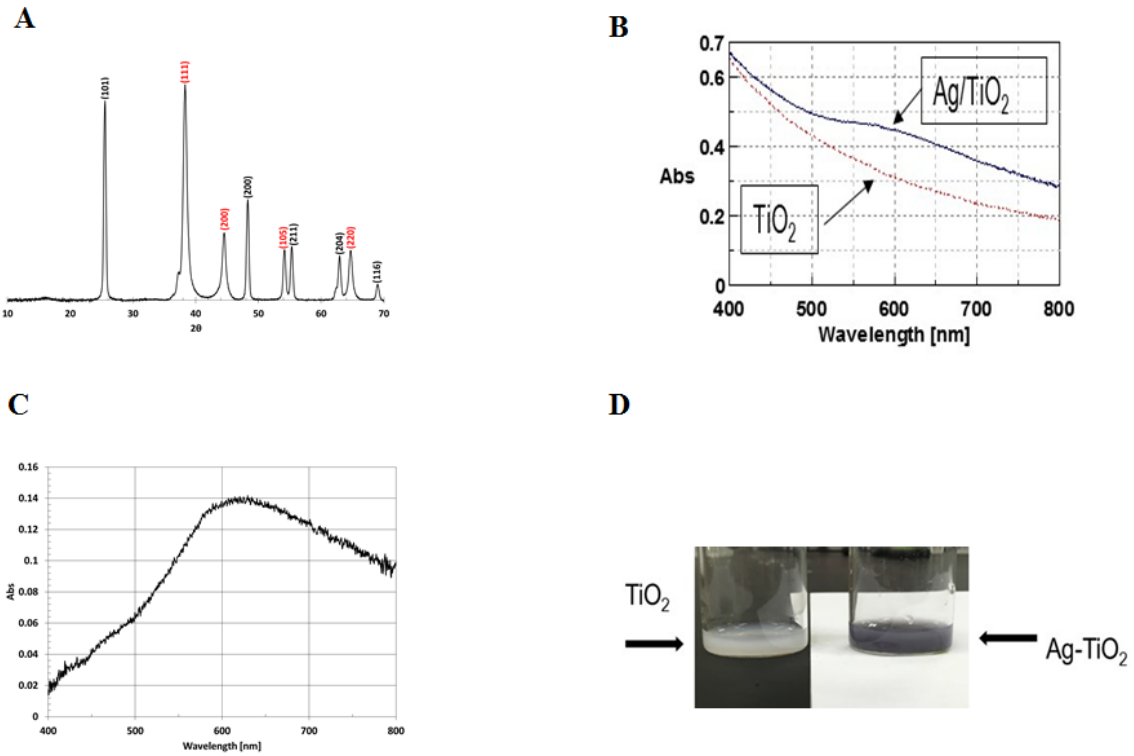

Figure 3. A) XRD diffraction pattern of Ag (red) grown on the surface of TiO_2 (black). B) Visible spectra of TiO_2 nanorod suspension (red curve) and Ag/TiO_2 composite (black curve). C) Difference spectra between the Ag–TiO_2 composite and TiO_2 nanorod suspensions. A broad resonance with a maxima near 620 nm is observed. D) Image of TiO_2 nanorod suspension (on left) and TiO_2/Ag nanocomposite suspension (on right). The TiO_2/Ag nanocomposite suspension exhibits a bluish color.

UV-vis spectroscopy was subsequently used to measure the optical properties of the TiO_2 nanorod and Ag–TiO_2 nanocomposite suspensions. These results are provided in Figure 3B. As demonstrated by the black curve in Figure 3B, the TiO_2/Ag nanocomposite suspension exhibits a noticeable increase in absorption near 620 nm. Figure 3C provides the spectral difference between these two curves. A broad resonance is clearly observed for the TiO_2/Ag nanocomposite. This resonance is characteristic of the resonances that are exhibited by silver nanoplatelets (as shown in Figure 2A). Hence, we hypothesized that the peak generated near 620 nm was due to the formation of anisotropic silver particles on the surface of the TiO_2. Our hypothesis was further strengthened upon visual inspection of the TiO_2/silver nanocomposite suspension. A bluish color is clearly evident for the TiO_2/silver nanocomposite suspension (shown in Figure 3D), which is consistent with the color that is exhibited by silver nanoplatelets (as shown in Figure 1C). Finally, TEM images provided in Figure 4 confirm the presence of anisotropic silver nanoparticles along the surface of TiO_2 nanorods. Several anisotropic silver particles shapes, including triangular platelets are observed on the surface of the nanorods.

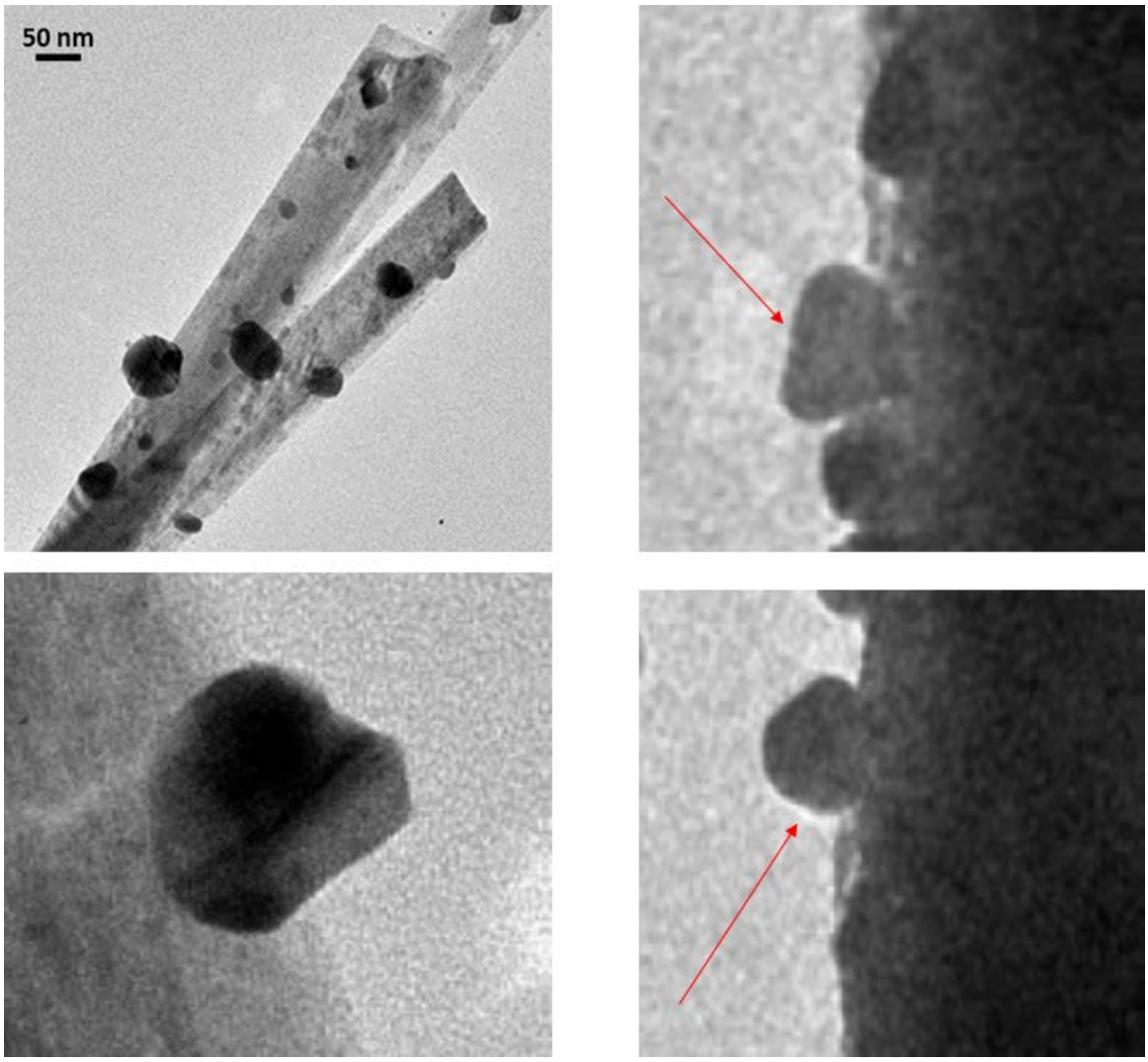

Figure 4. TEM images of TiO_2/Ag nanocomposite nanoparticles. Several anisotropic platelet shapes are observed along the surface of the TiO_2. Scale bar = 50 nm.

Finally, zeta potential measurements were used to test our hypothesis that a base-treated TiO_2 surface promotes the growth of anisotropic silver. The zeta potentials of the TiO_2 nanorods and nanofibers, before and after silver deposition, are provided in Table 1.

Table 1. Zeta potential of TiO_2 nanorods and nanofibers, before and after Ag deposition, and impact on Ag particle shape.

Sample	Zeta Potential (mV) Before Ag Growth	Zeta Potential (mV) After Ag Growth	Ag Particle Shape
Base-treated TiO_2 Nanorods	-26	-5	Platelets
TiO_2 Nanofibers	-25	-22	Spheres
Base-treated TiO_2 Nanofibers	-50	-29	Platelets

Inspection of Table 1 reveals that, regardless of whether the TiO_2 nanorods or nanofibers were base-treated prior to silver deposition, a highly negative zeta potential was observed. However, the growth of anisotropic silver nanoparticle shapes was only observed for the nanofibers/nanorods that were base-treated prior to silver growth. For the case in which the fiber was not base-treated, only spherical silver growth was observed. These observations corroborate our decision to omit the use of H_2O_2 during silver growth, since previous studies have shown that exposure of TiO_2 to a

high pH generates a "peroxide-like" surface. Further inspection of Table 1 reveals that the difference in zeta potential between the pre- and post-growth of silver was significant for the platelet formation, yet minimal for the spherical Ag particle formation. Further studies should be conducted to definitively determine why such a difference in zeta potential exists between the pre- and post-growth of silver.

5. CONCLUSIONS

In summary, a facile approach for growing anisotropic silver nanoparticles on the surface of TiO_2 nanorods and nanofibers has been described. Visible spectra, XRD, TEM imaging, and visual inspection all indicate that anisotropic silver nanoparticles were grown on the surface of the nanorods and nanofibers. H_2O_2, a typical reactant used in the formation of anisotropic silver particles, was purposefully omitted from our approach of growing anisotropic silver nanoparticles on the surface of TiO_2 nanorods and nanofibers. This omission was based on our hypothesis that a base-treated TiO_2 surface resulted in a "peroxide-like" surface, which previous studies in the literature have also described. Zeta potential measurements of the nanorod and nanofibers surface were made to determine the impact of nanorod/nanofiber surface charge on the growth of anisotropic silver. This analysis revealed that a significant difference in pre- and post-zeta potential was observed for those nanofibers and nanorods that were base-treated prior to anisotropic silver growth.

ACKNOWLEDGMENTS

The authors would like to acknowledge U.S. Army funding provided through the Edgewood Chemical Biological Center's Surface Science Initiative program.

REFERENCES

[1] Clavero, C. Plasmon-induced hot-electron generation at nanoparticle/metal-oxide interfaces for photovoltaic and photocatalytic devices. *Nat. Photonics.* **2014,** *8* (2), pp 95–103.

[2] Mubeen, S.; Hernandez-Sosa, G.; Moses, D.; Lee, J.; Moskovits, M. Plasmonic Photosensitization of a Wide Band Gap Semiconductor: Converting Plasmons to Charge Carriers. *Nano Lett.* **2011,** *11* (12), pp 5548–5552.

[3] Christopher, P.; Ingram, D.B.; Linic, S. Enhancing Photochemical Activity of Semiconductor Nanoparticles with Optically Active Ag Nanostructures: Photochemistry Mediated by Ag Surface Plasmons. *J. Phys. Chem. C.* **2010,** *114* (19), pp 9173–9177.

[4] Hou, W.; Cronin, S.B. A Review of Surface Plasmon Resonance-Enhanced Photocatalysis. *Adv. Funct. Mater.* **2013,** *23* (13), pp 1612–1619.

[5] Li, J.; Cushing, S.K.; Bright, J.; Meng, F.; Senty, T.R.; Zheng, P.; Bristow, A.D.; Wu, N. Ag@Cu_2O Core-Shell Nanoparticles as Visible-Light Plasmonic Photocatalysts. *ACS Catal.* **2013,** *3* (1), pp 47–51.

[6] Linic, S.; Christopher, P.; Ingram, D.B. Plasmonic-metal nanostructures for efficient conversion of solar to chemical energy. *Nat. Mater.* **2011,** *10* (12), pp 911–921.

[7] Cushing, S.K.; Li, J.; Bright, J.; Yost, B.T.; Zheng, P.; Bristow, A.D.; Wu, N. Controlling Plasmon-Induced Resonance Energy Transfer and Hot Electron Injection Processes in Metal@TiO2 Core–Shell Nanoparticles. *J. Phys. Chem. C.* **2015,** *119* (28), pp 16239–16244.

[8] Awazu, K.; Fujimaki, M.; Rockstuhl, C.; Tominaga, J.; Murakami, H.; Ohki, Y.; Yoshida, N.; Watanabe, T.A. Plasmonic Photocatalyst Consisting of Silver Nanoparticles Embedded in Titanium Dioxide. *J. Am. Chem. Soc.* **2008,** *130* (5), pp 1676–1680.

[9] Xin, B.; Jing, L.; Ren, Z.; Wang, B.; Fu, H. Effects of Simultaneously Doped and Deposited Ag on the Photocatalytic Activity and Surface States of TiO2. *J. Phys. Chem. B.* **2005,** *109* (7), pp 2805–2809.

[10] Georgekutty, R.; Seery, M.K.; Pillai, S.C. A Highly Efficient Ag-ZnO Photocatalyst: Synthesis, Properties, and Mechanism. *J. Phys. Chem. C.* **2008,** *112* (35), pp 13563–13570.

[11] Choi, J.; Park, H.; Hoffmann, M.R. Effects of Single Metal-Ion Doping on the Visible-Light Photoreactivity of TiO_2. *J. Phys. Chem. C.* **2010,** *114* (2), pp 783–792.

[12] Wolfe, D.B.; Oldenburg, S.J.; Westcott, S.L.; Jackson, J.B.; Paley, M.S.; Halas, N.J. Photodeposition of Molecular Layers on Nanoparticle Substrates. *Langmuir.* **1999,** *15* (8), pp 2745–2748.

[13] Westcott, S.L.; Oldenburg, S.J.; Lee, T.R.; Halas, N.J. Construction of simple gold nanoparticle aggregates with controlled plasmon–plasmon interactions. *Chem. Phys. Lett.* **1999,** *300* (5–6), pp 651–655.
[14] Porter, L.A.; Ji, D.; Westcott, S.L.; Graupe, M.; Czernuszewicz, R.S.; Halas, N.J.; Lee, T.R. Gold and Silver Nanoparticles Functionalized by the Adsorption of Dialkyl Disulfides. *Langmuir.* **1998,** *14* (26), pp 7378–7386.
[15] Pham, T.; Jackson, J.B.; Halas, N.J.; Lee, T.R. Preparation and Characterization of Gold Nanoshells Coated with Self-Assembled Monolayers. *Langmuir.* **2002,** *18* (12), pp 4915–4920.
[16] Banholzer, M.J.; Osberg, K.D.; Li, S.; Mangelson, B.F.; Schatz, G.C.; Mirkin, C.A. Silver-Based Nanodisk Codes. *ACS Nano.* **2010,** *4* (9), pp 5446–5452.
[17] Hurst, S.J.; Lytton-Jean, A.K.R.; Mirkin, C.A. Maximizing DNA Loading on a Range of Gold Nanoparticle Sizes. *Anal. Chem.* **2006,** *78* (24), pp 8313–8318.
[18] Millstone, J.E.; Georganopoulou, D.G.; Xu, X.; Wei, W.; Li, S.; Mirkin, C.A. DNA-Gold Triangular Nanoprism Conjugates. *Small.* **2008,** *4* (12), pp 2176–2180.
[19] Miller, O.D.; Hsu, C.W.; Reid, M.T.H.; Qiu, W.; DeLacy, B.G.; Joannopoulos, J.D.; Soljačić, M.; Johnson, S.G. Fundamental Limits to Extinction by Metallic Nanoparticles. *Phys. Rev. Lett.* **2014,** *112* (12), p 123903.
[20] Zhang, J.; Langille, M.R.; Mirkin, C.A. Photomediated Synthesis of Silver Triangular Bipyramids and Prisms: The Effect of pH and BSPP. *J. Am. Chem. Soc.* **2010,** *132* (35), pp 12502–12510.
[21] Métraux, G.S.; Mirkin, C.A. Rapid Thermal Synthesis of Silver Nanoprisms with Chemically Tailorable Thickness. *Adv. Mater.* **2005,** *17* (4), pp 412–415.
[22] Zhang, Q.; Li, N.; Goebl, J.; Lu, Z.; Yin, Y. A Systematic Study of the Synthesis of Silver Nanoplates: Is Citrate a "Magic" Reagent? *J. Am. Chem. Soc.* **2011,** *133* (46), pp 18931–18939.
[23] Mudunkotuwa, I.A.; Grassian, V.H. Citric Acid Adsorption on TiO2 Nanoparticles in Aqueous Suspensions at Acidic and Circumneutral pH: Surface Coverage, Surface Speciation, and Its Impact on Nanoparticle–Nanoparticle Interactions. *J. Am. Chem. Soc.* **2010,** *132* (42), pp 14986–14994.
[24] Ahmed, S.; Rasul, M.G.; Martens, W.N.; Brown, R.; Hashib, M.A. Advances in Heterogeneous Photocatalytic Degradation of Phenols and Dyes in Wastewater: A Review. *Water, Air, Soil Pollut.* **2011,** *215* (1), pp 3–29.
[25] Li, Y.-F.; Selloni, A. Pathway of Photocatalytic Oxygen Evolution on Aqueous TiO2 Anatase and Insights into the Different Activities of Anatase and Rutile. *ACS Catal.* **2016,** *6* (7), pp 4769–4774.
[26] Sherry, L.J.; Chang, S.-H.; Schatz, G.C.; Van Duyne, R.P.; Wiley, B.J.; Xia, Y. Localized Surface Plasmon Resonance Spectroscopy of Single Silver Nanocubes. *Nano Lett.* **2005,** *5* (10), pp 2034–2038.
[27] Xia, Y.; Halas, N.J. Shape-Controlled Synthesis and Surface Plasmonic Properties of Metallic Nanostructures. *MRS Bull.* **2005,** *30* (5), pp 338–348.
[28] Wiley, B J.; Im, S.H.; Li, Z.-Y.; McLellan, J.; Siekkinen, A.; Xia, Y. Maneuvering the Surface Plasmon Resonance of Silver Nanostructures through Shape-Controlled Synthesis. *J. Phys. Chem. B.* **2006,** *110* (32), pp 15666–15675.
[29] Zander, Z.; Yagloski, R.; DeCoste, J.; Zhang, D.; DeLacy, B.G. One-pot synthesis of high aspect ratio titanium dioxide nanorods using oxalic acid as a complexing agent. *Mater. Lett.* **2016,** *163*, pp 39–42.
[30] Liu, J.; McCarthy, D.L.; Cowan, M.J.; Obuya, E.A.; DeCoste, J.B.; Skorenko, K.H.; Tong, L.; Boyer, S.M.; Bernier, W.E.; Jones Jr, W.E. Photocatalytic activity of TiO2 polycrystalline sub-micron fibers with variable rutile fraction. *Appl. Catal., B.* **2016,** *187*, pp 154–162.
[31] Mahshid, S.; Askari, M.; Ghamsari, M. S. Synthesis of TiO2 nanoparticles by hydrolysis and peptization of titanium isopropoxide solution. *J. Mater. Process. Technol.* **2007,** *189* (1–3), pp 296–300.
[32] Su, C.; Liu, L.; Zhang, M.; Zhang, Y.; Shao, C. Fabrication of Ag/TiO2 nanoheterostructures with visible light photocatalytic function via a solvothermal approach. *CrystEngComm.* **2012,** *14* (11), pp 3989–3999.
[33] Patterson, A.L. The Scherrer Formula for X-Ray Particle Size Determination. *Phys. Rev.* **1939,** *56* (10), pp 978–982.

Cavity-based aluminum nanohole arrays with tunable infrared resonances

Bryan Debbrecht[a], Morgan McElhiney[a], Victoria Carey[a], Chris Cullen[a], Mark S. Mirotznik[a], Brendan G. DeLacy[b*]
[a]University of Delaware, Department of Electrical & Computer Engineering, 140 Evans Hall, Newark, DE 19716
[b]U.S. Army Edgewood Chemical Biological Center, Research & Technology Directorate, 5183 Blackhawk Rd, Aberdeen Proving Ground, MD 21010

ABSTRACT

This work details the successful computational design, fabrication, and characterization of a cavity-based aluminum nanohole array. The designs incorporate arrays of aluminum nanoholes that are patterned on a dielectric-coated (SiO_2 or ZnSe) aluminum-base mirror plane. This architecture provided a means of exploring the coupling of the localized resonances, exhibited by the aluminum nanohole array, with the cavity resonance that is generated within the dielectric spacer layer, which resides between the base plane mirror and the nanohole array. Rigorous coupled-wave analysis was first used to computationally design the structures. Next, a range of lithographic techniques, including photolithography, e-beam lithography, and nanosphere lithography, were used to fabricate the structures. Finally, infrared spectroscopy and scanning electron microscopy were used to characterize the spectral and structural properties of the multilayered devices, respectively. The overall goal of this study was to demonstrate our ability to design and fabricate aluminum-based structures with tunable resonances throughout the infrared region (i.e., from the short-wave through long-wave infrared regions (1.5–12 μm) of the electromagnetic spectrum).

Keywords: subwavelength structures, nanostructures, optoelectronics

1. INTRODUCTION

The optimization and design of metallic nanostructures arrays continue to highlight progress being made in the nanophotonic field of research. This progress is largely due to the capability of these structures to control light-matter interactions at the nanoscale. The optical properties of these engineered materials are highly dependent on the size, shape, and periodicity of metallic and dielectric components. Hence, a plethora of designs have been explored as a means of generating and tuning various optical properties, including transmission, reflection, absorption, and emission.[1–4]

One particularly intriguing design that complements the metallic nanostructure arrays is the integration of the metal arrays within a metal-dielectric-metal (MDM) stack. These multilayer thin films typically consist of a solid metallic base plane mirror, an intermediate dielectric cavity layer with variable thickness, and a top layer consisting of the metallic grating with subwavelength features. The addition of the dielectric and metallic base plane mirror in the MDM structure creates a Fabry-Perot (FP)-like cavity that can be used to enhance and tune a strong resonant absorption.[5,6] As incident radiation impinges upon the top metallic grating layer, a resonance or absorption is generated somewhere in the UV through infrared (IR) regions, depending upon the size, shape, and periodicity of the metallic nanostructures within an array. The portion of incident radiation that is not attenuated by the array traverses into the transparent dielectric layer and propagates towards the base plane mirror. This radiation is then reflected back through the dielectric cavity and toward the top grating surface, where it is either absorbed, transmitted back toward its original location, or reflected back to the mirror base plane where the process starts over again. At particular wavelengths, the light will strongly resonate within the cavity, resulting in nearly 100 % absorption within the top metal grating.

The nanohole array is one of many metal-optic designs that have been explored as means of generating so called “hot spots,” or enhanced electromagnetic near fields. These “hot spots” may be used as a means of enhancing detection in techniques such as surface-enhanced Raman spectroscopy (SERS), surface-enhanced fluorescence (SEF), and surface-enhanced IR absorption (SEIRA).[7–9] Metallic nanohole arrays are particularly attractive for these applications since they can support both localized and propagating surface plasmon resonances in the visible and UV spectra. At longer IR wavelengths, the absorption response is dominated by the FP effects. Depending upon the periodicity and size of the nanoholes, and the composition of the metal, the spectral properties of these structures may be tuned from the UV through IR spectral regions.

To date, the vast majority of nanohole array designs have incorporated noble metals such as gold and silver. Gold and silver intrinsically exhibit low losses in the visible through near-IR ranges, and therefore represent ideal candidates for optimizing resonances in this wavelength regime. Gold is ideal for exposure to biological media, due to its chemical stability. Conversely, silver presents toxicity issues in biological media and is therefore more suitable for environmental studies. The high cost of both gold and silver limits their use and large-scale commercialization of these sensors.

The use of aluminum represents a viable alternative to the gold and silver plasmonic nanostructures that are commonly used in plasmonic arrays.[9] First, aluminum supports resonances that occur in the UV and visible regions.[9] Second, aluminum is low-cost, abundant, and is easily processed, due to its use in a wide range of manufacturing processes. A significant consideration in using aluminum is its tendency to form an oxidative layer on its surface. Upon exposure to air, a thin layer of aluminum oxide is commonly formed. This layer provides an insulating, water-insoluble, and waterproof film that protects the inner aluminum layer. However, depending on its thickness, this thin aluminum oxide film can produce a change in the expected resonance wavelength.[9]

There have been recent studies in which aluminum nanoarrays were employed for a range of applications. Wei et. al. recently employed a capped aluminum nano-slit array for use as a biosensor with tailorable Fano resonances.[10] Zhou et al. employed an aluminum nano-pyramid array with tunable resonances in the UV through IR regions for the detection of carbohydrate antigen 199.[11] Du et. al. detailed the use of an aluminum nanohole array as a transparent electrode, demonstrating a broadband transmittance of > 60 %.[12] A major structural feature that was omitted in all of these studies was the use of a cavity and base plane mirror to complement the tunability of the top aluminum array. Hence, in the study described herein, our specific goal was to explore the impact of a FP-like cavity on the resonances generated by an aluminum nanohole array.

2. COMPUTATIONAL MODELING AND DESIGN

2.1 Electromagnetic modelling of aluminum nanohole arrays

The basic geometry of the cavity-based nanohole array, illustrated in Figure 1 is composed of three layers. The bottom layer is a planar aluminum mirror of sufficient thickness (> 100 nm) to ensure zero transmittance. The middle layer is composed of a low loss dielectric material with thickness, $d_{substrate}$, and refractive index, $n_{substrate}$. The top layer is the planar aluminum surface with a hexagonal array of circular holes removed. The distance between holes was assumed to be subwavelength and is denoted by Λ in the figure.

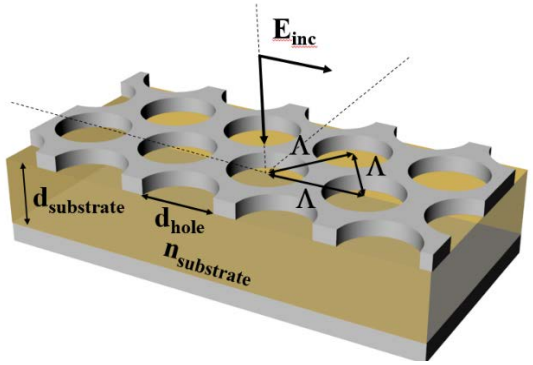

Figure 1. (Top layer) Aluminum nanohole array. (Middle layer) Transparent dielectric layer (SiO_2 of ZnSe). (Bottom layer) Aluminum base plane mirror. This “sandwiching” effect creates the necessary resonant cavity for increased use response.

Rigorous electromagnetic modeling was used to predict and design the optical properties of the cavity-based nanohole arrays. Several rigorous electromagnetic models can be used for this calculation; however, we chose the rigorous coupled wave (RCW) algorithm originally presented by Moharam and Gaylord.[13] Our specific implementation is based on the enhanced transmittance matrix approach introduced by Moharam et al., and later refined by Lalanne, Noponen, and Turunen.[13–15] For the sake of brevity, we refer the reader to these references for details on the RCW method. While accurate, the RCW method does assume the grating structure, shown in Figure 1, is infinite in the transverse directions.

Using RCW, we calculated the reflective and absorptive optical properties of the cavity-based nanohole array. Specific parameters that were varied in the calculations included cavity thickness and dielectric material composition (ZnSe or SiO_2), aluminum nanohole array dimensions (e.g., film thickness, nanohole diameter, hole-to-hole distance).

2.2 Absorption theory

To illustrate the light absorption properties of the cavity-based nanohole array (shown in Figure 1), we conducted rigorous simulations using the RCW method. Example results from a typical simulation are shown in Figure 2. For this example, the distance between the nanoholes (Λ) was fixed at 3 µm, the hole diameter (d_{hole}) fixed at 2 µm, and the index of refraction of the substrate ($n_{substrate}$) was assumed to be 2.41 (i.e., the index of zinc selenide). The thickness of the dielectric cavity ($d_{substrate}$) was varied from 1 µm to 7 µm. The RCW method was used to calculate the total absorption at normal incidence as a function of incident wavelength and cavity thickness. Superimposed upon those results are lines that represent the first three FP modes. Specifically, each FP mode can be described by a resonant wavelength, λ_q, given by

$$\lambda_q = \frac{2nd}{q}\left(1-\frac{n_i^2}{n^2}\sin^2\theta\right)^{-1}, \tag{1}$$

where n_i is the refractive index of the incident region, n is the refractive index of the dielectric cavity, d is the cavity thickness, θ is the incident angle (e.g., $\theta = 0$ is normal incidence), and q is a non-zero integer that describes the mode shape. The grating and ground plane thicknesses are assumed negligible.

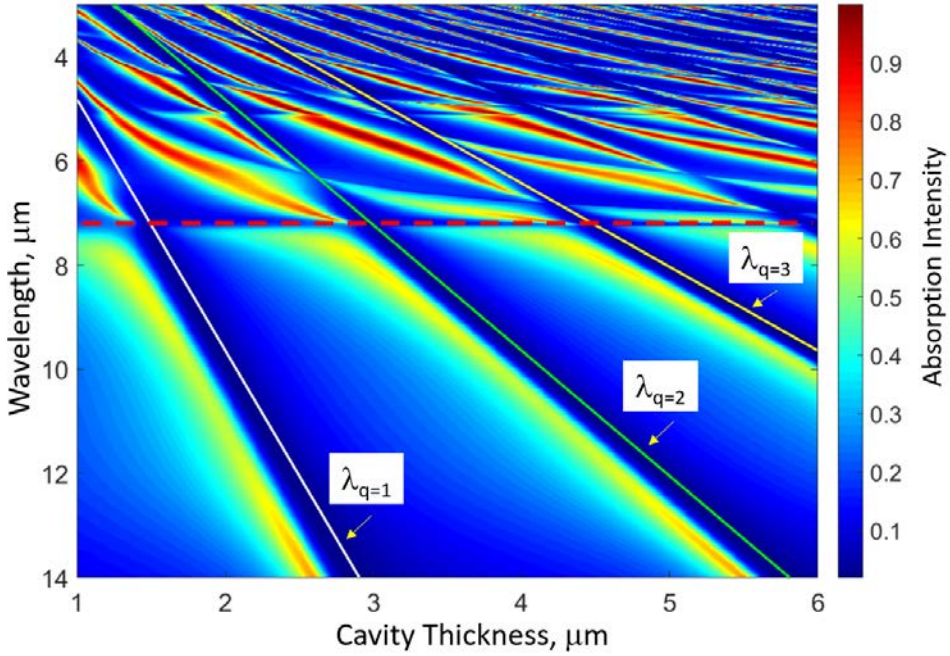

Figure 2. Simulated absorption intensity for normally incident plane wave illuminating a cavity-based nanohole array structure shown in Figure 1 as a function of the wavelength and cavity thickness. Superimposed on are the first three FP modes given by equation (1). The dashed red line was added to separate two distinct regions in which the absorption phenomenon changes from being dominated by lossy surface and guided modes (upper region) to being dominated by the FP modes (lower region).

The results in Figure 2 indicate two interesting regions, separated by the red dashed line, in which the characteristics of the absorption phenomenon change. For wavelengths above some critical value, the absorption is dominated by the FP effect. In this region, the resonant wavelengths predicted by RCW are slightly red-shifted from the wavelengths predicted by equation (1), but follow the general trend of the FP modes. The red-shift can be accounted for by the inductive response of the metallic grating. For shorter wavelengths however, the resonant phenomenon is more complicated due to the presence of guided and surface modes, such as lossy guided mode resonances (GMR). While the effect of the coupling between the cavity and the metallic grading is still strong in this region, it is much more difficult to predict the specific response without the use of full-wave simulations.

2.3 Iterative design of aluminum nanohole arrays

The resonant absorption properties of the structure shown in Figure 1 have a complicated dependence on a number of geometrical parameters. As a result, it is unlikely that any simple analytical design equation could be derived and used to determine an optimal structure for a given desired response. Consequently, we implemented a numerical iterative design algorithm. Here, the RCW method is used to calculate the full-wave solution for the reflectance as a function of wavelength and polarization for a given substrate thickness, grating period and nanohole diameter. An optimization algorithm is then used to refine the geometry until an objective function is minimized. The objective function may vary depending on the application, but in most cases, we chose to minimize the total reflectance (i.e., maximize absorption) over some desired wavelength band. A number of iterative optimization algorithms could be employed, including traditional derivative-based algorithms, genetic algorithms, or direct pattern search algorithms. An advantage of both genetic and pattern search algorithms is that they do not require derivatives, and as a consequence, work well on non-differentiable, stochastic, and discontinuous objective functions. Both simple genetic algorithms and direct pattern search algorithms were implemented and tested for the application of interest here. While both methods produced comparable results, the pattern search algorithm was often computationally less expensive.

3. EXPERIMENTAL METHODS

The generation of resonances within a given wavelength band is dependent on the feature sizes of the array, the composition of the dielectric cavity, and the thickness of the cavity. For applications in the visible and near IR bands, the nanohole diameters and grating periods can become quite small (<< 1 μm). In the long-wave IR band (LWIR), the feature sizes can be as large as several micrometers. Consequently, no single fabrication methodology is optimal across all wavelength bands. As a result, we explored three different fabrication processes—optical lithography, electron-beam (e-beam) lithography, and nanosphere lithography. The specific fabrication methods and materials used are described in the following sections.

3.1 Al nanohole structure fabrication—photolithography

Photolithography was first employed to fabricate structures that exhibited resonances in the 5–12μm region. A depiction of this process is provided in Figure 3. Al was first deposited by e-beam evaporation on the substrate in order make a back-plane mirror, preventing radiation from transmitting through the Si substrate. Next, a ZnSe cavity was created atop this mirror via thermal evaporation (Figure 3a). ZnSe was chosen as the dielectric cavity material due to its inherent transparency in this spectral region of interest. This was followed by multiple steps which involved the generation of the aluminum nanohole array. In this multi-step process, a layer of NR9-1500PY was first spin-coated onto the surface of the ZnSe (Figure 3b), followed by a short exposure to UV light through a patterned square array mask (Figure 3c). The mask had several square array patterns, with holes ranging from 1–3 μm and periods of 2–5 μm. The chosen hole diameter and period dictated the eventual dimensions of the nanohole array. After exposure to UV, the photoresist was then developed in RD-6®. Next, after an appropriate solvent (acetone) was used to remove the underdeveloped resist, an array of discs remained (Figure 3d). Next, a layer of aluminum was deposited over the entire disc array by means of e-beam evaporation (Figure 3e). Finally, upon exposure to acetone and ultrasonic bath, the NR9/aluminum discs were removed, leaving behind the desired aluminum nanohole array (Figure 3f).

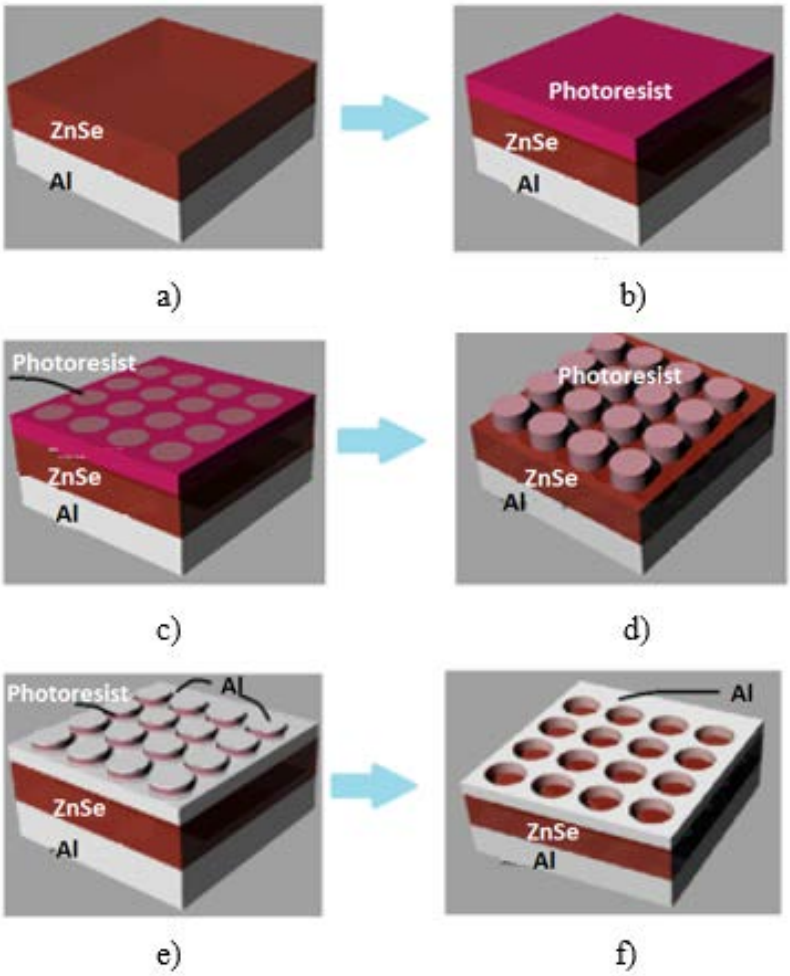

Figure 3. From left to right, starting at the top. a) 100 nm of Al and ZnSe cavity, b) photoresist layer, c) photoresist layer after UV contact lithography exposure, d) photoresist layer after development, e) 100 nm of Al e-beam evaporated onto SiO_2 and photoresist, f) photoresist and aluminum discs removed after lift-off.

3.2 Aluminum nanohole structure fabrication—e-beam lithography

In order to generate a nanohole array with smaller features, and shift resonances towards the short-wavelength infrared (SWIR) and mid-wavelength infrared (MWIR) regions (1.5–5 µm), e-beam lithography fabrication was employed. A 100-nm layer of aluminum was first evaporated onto a silicon wafer in order to create a base plane mirror, which prevented the transmission of incident radiation through the device. The SiO_2 cavity (200–600 nm) was then deposited onto the base plane mirror via plasma-enhanced chemical vapor deposition (PECVD) using SiH_4 and N_2O gases. The nanohole array was generated by e-beam lithography using a 4 % dilution of polymethyl methacrylate in anisole (PMMA A4), which was developed in a methyl isobutyl ketone/isopropanol (MIBK/IPA) mixture (1:3 v/v) after exposure. Once developed, 50 nm of aluminum was sputtered and lifted off to form the array on the surface of the device.

The choice of sputtering (versus e-beam evaporation) was justified when considering the negative effects of e-beam on the PMMA photoresist development. E-beam evaporation can heat the PMMA and potentially deform the PMMA during development. Conversely, sputtering did not introduce this risk, and therefore provided a more suitable means of depositing a layer of aluminum.

3.3 Aluminum nanohole structure fabrication—nanosphere lithography

Nanosphere lithography has been shown by a number of previous investigators to be a cost-effective means of fabricating sub-micron hole arrays, as well as other feature geometries.[16–20] A description of the nanosphere lithographic approach is provided schematically in Figure 4.

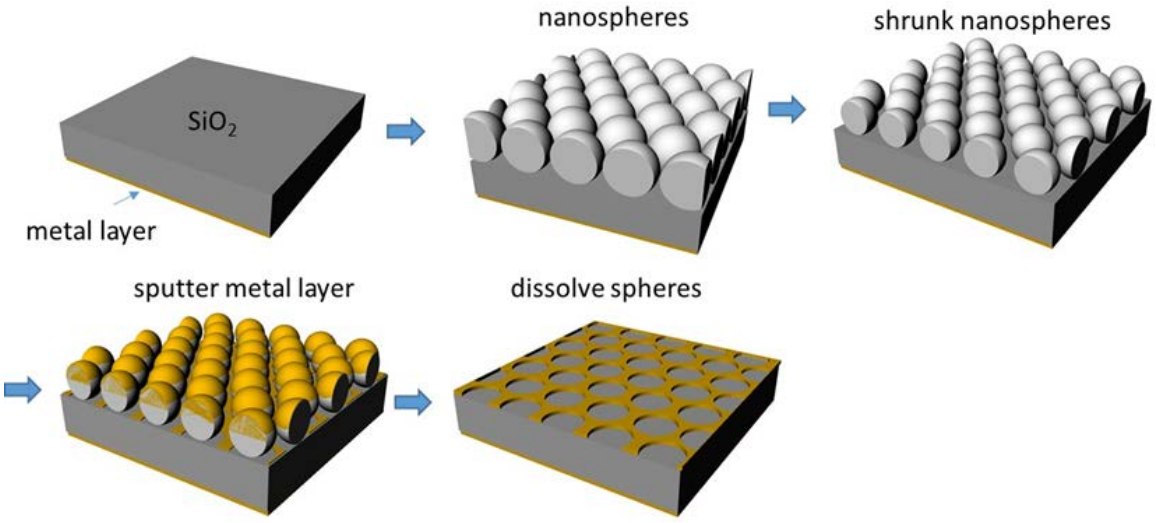

Figure 4. Nanosphere lithography fabrication process for generating a cavity-based nanohole array structure. 1) A base-plane metallic mirror is first deposited on a given substrate using physical vapor deposition (PVD). 2) A dielectric cavity layer, in this case SiO_2, with a given thickness is subsequently deposited using chemical vapor deposition (CVD). 3) Next, polystyrene latex spheres are spin-coated on the SiO_2 layer, forming a tightly-packed layer of nanospheres. 4) The nanospheres are then shrunk to a given size, using a reactive ion-etch (RIE) approach (e.g., oxygen plasma). 5) A thin layer of aluminum is deposited onto the spheres and into the interstitial spaces between the spheres, using electron beam evaporation. 6) Finally, the polystyrene latex spheres are dissolved in a suitable solvent such as toluene with the aid of sonication, leaving the patterned nanohole array.

Briefly, a new 4-inch silicon wafer was first cleaved into 35-mm square samples. The samples were cleaned in an oxygen plasma for 10 minutes at high power. Silicon naturally forms a layer of SiO_2 at room temperature. Utilizing this phenomenon and the hydrophilic nature of silica, the polystyrene spheres were simply spin-coated onto the substrate. 490-nm polystyrene spheres were drop-coated onto the sample, and then spun at 3,000 rpm for 45 seconds. The sample was then subjected to reactive ion etch (oxygen plasma) for 2 minutes, in order to shrink the spheres and create interstitial spaces between the spheres. Next, the sample was loaded into an e-beam evaporation system. During the subsequent evaporation steps, the sample holder was not rotated. A pressure of 8×10^{-7} Torr was achieved before any deposition was initiated. A 10-nm layer of titanium was first deposited at a rate of 0.5 Å/second. This layer promoted the eventual adhesion of aluminum to the substrate. Next, a 100-nm layer of aluminum was deposited at a rate of 0.5 Å/second. The sample was subsequently removed from the evaporator. In order to remove the aluminum-coated spheres, the sample was submerged in a beaker of toluene, and placed in an ultrasonic bath for 5 minutes.

3.4 Optical characterization

The spectral features of the nanohole arrays were determined using a Fourier-transform IR (FTIR) spectrometer (Bio-Rad Digilab Excalibur HE Series with UMA 600 Microscope). To obtain the reflectance, our FTIR spectrometer projected LWIR light through a ZnSe polarizer, focused it onto the sample with a ZnSe lens, and measured the reflected intensity with a mercury cadmium telluride (MCT) detector. The impinging beam (i.e., the beam incident on the sample following the ZnSe lens) had a spot size of approximately 0.5 mm, and a half-beam width of approximately 3°. This variation in incident angle was found through RCW simulations to have an insignificant effect on resonant wavelength. As a result, we assumed a normally incident beam in all expected results. A Philips XL 30 environmental scanning electron microscope (SEM) was used to image the nanohole array devices. SEM and FTIR results are provided in section 4., Results and Discussion.

4. RESULTS AND DISCUSSION

4.1 SEM images of nanohole arrays

SEM images of aluminum nanohole arrays fabricated using the previously described lithographic techniques are provided in Figure 5. In Figure 5A, an image of an array fabricated using photolithography is provided. Relatively large holes (average diameter = 2.28 µm) and periods (2.95 µm) were observed for this particular structure. In general, structures with these approximate nanohole array dimensions were explored as a means of generating resonances in the 5–12 µm range.

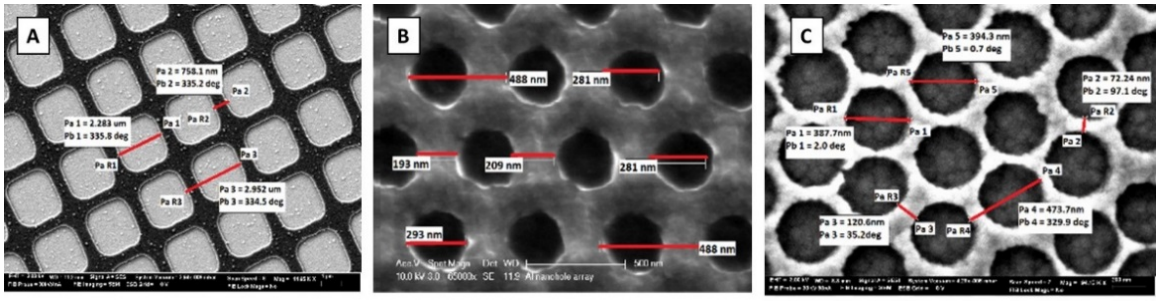

Figure 5. (A) SEM image aluminum nanohole array fabricated using photolithography. Period = 2.95 µm, average hole diameter = 2.28 µm. (B) SEM image aluminum nanohole array fabricated using e-beam lithography. Period = 0.4 µm, average hole diameter = 0.281 µm. (C) SEM image aluminum nanohole array fabricated using nanosphere lithography. Period = 0.5 µm, average hole diameter = 0.4 µm.

In Figure 5B, an SEM image of a typical array fabricated using e-beam lithography is provided. In general, much smaller hole diameters and periods were achieved using e-beam lithography. The average period and hole diameter for this particular structure was 0.4 µm and 0.5 µm, respectively. The goal of using e-beam lithography was to generate smaller array features in order to shift the resonances towards the SWIR and MWIR spectral regions. Figure 5C demonstrates a typical nanohole array fabricated using the nanosphere lithography technique. Nanosphere lithography is a much simpler and cheaper alternative to both photolithography and e-beam lithography. Hence, our goal with this technique was to demonstrate its viability in fabricating aluminum nanoholes arrays with resonances in the SWIR and MWIR spectral regions. An average period of 0.5 µm and a hole diameter of 0.4 µm was observed for this particular device.

4.2 IR spectral properties of cavity-based nanohole array

4.2.1 Devices fabricated with photolithography

The simulated and experimental spectral properties for the cavity-based nanohole arrays are provided in Figures 6 and 7. In this set of experiments, ZnSe was chosen as the cavity material, due to its transparent spectral properties in the MWIR to LWIR spectral regions (5–12 µm). For the data generated in Figure 6, an aluminum nanohole array thickness of 50 nm, a dielectric cavity thickness of 1.4 µm, and an aluminum base-plane mirror thickness of 100 nm were held constant, while the impact of hole diameter, periodicity, and the size parameter ($2a/\Lambda$) were varied (here a represents the nanohole radius, and Λ represents the periodicity).

Inspection of Figure 6 reveals that there are some clearly observable trends in both the simulated and experimental data. First, as both the hole diameter and period are decreased, the major resonances exhibited by the device are consistently blue-shifted. This observation is consistent with metal optics theory, which stipulates that, as the given structural features become smaller, the wavelength at which the resonance occurs becomes blue-shifted. Another observable feature in Figure 6 is revealed when comparing Figure 6c and 6d, where an increase in size parameter produces a blue shift in the observed resonance. This result is also consistent with metal optics theory in terms of diminishing the distance between adjacent plasmonic structures. Of particular note is the magnitude of the resonances that were observed in the four test cases provided in Figure 6. The smallest nanohole diameter of 1 µm generated the weakest resonance. Whereas the relatively larger hole diameters of 2–3 µm generated much stronger resonances, in terms of computational and experimental results. When comparing Figure 6a, 6b, and 6c, the strongest resonances were observed for those scenarios in which the size parameter was in the 0.6–0.7 range (as shown in Figures 6a and 6c). A size parameter of 0.5 yielded slightly lower magnitudes in the resonances, as observed in Figure 6d.

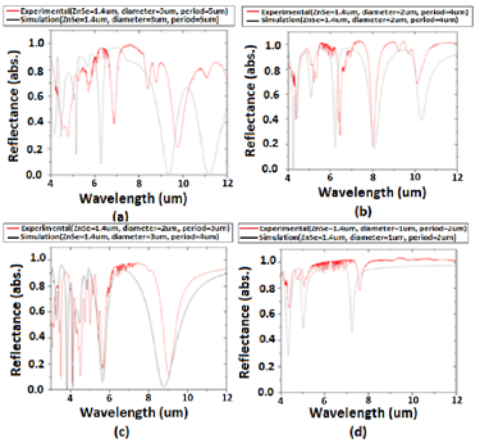

Figure 6. Simulated and experimental spectra of cavity-based nanohole arrays fabricated using photolithography. The aluminum nanohole array thickness (50 nm), the dielectric cavity thickness (1.4 µm), and the aluminum base-plane mirror thickness (100 nm) were held constant. (a) Hole diameter = 3 µm, period = 5 µm. (b) Hole diameter = 2 µm, period = 4 µm. (c) Hole diameter = 2 µm, period = 3 µm. (d) Hole diameter = 1 µm, period = 2 µm.

The impact of cavity thickness on spectral properties was the primary parameter that was explored for the data generated in Figure 7. In this set of experiments, the aluminum nanohole array thickness (50 nm), nanohole diameter (2 µm), periodicity (3 µm), and base-plane mirror thickness (100 nm) were held constant. Inspection of data produced in Figure 7 reveals that a distinct trend is readily observable. Namely, as the cavity thickness is increased from 1.1 µm to 2.0 µm, the spectral features of the resonances are steadily red-shifted. This trend is clearly observable in Figures 7a–c, and less so in Figure 7d. For the results in Figure 7d, we anticipated a resonance near 14 µm, as shown in the computational plot. However, this resonance was not experimentally verified since the FTIR analysis was cutoff at 12 µm.

In summarizing the results provided in Figures 6 and 7, the main parameters that dictate the resonance wavelength are the cavity thickness, nanohole diameter, and periodicity, while the size parameter played a role in the magnitude of the resonance. While the measured results were reasonably close to the predictions, there were some clear discrepancies. We believe there are several potential reasons for the differences. One is that the index of refraction used for ZnSe (2.41) was taken from that reported in the literature for crystalline ZnSe wafers. However, the actual index for ZnSe films could be different due to the amorphous nature of the films. Secondly, the models assumed a uniform grating with circular holes. As clearly shown in the SEM figures of Figure 5, the actual nanohole geometries slightly deviated from the pure circular model. Lastly, since the results are very dependent on the thickness of the ZnSe cavity, any errors in the film thickness measurements would shift the resonance response.

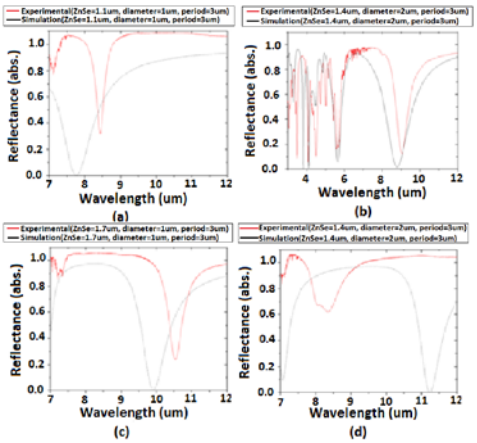

Figure 7. Simulated and experimental spectra of cavity-based nanohole arrays fabricated using photolithography. The aluminum nanohole array thickness (50 nm), the hole diameter (2 µm), the period (3 µm), and the aluminum base-plane mirror thickness (100 nm) were held constant. The ZnSe cavity thickness was varied as follows: (a) cavity thickness = 1.1 µm, (b) cavity thickness = 1.4 µm, (c) cavity thickness = 1.7 µm, (d) cavity thickness = 2.0.

4.2.2 Devices fabricated with e-beam lithography and nanosphere lithography

Photolithography was the primary fabrication technique used to explore the impact of structural features in our study of these aluminum nanohole arrays. As a follow-on to this effort, our goal was to demonstrate our ability to generate resonances in the SWIR to MWIR spectral regions by fabricating smaller structural features, such as smaller nanohole diameters and periods. To achieve this goal, e-beam and nanosphere lithographic techniques were developed to fabricate the aluminum nanohole arrays with smaller structural features. Figures 8a and 8b provide computational and experimental results for devices made with e-beam lithography and nanosphere lithography, respectively.

Inspection of Figure 8 reveals that the e-beam and nanosphere lithographic techniques both provided a means of generating resonances in the SWIR spectral (1.5–3.0 µm) region. As expected, in comparison to those results generated via photolithography, smaller structural features were achieved (as demonstrated by SEM images in Figure 5, leading to resonances that were significantly blue-shifted.

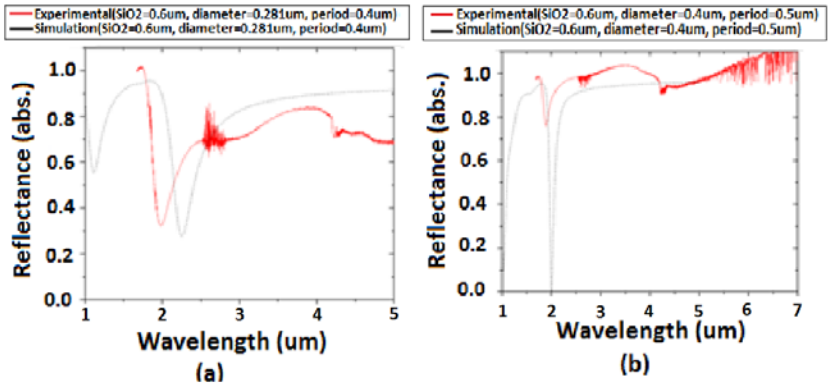

Figure 8. Simulated and experimental spectra of cavity-based nanohole arrays fabricated using (a) e-beam lithography and (b) nanosphere lithography.

5. CONCLUSION

Aluminum cavity-based nanohole arrays were successfully designed computationally, fabricated, and characterized. The impact of cavity thickness on tuning the resonance of an aluminum nanohole array was the primary focus of this study. Photolithography, e-beam lithography, and nanosphere lithography were explored as a means of fabricating these devices. Nanohole diameter, periodicity of the array, and cavity thickness were all found to play a significant role in tuning the spectral properties of the devices. Photolithography was successfully used to generate devices with resonances in the LWIR (5–12 µm) region. E-beam and nanosphere lithography were successfully used to generate resonances at shorter wavelengths (the SWIR spectral region). To our knowledge, this study was the first documented attempt to explore the impact of cavity thickness on tuning the resonances that are generated by aluminum-based nanohole arrays. The nanosphere lithography results also demonstrate that it is a viable technique for fabricating aluminum arrays, in addition to providing a cheaper and simpler alternative to photolithography and e-beam lithography. We anticipate that this study will serve as a basis for future studies in which cavity-based nanohole arrays will be explored as a means of enhancing detection sensitivity in SERS, SEF, and SEIRA.

ACKNOWLEDGMENTS

The authors would like to acknowledge U.S. Army funding provided through the Edgewood Chemical Biological Center's Surface Science Initiative program. Support was also provided by the U.S. Army Research Office under contract W911NF-14-2-0104.

REFERENCES

[1] Landy, N.; Sajuyigbe, S.; Mock, J.; Smith, D.; Padilla, W. Perfect Metamaterial Absorber. *Phys. Rev. Lett.* **2008,** *100*, p 207402.

[2] Aydin, K.; Ferry, V.E.; Briggs, R.M.; Atwater, H.A. Broadband, polarization-independent resonant light absorption using ultrathin, plasmonic super absorbers. *Nat. Comm.* **2011,** *2*, p 517.

[3] Pala, R.A; White, J.; Barnard, E; Liu, J.; Brongersma, M.L. Design of a plasmonic thin-film solar cells with broadband absorption enhancements. *Adv. Mater.* **2009,** *21* (34), pp 3504–3509.

[4] Chanda, D.; Shigeta, K.; Truong, T.; Lui, E.; Mihi, A.; Schulmerick, M.; Braun, P.V.; Bhargava, R.; Rogers, J.A. Coupling of plasmonic and optical cavity modes in quasi-three-dimensional plasmonic crystals. *Nat. Comm.* **2011,** *2*, p 479.

[5] Li, A.; Butun, S.; Aydin, K. Large-Area, Lithography-Free Super Absorbers and Color Filters at Visible Frequencies Using Ultrathin Metallic Films. *ACS Photonics.* **2015,** *2* (2), pp 183–188.

[6] Zheng, P.; Li, M.; Jurevic, R.; Cushing, S.K.; Liu, Y.; Wu, N. A gold nanohole array based surface-enhanced Raman scattering biosensor for detection of silver(I) and mercury(II) in human saliva. *Nanoscale*. **2015,** *7*, pp 11005–11012.

[7] Sanchez-Gonzalez, A.; Corni, S.; Mennucci, B. Surface-Enhanced Fluorescence within a Metal Nanoparticle Array: The Role of Solvent and Plasmon Couplings. *J. Phys. Chem. C.* **2011,** *115* (13), pp 5450–5460.

[8] Abb, M.; Wang, Y.; Papasimakis, N.; de Groot, C.H.; Muskens, O.L. Surface-Enhanced Infrared Spectroscopy Using Metal Oxide Plasmonic Antenna Arrays. *Nano Lett.* **2014,** *14* (1), pp 346–352.

[9] Knight, M.W.; King, N.S.; Liu, L.; Everitt, H.O.; Nordlander, P.; Halas, N.J. Aluminum for Plasmonics. *ACS Nano*. **2014,** *8* (1), 834–840.

[10] Lee, K.L.; Hsu, H.Y.; You, M.L.; Chang, C.C.; Pan, M.Y.; Shi, X.; Ueno, K.; Misawa, H.; Wei, P.I. Highly Sensitive Aluminum-Based Biosensors using Tailorable Fano Resonances in Capped Nanostructures. *Sci. Rep*. **2017,** *7*, p 44104.

[11] Li, W.; Qiu, Y.; Zhang, L.; Jiang, L.; Zhou, Z.; Chen, H.; Zhou, J. Aluminum nanopyramid array with tunable ultraviolet-visible-infrared wavelength plasmon resonances for rapid detection of carbohydrate antigen 199. *Biosens. Bioelectron*. **2016,** *79*, pp 500–507.

[12] Du, Q.G.; Yue, W.; Wang, Z.; Lau, W.T.; Ren, H.; Li, E.P. High optical transmittance of aluminum ultrathin film with hexagonal nanohole arrays as transparent electrode. *Opt. Express.* **2016,** *24* (5), pp 4680–4688.

[13] Mohoram M.G.; Gaylord, T.K. Rigorous coupled-wave analysis of planar-grating diffraction. *J. Opt. Soc, Am. A.* **1981,** *71*, pp 811–818.

[14] Lalanne, P. Improved formulation of the coupled-wave method for two-dimensional gratings. *J. Opt. Soc., Am. A.* **1997,** *14*, pp 1592–1598.

[15] Noponen E.; Turunen, J. Eigenmode method for electromagnetic synthesis of diffractive elements with three-dimensional profiles. *J. Opt. Soc. Am. A.* **1994,** *11*, pp 2494–2502.

[16] Liu, N.; Mesch, M.; Weiss, T.; Hentschel M.; Giessen, H. Infrared perfect absorber and its application as plasmonic sensor. *Nano Lett.* **2010,** *10* (7), pp 2342–2348.

[17] Zhao, J.; Frank, B.; Burger, S.; Giessen, H. Large-area high-quality plasmonic oligomers fabricated by angle-controlled colloidal nanolithography. *ACS Nano.* **2011,** *5* (11), pp 9009–9016.

[18] Gwinner, M.C.; Koroknay, E.; Patoka, P.; Kandulski, W.; Giersig, Ml; Giessen, H. Periodic Large-area Metallic Split-Ring Resonator Metamaterial Fabrication Based on Shadow Nanosphere Lithography. *Small.* **2009,** *5* (3), pp 400–406.

[19] Bonakdar, A.; Rezaei, M.; Brown, R.L.; Fathipour, V.; Dexheimer, E.; Jang, S.J.; Mohseni, H. Deep-UV microsphere projection lithography. *Opt. Lett.* **2015,** *40* (11), pp 2537–2540.

[20] Qu, C.; Kinzel, E.C. Polycrystalline metasurface perfect absorbers fabricated using microsphere photolithography. *Opt. Lett.* **2016,** *41* (15), pp 3399–3402.

Understanding the effect of substrate material and solvation on surface-enhanced Raman spectroscopy enhancement

Jason Guicheteau*, Ashish Tripathi, Erik Emmons, Augustus W. Fountain, III, Steven D. Christesen
U.S. Army Edgewood Chemical and Biological Center, Research & Technology Directorate, 5183 Blackhawk Rd, Aberdeen Proving Ground, MD 21010

ABSTRACT

The final year of this effort examined the effects of substrate geometry, deposited metals, and solvation on the yielded surface-enhancement value, as well as examining the effects of various experimental protocols to the resulting surface-enhancement value and traditional enhancement factor calculations. Following the Langmuir protocol we previously established, we demonstrated that, as geometry and metal change, the binding characteristics of an analyte differ, and can be explained by varying affinities for a particular metal, existence of geometry-dependent electrophilic and nucleophilic adsorption sites, as well as orientation changes of the binding between the metal and the analyte. Furthermore, to continue our focus of the thermodynamic influence on surface-enhanced Raman spectroscopy and the impact it may have on eventual commercial success, we examined various experimental protocols to demonstrate the effect on the two figures of merit calculations—the traditional enhancement factor and the Edgewood Chemical Biological Center-derived surface-enhancement value.

Keywords: surface-enhanced Raman spectroscopy, substrate, geometry, metals, experimental protocols

1. INTRODUCTION

Surface-enhanced Raman scattering (SERS) results when nanostructured metallic substrates (typically gold or silver) locally amplify electromagnetic fields at or near the substrate surfaces upon photon excitation. This phenomenon has been investigated for over 40 years, and since 1972 approximately 26,000 papers, patents, reviews, and proceedings have been published.[1] These reports detail fundamental understandings of the SERS phenomenon addressing the electromagnetic and chemical enhancement theories, substrate design and manufacturing, and potential application scenarios including biomedical, agriculture, chemical detection,[2–4] From this work, it is clear that the understanding of the SERS phenomenon is fairly mature. The noted potential benefits of SERS over normal Raman spectroscopy such as reduction of fluorescence, decreased integration times, and reduction of laser power required for analysis, positions SERS to be an ideal technique for trace-level detection schemes. However, despite these advantages, the successful transition from research laboratories to commercial applications has yet to materialize. While most of the SERS enhancement can be explained by the enhanced electric field produced by the metallic nanostructures, the effect of molecular properties on the binding and the thermodynamic contributions of the system relating to the SERS enhancement are less well understood. Understanding these effects are important in explaining why certain molecules exhibit very large SERS enhancements while other molecules, on the same substrate, yield little to no enhancement of the Raman signal.

Our work seeks to provide a greater fundamental understanding of what drives the binding between and analyte of interest and the nano-metallic surfaces. Previously, we described a modification to the Edgewood Chemical Biological Center-derived surface-enhancement value (SEV) which we were able to link with the traditional SERS enhancement factor (G) through the equilibrium constant (K).[5–7] This discovered relationship allowed for further refinement of SEV (F) and G that culminated with a new formula,

$$\ln(F_\alpha) = \underbrace{\ln\left\{G\frac{(1-\alpha)n_{max}A}{V}\right\}}_{Fn\ of\ substrate\ and\ detector} \underbrace{-\frac{\Delta G_{rxn}}{RT}}_{Fn\ of\ reaction\ parameters} \underbrace{+\frac{\Delta G_{solvation}}{RT}}_{Fn\ of\ solvation}. \quad (1)$$

The right-hand side of equation (1) can be viewed as a summation of three functions. Each of these functions describe different processes that we believe drive the SERS response—the design parameters of the SERS substrate (the first term, shown in red), the thermodynamics of adsorbate-substrate interaction (the second term, shown in green), and

the effect of solvent on the SERS response (the third term, shown in blue). A more strongly enhancing SERS substrate design results in higher values of G_{SERS}. However, if the metal does not react (via a chemical or physical bond) with the analyte, then $\Delta G_{reaction}$ becomes a positive number and, depending on the magnitude, can negate the gains made by getting a higher G_{SERS} value since few molecules will be present at the surface to experience plasmonic enhancement. In such a case, choosing a metal that strongly reacts with the analyte (resulting in a $\Delta G_{reaction}$ that is a large negative number) can perhaps overcome a decrease in G_{SERS} value and still make for a more practical SERS substrate. Similarly, choosing a solvent that does not dissolve the analyte strongly is better than the one that does. The low solubility of an analyte results in a lower magnitude of $\Delta G_{solvation}$ (a negative value), thus resulting in a higher value of F_{α}.

The goal of this project is to break down each function of equation (1) into experimental tasks in order advance the understanding of the SERS process, aimed at an improved predictability of the SERS activity of molecules of interest. In previous years, we discussed the effects of molecular properties, solvent-solute interactions, and identified two unique adsorption sites on SERS substrates. In this final year, we concentrated on the second term, which is related to the two geometry-dependent binding sites (electrophilic and nucleophilic) and metal of a substrate, as well as understanding the effect of various experimental protocols to the yielded SEV.

The work described here focuses on the second term in the equation, the effect of the Gibbs free energy of adsorption for the reaction between the analyte and the surface. A series of mono-substituted thiophenols and isomers of bromoisoquinoline were used in order to determine the effect of localized dipole moments on the Gibbs free energies of reaction. Changes in Gibbs free energy of binding of mono-substituted thiophenol molecules to gold SERS substrate as the function of electron affinity of the functional group attached to the *para* position of thiophenol was determined. Generally, it has been thought that thiols bind strongly, and essentially irreversibly, to gold surfaces. However, we have found that substituted thiophenols can have measurable equilibrium constants depending on if electron-donating or electron-withdrawing substituents are present. For thiophenol or substituted thiophenols with electron-donating groups such as amino groups, the equilibrium constant is too large to measure. However, for electron-withdrawing groups such as halogens, measurable equilibrium constants and Gibbs free energies of adsorption have been measured. Changes were also found in the Gibbs free energy of binding for the bromo-isoquinoline series as the position of the bromine atom was changed.

2. EXPERIMENTAL METHODS

2.1 Materials

1,2-di(4-pyridyl)ethylene (BPE), ethanol, acetonitrile, thiophenol, halogene-thiophenols, mono-substituted bromo-isoquinolines, dodecane, and toluene were purchased from Sigma-Aldrich® and used without further purification. Solutions were prepared in deionized water in concentrations ranging from 5×10^{-9} M to 0.1 M. All experiments were performed at room temperature (23 °C). Commercially-available gold SERS substrates (Klarite®, KLA-312, Renishaw® Diagnostics Ltd.; Gloucestershire, UK) were used for this work, along with K2 University of California Santa Barbara (UCSB) substrates coated with both silver and gold. These substrates provide adequately strong and reproducible SERS enhancement when 785 nm and 633 nm excitation are used.

2.2 Raman microscopy

Raman measurements were performed with a JASCO® NRS-3200 dispersive Raman microscope system operating at 785 nm excitation with approximately 4 mW power incident on the sample and 633 nm excitation with approximately 5 mW power. A 10X microscope objective was used both to focus the laser on the substrate and to collect the Raman-scattered light. The relatively modest laser power and magnification were used to minimize any laser-induced heating of the substrate. The laser spot size was not measured, but is estimated to be in the range of 1–5 µm. The Raman-scattered light was dispersed with a 600 grooves/mm diffraction grating (blazed at 750 nm) and a spectrometer entrance slit width of 100 µm was used to obtain a spectral resolution of approximately 8 cm^{-1}. All Raman spectra were acquired with 25 second integration time and averaged over three co-additions. The Raman-scattered light was detected with a thermoelectrically cooled charge-coupled device camera (Andor®; Belfast, UK). The strong Rayleigh-scattered light was suppressed with a notch filter (Semrock®; Rochester, NY). Raman spectral mapping of the substrate was performed by selecting a 36-location grid, in a rectangular 6 x 6 format, on the substrate and obtaining a Raman spectrum at each of the locations.

3. RESULTS AND DISCUSSION

Langmuir protocol equilibrium absorption isotherms were measured for gold-coated Klarite® and silver coated-K2 UCSB substrates with BPE and thiopehenol. In order to obtain valid Langmuir isotherms, the investigated substrate was immersed in a volume of analyte sufficient to ensure that, at any given concentration, there is an excess of molecules available for binding. In addition, it is ensured sufficient time to reach 99% equilibrium limited coverage on the surface of the substrate. This protocol allows for broader characterization of the substrate enhancement capability, while giving insight into the interactions and binding potential between the three components in the system; the analyte, solvent, and metallic substrate. The purpose of these experiments is to better understand the effect of geometry and metal relationship to the resulting SEV by keeping the solvents the same for each analyte investigated.

3.1 Effect of geometry and metal on F_α

3.1.1 Au-coated Klarite®—BPE versus Ag-coated K2 substrates

As previously reported, concentration-dependent isotherms for BPE adsorbed onto Au-coated Klarite® yielded a dual-site Langmuir isotherm. The equation describing the dual Langmuir isotherm is given as

$$I_{C_s} = I_{\max}\left(\frac{\beta_1 K_1 C_s}{1+K_1 C_s} + \frac{\beta_2 K_2 C_s}{1+K_2 C_s}\right), \tag{2}$$

which is the sum of two Langmuir isotherms.[7,8] Here β_1 and β_2 are the fractions representing each elementary space ($\beta_1 + \beta_2 = 1$), and K_1 and K_2 are the equilibrium constants for the different types of sites. The dual-Langmuir isotherm models the situation where two types of sites are available, as explained in our recent article.[7] The two types of sites correspond to binding of protonated and unprotonated molecules. The first isotherm, which appears at lower concentrations, corresponds to electrophilic sites where the nitrogen lone pairs on unprotonated BPE molecules adsorb. Spatially, these sites are located around sharp edges on the substrates. The second isotherm, which appears at higher concentrations, corresponds to nucleophilic sites where protonated molecules bind. These sites are located around flatter parts of the substrates.

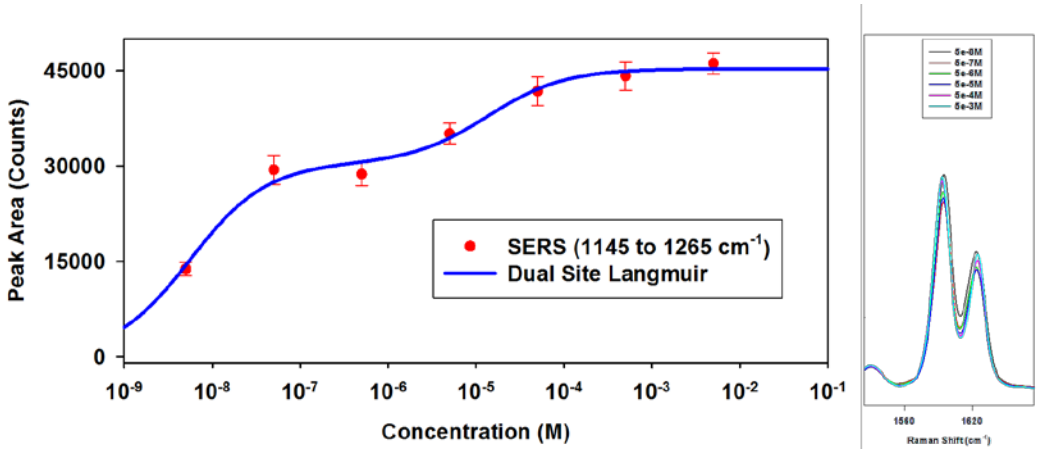

Figure 1. Dual-site Langmuir isotherm for Au-coated Klarite®.

Figure 1 shows the dual-site Langmuir isotherm along with a truncated spectral view of the two main corresponding spectral bands of BPE, at 1596 cm^{-1} and 1630 cm^{-1}, associated with the symmetric pyridyl ring breathing vibrational mode and the ethylene bridge C=C double bond stretching mode respectively. When comparing this data to Ag-coated K2 UCSB substrates, a significant difference is observed. Figures 2 and 3 show the resulting Langmuir isotherm and similar truncated spectral view of BPE vibrational bands. The isotherm shows a unique difference from the Au-goated Klarite® data in the response such that a single Langmuir isotherm model was used as opposed to the dual site model. The data appears to rise, and fall, and rise again in pattern not observed earlier. While we are still investigating the cause behind this data, Figure 3 shows a closer examination of the spectral data of the two bands (1596 cm^{-1} and 1630 cm^{-1} respectively), and how the features do not grow equally with increasing concentrations as observed in the Au-BPE data in Figure 1. This observation indicates that the mechanism of adsorption of BPE Au-coated Klarite® is

different than the one observed in the case of BPE to silver. This spectral region was studied by Chen et al.[9] while investigating binding of BPE to metallic and oxidized silver SERS substrates. Chen et al. reported that the change in the relative intensities of the two bands is due to change in orientation of the BPE molecule to the SERS substrate.[9] Their work indicates that the feature at 1630 cm^{-1} is more intense than the one at 1596 cm^{-1} when the BPE molecule is bound via one of the pyridyl nitrogen, and thus stands erect (perpendicular to the substrate). Conversely, the feature at 1596 cm^{-1} is more intense when the BPE molecule is bound to the substrate via both the pyridyl nitrogens and thus is lying flat on the substrate (parallel to the substrate). This indicates that the BPE moieties (neutral molecules and protonated ions) tend to bind via both the pyridyl nitrogens, and that the orientation of the BPE moieties, which is parallel to the surface, does not appear to change with increasing concentration of BPE in adsorbing to gold.

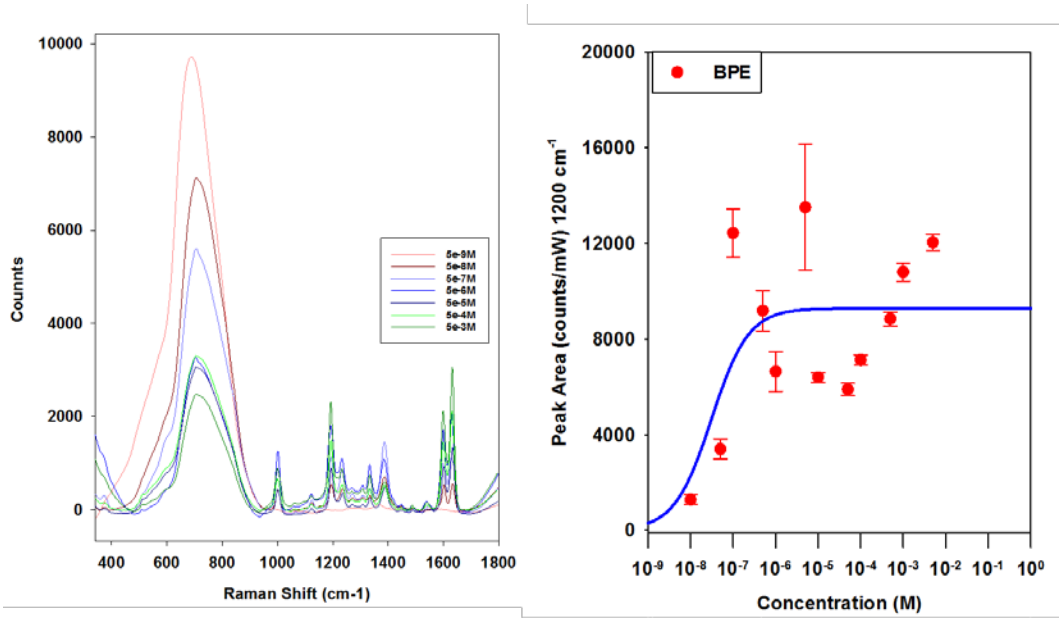

Figure 2. Concentration-dependent Langmuir isotherm detailing adsorption of BPE to silver-coated K2 UCSB substrates.

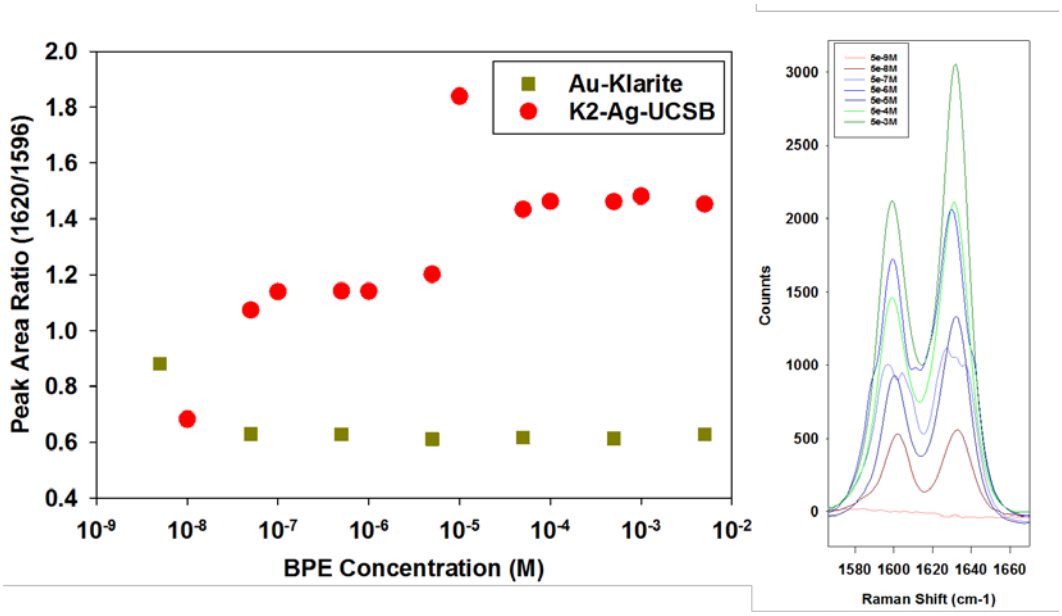

Figure 3. Vibrational band changes in BPE adsorbed onto silver coated K2 UCSB substrates, indicating probable orientation changes upon increasing concentration.

3.1.2 Au-coated Klarite®—thiophenol versus Au-coated K2 substrates

Further metal influences are observed when investigating thiophenol adsorption to Au-coated Klarite® and Ag-coated K2 UCSB substrates. Figure 4 shows the most prominent vibrational bands associated with thiophenol between 970 cm^{-1} and 1150 cm^{-1} respectively. First, as demonstrated with BPE adsorption, no rearrangement or orientation effects are observed between the two base surface metals; however, unique chemical and physical differences between the two are overserved. Upon initial examination, the silver-coated K2 UCSB results yield a 20X greater signal response than the accompanying Au-coated Klarite® results. As previously shown, thiophenol adsorbed onto Au surfaces forms a self-assembled monolayer, even at concentrations down to 5×10^{-9} M, and a resulting binding equilibrium is unobtainable due to this strong interaction. In the case of silver though, a measureable equilibrium is obtained, and thus the overall sensitivity of the metal is somewhat reduced. Furthermore, by displaying the bright field images taken during measurements at the various concentrations, visual changes are observed, which suggest plasmonic changes to the surface, indicating physical and chemical changes occurring at the surface. This observation was not observed with gold-coated Klarite®.

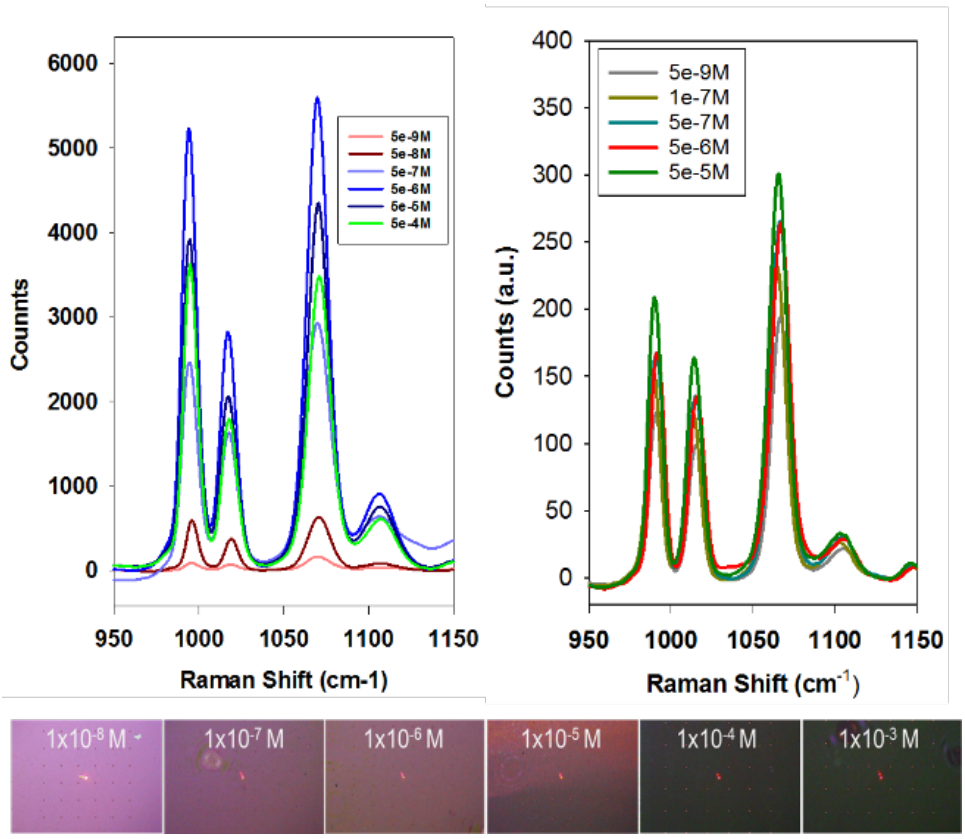

Figure 4. Data comparison of thiophenol bound to Ag and Au surfaces demonstrating differing sensivitiy to the base metals as well plasmonic changes of silver during analysis.

The examples shown in Figure 4 are two of six chemicals currently being investigated to determine the effect of substrate geometry and metals on the SEV Fα value. Table 1 shows the comparison of BPE and thiophenol data described above when benchmarked against the classical SERS enhancement factor (discussed previously) and the F_α value. It appears that for BPE, the Au-coated Klarite® yields increased enhancement values compared to Ag-coated K2 UCSB; however, for thiophenol, is observed to be slightly favored by the enhancement factor (EF) value. However, as mentioned above and observed in the SEV value, by taking into account the thermodynamics of the analyte/substrate/solvent system, a two order of magnitude increase in value is seen. A third substrate not shown here will also be included in the final results, and a complete and detailed manuscript will be prepared for publication.

Table 1. EF versus SEV comparison of various substrate-metal combinations.

Substrate	Metal	Laser	BPE		Thiophenol		8+ Cemicals
			EF	SEV ($F_{0.9}$)	EF	SEV($F_{0.9}$)	
Klarite	GOLD	785	7.29E+06	8.96E+07	9.55E+05	>2.0E+09	
Klarite	SILVER	633					
USCB-K2	GOLD	785					
UCSB-K2	SILVER	633	5.72E+04	5.85E+05	6.03E+06	2.25E+07	
ROK-KIM	GOLD	785					
ROK-KIM	SILVER	633					

3.2 Thermodynamic influences in SERS

The second part of the year focused on demonstrating the thermodynamic influences on SERS with respect to comparing the EF calculation and the SEV value when considering multiple types of experimental procedures. The EF defined in equation (3) is the essential metric in assessing a substrate's enhancing power; however, we have determined that it does not include intrinsic information relating to the binding affinity of the target analyte to the substrate. Commonly, the EF is defined as

$$G = \frac{I_S N_R}{I_R N_S}, \tag{3}$$

where I_S and I_R correspond to the intensities of the SERS and normal Raman responses and N_S and N_R number of probed molecules.[5] As previously described,[7] this approach requires knowledge of the number of binding sites occupied by the analyte on the substrate. Often, this requirement is met with assumptions in the EF calculation when estimating the number of molecules adsorbed onto the substrate in the field of view of the interrogating laser. This has the potential to add subjectivity to calculated EF results. Furthermore, the traditional EF may be a poor measure of the analytical sensitivity of the SERS substrate as it does not take into account the equilibrium established between the concentration of the analyte in the fluid phase and the SERS surface. We used an early form of equation (1) that originally took the equilibrium constant into account, and determined the influence of the therymodynamic properties of the complete system when comparing three different types of experimental protocols—drop-and-dry, constant time and volume (CTVP), and Langmuir.

The drop-and-dry protocol, also known as the drop-cast method, requires less than 1 mL of solution and can provide a rapid estimation of the EF value. In this procedure, a fixed volume of the analyte solution is deposited onto the surface of a substrate and allowed to dry (either by heating the substrate or under ambient conditions). While this method is common, there are significant sources of uncertainty when acquiring the SERS data. The greatest difficulty is caused by non-uniformity of precipitation from the droplet, and avoiding coffee-ring effects.

The second SERS analysis method is solution-based, where the SERS analysis occurs with the substrate immersed in a volume of the analyte solution during spectral data acquisition. This methodology removes issues of the drop-and-dry methodology, but introduces volume and time factors to be considered, as researchers typically carry out the analysis after some set time period. For the purposes of this paper, we utilized the CTVP protocol developed for DARPA with a 20-minute immersion time in 7 mL of analyte solution.[7]

The Langmuir protocol, described above, allows for a characterization of the substrate's enhancement capability while giving insight into the interactions and binding potential between the three components—the analyte, solvent, and metallic substrate. Each method can yield classical enhancement values (equation (3)) that we show are similar; however, the reported SEV values are significantly different.

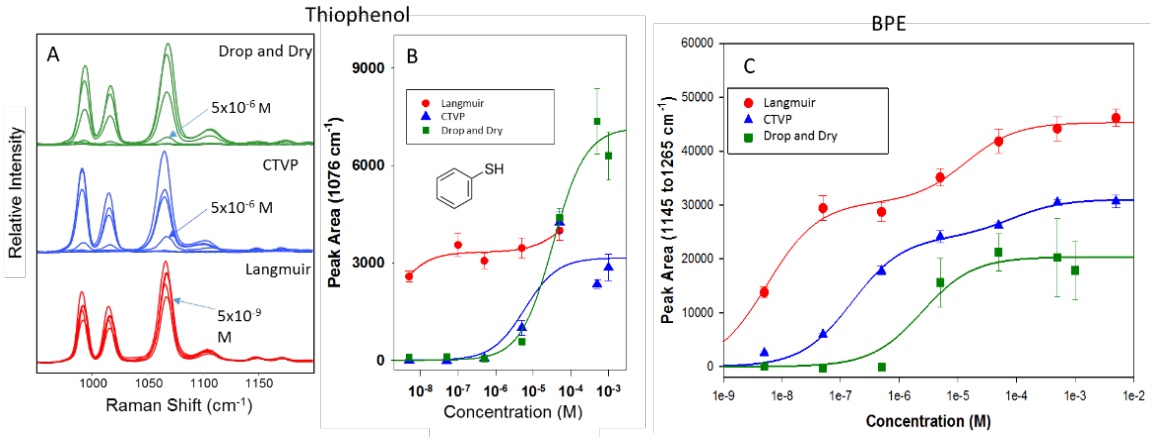

Figure 5. (A) spectral data showing differences between three experimental protocols of thiophenol adsorbed onto gold-coated Klarite®. Constructed Langmuir isotherms comparison of experimental protocls for thiophenol (B) and BPE (C).

Figure 5A shows a spectral comparison and constructed concentration dependent isotherms (*B*) following the three described protocols above. Examining the drop-and-dry and CTVP, extracted equilibrium values (*K*) were obtained to be 3.0×10^4 and 1.7×10^5 respectively. While these generally agree with reported literature values,[10] when compared to the resulting Langmuir protocol, the values do not agree. This can be explained from the fact that thiophenol is believed to irreversibly bind to gold, making an equilibrium constant difficult to calculate as mentioned above. The spectral signatures demonstrate differences and confirm that, for the first two protocols, drop-and-dry and CTVP, the sensitivity is lower due to the fact that the available binding sites are starved of potential molecules, thus producing minimal signal response when compared to the Langmuir isotherm. Figure 5C shows further evidence of experimental differences when studying the binding of BPE to gold.

Empirical enhancement factors and SERS enhancement values were calculated for the two investigated molecules (BPE and thiophenol). Traditional enhancement factors (*G*), from equation (2), were calculated by comparing ratios of the maximum SERS signal-per-molecule over the maximum normal Raman signal per molecule, assuming a focal volume of 2.2×10^{-12} L and interrogated area of 2.2×10^{-8} cm^2. Values for SEV (*F*) were calculated following procedures outlined previously[7] using an $\alpha = 0.9$. As stated above, the traditional enhancement factor calculations all yield similar results, 10^6 for BPE and 10^5 for thiophenol, respectively. These values help to determine a general "enhancement" of the substrate, but don't necessarily yield any information on the adsorption capability of the substrate. However, utilizing the SEV calculation from equation (1) and following the Langmuir protocol, a > 600X increase for BPE was observed. In the case for thiophenol, a SEV value of $> 2.0 \times 10^9$ was calculated from the assumption of an equilibrium constant of 1×10^{10}, due to the fact that the molecule forms a self-assembled monolayer at $< 5 \times 10^9$ M.

Table 2. EF versus SEV value comparison of the three experimental protocols.

Analysis Protocol	BPE		Thiophenol	
	EF (G)	SEV (F_{90})	EF (G)	SEV (F_{90})
Drop and Dry	4.87E+06	1.36E+05	1.71E+06	1.57E+04
CTVP	5.74E+06	2.51E+06	7.55E+05	3.89E+04
Langmuir	7.29E+06	8.96E+07	9.55E+05	> 2.0E+09

4. CONCLUSION

We believe the work detailed here demonstrates the effect that geometry and metal have on the adsorption of analytes and resulting SERS enhancements, as well as the need to consider the analysis method when characterizing a SERS surface, especially when reporting EF. While the classical EF calculation defined in equation (3) will continue to be used, the inclusion of thermodynamic properties into enhancement value calculations are critical in real-world application of SERS. We believe that with our work, and the final working SEV equation (equation (1)), it is possible to separate SERS enhancement into independent contributions from the substrate and detector, thermodynamic

properties of the reaction, and functions of solvation-free energies and temperature of the solution. By characterizing the contributions of the SERS response into more practical metrics, substrate development can be focused in a new direction to drive SERS toward commercialization success.

ACKNOWLEDGMENTS

The authors would like to acknowledge U.S. Army funding provided through the Edgewood Chemical Biological Center's Surface Science Initiative program.

REFERENCES

[1] SciFinder Search, March 7, 2017, keyword "Surface enhanced Raman".
[2] Wang, W.; Yan, B.; Chen, L. SERS Tags: Novel Optical nanoprobes for Bioanalysis. *Chem. Rev.* **2013,** *113* (3), pp 1391–1428.
[3] Sinha, S.; Jones, S.; Pramanik, A.; Ray, P. Nanoarchitecture Based SERS for Biomolecular Fingerprinting and label-free Disease Markers Diagnosis. *Acc. Chem. Res.* **2016,** *49* (12), pp 2725–2735.
[4] Farquharson, S.; Shende, C.; Smith, W.; Huang, H.; Inscore, F.; Sengupta, A.; Sperry, J.; Sickler, T.; Prugh, A.; Guicheteau, J. Selective Detection of 1000 B. anthracis spores within 15 minutes using peptide functionalization SERS assay. *Analyst.* **2014,** *139*, pp 6366–6370.
[5] Le Ru, E.C.; Blackie, E.; Meyer, M.; Etchegoin, P.G. Surface enhanced Raman scattering enhancement factors: A comprehensive study. *J. Phys. Chem. C.* **2007,** *111* (37), pp 13794–13803.
[6] Guicheteau, J.A.; Farrell, M.E.; Christesen, S.D.; Fountain III, A.W.; Pellegrino, P.M.; Emmons, E.D.; Tripathi, A.; Wilcox, P.; Emge, D. Surface enhanced Raman scattering (SERS) evaluation protocol for nanometallic surfaces. *Appl. Spectrosc.* **2013,** *67* (4), pp 396–403.
[7] Tripathi, A.; Emmons, E.; Fountain III, A.W.; Guicheteau, J.A.; Moskovits, M.; Christesen, S.D. Critical role of adsorption equilibria on the determination of surface-enhanced Raman enhancement. *ACS Nano.* **2015,** *9* (1), pp 584–593.
[8] Langmuir, I. The adsorption of gases on plane surfaces of glass, mica, and platinum. *J. Am. Chem. Soc.* **1918,** *40* (9), pp 1361–1403.
[9] Chen, T.; Pal, A.; Gao, J.; Han, Y.; Chen, H.; Sukhishvili, S.; Du, H.; Podkolzin, S.G. Identification of Vertical and Horizontal Configurations for BPE Adsorption on Silver Surfaces. *J. Phys. Chem. C.* **2015,** *119* (43), pp 24475–24488.
[10] Wang, H.; Levin, C.; Halas, N. Nanosphere Arrays with Controlled Sub-10-nm Gaps as Surface enhanced Raman Substrates. *J. Am. Chem. Soc.* **2005,** *127* (43), pp 14992–14993.

Matrix-free assisted laser desorption ionization using metal-organic frameworks

Rabih E. Jabbour*, Gregory W. Peterson, Jared B. DeCoste
U.S. Army Edgewood Chemical Biological Center, Research & Technology Directorate,
5183 Blackhawk Rd, Aberdeen Proving Ground, MD 21010

ABSTRACT

Metal-organic frameworks are gaining wide-spread applicability across many fields. We utilized metal-organic frameworks to develop a universal matrix for a new matrix-assisted laser desorption ionization mass spectrometry technique. The matrix-assisted laser desorption ionization technique is a powerful ionization method used to improve mass spectrometry characterization of biological samples. The current matrices used in the matrix-assisted laser desorption ionization process are not universal, and usually depend heavily on the nature of the analytes being analyzed. As such, there are many matrices that are used and based on the nature and type of analytes suitable matrices will be selected to provide optimal matrix-assisted laser desorption ionization mass spectrometry analysis. We proposed to utilize metal-organic framework compounds with multifunctional groups and various pores structures to address this technological gap. Understanding the basic mechanism of ionization during matrix-assisted laser desorption ionization-mass spectrometry process is vital to design an effective metal-organic framework surface to act as universal matrix. Such metal-organic frameworks can be synthesized with porous solid and could have regular or predicted geometry. In this report, we investigated the utilization of low-frequency Raman spectroscopy to address some fundamental question about the interactions and binding mechanisms between metal-organic frameworks and analytes of interest. The data showed that there are intramolecular and intermolecular changes that occur among these compounds.

Keywords: metal-organic frameworks, mass spectrometry, matrix-assisted laser desorption ionization, charge transfer, desorption, matrix, film

1. INTRODUCTION

1.1 Background

Matrix-assisted laser desorption ionization (MALDI), is a soft ionization technique that has witnessed wide application in the characterization of large biomolecules using various mass spectrometry analyzers, specifically time-of-flight ones.[1–4] The MALDI process involves the deposition of an analyte solution onto a metal substrate followed by the addition of a matrix.[5] The matrix/analyte dry spot is exposed to a UV laser, and the laser energy absorbed by the matrix/analyte is converted into heat energy that initiates charge transfer, resulting in the desorption of the matrix and analyte molecules in ionized form. The positive ions are then accelerated through a vacuum into mass spectroscopy (MS) analyses. Nevertheless, MALDI has faced a lack of guiding systematic principles, which has resulted in mostly empirical work. For example, there is no universal matrix that can be used in the MALDI-MS analysis of biomolecules. Hundreds of compounds have been tried with several analytes and were given qualitative ratings.[6–8] These variabilities were the result of differences in charge transfer efficiency between the matrix and analytes due to chemical and structural factors[7]. This problem requires an urgent analytical need that can advance the MALDI process toward mechanistic understanding. Metal-organic frameworks (MOF) are an emerging class of porous materials that have been studied in multiple areas, including gas storage,[9,10] sensing,[11] air purification,[12] and catalysis.[13] MOFs are typically synthesized from metal oxide secondary building units (SBU) connected by organic linkers to form a reticulated, porous network. MOFs are utilized because of their versatility and thermal stability. The unique physical and chemical properties of MOFs provide the potential to serve as a MALDI matrix capable of ionizing a wide range of analytes. However, because of their structural complexity, we attempted to determine first if there is any interaction between analytes and the MOFs when they are mixed together. Low-frequency Raman spectroscopy (LFRS) was used to determine the intermolecular and intramolecular changes between free MOFs, and when mixed with analytes in an amorphous environment.[1–16] The LFRS is an emerging technique that provides, concurrently, vibrational spectra for tested compounds in the terahertz and normal Raman spectral regions that are indicative of any potential physical and

chemical changes in a given analyte. Using LFRS can provide a wealth of information about material properties in a fast and non-destructive manner. In the case of MOFs, LFRS can be used to investigate the binding properties of MOFs with analytes of interest, and to determine the nature of such binding.

Currently, there are two different mechanisms that explain the ionization process in MALDI-MS analysis. The first mechanism is based on the coupled chemical and physical dynamics (CCPD) model, which involves charge transfer during the excitation stage of a matrix-analyte mixture, resulting from exposure to laser power.[17] The second mechanism is based on a cluster model, which involves a combination of proton and intra-cluster charge transfer during the desolvation step of the MALDI process.[18] Accordingly, we designed our experimental approach for MOF-analyte interaction during the MALDI process to determine which ionization model is governing their ionization step. This report addresses the results of these mechanistic oriented experiments to help us determine the basic elements that contribute to the MALDI ionization process of the MOF-analyte mixtures. This base knowledge will aid in the development of efficient matrix-free desorption substrates for MS analyses. MOF materials have demonstrated superior homogenous and heterogeneous catalysis characteristics that will be transcribed to the MALDI process. Moreover, the diversity of MOFs can be envisioned to act as a selective desorption surface for specific groups of analytes without relying on the addition of external reagents.

1.2 Research focus and approach

The overall goal of this project is to study the mechanism of ionization, and determine the influence of factors that affect charge transfer process during the MALDI-MS ionization process. This year, we also addressed the binding affinity issue between MOF and analytes using LFRS to determine intermolecular and intramolecular changes between crystalline and amorphous states of the MOFs with different analytes. Those analytes studied were classified as acidic or basic compounds. Once we understand the basic properties of the MOF-analyte mixture, we will be able to determine how to design MOFs that can enhance the ionization efficiency for a wide range of compounds during MALDI-MS analysis. This knowledge-base will be used to design and develop a reliable, functionalized MOF substrate that can desorb biomolecules and selectively capture analytes of interest.

This study addressed the potential intramolecular and intermolecular changes for MOF-analyte mixtures using LFRS and MALDI-MS techniques. The MOFs used in the LFRS were UiO–66–COOH and UiO–66–NH_2, and the analytes used were pyridine, benzoic acid, cytidine, lauric acid, and guanine. More MOFs than those tested by the LFRS technique were used for the MALDI-MS analyses. Most of the MOFs were obtained from internal sources either through synthesis or leveraged from already funded projects that utilize MOFs. The structures for some of the MOFs and analytes used are shown in Figure 1.

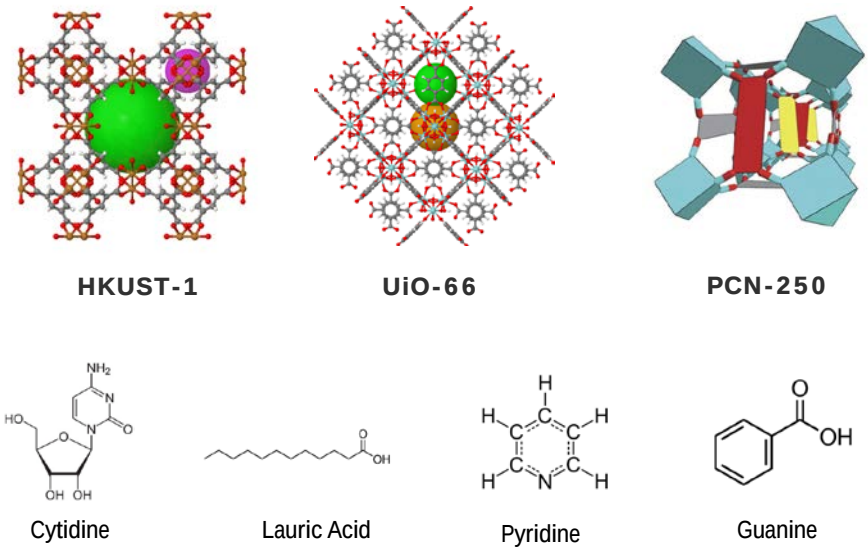

Figure 1. Representative MOFs used in this study including HKUST–1, modified UiO–66 with –COOH and –NH2 functional groups, and poly-coordinated network (PCN)–250 MOFs. The ball embedded in the MOF structures represent the relative pore sizes that are found within the structure of the MOFs. The analytes shown are cytidine, lauric acid, pyridine, and guanine.

2. MATERIALS AND METHODS

2.1 Metal-organic framework network synthesis

Various MOFs with different porosity and linker groups were used in this research project to determine their MALDI-MS performance. The selected MOFs were UiO–66, UiO–66–COOH, UiO–66–NH_2, Copper (II) Benzene–1,3,5–tricarboxylate (Cu-BTC/HKUST–1), PCN–250, PCN–250–Ni, and MOF–545 with different metal ions. All of these MOFs were synthesized elsewhere using the methods reported in the literature.[19–21] Briefly, the synthesis of UiO–66–NH_2 was performed by dissolving 1.5 g of $ZrCl_4$ and 1.5 g of 2–amino–1,4–benzene dicarboxylic acid in 180 mL of dimethylformamide at room temperature in a volumetric flask. The resulting mixture was preheated in an oven at 80 °C for 12 hours, and then held at 100 °C for 24 hours. After cooling to room temperature in air, the resulting solid was filtered and repeatedly washed with absolute ethanol for 3 days at 60 °C in a water bath. The resulting yellow powder was filtered and transferred for drying under vacuum at room temperature. All the tested MOF substrates were characterized and validated using appropriate techniques to ensure the formation of the desired chemical network and determine the surface coverage area, pore size, and volume.[22,23]

2.2 Low-frequency Raman spectroscopy measurements

The measurement of the low-frequency Raman scattering from a MOF sample was taken in stokes and antistokes vibrational spectra. The Raman spectroscopy experiments were performed using a WItec alpha300 R confocal Raman microscopy system. A 100X microscope objective in the Raman microscopy was used. A Rayshield™ notch filter was used to provide LFRS features (from a wavenumber of 10 cm^{-1}). The laser used was a solid-state laser with a wavelength of 532.1 nm. A wavelength of 532 nm was used for excitation, with a power of ~2 mW incident on the substrate. The Raman-scattered light was collected in the backscattering configuration and transmitted through a 100-µm slit to a 600 grooves/mm grating, which dispersed the light onto a thermoelectrically cooled CCD camera (WItec DV401 A). A spectral resolution of approximately 5 cm^{-1} was obtained. Spectra were acquired with 5-second to 10-second acquisition times. At a lower Raman shift, spurious contributions from the elastic line can be detected by measuring the scattering from a metal surface. In the anti-Stokes side, our spectrometer instrument response is better, which allowed us to measure the Raman spectrum down to 5 cm^{-1} of the Raman shift. The sample image in the entrance spectrometer plane was selected in such a way that the contribution from the glassy slide did not come into the spectrometer. No polarization selection was used.

2.3 Metal-organic frameworks as a matrix for MALDI mass spectrometry analysis

The standard sample preparation protocol for conventional MALDI-MS was used to perform all of the MALDI-MS analyses. Briefly, mass spectra were recorded with a MALDI Synapt® G2-S high-definition mass spectrometer (Waters®, Milford, MA). The buffer gas was adjusted using the default gas line connected to the hexapole ion guide compartment. The standard MALDI matrices and analytes kit were purchased from Sigma-Aldrich® (St. Louis, MO). The kit contains 1 mg of CA, 1 mg of 98 % SA, 4,6-dinitrophloroglucinol (97%), insulin (from bovine pancreas), ubiquitin (from bovine erythrocytes), and carbonic anhydrase (from bovine erythrocytes). Each kit also contained a sufficient amount of MALDI solvent composed of acetonitrile (ACN), high-performance liquid chromatography-grade water, and triflouroacetic acid (TFA). High-performance liquid chromatography-grade methanol (MeOH) and water were purchased from Thermo Fisher Scientific, Inc. (Waltham, MA). A saturated solution of the matrices was prepared at a concentration of 1 µg/mL and dissolved in 50 %:50 %:0.1 % ACN:water:TFA for CA and SA. The standard calibration analytes supplied in the same MALDI kit were diluted in the same solvent composition as that of the MALDI matrix. A MALDI target plate was spotted with 1–2 µL of the samples using a stacking or a mixing approach. The stacking approach consisted of spotting 1 µL of the matrix solution on the MALDI plate, allowing it to dry, followed by spotting with 1 µL of the analyte solution. The mixing approach utilized was the conventional MALDI spotting approach in which a 1:10 mixture of analytes:matrix is mixed prior to spotting on the MALDI substrate. Once mixed, 1–2 µL was spotted on the MALDI target plate and allowed to dry prior to insertion of the plate into the MALDI instrument. The same sample preparation protocol used in the conventional MALDI setup was also utilized with the tested MOFs. Every MOF:analyte mixture was spotted in triplicates on the MALDI target plate and allowed to dry prior to MS analysis.

A Waters® SYNAPT® G2-Si mass spectrometer equipped with a commercial MALDI source and operated with a Nd:YAG laser (355 nm, 200 Hz) was used. The mass spectral acquisitions were performed in positive ion mode using the following MALDI settings: 0 V on the sample plate holder, 10 V for extraction, 350 V for Hexapole, and 10 V for aperture. The laser power used was 250 amu for 25–50 % laser fluence and at a 200 Hz firing rate. The sample plate

voltage was held at 10 kV. Calibration was performed using polyethylene glycol adducts between 300 *m/z* and 3000 *m/z*.

The mass spectra were acquired using the reflectron positive ion mode with a reflectron voltage of 18 kV and an ion source lens voltage of 10 kV. Laser repetition rate was set at 20 Hz and increments of 20 laser shots were used to acquire the mass spectrum with a total of 100 shots per each mass spectrum. The MALDI instrument's vendor software was used to process the data and to obtain the MALDI mass spectra of the studied MOFs.

3. RESULTS AND DISCUSSIONS

3.1 Effect of functional groups on the LFRS analysis of UiO–66–COOH complexes

The LFRS was used to study the potential chemical and physical changes when the UiO–66–COOH was mixed with different acidic and basic analytes. The mixture was suspended in water and allowed to mix for 20 minutes using vortexing. The mixture was then centrifuged, the supernatant and pellet were aliquoted and deposited on aluminum oxide slides followed by LFRS analysis. Figure 2 shows the LFRS spectra for UiO–66–COOH, and its mixture with benzoic acid, lauric acid, cytidine, and guanine. The LFRS results showed that there is a subtle difference in the spectral signatures for the MOF-analyte mixtures in the normal Raman and terahertz regions. There is a Raman shift band for UiO–66–COOH–cytidine mixture at 954 cm^{-1} that is unique and not found spectra of the other UiO–66–COOH mixtures. The Raman spectral data also revealed different shifts for acidic and basic compounds, as reflected by the increased intensity for Raman shift signals in the region of 720 cm^{-1}, 954cm^{-1}, and 1010 cm^{-1}. Based on these LFRS data, we can observe that cytidine, guanine, and benzoic acid have certain chemical interactions with the UiO–66–COOH.

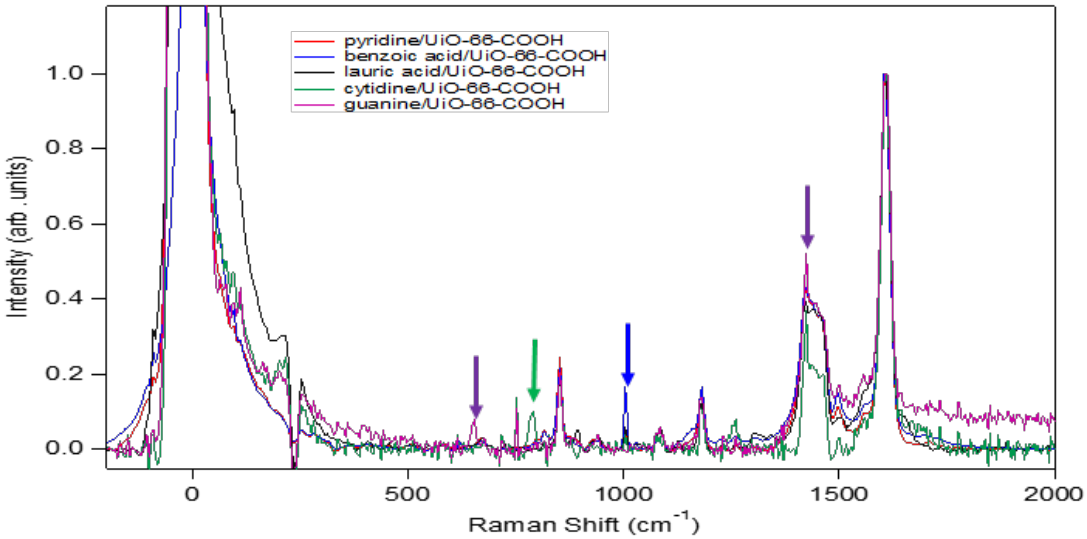

Figure 2. The LFRS spectra for UiO–66–COOH and different analytes. All samples were mixed with the MOF, UiO–66–COOH, and the resulting LFRS are stacked.

Moreover, there is a loss of crystalline structure as evident by the terahertz data at around 0 cm^{-1} Raman shift, which indicates a physical change to the structure of the UiO–66–COOH when mixed with analytes. The latter observation was further investigated by the LFRS analyses of pure UiO–66–COOH and its mixture with benzoic acid, as shown in Figure 3. This LFRS data showed that benzoic acid is crystalline when in its pure state, while it has amorphous features when mixed with the UiO–66–COOH. This subtle difference in the terahertz region supports the observation seen in the Raman shift for the UiO–66–COOH interaction with different analytes, in which all of these mixtures showed loss of crystalline structures as evident by loss of stokes and anti-stokes peaks in the terahertz region.

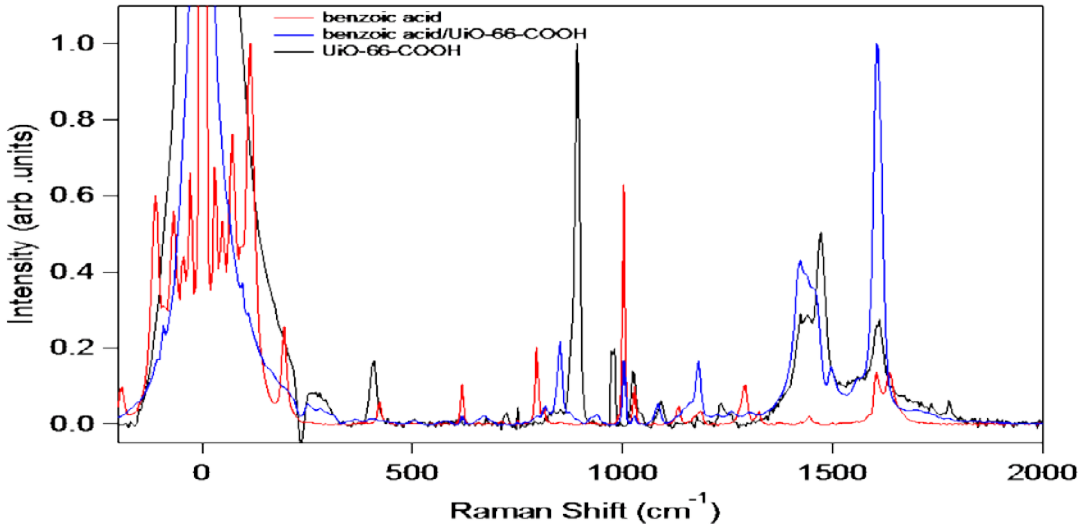

Figure 3. The LFRS spectra for UiO– 66– COOH, benzoic acid, and a mixture of UiO– 66– COOH and benzoic acid.

Moreover, Figure 3 shows the strong interaction between benzoic acid and UiO–66–COOH as evident in the Raman vibrational bands shift observed when comparing between the pure UiO–66–COOH MOF and its mixture with benzoic acid. It is noteworthy to mention that the normal Raman spectral features of pure benzoic acid also differ from the normal Raman spectral features of UiO–66–COOH–BA ones. However, there are some common vibrational Raman bands seen in the pure benzoic and the UiO–66–COOH–BA mixture. Overall, the LFRS analysis of UiO–66–COOH and mentioned acids and bases showed there is some acid/base chemistry taking place, as evidenced by more observable changes with basic compounds, and to a lesser extent, with acidic ones. This is based on the appearance of new vibrational bands for basic compounds in the normal Raman shift region as compared with only enhancement of common features for acidic compounds in the same spectral region.

3.2 Effect of functional groups on the LFRS analysis of UiO–66–NH_2 complexes

The LFRS was also used to characterize the potential interaction of the UiO–66–NH_2 with the studied analytes. The same LFRS procedure was followed as mentioned in section 3.1, Effect of functional groups on the LFRS analysis of UiO–66–COOH complexe. In this part of the study, the UiO–66–NH_2 is a modified UiO–66 structure with the addition of benzyl amine group as an active site on the MOF surface for potential interaction with the analyte molecules. The LFRS analysis experienced a large number of fluorescent signals in the background for the UiO–66–NH_2 that required longer photo bleaching times prior to data collection. The mixtures of UiO–66–NH_2 and guanine, lauric acid, or cytidine showed a dominant vibrational saturation that overlapped the normal Raman vibrational bands and thus are not included in this discussion. The LFRS results that showed satisfactory signal-to-noise ratio responses were the mixtures of UiO–66–NH_2 with pyridine or with benzoic acid.

The LFRS spectra of pure pyridine and benzoic acids suspended in pure H_2O solution were acquired. These LFRS results are shown in Figure 4. The benzoic acid and pyridine have several vibrational bands that are different in their respective normal Raman and the terahertz spectral regions. The benzoic acid has sharp vibrational bands in the terahertz while these bands are absent from the LFRS spectrum of pyridine. This is indicative of different structures that exist between these two compounds, with benzoic acid preserving its crystallinity as evident by sharp terahertz spectral peaks but not the case with pyridine. Moreover, the vibrational bands in normal Raman region showed that there are shifts between common features for the two compounds, while the C=C stretch band at 1620 cm^{-1} for pyridine has higher intensity and is shifted by several cm^{-1} for benzoic acid. However, the aromatic band at 1000 cm^{-1} is the same for both, but with a higher intensity for pyridine than that of benzoic acid.

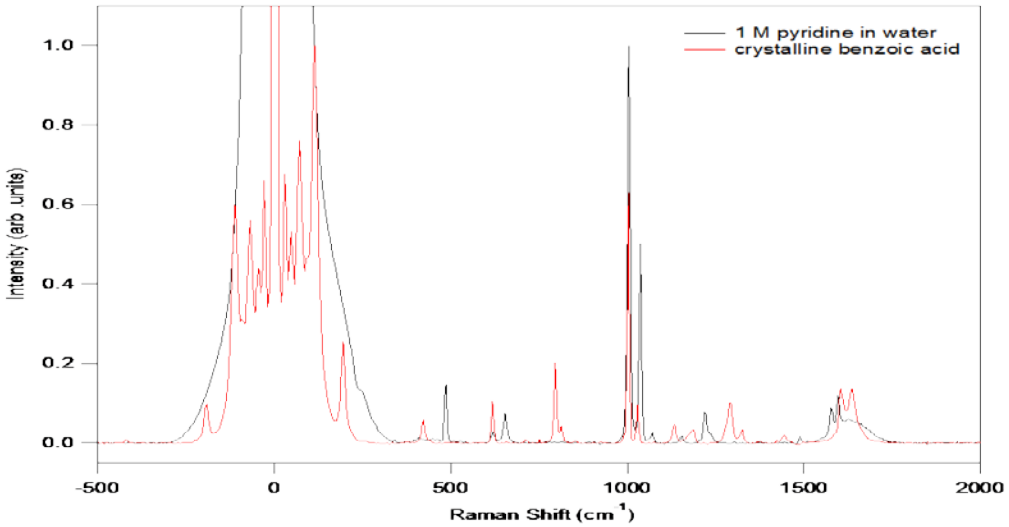

Figure 4. LFRS spectra comparing the normal Raman and terahertz regions for pure pyridine and benzoic acids suspended in water.

When either of these analytes mixed with UiO–66–NH_2, there was a shift for both in the normal and terahertz regions of the Raman spectra, as shown in Figure 5. Figure 5 represents the LFRS spectra for UiO–66–NH_2–pyridine and UiO–66–NH_2–benzoic acid mixtures. The normal Raman spectra for both compounds when mixed with UiO–66–NH_2 had different vibrational band changes for the two analytes, with the aromatic band for pyridine at 1000 cm^{-1} being reduced as compared to that of benzoic acid. Also, there a loss of crystallinity for benzoic acid when mixed with UiO–66–NH_2 as compared to the pure compound's terahertz spectral signature. This is indicative of structural changes that could be the result of interactions between the analyte molecules and UiO–66–NH_2. Also, the change in the normal Raman is supportive for such assumption because of the different vibrational bands that changed for the two compounds that indicate alteration of the molecular structure of the analyte upon mixing with UiO–66–NH_2.

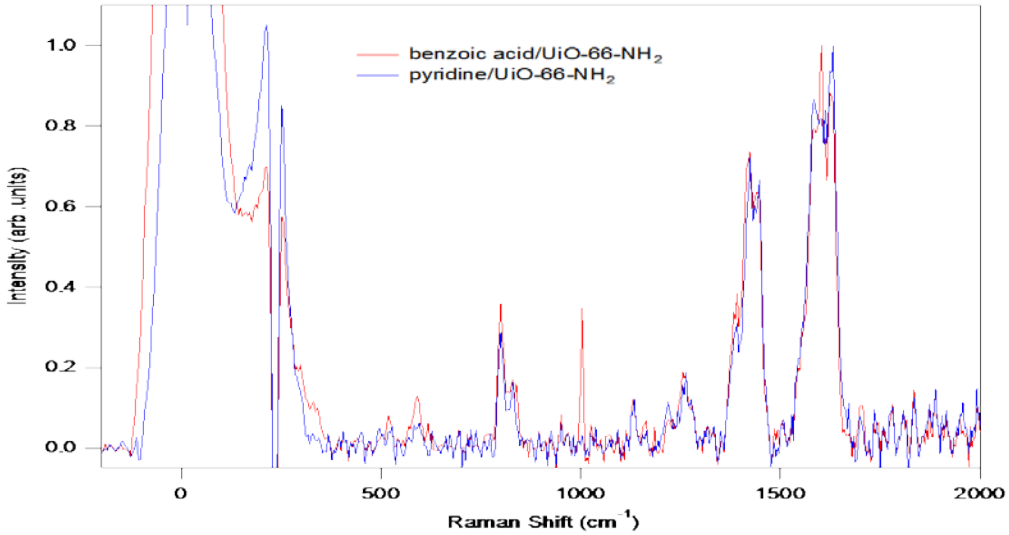

Figure 5. The LFRS spectra comparing the normal Raman and terahertz regions for pure pyridine and benzoic acids suspended with UiO–66–NH_2 MOF in pure water.

Overall, the LFRS, showed that there are differing degrees of chemical and physical changes for the studied compounds when mixed with different MOFs. Also, the MOF itself has subtle Raman spectral signatures and characteristics that need to be addressed in a separate study; such as the differing degree of fluorescence for amine-modified UiO–66 as compared to that of carboxylic acid modification of the same base MOF structure. It is worth mentioning that such a high fluorescence level of UiO–66–NH_2 was also observed using fluorescence emission spectroscopy.

3.3 Effect of the functional groups of MOFs on the MALDI-MS analysis of acidic and basic compounds

The MALDI-MS analyses were performed on mixtures of UiO–66, UiO–66–COOH, and UiO–66–NH_2 with the same analytes utilized in the LFRS spectral analyses. Different mixtures of the mentioned MOFs were prepared as described in section 2., Materials and methods, and then 1 µL of mixture suspension was deposited on the MALDI plates, allowed to dry, and followed by the MALDI-MS analysis. The MALDI-MS results showed that acidic compounds, lauric and benzoic acids, mixed with UiO–66–NH_2 have lower signal intensity as compared with their basic counter parts, pyridine and cytidine. The opposite results were observed when the same analytes were mixed with UiO–66–COOH. However, acidic compounds did have relatively higher signals when mixed with UiO–66, as shown in Figure 6. These MALDI-MS data indicate that there is an acid/base chemistry taking place in which proton exchange is occurring. When this acid/base chemistry is stronger between the analyte and the MOF, their interaction requires higher energy, and thus the MALDI-MS signal intensity is lower because of the higher energy requirement to break the binding between the MOF and the analytes. Such energy may not be sufficient during the MALDI ionization step. Moreover, the UiO–66 surface is considered acidic due to the presence of coordinated zirconium ions, which been reported as a hard Lewis acid, with Zr(IV) having a pK_a = 0.22.[19,20] Overall, the surface modification of the MOFs surface affected the MALDI-MS response when acidic and basic compounds were analyzed with the mentioned MOFs. Such differences in acidic and basic properties of the analytes, and to a lesser extent the MOFs, were the major factors that affected their respective MALDI-MS responses. In order to support such postulates, we will utilize other MOFs that have clear differences in their acidic and basic properties in order to determine if proton exchange among the mixtures of the MOFs and acidic and basic analytes is a dominant factor in determining the level of response during MALDI-MS analysis.

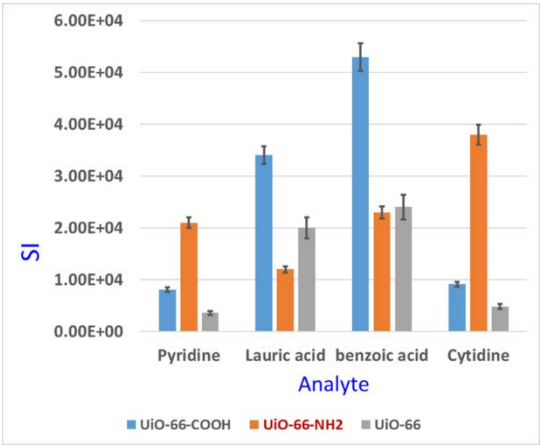

Figure 6. Comparative MALDI-MS response for three different MOFs, UiO–66, UiO–66–COOH, and UiO–66–NH_2, mixed with four different analytes—pyridine, cytidine, lauric acid, and benzoic acid.

3.4 Effect of the metal ions on the MOF structures and MALDI-MS analysis of acidic and basic compounds

We examined the MALDI-MS ionization response for mixtures of the acidic and basic compounds with MOFs containing different metal ions coordinated in their SBU. The MOFs used were HKUST-1, also known as Cu_3(1,3,5-benzenetricarboxylate=btc)$_2$/Cu–BTC, PCN–250, and PCN–250–Ni, and the same acidic compounds were used as reported in section 3.3. The Cu–BTC is a neutral coordination polymer that has dimeric cupric tetracarboxylate units and twelve carboxylate oxygen atoms from the two BTC ligands bound to four coordination sites for each of the three Cu^{2+} ions.[22] These copper complex units form a face-centered crystal lattice. Cu–BTC has main pores of approximately 0.9 nm in diameter and forms a cubic network (Figure 7). We also examined PCN MOFs, namely PCN–250 and PCN–250–Ni, with the former having iron ions in its SBU. The PCN–250 consists of six connected $Fe_2M(\mu_3–O)$ building blocks and rectangular tetratopic L22. The PCN–250 series of MOFs is very stable in various solvents. The pore size of its coordination channels ranges from 0.5 nm to 1.0 nm and consists of Zr_6 clusters linked by porphyrin ligands. Each Zr cluster is capped by m3–OH groups and connected to eight porphyrin ligands. The PCN–250 MOFs showed great chemical stability in various solvents, including a solution of hydrochloric acid.[23–26]

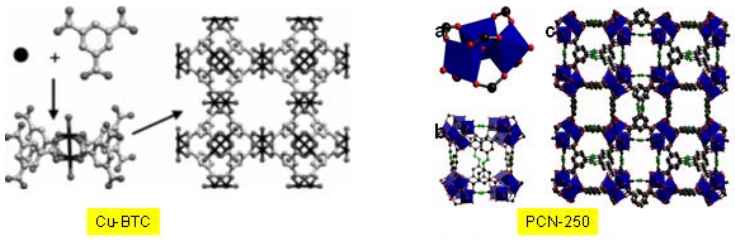

Figure 7. The 3D structures of Cu–BTC and PCN–250 MOFs used in the MALDI-MS analysis.

These MOF-analyte mixtures showed different MALDI-MS responses, as shown in Figure 8. The HKUST–1–acidic compound mixtures have higher MALDI-MS responses than those of the HKUST–1–basic mixtures. However, the basic analytes, mixed with PCN–250–Ni, have higher MALDI-MS responses than those of the PCN–250–Ni–acidic analytes mixtures. In fact, the acidic analytes mixed with PCN–250–Ni have negligible MALDI-MS responses as compared with their HKUST–1 and PCN–250 mixture counterparts. The trend in these MALDI-MS responses is not clear enough to draw a definite conclusion. Moreover, the acidic analytes had higher MALDI-MS responses when mixed with the PCN–250 MOF than with the PCN–250–benzoic acid mixture, showing the highest MALDI-MS response as compared to the other MOFs acidic and basic mixtures. While the PCN–250 mixtures have better MALDI-MS responses with the acidic compounds, the PCN–250–pyridine mixture also has a comparable MALDI-MS response to these PCN–250–acidic mixtures. This may not provide a definite conclusion on the impact of the presence of the metal ions in the MOF structures and its effect or contribution to the acid/base chemistry during the MALDI-MS process. However, if the Lewis acidity strength is considered as a factor, we find out that Cu ions, (HKUST–1) are stronger Lewis acids than that of Fe ions (PCN–250), with Ni ions (PCN–250–Ni), being the weakest Lewis acid.[27] If such factors have potential impact on the overall acid/base chemistry of the MOF, then the resulting MALDI-MS analysis response was, to a large extent, similar to the one observed with UiO–66 MOFs.

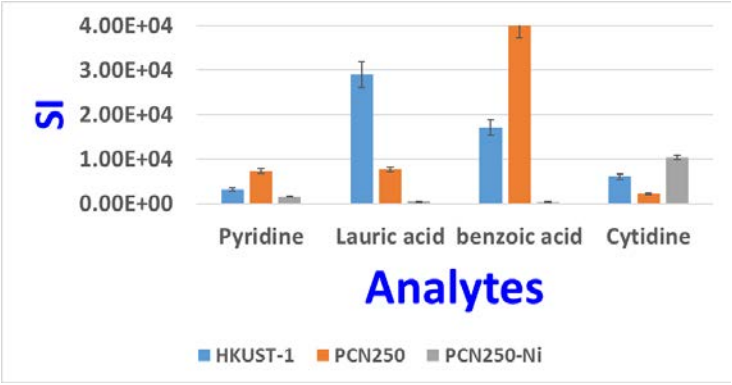

Figure 8. Comparative MALDI-MS response for three different MOFs, HKUST–1/Cu–BTC, PCN–250, and PCN–250–Ni, mixed with four different analytes—pyridine, cytidine, lauric acid, and benzoic acid.

3.5 Stability of MOFs during MALDI-MS analysis

The MALDI-MS response's stability of the MOFs was also investigated for MOF–545, MOF–545–Cu, PCN–250, and PCN–250–Ni. This set of experiments did show that all of the MOFs were stable in their MALDI-MS signal response with the same analyte mixtures. While MOF–545 showed great variability, it did not diminish its instrumental response, and high signal intensity was consistently obtained for this MOF even after eight days of analyzing the same mixture. Also, the signal intensity remained within the instrumental variance error. This increase in signal intensity for MOF–545 was not observed with the other MOFs or the conventional MALDI matrices. This could be due to increased residence time for the analyte molecules on MOF–545 that could be trapped inside the porous channel that have an equivalent size to that of the analyte, and could indicate that the binding of such an analyte with MOF–545 is kinetically driven (Figure 9). The other MOFs have similar responses and less variance than that of MOF–545. This could be due to many factors that are contributing to such an observation in the MALDI-MS analyses. Overall, the MALDI-MS response for the analyzed MOF-analyte mixtures indicates that, regardless of the analyte used in the mixture, reproducibility of the MOFs was evident over up to eight days of analyses. This is encouraging from the practical aspect of utilizing MOFs in MALDI analysis, as it is imperative to obtain reproducible responses using the same MOFs for repetitive runs. This reproducibility feature of the MOFs will reduce the consumption of matrix

material, as is the case with conventional MALDI-MS matrices, and eventually, when bound to the MALDI plate surface as a film, it may potentially result in more samples analyzed and an increased time of stability on the MALDI plate.

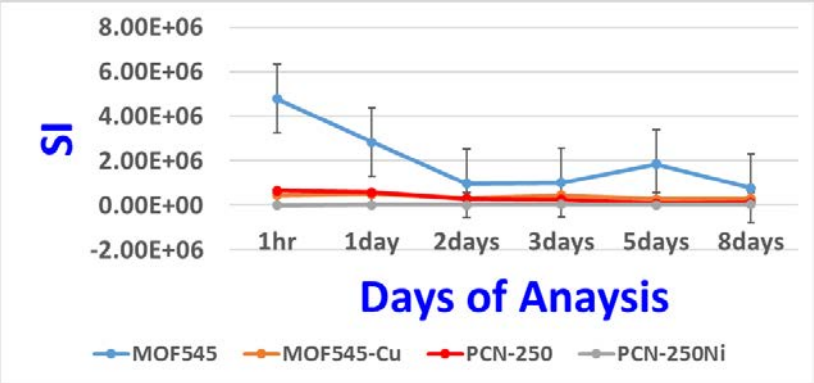

Figure 9. Reproducibility response of various MOFs (MOF–545, MOF–545–Cu, PCN–250, and PCN–250–Ni) during the MALDI-MS process.

4. CONCLUSIONS

The experimental results showed that MOF substrates can be utilized to establish understanding on the ionization mechanism during the MALDI-MS process. While there is still more work needed to confirm the findings, this is useful preliminary data toward understanding the MALDI-MS ionization mechanism—an important factor to guide design of the most efficient MOF to act as a universal MALDI matrix. Clearly, there is an acid/base chemistry taking place between the MOFs and the acidic and basic analytes. This mechanism needs to be explored further to determine and understand all the factors involved in the acid/base or proton exchange during the MOF-analyte MALDI-MS process. The MALDI response factor using different MOFs, such as Cu–BTC and MOF–545, showed significant improvement over utilizing the conventional MALDI matrices. There seem to be other factors that contribute to the acid/base chemistry, such as the functional groups on the MOF surfaces as seen in the UiO–66 series and nature of metal ions in the MOF structure (e.g., PCN–250 and Cu–BTC).

We are planning to better understand the ionization mechanism during utilization of MOF as a MALDI matrix. This will be done by choosing an additional set of analytes that offer similar bulk structures, but with different functional groups that affect their respective acid/base properties. Also, we will investigate the impact of immobilized conventional MALDI matrices on MOFs and the effect of such binding on their MALDI ionization efficiency. The determination of the charge transfer mechanism and its correlation with the MALDI desorption is beneficial—understanding will provide broader benefits to the utilization of MOFs in biocatalysis, biomimetics, and bioprocesses.

ACKNOWLEDGMENTS

The authors would like to acknowledge U.S. Army funding provided through the Edgewood Chemical Biological Center's Surface Science Initiative program.

REFERENCES

[1] Rosinke, B.; Strupat, K.; Hillenkamp, F.; Rosenbusch, J.; Dencher, N.; Krüger, U.; Galla, H.J. Matrix-assisted laser desorption/ionization mass spectrometry (MALDI-MS) of membrane proteins and non-covalent complexes. *J. Mass Spectrom.* **1995,** *30* (10), pp 1462–1468.

[2] Cohen, S.L.; Chait, B.T. Influence of matrix solution conditions on the MALDI-MS analysis of peptides and proteins. *Anal. Chem.* **1996,** *68* (1), pp 31–37.

[3] Fenselau, C.; Demirev, P.A. Characterization of intact microorganisms by MALDI mass spectrometry. *Mass Spectrom. Rev.* **2001,** *20* (4), pp 157–171.
[4] Chaurand P; Norris J.L.; Cornett, D.S.; Mobley, J.A.; Caprioli, R.M. New developments in profiling and imaging of proteins from tissue sections by MALDI mass spectrometry. *J.Prot. Res*. **2006,** *5* (11), pp 2889–900.
[5] Tanaka, K.; Waki, H.; Ido, Y.; Akita, S.; Yoshida, Y.; Yoshida, T.; Matsuo, T. Protein and polymer analyses up to m/z 100 000 by laser ionization time-of-flight mass spectrometry. *Rapid Comm. Mass Spec.* **1988,** *2* (8), pp 151–153.
[6] Demeure, K.; Quinton, L.; Gabelica, V.; De Pauw, E. Rational selection of the optimum MALDI matrix for top-down proteomics by in-source decay. *Ana. Chem.* **2007,** *79* (22), pp 8678–8685.
[7] Cohen, S.L.; Chait, B.T. Influence of matrix solution conditions on the MALDI-MS analysis of peptides and proteins. *Anal. Chem.* **1996,** *68* (1), pp 31–37.
[8] Dong, X.; Cheng, J.; Li, J.; Wang, Y. Graphene as a novel matrix for the analysis of small molecules by MALDI-TOF MS. *Anal. Chem.*, **2010,** *82* (14), pp 6208–6214.
[9] Farha, O.K.; Yazaydın, A.Ö.; Eryazici, I.; Malliakas, C.D.; Hauser, B.G.; Kanatzidis, M.G.; Nguyen, S.T.; Snurr, R.Q.; Hupp, J.T. De novo synthesis of a metal–organic framework material featuring ultrahigh surface area and gas storage capacities. *Nat. Chem.* **2010,** *2* (11), pp 944–948.
[10] Kaye, S.S.; Dailly, A.; Yaghi, O.M.; Long, J.R. Impact of preparation and handling on the hydrogen storage properties of Zn4O (1, 4-benzenedicarboxylate) 3 (MOF-5). *J. Am. Chem. Soc.* **2007,** *129* (46), pp 14176–14177.
[11] Kreno, L.E.; Leong, K.; Farha, O.K.; Allendorf, M.; Van Duyne, R.P.; Hupp, J.T. Metal–organic framework materials as chemical sensors. *Chem. Rev.* **2012,** *112* (2), pp 1105–1125.
[12] DeCoste, J.B.; Peterson, G.W. Metal-organic frameworks for air purification of toxic chemicals. *Chem. Rev.* **2014,** *114* (11), pp 5695–5727.
[13] Lee, J.; Farha, O.K.; Roberts, J.; Scheidt, K.A.; Nguyen, S.T.; Hupp, J.T. Metal–organic framework materials as catalysts. *Chem. Soc. Rev.* **2009,** *38* (5), pp 1450–1459.
[14] Colaianni, S.M.; Nielsen, O.F. Low-frequency Raman spectroscopy. *J. Mol. Struct.* **1995,** *347*, pp 267–283.
[15] Puretzky, A.A.; Liang, L.; Li, X.; Xiao, K.; Sumpter, B.G.; Meunier, V.; Geohegan, D.B. Twisted MoSe2 bilayers with variable local stacking and interlayer coupling revealed by low-frequency Raman spectroscopy. *ACS Nano.* **2016,** *10* (2), pp 2736–2744.
[16] Ferrari, A.C.; Basko, D.M. Raman spectroscopy as a versatile tool for studying the properties of graphene. *Nat. Nano.* **2013,** *8* (4), pp 235–246.
[17] Kirmess, K.M.; Knochenmuss, R.; Blanchard, G.J.; Kinsel, G.R. MALDI ionization mechanisms investigated by comparison of isomers of dihydroxybenzoic acid. *J. Mass Spectrom.* **2016,** *51* (1), pp 79–85.
[18] Knochenmuss, R. Ion formation mechanisms in UV-MALDI. *Analyst.* **2006,** *131* (9), pp 966–986.
[19] Wadas, T.J.; Wong, E.H.; Weisman, G.R.; Anderson, C.J. Coordinating Radiometals of Copper, Gallium, Indium, Yttrium and Zirconium for PET and SPECT Imaging of Disease. *Chem Rev.* **2010,** *110* (5), pp 2858–2902.
[20] Shih, Y.H.; Chien, C.H.; Singco, B.; Hsu, C.L.; Lin, C.H.; Huang, H.Y. Metal–organic frameworks: new matrices for surface-assisted laser desorption–ionization mass spectrometry. *Chem. Comm.* **2013,** *49* (43), pp 4929–4931.
[21] Cavka, J.H.; Jakobsen, S.; Olsbye, U.; Guillou, N.; Lamberti, C.; Bordiga, S.; Lillerud, K.P. A new zirconium inorganic building brick forming metal organic frameworks with exceptional stability. *J. Am. Chem. Soc.* **2008,** *130* (42), pp 13850–13851.
[22] An, J.; Farha, O.K.; Hupp, J.T.; Pohl, E.; Yeh, J.I.; Rosi, N.L. Metal-adeninate vertices for the construction of an exceptionally porous metal-organic framework. *Nat. Comm.* **2012,** *3*, p 604.
[23] Morris, W.; Volosskiy, B.; Demir, S.; Gándara, F.; McGrier, P.L.; Furukawa, H.; Cascio, D.; Stoddart, J.F.; Yaghi, O.M. Synthesis, structure, and metalation of two new highly porous zirconium metal–organic frameworks. *Inorg. Chem.*, **2012,** *51* (12), pp 6443–6445.
[24] Mondloch, J.E.; Bury, W.; Fairen-Jimenez, D.; Kwon, S.; DeMarco, E.J.; Weston, M.H.; Sarjeant, A.A.; Nguyen, S.T.; Stair, P.C.; Snurr, R.Q.; Farha, O.K. Vapor-phase metalation by atomic layer deposition in a metal-organic framework. *J. Am. Chem. Soc.* **2013,** *135* (28), pp 10294–10297.
[25] Kandiah, M.; Nilsen, M.H.; Usseglio, S.; Jakobsen, S.; Olsbye, U.; Tilset, M.; Larabi, C.; Quadrelli, E.A.; Bonino, F.; Lillerud, K.P. Synthesis and stability of tagged UiO-66 Zr-MOFs. *Chem. Mat.* **2010,** *22* (24), pp 6632–6640.
[26] Mondloch, J.E.; Karagiaridi, O.; Farha, O.K.; Hupp, J.T. Activation of metal–organic framework materials. *Cryst. Eng. Comm.* **2013,** *15* (45), pp 9258–9264.
[27] Lawrance, G.A. Reactions Involving the Metal Oxidation State. In Introduction to Coordination Chemistry. John Wiley & Sons, Ltd.: New York, 2010, p 191.

Probing the connection between low-frequency vibrational modes and macroscopic structural behavior of metal-organic frameworks

Neal D. Kline[a*], Ann M. Ploskonka[b], Ivan O. Iordanov[a], Craig K. Knox[b], Gregory W. Peterson[a]
[a]U.S. Army Edgewood Chemical Biological Center, Research & Technology Directorate, 5183 Blackhawk Rd, Aberdeen Proving Ground, MD 21010
[b]Leidos, Inc., P.O. Box 68, Gunpowder Branch, Aberdeen Proving Ground, MD 21010

ABSTRACT

Metal-organic frameworks are hybrid porous materials that have been widely studied due to their promising applications in fields such as gas storage, catalysis, and sensing. Among the variety of reported metal-organic frameworks is a sub group that have been observed to display large scale structural flexibility. The flexibility in the metal-organic framework corresponds to a fully reversible transition between different framework conformations triggered by external stimuli including temperature, pressure, and the guest molecule. This study will investigate the MIL-53 family of metal-organic frameworks by systematically varying the components (metal node, functionalization of linker) and examining the collective vibrations of the frameworks (located in the THz region) using low-frequency Raman spectroscopy. The Al^{3+}, Fe^{3+}, Cr^{3+} derivatives of the MIL-53 metal-organic frameworks were synthesized at Edgewood Chemical Biological Center along with a commercially available sample of the Al^{3+} derivative being obtained from Sigma-Aldrich®. The low-frequency Raman spectra was collected on the metal-organic framework samples and clearly resolved bands in the Al^{3+} derivative were observed indicating the presence of lattice vibrations of the metal-organic framework.

Keywords: metal organic frameworks, lattice dynamics, terahertz vibrations, low-frequency Raman spectroscopy, MIL-53

1. INTRODUCTION

Metal-organic frameworks (MOF) are porous crystalline materials with metal ions or clusters as the nodal points and organic linkers regularly arranged in between them. The periodic and porous structures give MOFs advantages for applications such as gas storage, gas separations, catalysis and sensing.[1,2] While MOFs are similar to other microporous materials, such as inorganic zeolites and activated carbon, they have larger surface areas and can be processed at much lower temperatures. MOFs can also be built from a wider range of constituents allowing the ability to fine tune structural aspects of the material or a specific interaction with an adsorbate. However, in contrast to the rigid structure of zeolites and carbon materials, a limited number of MOFs display large scale structural flexibility upon the application of external stimuli that can drastically alter their characterisctics.[3,4]

This unique large scale structural flexibility of MOFs has stimulated research to specifically study the phenomenon. Several techniques have been used including X-ray diffraction methods, nuclear magnetic resonance (NMR), and infrared (IR)/Raman.[5,6] These methods are usually implemented as an *in situ* characterization approach performed by applying an external stimuli such as introducing guest molecules, applying pressure or temperature and probing the MOF under the influence of the stimuli.

Recently, investigations studying the low-frequency vibrational modes of the zeolitic imidazolate framework family of MOFs located in the THz region (0.1–10 THz, 3–300 cm^{-1}) have been performed.[7–9] The authors discovered that the low-frequency modes of MOFs showed the standard lattice vibrations but also physical properties unique to the particular MOFs included in the study. It also allowed the authors to identify possible phase change mechanisms through which the framework may destabilize, distort, or collapse when mechanical force is applied. Several techniques were used to uncover these low-frequency vibrational modes including inelastic neutron scattering, low-frequency Raman spectroscopy, synchrotron radiation far-IR absorption spectroscopy, and terahertz time domain spectroscopy. The experimental investigations were also supported by theoretical density functional theory (DFT)

calculations in order to help assign the spectra that were obtained. Combining spectroscopic techniques capable of reaching the THz region with theoretical calculations to model the low-frequency vibrations provides an approach for a comprehensive description of MOF framework properties much more efficiently than current methods.

The structural flexibility of MOFs is associated with an anisotropic stiffness of the crystal pore which allows the material to be deformed easily in one direction but not in another. Because of this directional flexibility, the barrier between structural conformations is small allowing the material to transition to different conformations. Ferey and Serre[4] have identified a number of structural characteristics that are indicative of framework flexibility including the nature of the organic ligand, the characteristics of the secondary building unit present in the MOF, the periodic structure of the MOF, and the coordination of the metal nodes. There are also different categories of flexibility which generally illustrate the dynamic structural transformation that the MOF undergoes when exposed to the proper stimulus. One category of flexibility that will be investigated in this study is breathing (Figure 1).

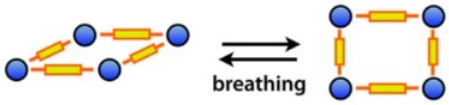

Figure 1. Structural flexibility in MOFs illustrated by the breathing phenomenon in MIL-53.[11]

Breathing is defined as reversible structural transitions between different framework conformations of a MOF during which the substantial displacement of atoms of the framework is accompanied by a change in unit cell volume.[2] In breathing, characteristic distances and angles of the unit cell change and the crystallographic space groups of the two distinct phases (narrow pore and large pore) may be different. The representative example of this kind of flexibility is the MIL-53 family of MOFs ([M(bdc)(OH)] where bdc = 1,4-benzenedicarboxylate and M = Al^{3+}, Fe^{3+}, Cr^{3+}, Sc^{3+}, Ga^{3+}, In^{3+}.

The present study reports the results of a low-frequency analysis of the Al^{3+}, Fe^{3+}, Cr^{3+} derivatives of the MIL-53 family. Previous findings have indicated that changing the metal node of the MOF can affect its macroscopic structural behavior and also that the low-frequency vibrations are intrinsically linked to observed physical phenomena such as breathing. Our primary hypothesis is that the differences observed in the overall structural behavior of the MIL-53 MOFs from changing the metal node originate in the lattice dynamics of the MOF, which can be studied using spectroscopic techniques capable of reaching very low frequencies (< 100 cm^{-1}). We can then use differences in the low-frequency spectra of these MOFs to help explain their differing structural behavior.

2. EXPERIMENTAL PROCEDURE

2.1 Metal-organic framework synthesis

The various MIL-53 MOFs were synthesized according to methods reported in the literature. All chemicals were obtained from Sigma-Aldrich® and were used without further purification.

2.1.1 MIL-53 Al^{3+}

To a Parr bomb was added terephthalic acid (0.56 eq.) and aluminum chloride hexahydrate (0.493 g)* 5 mL of water was slowly added to the combined solids. Solution was sonicated for approximately 15 minutes before being placed in a 150 °C oven for 16 hours. Solution was filtered, washed with water (5 mL x 5 mL), dried, and collected. Solid was placed in a Parr bomb with 5 mL dimethylformamide (DMF) and heated to 150 °C overnight. Solution was filtered and precipitate was washed with DMF (3 mL x 5 mL), dried, and collected.[11] Basolite® A100 (MIL-53 Al^{3+}) was also obtained from Sigma-Aldrich® and was used after the activation procedure was performed on the ordered sample.

2.1.2 MIL-53 Cr^{3+}

To a 20-mL scintillation vial was added chromium (III) nitrate (0.601 g), terephthalic acid (0.350 g), and hydrofluoric acid (30 mg, 26 µL). Water was added slowly to the mixture and solution was stirred for 30 minutes at room temperature. Solution was transferred to Parr bomb and heated in 220 °C oven for 3 days. Solution was removed from the oven and allowed to cool before the precipitate was collected by vacuum filtration and dried in drying oven.[12]

2.1.3 MIL-53 Fe^{3+}

To 5 mL of DMF in a Parr bomb Teflon™ liner was added iron (III) chloride (0.270 mg) and terephthalic acid (0.233 g). Solution was sonicated for 5 minutes before being placed in a 150 °C oven for 6 hours. Solution was then filtered and precipitate was washed with methanol (3 mL x 5 mL) before being dried and collected.[13]

2.2 MOF characterization

2.2.1 X-Ray diffraction

X-Ray diffraction (XRD) data were obtained on a Rigaku® Miniflex 600 diffractometer equipped with a Rigaku® Smart Lab® D/teX Ultra Detector. Samples were analyzed at 40 kV and 15 mA using Cu–Kα radiation (λ = 1.5418 Å) over a range of 3–50 2θ at a scan rate of 5° per minute, utilizing zero background disks. Composite samples were mounted to the zero background disks utilizing double sided tape. A background correction was performed in the Rigaku PDXL software (Version 2.1.3.6) to account for the tape.

2.2.2 Attenuated total reflectance Fourier-transform IR spectroscopy

Attenuated total reflectance (ATR) Fourier-transform IR spectroscopy (FTIR) spectra were taken using a Bruker® TENSOR™ 27 FTIR with a Bruker® PLATINUM ATR accessory equipped with a single reflection diamond crystal. Sixteen scans were averaged over a range of 4000 cm^{-1} to 600 cm^{-1} with a resolution of 4 cm^{-1}.

2.2.3 Low-frequency Raman measurements

Samples for Raman analysis were prepared by casting thin films of the various MIL-53 MOFs on aluminum coated slides. Raman spectra were recorded using an Alpha 300R confocal microscope with a 100X objective and with a 532-nm laser with the following laser power for each sample: 6.0 mW for MIL-53 Al^{3+}, 150.0 µW for MIL-53 Fe^{3+}, and 400.0 µW for MIL-53 Cr^{3+}. Raman spectra were acquired with a 20-second integration time with 5 co-added spectra. Data for high frequency (-250–2000 cm^{-1}) portion of Raman spectra was recorded using the 1,200 line/mm grating, while the low-frequency data (-200–1000 cm^{-1}) was recorded using the 1,800 line/mm grating.

2.3 Theoretical methods

Periodic solid-state (plane-wave) DFT using geometry optimizations and phonon dispersion calculations in CRYSTAL14 and Quantum Espresso, as well as Born-Oppenheimer *ab initio* molecular dynamics simulations (AIMD) in CP2K—which employs a hybrid of plane waves and Gaussian (molecular) basis sets—have been used to calculate the IR and Raman spectra of a 304-atom unit cell (monoclinic crystal structure with a, b, c, α, β, γ cell parameters = 20.217 Å, 11.348 Å, 14.872 Å, 90°, 90°, 77.408°, respectively) of MIL-53 Al^{3+} MOF at room temperature (Figure 2). The PBE functional was used with norm-conserving pseudopotentials and a 400 Ry plane-wave cutoff. The Gaussian basis sets were double-ζ with polarization functions optimized for molecular calculations. Dispersion was included using the Grimme D3 semi-empirical approach, and the AIMD trajectories were obtained using the Nose-Hoover thermostat.

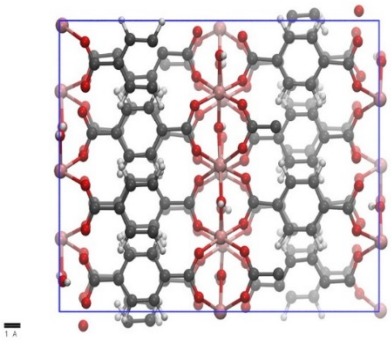

Figure 2. Unit cell of MIL-53 Al^{3+}.

The IR spectrum was computed using the Fourier-transform of the autocorrelation function of the total system dipole moment, μ, obtained from a 40-picosecond long (with a 0.5-femtosecond time step) AIMD trajectory. The spectrum is given by

$$I(\omega) = \frac{\hbar\omega^2}{2\pi k_B T}\int dt\, e^{-i\omega t} < \mu(0)\mu(t) >, \quad (1)$$

where, k_B is the Boltzmann constant, $\hbar$ is the Planck constant divided by 2π, ω is frequency, T is temperature, t is time, $I(\omega)$ is the oscillator strength (arbitrary intensity), and $\mu(0)\mu(t)$ is a dot product between the dipole moment vectors at time = 0 and time = t, which is averaged over all such time intervals of length t in the trajectory. Calculation of the Raman spectrum will be performed analogously by replacing the dipole moment vectors, $\mu(0)\mu(t)$, with polarizability tensors, $\alpha(0):\alpha(t)$, and replacing the dot product with the double dot product or scalar product of two tensors. Calculation of $I(\omega)$ was done using Visual Molecular Dynamics (VMD) with the IR Spectral Density Calculator plugin. Effective atomic partial charges were estimated using two different methods: Mulliken population analysis and maximally-localized Wannier centers. Dipole moment vectors were calculated by summing the product of these partial charges and the Cartesian coordinates (x, y, z) of the atoms. Polarizabilities (α) will be calculated by applying an external electric field in each direction, ε, and computing the resulting change in the dipole moment of each sampled time step in the MD trajectory. The polarizability tensor is defined as the change in the dipole moment vector with respect to the electric field vector ($d\mu/d\varepsilon$), in each of the nine combinations (rigorously accounting for possible anisotropic effects) of the respective Cartesian dimensions (xx, yy, zz, xy, yx, xz, zx, yz, zy), and can be obtained through numerical differentiation. This calculation method includes the effects of anharmonicity.

3. RESULTS AND DISCUSSION

The MIL-53 family of MOFs are composed of terephthalate anions and trans chains of metal (III) octahedral sharing OH groups, creating three-dimensional framework with a one-dimensional pore channel system. Their formulas are $M^{III}(OH)\cdot[O_2C\text{-}C_6H4\text{-}CO_2]H_2O$ (M^{III}=Al, Cr, Fe) for the hydrated forms (MIL-53lt; "lt"=low temperature or "np"=narrow pore) are $M^{III}(OH)\cdot[O_2C\text{-}C_6H_4\text{-}CO_2]$ for the dehydrated compounds (MIL-53ht; "ht"=high temperature or "lp"=large pore). XRD and FTIR (Figures 3–5) data were collected on the activated MOFs from the Edgewood Chemical Biological Center and Sigma-Aldrich® and compared to literature sources to confirm their identity.[14,15] The FTIR spectra of the Fe^{3+}, Cr^{3+}, and Al^{3+} derivatives all exhibit vibrational bands in the 1400–1700 cm^{-1} region which indicates the presence of a carboxylic acid functionality. The vibrational bands around 1580 cm^{-1} and 1403 cm^{-1} are characteristic of the $–CO_2$ asymmetric and symmetric stretching, respectively. The Al^{3+} derivative also has a peak at ~3600 cm^{-1} corresponding to the O–H stretching mode of water, but does not appear to be in the Cr^{3+} or Fe^{3+} spectra.

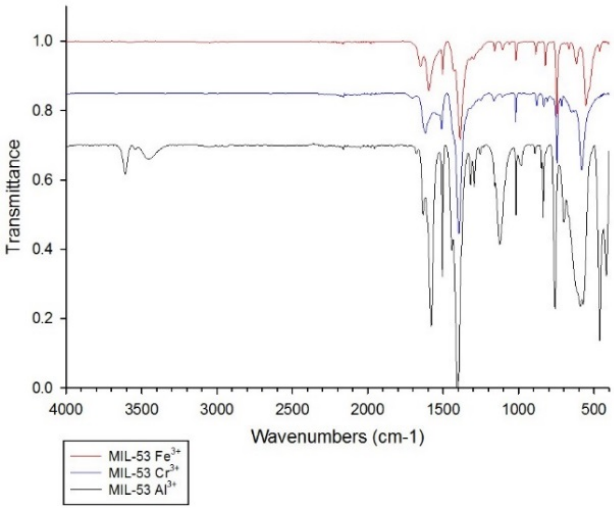

Figure 3. FTIR data for the Fe^{3+}, Cr^{3+}, and Al^{3+} MIL-53 analogues.

Further confirmation of the synthesis of the MIL-53 compounds was done by collecting XRD data (Figures 3 and 4) of the synthesized powders and comparing to literature. The XRD was performed on the powder samples after activation which would render the MOFs in the hydrated "np" form. The Cr^{3+} and Fe^{3+} analogues are depicted in Figure 3 and don't appear to correlate well to what has been reported in the literature; while the Edgewood Chemical Biological Center-synthesized Al^{3+} sample in Figure 4 matches well with the "np" form and the Sigma-Aldrich® Al^{3+} sample matches with the "lp" form.[14–16] The XRD pattern of the "np" form should look roughly the same for the different MIL-53 analogues as the main difference between the structures will be the metal center with minor changes in the structural parameters due to differing metal size. The Sigma-Aldrich® MIL-53 Al^{3+} sample appearing in the "lp" form is puzzling as the sample was packaged after activation and the activation procedure was repeated once more after it was received; the MOF should be presenting in the "np" form.

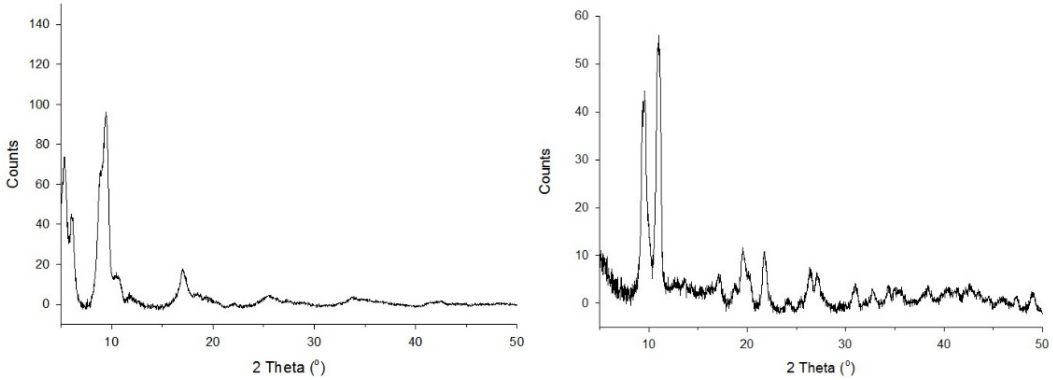

Figure 4. XRD data for the Cr^{3+} (right panel) and Fe^{3+} (left panel) derivatives of MIL-53.

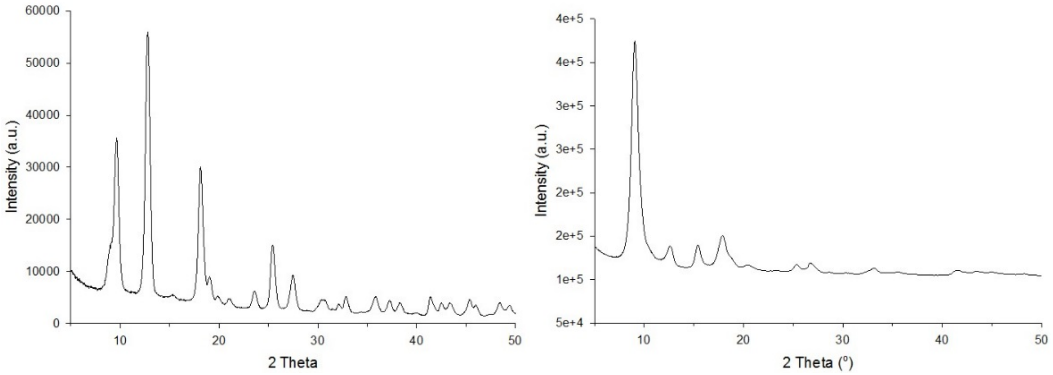

Figure 5. XRD data for the Al^{3+} analogue of MIL-53 obtained from the Edgewood Chemical Biological Center (left panel) and Sigma-Aldrich® (right panel).

The Sigma-Aldrich® MIL-53 Al^{3+} sample adopting a different form is due to an electrochemical synthetic procedure being used (as opposed to the hydrothermal route used at the Edgewood Chemical Biological Center) to allow the scaling up the amount of MOF produced. Joaristi et al.[17] studied the electrochemical synthesis of several different MOFs, one of which was Al^{3+} MIL-53 and discovered that the electrochemically synthesized version of Al^{3+} MIL-53 adopted the "lp" configuration as opposed to "np". Curiously, they also reported that the Al^{3+} MIL-53 that was electrochemically synthesized did not display any breathing behavior that is typical of this family of MOFs. The authors speculated that this was due to the faster kinetics of the electrochemical synthesis producing inter-grown MOF particles containing a large density of grain boundaries. The presence of the grain boundaries within a single particle would stabilize the structure and impede the breathing. The authors cite the fact that kinetics of formation strongly influence the degree of structure opening to support their speculation that samples synthesized in the presence of DMF and at higher temperatures (faster reaction) show a high fraction of "lp" over "np" while samples synthesized in pure water and at low temperatures (slower reaction) are mostly in the "np" form.

The Raman spectra for the Al^{3+}, Fe^{3+}, Cr^{3+} analogues of MIL-53 are shown in Figure 4. The low-frequency data (< 200 cm^{-1}) collected is indicative of the lattice vibrations of the MOF while the higher frequency data details chemical information. In fact, from about 500 cm^{-1} on up the Raman spectra of the different analogues is dominated by signatures from the 1,4-benzenedicarboxylate linker indicating a very high chemical similarity between the different species. However, in the low-frequency spectra there are dramatic differences between the MIL-53 analogues. Both the Cr^{3+} and Fe^{3+} have very broad spectra with no discernible features below 200 cm^{-1} indicating the absence of collective vibrations of the crystal lattice. This data in conjunction with the poor correlation of the XRD data in Figure 3 to what has been reported suggests that these particular MOFs may be of low quality.

The Al^{3+} MOF prepared at the Edgewood Chemical Biological Center has two distinct features at 52 cm^{-1} and 92 cm^{-1}, while the Sigma-Aldrich® Al^{3+} has a doublet with peaks at 27 cm^{-1} and 40 cm^{-1}. As was mentioned previously, the Al^{3+} MOF obtained from Sigma-Aldrich® was synthesized using an electrochemical method (as opposed to hydrothermal) and the different synthetic method resulted in the MOF adopting a different structural form and the supposed absence of breathing which was determined through in situ monitoring of the MOF using XRD in the presence of toluene, methanol, and CO_2. The hydrothermally synthesized MOF shows cell expansion and contraction which can be observed by probing the MOF with XRD at different points along the isotherm. The low-frequency data collected in Figure 5 shows that the lattice vibrations of the Sigma-Aldrich® MOF are drastically different than those of the Edgewood Chemical Biological Center MOF indicating very different lattice vibrations between the two MOFs. Theoretical modeling is currently underway in order to help with the assignment of the low-frequency data and explain the fascinating phenomena that is occurring with these MOFs.

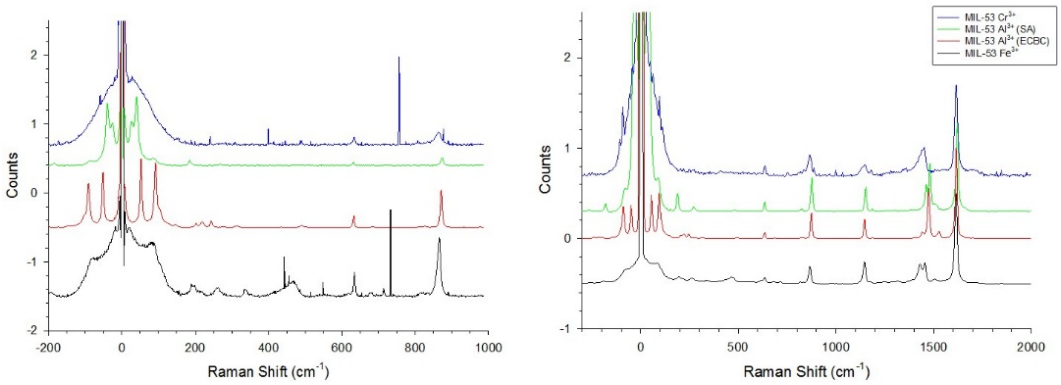

Figure 6. Low-frequency (left panel) and high-frequency (right panel) Raman data for the different MIL-53 analogues.

4. CONCLUSIONS

Several MIL-53 derivatives were synthesized and characterized in this investigation to study their low-frequency vibrational modes. The low-frequency Raman data collected shows that there are signatures related to collective lattice vibrations for the MIL-53 series of MOFs. The Al^{3+} MIL-53 derivative was successfully synthesized using hydrothermal synthetic procedure while an electrochemically synthesized sample was obtained from Sigma-Aldrich® and their low-frequency data compared. Due to the different synthetic procedures that were used to prepare the Edgewood Chemical Biological Center and Sigma-Aldrich® MOFs, the low-frequency spectra of the MOFs are quite different indicating distinct lattice vibrations present in each species. Initial theoretical results have predicted the IR spectra of MIL-53 Al^{3+}, more modeling is underway will help to assign the Raman spectra and elucidate the lattice dynamics of these species.

ACKNOWLEDGMENTS

The authors would like to acknowledge U.S. Army funding provided though the Edgewood Chemical Biological Center's Surface Science Initiative.

REFERENCES

[1] Furukawa, H.; Cordova, K.E.; O' Keefe, M.; Yaghi, O.M. The Chemistry and Applications of Metal-Organic Frameworks. *Science.* **2013,** *341* (6149), pp 1230444-1–12340444-11.

[2] Kuppler, R. J.; Timmons, D. J.; Fang, Q.; Makal, T. A.; Young, M. D.; Yuan, D.; Zhuang, W.; Zhou, H. Potential Applications of metal-organic frameworks. *Coord. Chem. Rev.* **2009,** *253* (23–24), pp 3042–3066.

[3] Schneeman, A.; Bon, V.; Schwedler, I.; Senkovska, I.; Kaskel, S.; Fischer, R.A. Flexible metal-organic frameworks. *Chem. Soc. Rev.* **2014,** *43* (16), pp 6062–6096.

[4] Ferey, G.; Serre, C. Large breathing effects in three-dimensional porous hybrid matter: facts, analyses, rules, and consequences. *Chem. Soc. Rev.* **2009,** *38* (5), pp 1380-1399.

[5] Miller, S.R.; Wright, P.A.; Devic, T.; Serre, C.; Ferey, G.; Llewellyn, P.L.; Denoyel, R.; Gaberova, L.; Filinchik, Y. Single Crystal X-ray Diffraction Studies of Carbon Dioxide and Fuel-Related Gases Adsorbed on the Small Pore Scandium Terephthalate Metal Organic Framework, $Sc_2(O_2CC_6H_4CO_2)_3$. *Langmuir.* **2009,** *25* (6), pp 3618–3626.

[6] Klein, N.; Herzog, C.; Sabo, M.; Senkovska, I.; Getzschmann, J.; Paasch, S.; Lohe, M.R.; Brunner, E.; Kaskel, S. Monitoring adsorption-induced switching by ^{129}Xe NMR spectroscopy in a new metal–organic framework $Ni_2(2,6\text{-ndc})_2(dabco)$. *Phys. Chem. Chem. Phys.* **2010,** *12* (37), p 11778.

[7] Ryder, M.R.; Civalleri, B.; Bennett, T.D.; Henke, S.; Rudic, S.; Cinque, G.; Fernandez-Alonso, F.; Tan, J. Identifying the Role of Terahertz Vibrations in Metal-Organic Frameworks: from Gate-Opening Phenomenon to Shear-Driven Structural Destabilization. *Phys. Rev. Lett.* **2014,** *113* (21), p 215502.

[8] Ryder, M.R.; Civalleri, B.; Cinque, G.; Tan, J. Discovering connections between terahertz vibrations and elasticity underpinning the collective dynamics of HKUST-1 metal-organic framework. *Cryst. Eng. Comm.* **2016,** *18* (23), pp 4303–4312.

[9] Tan, N.Y.; Ruggiero, M.T.; Orellana-Tavra, C.; Tian, T.; Bond, A.D.; Korter, T.M.; Fairen-Jimenez, D.; Zeitler, J.A. Investigation of the terahertz vibrational modes of ZIF-8 and ZIF-90 with terahertz tim-domain spectroscopy. *Chem. Comm.* **2015,** *51* (89), pp 16037–16040.

[10] Coudert, F.; Boutin, A.; Fuchs, A.; Neimark, A.V. Adsorption Deformation and Structural Transitions in Metal-Organic Frameworks: From the Unit Cell to the Crystal. *J. Phys. Chem. Lett.* **2013,** *4* (19), pp 3198–3205.

[11] Ahnfeldt, T. Gunzelmann, D.; Loiseau, T.; Hirsemann, D.; Senker, J.; Ferey, G.; Stock, N. Synthesis and Modification of a Functionalized 3D Open-Framework Structure with MIL-53 Topology. *Inorg. Chem*. **2009,** *48* (7), pp 3057–3064.

[12] Serre, C.; Millange, F.; Thouvenot, C.; Nogues, M.; Marsolier, G.; Louer, D.; Ferey, G. Very Large Breathing Effect in the first Nanoporous Chromium(III)-Based Solids: MIL-53 or $Cr^{III}(OH)\cdot\{O_2C\text{-}C_6H_4\text{-}CO_2\}\cdot\{HO_2C\text{-}C_6H_4\text{-}CO_2H\}_x\cdot H_2O_y$ *J. Am. Chem. Soc*. **2002,** *124* (45), pp 13519–13526.

[13] Ai, L.; Li, L.; Zhang, C.; Fu, J.; Jiang, J. MIL-53(Fe): A Metal-Organic Framework with Intrinsic Peroxidase. *Chem. Eur. J.* **2013,** *19* (45), pp 15105–15108.

[14] Horcajada, P.; Serre, C.; Maurin, G.; Ramsahye, N.A.; Balas, F.; Vallet-Regi, M.; Sebban, M.; Taulelle, F.; Ferey, G. Flexible Porous Metal-Organic Frameworks for a Controlled Drug Delivery. *J. Am. Chem. Soc*. **2008,** *130* (21), pp 6774–6780.

[15] Loiseau, T.; Serre, C.; Huguenard, C.; Fink, G.; Taulelle, F.; Henry, M.; Bataille, T.; Ferey, G.A. Rationale for the Large Breathing of the Porous Aluminum Terephthalate (MIL-53) Upon Hydration. *Chem. Eur. J.* **2004,** *10* (6), pp 1373–1382.

[16] Li, Z.; Wu, Y.; Li, J.; Zhang, Y.; Zou, X.; Li, F. The Metal-Organic Framework MIL-53 (Al) Constructed from Multiple Metal Sources: Alumina, Aluminum Hydroxide, and Boehmite. *Chem. Eur. J.* **2015,** *21* (18), pp 6913–6920.

[17] Joaristi, A.M.; Juan-Alcaniz, J.; Serra-Crespo, P.; Kapteijn, F.; Gascon, J. Electrochemical Synthesis of Some Archetypical Zn^{2+}, Cu^{2+}, and Al^{3+} Metal Organic Frameworks. *Cryst. Growth Des.* **2012,** *12* (7), pp 3489–3498.

Determination of mechanisms and transport enhancement in liquid-phase extraction of penetrants from polymers

Brent A. Mantooth[a*], Mark J. Varady[a], Thomas P. Pearl[b], Devon A. Boyne[c], Craig K. Knox[d], Jerry B. Cabalo[a], John A. Escarsega[e], Robert H. Lambeth[e]
[a]U.S. Army Edgewood Chemical Biological Center, Research & Technology Directorate, 5183 Blackhawk Rd, Aberdeen Proving Ground, MD 21010
[b]DCS Corp., 100 Walter Ward Blvd, Abingdon, MD 21009
[c]Leidos, Inc., P.O. Box 68, Gunpowder Branch, Aberdeen Proving Ground, MD 21010
[d]Science and Technology Corporation, 111 C. Bata Blvd, Belcamp, MD 21017
[e]U.S. Army Research Laboratory, 4600 Deer Creek Loop, Aberdeen Proving Ground, MD 21005

ABSTRACT

Several practical processes utilize transport of species across liquid-solid boundaries, including material decontamination, membrane separation, and transdermal drug delivery. Identification of the mechanisms associated with liquid-phase extraction of absorbed species (penetrants) from polymers (specifically how absorbing solvents promote bulk penetrant diffusion) is critical to understanding and optimizing these processes. This work has focused specifically on the role of hydrogen bonding on simultaneous penetrant and solvent diffusion in polyurethane polymers. Most previous work has focused on single component diffusion in polymers, and it is important to understand the impact of the three-way penetrant-polymer, solvent-polymer, and penetrant-solvent interactions on the diffusivity in such systems. Molecular dynamics simulations provided measures of associative interactions between the species in multicomponent mixtures along with penetrant and solvent diffusivities. Infrared spectroscopy experiments were performed to study the influence of solvent on penetrant desorption rate from the polymers. The dynamic uptake information from the infrared spectroscopy experiments coupled with equilibrium mass absorbed from quartz crystal microbalance experiments enabled the fitting of multicomponent Maxwell-Stefan diffusivities. Results show that the exposure of a contaminated polymer to particular solvents can greatly enhance the penetrant desorption rate, and that competitive hydrogen bonding interactions play a critical role in the system behavior.

Keywords: multicomponent transport, liquid-phase extraction, Maxwell-Stefan, Flory-Huggins, molecular dynamics, polymer, decontamination, Fourier-transform infrared spectroscopy

1. INTRODUCTION

The rate at which chemical species (i.e., penetrants) absorbed in a polymer (i.e., in solution where the penetrant is the solute and the polymer is the solvent) can be extracted into an adjacent liquid is often limited by diffusive transport in the bulk-phase. As shown in Figure 1, the absorbed penetrant must migrate from the bulk to the phase interface where it partitions into the liquid phase according to local thermodynamic equilibrium. This configuration has practical applications in decontamination of chemical warfare agents from absorbing materials,[1–3] leaching of organics from solid waste material,[4–6] and controlled transdermal drug delivery.[7–9] Another closely related, practical application is membrane separations processes in which a feed consisting of a gaseous or liquid mixture of species is passed over a polymeric membrane and one of the species is selectively transported across the membrane due to differences in solubility or diffusivity.[10–12]

Several studies in the literature have attempted to draw correlations between penetrant diffusivity and chemical interactions in penetrant-polymer systems. Elabd and Barbari[13] experimentally studied the diffusion of methyl ethyl ketone and 1-butanol mixtures in polyisobutylene polymer, finding that the hydrogen bonding interactions between each of the penetrants with the crystalline segments of the polymer had an influence on the measured diffusion coefficients. Chang et al.[14] performed molecular dynamics (MD) simulations demonstrating that ethanol diffuses slower than water in a polydimethylsiloxane (PDMS) membrane due to a higher affinity of the ethanol for the membrane interface. Ling et al.[15] simulated the diffusion of model diesel constituent species in four different polymer

membranes using MD simulations with the aim of understanding the fuel desulfurization process. Calculated diffusion coefficients were found to correlate to the penetrant-polymer interaction strength.

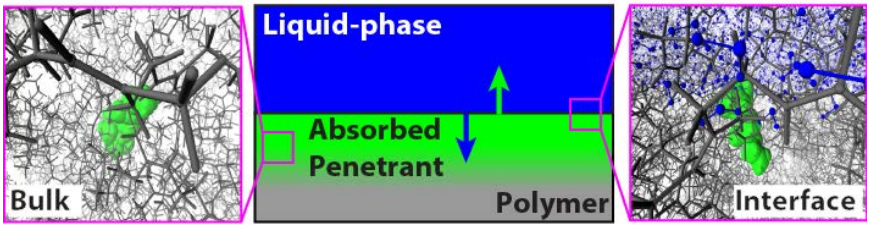

Figure 1. Schematic of liquid-phase extraction at macroscale showing the transport of both liquid and penetrant across the phase boundary, along with molecular scale depictions of partitioning of penetrant across the phase boundary and penetrant within the bulk of the polymer.

Previous research in our laboratory studying the decontamination of the nerve agent VX absorbed in a silicone elastomer revealed that adding methanol to aqueous sodium hydroxide solutions accelerated the extraction of VX from the silicone.[3] This was partially due to the increased solubility of VX in the liquid-phase solution, but it was also found that the diffusivity of VX in the silicone elastomer increased as methanol absorbed into the silicone; suggesting that associative interactions experienced by the penetrant (VX in this case) changed in the presence of another penetrant (methanol), resulting in an enhancement in diffusivity. A subsequent MD study confirmed that associative interactions between the different species had a significant impact on the transport of VX in PDMS, of which silicone is a derivative.[16] Perhaps of more importance, is the transport of chemicals in polyurethanes (PU) since this class of polymers serves as the binder in a class of military coatings.[17,18] The amide and carbonyl functional groups of PU have been shown to form interchain H–bonds,[19,20] and it is expected that penetrants with H–bond acceptors or donors would form H–bonds with the polymer. The interaction energy between penetrants and the polymer could be modified by the number and strength of the H–bonds, influencing transport within the material.

The intent of this work is to develop a fundamental molecular level understanding of the mechanisms responsible for increased penetrant transport rate in polymers exposed to selected solvents. Emphasis is placed on the influence of polymer-penetrant, polymer-solvent, and penetrant-solvent interactions; how these evolve over the course of a dynamic extraction process; and how the penetrant mobility correspondingly changes. This is accomplished by a combined experimental and computational approach. The experimental effort employs Fourier-transform infrared spectroscopy–attenuated total reflection (FTIR-ATR) to examine the time-resolved absorption and desorption of chemical species in PUs and the corresponding changes in hydrogen bonding with the PU polymer. The computational work utilizes MD simulations to characterize the molecular-scale hydrogen bonding interactions that influence penetrant diffusion in two polyurethanes and draws correlations between the probability and strength of H–bonds between the different components in the system and their corresponding diffusivities.

2. METHODOLOGY

2.1 Polymer synthesis and characterization

Structurally analogous PU and polyhydroxyurethane (PHU) polymers, shown in Figure 2, were prepared to examine how the presence of pendant hydroxyl groups affects penetrant and solvent transport. The model PU polymer was prepared using standard polyol-isocyanate chemistry. The model PHU was prepared by an organocatalytic cyclic carbonate-amine polymerization developed by the U.S. Army Research Laboratory. The backbones of the two polymers are nearly identical, differing only in the pendant hydroxyl group present in the PHU structure, providing different hydrogen bonding environments for absorbing species.

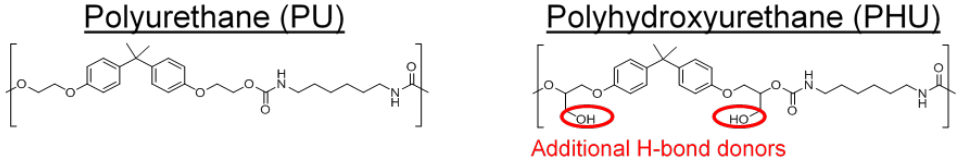

Figure 2. Monomer units for PU and PHU with an indication of the additional hydrogen bonding donors available on the PHU backbone.

2.2 Penetrant and solvent selection

Penetrants and solvents were selected for varying hydrogen bonding interactions with the PU and PHU polymers. Priority was placed on selecting series of homomorphic compounds differing only in hydrogen bonding capability with similar molar volumes and to allow for a focus on chemical interaction effects with minimal molecular size influences. Table 1 lists the penetrants and solvents chosen for initial study in order to specifically probe hydrogen bonding interactions. The homomorphic series of hexane, pentylamine, and butyldiamine (linear amines) have increasing number of hydrogen bonding donors and acceptors; the series of *p*-Xylene, lutidine, and dimethylpyrazine (pyridine derivatives) have increasing number of hydrogen bonding acceptors only; and the solvent series of methylamine, formaldehyde, and methanol have a single hydrogen bond acceptor with varying functional group electronegativity.

Table 1. Penetrants and solvents chosen for initial studies that permit systematic variations in hydrogen-bonding interactions through three different homomorphic series.

Chemical	Structure	Molar Volume[a] (cm^3/mol)	No. of H–bond Acceptors	No. of H–bond Donors	Functional Group Electronegativity[21]
Penetrants					
hexane	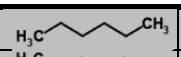	127	0	0	2.23
pentylamine	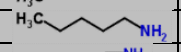	114.7	1	2	2.61
butyldiamine		101.9	2	4	2.61
p-Xylene	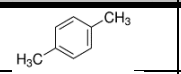	122.0	0	0	N/A
lutidine	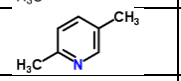	115.2	1	0	N/A
dimethylpyrazine	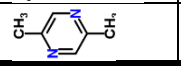	108.4	2	0	N/A
Solvents					
methylamine	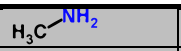	48.7	1	2	2.61
formaldehyde	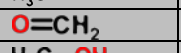	43.8	1	0	3.14
methanol	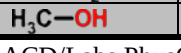	40.8	1	1	3.51

(a) Estimated from ACD/Labs PhysChem Module

2.3 Molecular dynamics simulations

MD simulations were run on ternary systems consisting of penetrant (5 wt%), solvent (10 wt%), and polymer (85 wt%) for all penetrant-solvent-polymer combinations, for a total of 36 unique systems. Self-diffusivities of penetrants and solvents in both PU and PHU were obtained by MD simulation. Ten full-length chains (each a 43-mer) were placed in a periodic simulation box with 1 wt% penetrant or 5 wt% penetrant with 0 % or 10 % solvent. All-atom simulations were performed in LAMMPS using the polymer consistent force field to quantify interactions between atoms and bonds. Using a 1-fs time-step, the dynamics were run for over 10 nanoseconds, and the mean-squared displacement (MSD) of each penetrant molecule was calculated using a shifting origin technique. In other words, all possible time origins over the entire 10-nanosecond simulation were used to calculate the MSD for a given time interval, Δt. Because the MSD for the penetrants displayed anomalous behavior (departure from linear MSD versus time) over the first 2 nanoseconds of the trajectory, and the last 3–4 nanoseconds of the trajectory were under-sampled due to a small number of time origins, only the MSD data between 4 nanoseconds and 6 nanoseconds of the total 10-nanosecond trajectory were used to compute the diffusivity by fitting this data to the linear function

$$D = \frac{1}{N}\sum_{i=1}^{N}\frac{\left\langle[\mathbf{r}_i(t)-\mathbf{r}_i(0)]^2\right\rangle}{6t}. \quad (1)$$

Partial pair distribution functions (PDF) were computed between species α and β in the mixtures only considering oxygen–oxygen (O–O), nitrogen–nitrogen (N–N), and oxygen–nitrogen (O–N or N–O) pairs; in other words, only

accounting for atoms contributing to hydrogen bonding atoms within each species. This quantity provided a correlation between the two species at a given distance. Mathematically, this was calculated according to

$$g_{\alpha\beta}(r) = \frac{1}{\rho}\frac{N}{N_\alpha N_\beta}\sum_{i=1}^{N_\alpha}\sum_{j=1}^{N_\beta}\sum_{k=O,N}\sum_{l=O,N}\left[\left\langle \delta\left(r - \left|r_j^k - r_i^l\right|\right)\right\rangle\right]. \quad (2)$$

The quantity $g_{\alpha\beta}(r)$ was computed every 1,000 time steps and averaged over the entire 10-nanosecond simulation. Additionally, the number of H–bonds between species were computed by counting the number of O–O, N–N, O–N, or N–O pairs between two species that were within 3.0 Å and angle of 120 degrees. The H–bonds were computed every 1,000 time steps, and averaged over the entire 10 ns simulation.

Additional simulations were performed for the penetrants dimethylpyrazine and diaminobutane using larger systems of 200,000 total atoms (about ten times as large as previously run). Also, additional RDFs were computed for specific functional groups on the polymer to better assess where the penetrant and solvent were interacting. Finally, third order RDFs were computed to assess three body interactions (i.e., simultaneous hydrogen bonding interactions of polymer-solvent-penetrant).

2.4 Controlled vapor flow for quartz crystal microbalance and FTIR-ATR experiments

While the intent is to understand how solvents, typically applied as liquids to materials may influence transport, vapor exposure is used to created controlled concentrations of each species in the polymer. Further, this study characterizes the interactions occurring in the material, and thus the phase of the chemicals at the vapor-material surface does not influence the transport observed by FTIR-ATR at the distal material surface. To generate the chemical vapor, N_2 gas was flowed as a carrier gas through a custom blown, glass saturator cell (heated to 38 °C in a sand bath) containing a porous ceramic cylinder (Glassblowers, Inc.) that was saturated with the desired liquid chemical. The total flow rate delivered over the films was 1 sccm for the quartz crystal microbalance (QCM) experiments and 50 sccm for the FTIR-ATR experiments. The amount of vapor delivered (i.e., effective partial pressure/activity) was modulated by dividing the total flow between pure N_2 and N_2 gas saturated with the desired chemical vapor (solvent/penetrant). The flow was combined at a junction, passed through a heated vapor line (40 °C), and finally introduced into the flow cell. The flow cell housing attached to the ATR was maintained at 27 °C. The flow rate of each line was controlled by laminar-based mass flow controllers (MFC). A schematic of the setup is shown in Figure 3.

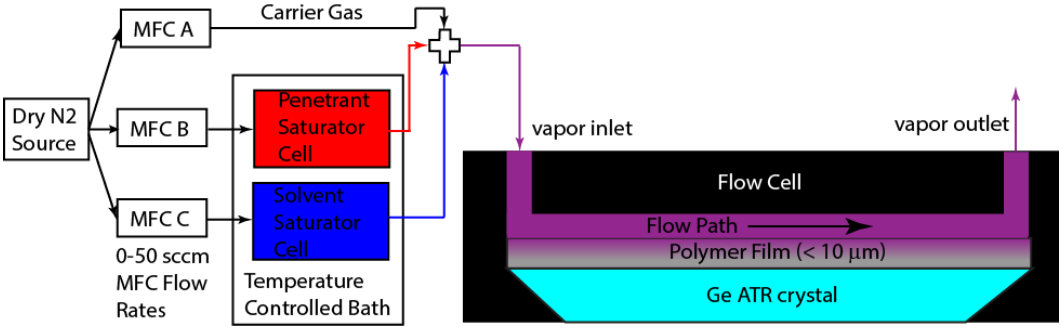

Figure 3. Schematic of experimental setup for vapor delivery system connected to FTIR-ATR flow cell.

2.5 QCM experiments

Mass sorption of both penetrant and solvent species into the polymers was characterized by QCM. In the QCM technique, a polymer in solution was spin cast onto a quartz crystal (5 MHz, AT crystal cut, Au/Cr polished electrodes) and the films are cured, creating films of final thickness 2–5 µm. The clean polymer films were exposed to a chemical vapor of controlled activity (described in Section 2.4, Controlled vapor flow for quartz crystal microbalance and FTIR-ATR experiments). During this exposure, an INFICON Research QCM was used to measure the change in resonance frequency of the quartz crystal, Δf, which can be related to the mass of vapor absorbed into the polymer film, m_{abs}, via the Sauerbrey equation

$$\Delta f = \frac{-2 f_{ro}^2}{A\sqrt{\rho_q G_q}} m_{abs}, \quad (3)$$

where f_{ro} is the resonant frequency of the quartz crystal coated with the polymer film, and A, ρ_q, and G_q are active area, the mass density, and shear modulus of the quartz crystal, respectively.

2.6 FTIR-ATR experiments

For the FTIR-ATR experiments, polymers were spin cast onto a PIKE Technologies horizontal ATR (HATR), 45° cut Ge crystals, to create films of thickness 5–10 µm. By shining light from an IR source through the backside of the crystal, an evanescent wave is created at the polymer-crystal interface. Monitoring the intensity of the reflected IR light as a function of wavelength allows the presence of species with corresponding absorption bands to be detected. Because the evanescent wave penetrates less than 600 nm into the polymer, this measurement only detects species near the polymer-crystal interface. Integration over the absorption band(s) corresponding to a particular species of interest allows quantification of the amount of species absorbed as a function of time.

3. RESULTS

3.1 MD simulations

It was previously established that in ternary systems consisting of penetrant (5 wt%), solvent (10 wt%), and polymer (85 wt%), stronger solvent-polymer H–bonds led to decreased penetrant-polymer H–bonds (i.e., there was competition between penetrant and solvent for hydrogen bonding sites on the polymer). However, the RDFs calculated in the previous studies were total RDFs and did not differentiate between different functional groups of the polymer. In this analysis, RDFs were computed for select penetrants (diaminobutane and dimethylpyrazine) and all solvents with each specific functional group of the polymer, as shown in Figure 4. For the solvents, MeOH forms the strongest H–bonds with the C=O groups of PU, while for PHU it also forms H–bonds with –OH groups, and to a lesser extent with –NH groups. CH_2O tends to form H–bonds with amine groups of PU and with –OH groups of PU, but not with the C=O groups since both are H–bond acceptors and cannot form H–bonds. $MeNH_2$ interacts relatively weakly with all functional groups of both PU and PHU. For the penetrants, in PU, the penetrant diaminobutane tends to H–bond with the carbonyl groups, but in PHU, hydrogen bonding with the carbonyls decreases due to competition with hydrogen bonding with the hydroxyls. For the penetrant dimethylpyrazine, H–bonds form with the NH groups in PU, but these H–bonds do not seem to weaken in PHU, rather additional H–bonds with the hydroxyls of PHU are formed. In general, the penetrant-polymer functional group hydrogen bonding decreases with increasing solvent-polymer hydrogen bonding, again supporting the view of competition between penetrant and solvent for hydrogen bonding with specific polymer functional groups.

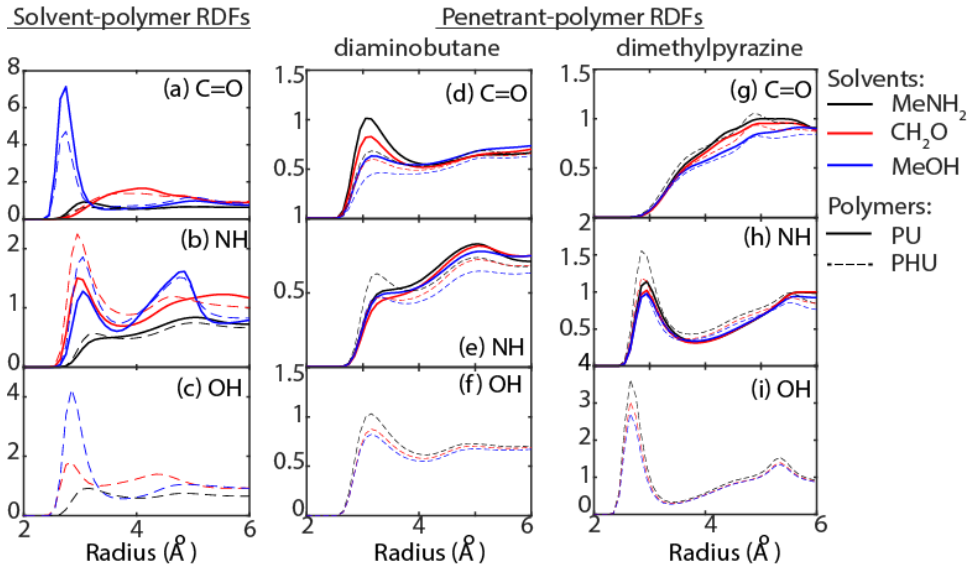

Figure 4. Solvent-polymer RDFs with specific polymer functional groups, (a) carbonyl, (b) amide, (c) hydroxyl. Diaminobutane-polymer RDFs with specific polymer functional groups, (d) carbonyl, (e) amide, (f) hydroxyl. Dimethylpyrazine-polymer RDFs with specific polymer functional groups, (g) carbonyl, (h) amide, (i) hydroxyl.

Third-order RDFs also indicated three-body interactions between the PHU hydroxyl, methanol, and the pyridine derivative. An example RDF and schematic of the three-body interaction is shown in Figure 5. This shows the high probability of the pyridine derivatives hydrogen bonding with methanol that is simultaneously hydrogen bonding with the polymer, so methanol may act as a mediator between lutidine/dimethylpyrazine and PHU.

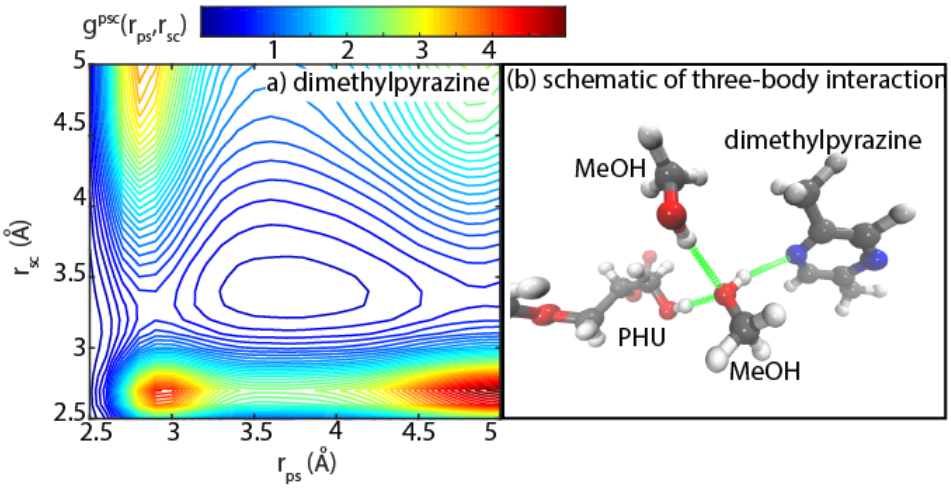

Figure 5. Contour plots of third order (triplet) radial distribution functions, for (a) dimethylpyrazine with PHU as polymer and methanol as solvent. Solvent-polymer distances (r_{sp}) are on the x axis and solvent-penetrant (r_{sc}) distances are on the y-axis. (b) Schematic showing three-body interaction between hydroxyl group of PHU, methanol, and dimethylpyrazine with green helices indicating interactions between molecules.

3.2 Penetrant and solvent interactions with polymer

Penetrant-polymer and solvent-polymer interactions were assessed by examining the IR absorption difference spectra upon sorption of the penetrant or solvent into the polymer in single component experiments. Difference spectra were computed by subtracting off the initial spectrum (at time = 0) from each subsequent spectrum collected in the experiment.

For brevity, an example of polymer-penetrant interactions and resulting structural changes is shown for the penetrant lutidine in Figure 6. In Figure 6a, the increasing peak at 1492 cm^{-1} is attributed to lutidine sorption (the C–C stretch in the aromatic ring). At the same time, an increase in intensity is observed in the peaks assigned to the free carbonyls $(C=O)_{free}$ (1720 cm^{-1}) as well as a decrease in the bound carbonyls $(C=O)_{bound}$ for PU (1700 cm^{-1}) . This indicates that the hydrogen bonding between C=O and –NH groups on adjacent polymer chains is being disrupted. The simultaneous decrease in $(NH)_{free}$ groups on the polymer indicates that initially free –NH sites are being occupied by the absorbing lutidine. There is also the appearance of a peak at 3230 cm^{-1} assigned to the vibrational mode of H–C=N of lutidine interacting with –NH groups on the polymer. These processes are depicted schematically in Figure 6b and c.

Similar disruption of interchain hydrogen bonding as observed for lutidine is also observed during the absorption of acetonitrile (ACN) (which is also aprotic) into PU. During the sorption of methanol (protic solvent) the behavior is somewhat different. Here, the $(C=O)_{bound}$ of the PU increases while the $(C=O)_{free}$ decreases, which is indicative of methanol occupying the carbonyl sites on the polymer as the interchain hydrogen bonds break.

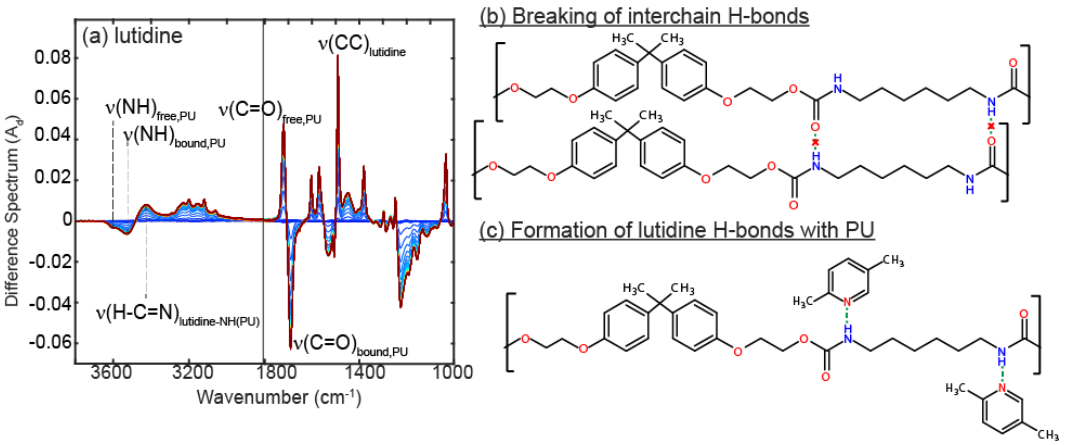

Figure 6. (a) Difference spectra during absorption of lutidine, schematics of (b) breaking of interchain H–bonds for PU, and (c) formation of H–bonds between lutidine and –NH groups of PU.

3.3 Solvent-assisted codesorption of penetrant from polymer

Desorption of lutidine from PU into pure N_2 is shown in Figure 7a (dotted line), and it is seen that the desorption process is slow and incomplete, approximately 48 % remains after a period of 200 minutes. Additional experiments performed by exposing the contaminated polymer to N_2 saturated with methanol speeds the desorption rate and lutidine completely desorbed within 150 minutes. Even faster lutidine removal was observed when N_2 saturated with ACN was used, and complete desorption was attained within about 60 minutes. Figure 7b shows the absorption of ACN into PU both for the single component case and for the codesorption case. The change in intensity with time is the same for both single and multicomponent cases, indicating that the presence of lutidine in the polymer does not significantly affect the solubility of ACN in PU. Figure 7c shows the difference spectra during the solvent exposure (time points A-B) and after the solvent exposure (time points B–C). In region A–B, the $\nu(CN)_{ACN}$ band at 2250 cm^{-1} increases signifying ACN absorption, while the $\nu(CC)_{lutidine}$ band at 1492 cm^{-1} decreases suggesting lutidine is being desorbed. In region B–C, the $\nu(CN)_{ACN}$ peak at 2250 cm^{-1} decreases indicating that after the solvent is turned off, the ACN is being desorbed from the polymer. These chemical interactions are shown in schematic form in Figure 7d.

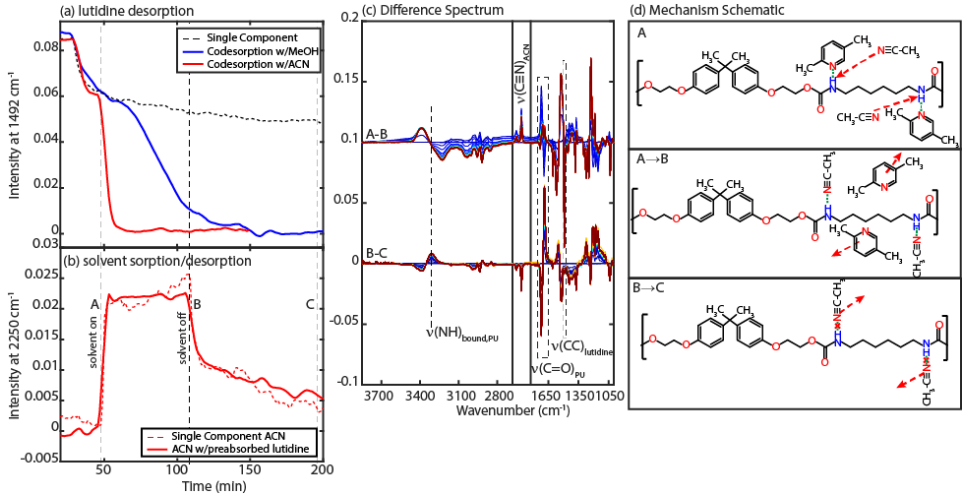

Figure 7. (a) Desorption of lutidine from PU into pure N_2 (dashed line), exposed to N_2 saturated with methanol (blue line), or ACN (red line). (b) Sorption of ACN into clean PU (dashed red line) and into PU with absorbed lutidine (solid red line). (c) Difference spectra for codesorption of lutidine with ACN during solvent exposure phase (A–B) and during solvent desorption phase (B–C). (d) Schematic of competitive H–bond interactions occurring during codesorption process.

3.4 Single-component penetrant and solvent diffusivities

From the time resolved normalized absorbance (obtained from the difference spectra) during the absorption and desorption of single components in the polymer at different species concentrations, the diffusivity and its composition

dependence can be assessed. Figure 8 shows the normalized absorbance for the lutidine peak at 1492 cm^{-1} during (a) absorption and (b) desorption from PU at multiple activities. In Figure 8a, a significant delay between the introduction of lutidine vapor and the appearance of lutidine at the polymer/crystal interface is observed for lower vapor activities. It is also apparent that after the initial delay, the absorption dynamics are faster for the higher activities. In Figure 8b, the initial desorption rate of lutidine is lowest for a = 0.6 and increases up to a = 1.0, although in all cases there is residual lutidine remaining in the polymer after a period of > 8 hours. All of these observations led to a diffusivity model for lutidine in PU in which there is a phase transition at a critical lutidine concentration (ϕ_c) below which the diffusivity is low ($\mathcal{D}_l$), (explaining the delay time in absorption and residual amount remaining in the desorption) and an exponential composition dependence of the diffusivity above the critical concentration (explaining the differences in absorption and desorption rates at the different activities). The mathematical form of the diffusivity is

$$\mathcal{D}_{ip} = \begin{cases} \mathcal{D}_l & \phi < \phi_c \\ \mathcal{D}_l \exp(\alpha\phi) & \phi \geq \phi_c \end{cases}. \quad (4)$$

Fitting this model to the absorption and desorption curves simultaneously for each individual activity is shown as the dotted lines in Figure 8. Using values of $\mathcal{D}_0$ = 1.5 × 10^{-15} m^2/s and α = 0.0035, it was found that values of $\mathcal{D}_l$ = 1 × 10^{-16} m^2/s and ϕ_c = 0.045.

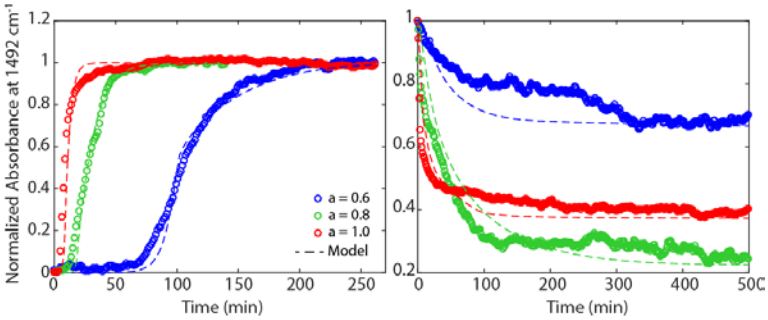

Figure 8. (a) Absorption and (b) desorption of lutidine from PU at multiple vapor activities: a = 0.6 (blue), a = 0.8 (green), and a = 1.0 (red). Open circles denote experimental data and dotted lines denote fits to diffusivity data.

3.5 Multicomponent diffusion analysis

To analyze the multicomponent FTIR-ATR data to obtain quantitative diffusivities, a calibration was needed to convert penetrant and solvent absorbance into volume fraction in the polymer. To do this, analogous single component FTIR-ATR and QCM experiments were performed over activity ranges of 0.1–1.0, and the equilibrium absorbance and volume fraction were obtained, respectively, at each activity step. By combining these two pieces of information, a plot of equilibrium volume fraction versus absorbance was constructed and a linear calibration curve fit to the data, as shown in the example for ACN in Figure 9.

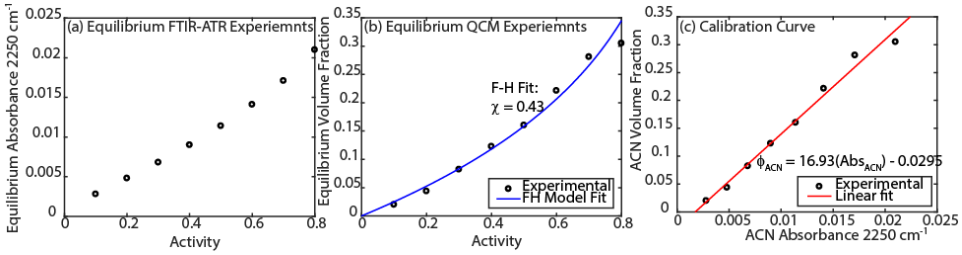

Figure 9. Example of equilibrium absorption experiments for ACN in PU at multiple activities, (a) FTIR-ATR absorbance at 2250 cm^{-1}, (b) gravimetric uptake by QCM, and (c) calibration curve relating ACN absorbance at 2250 cm^{-1} to volume fraction absorbed in polymer.

To obtain the composition dependence of penetrant and solvent diffusivities when both chemical species are present in the polymer, FTIR-ATR experiments were devised to set the solvent activity, allow the polymer to come to equilibrium with the solvent, then increase the penetrant activity in predefined step changes. The penetrant uptake was fit at each step change to obtain the diffusivity over the given penetrant and solvent composition range. This experiment was repeated for multiple solvent activities. Figure 10a shows an example multicomponent experiment in which the polymer was allowed to reach equilibrium with ACN vapor at an activity of 0.3, followed by activity steps of lutidine from 0.3 to 0.7.

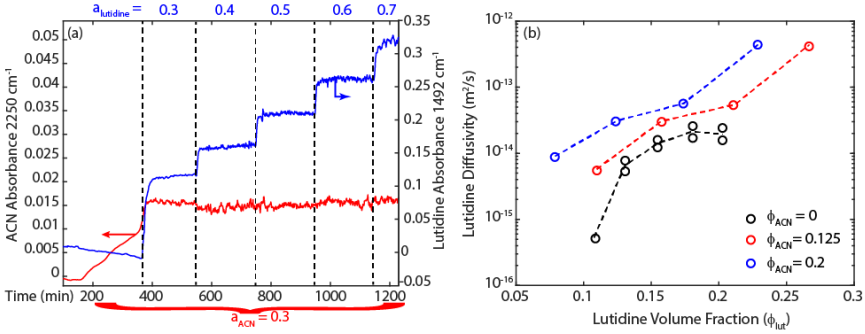

Figure 10. (a) Absorption of lutidine in PU at multiple activities from 0.3–0.7 keeping ACN activity fixed at 0.3. (b) Fit of lutidine diffusivity for each step in (a) is shown by the red circles, while the black circles indicate fit lutidine diffusivities in the absence of ACN and the blue circles indicate fit lutidine diffusivities with ACN activity = 0.4. Dotted lines in (b) pass through the data points and are only intended to guide the eye.

The one-dimensional transport equations (5–7) were used to fit the penetrant diffusivity at each penetrant activity step, where advantage was taken of the fact that ACN concentration remained constant within the polymer as lutidine activity was stepped up.

$$\frac{1}{\overline{V}_1}\frac{\partial \phi_1}{\partial t} + \frac{\partial \mathbf{N}_1}{\partial z} = 0, \tag{5}$$

$$\frac{\phi_1}{\overline{V}_1}\frac{\partial \ln a_1}{\partial z} = -\frac{\overline{V}_1}{\overline{V}_r}\left(\frac{\phi_2}{\not{D}_{12}} + \frac{\phi_p}{\not{D}_{1p}}\right)\mathbf{N}_1, \tag{6}$$

$$\ln a_1 = \ln \phi_1 + \left(1 - \frac{\overline{V}_1}{\overline{V}_2}\right)\phi_2 + \left(1 - \frac{\overline{V}_1}{\overline{V}_p}\right)\phi_p + \left(\chi_{12}\phi_2 + \chi_{1p}\phi_p\right)\left(1-\phi_1\right) - \chi_{2p}\frac{\overline{V}_1}{\overline{V}_2}\phi_2\phi_p. \tag{7}$$

Here, ϕ_1, $\mathbf{N}_1$, $\overline{V}_1$, and a_1 are the volume fraction, molar flux in the polymer, molar volume, and vapor activity of the penetrant, ϕ_2 and $\overline{V}_2$ are the volume fraction and molar volume of the solvent, and the χ_{ij} are the Flory interaction parameters between species *i* and *j* in the mixture. The diffusivity of the penetrant, $\not{D}_{1p}$, is the value to be fit to the experimental sorption data.

Figure 10b shows the results of fitting lutidine diffusivity at each activity step for different fixed values of ACN activity (black:zero, red: 0.3, blue: 0.4). It is clear that increasing ACN activity increases lutidine diffusivity in PU at a given lutidine volume fraction. The qualitative results align with expectations, but the combination of QCM and FTIR-ATR experiments provide quantitative diffusivity results. These results can be used to quantitatively assess the effectiveness of different solvents and the amounts required to remove undesirable penetrant chemicals from a polymer.

4. CONCLUSIONS

Through computational MD simulations and experimentation combining gravimetric and spectroscopic methods, this work elucidated the key hydrogen bonding mechanisms responsible for increased penetrant transport rate in polymers exposed to selected solvents. Specifically, it was found through that competitive interactions between penetrant and solvent for hydrogen bonding sites on polymer functional groups control the absorption and desorption rate of chemical. By performing combined QCM and FTIR-ATR experiments, the governing transport equations were fit to yield quantitative values for the penetrant diffusivity. A mechanistic understanding of the transport processes combined with the ability to quantify transport rates allows for rational investigation and identification of viable solvents for removing undesirable penetrant chemicals that are absorbed in a polymer.

ACKNOWLEDGMENTS

The authors would like to acknowledge U.S. Army funding provided through the Edgewood Chemical Biological Center's Surface Science Initiative program.

REFERENCES

[1] Yang, Y.C.; Baker, J.A.; Ward, J.R. Decontamination of Chemical Warfare Agents. *Chem. Rev.* **1992,** *92*, pp 1729–1743.
[2] Love, A.H.; Bailey, C.G.; Hanna, M.L.; Hok, S.; Vu, A.K.; Reutter, D.J.; Raber, E. Efficacy of Liquid and Foam Decontamination Technologies for Chemical Warfare Agents on Indoor Surfaces. *J. Hazard. Mater.* **2011,** *196*, pp 115–122.
[3] Varady, M.J.; Pearl, T.P.; Stevenson, S.M.; Mantooth, B.A. Decontamination of Vx from Silicone: Characterization of Multicomponent Diffusion Effects. *Ind. Eng. Chem. Res.* **2016,** *55* (11), pp 3139–3149.
[4] Bishop, P. Leaching of Inorganic Hazardous Constituents from Stabilized/Solidified Hazardous Wastes. *Hazard. Waste Hazard. Mater.* **1988,** *5* (2), pp 129-143.
[5] Yamamoto, T.; Yasuhara, A. Quantities of Bisphenol a Leached from Plastic Waste Samples. *Chemosphere.* **1999,** *38* (11), pp 2569–2576.
[6] Lee, C.K.; Rhee, K.-I. Reductive Leaching of Cathodic Active Materials from Lithium Ion Battery Wastes. *Hydrometallurgy.* **2003,** *68* (1–3), pp 5–10.
[7] Bigucci, F.; Abruzzo, A.; Saladini, B.; Gallucci, M.C.; Cerchiara, T.; Luppi, B. Development and Characterization of Chitosan/Hyaluronan Film for Transdermal Delivery of Thiocolchicoside. *Carbohydr. Polym.* **2015,** *130*, pp 32–40.
[8] Ouriemchi, E.M.; Vergnaud, J.M. Processes of Drug Transfer with Three Different Polymeric Systems with Transdermal Drug Delivery. *Comput. Theor. Polym. Sci.* **2000,** *10* (5), pp 391–401.
[9] Rao, P.R.; Ramakrishna, S.; Diwan, P.V. Drug Release Kinetics from Polymeric Films Containing Propranolol Hydrochloride for Transdermal Use. *Pharm. Dev. Technol.* **2000,** *5* (4), pp 465–472.
[10] Mulder, M.H.V.; Smolders, C.A. On the Mechanism of Separation of Ethanol/Water Mixtures by Pervaporation: 1. Calculations of Concentration Profiles. *J. Membr. Sci.* **1984,** *17* (3), pp 289–307.
[11] Cunha, V.S.; Paredes, M.L.L.; Borges, C.P.; Habert, A.C.; Nobrega, R. Removal of Aromatics from Multicomponent Organic Mixtures by Pervaporation Using Polyurethane Membranes: Experimental and Modeling. *J. Membr. Sci.* **2002,** *206* (1–2), pp 277–290.
[12] Kamaruddin, H.D.; Koros, W.J. Some Observations About the Application of Fick's First Law for Membrane Separation of Multicomponent Mixtures. *J. Membr. Sci.* **1997,** *135* (2), pp 147–159.
[13] Elabd, Y.A.; Barbari, T.A. Multicomponent Diffusion of Hydrogen-Bonding Solutes in a Polymer. *Aiche J.* **2002,** *48* (8), pp 1610–1620.
[14] Chang, K.S.; Chung, Y.C.; Yang, T.H.; Lue, S.J.; Tung, K.L.; Lin, Y.F. Free Volume and Alcohol Transport Properties of Pdms Membranes: Insights of Nano-Structure and Interfacial Affinity from Molecular Modeling. *J. Membr. Sci.* **2012,** *417*, pp 119–130.
[15] Ling, C.J.; Liang, X.Y.; Fan, F.C.; Yang, Z. Diffusion Behavior of the Model Diesel Components in Different Polymer Membranes by Molecular Dynamic Simulation. *Chem. Eng. Sci.* **2012,** *84*, pp 292–302.
[16] Bringuier, S.A.; Varady, M.J.; Pearl, T.P.; Mantooth, B.A. Characterization of Composition-Dependent Maxwell-Stefan Diffusivities in Mixtures of Polydimethylsiloxane, Nerve Agent Vx, and Methanol. *Ind. Eng. Chem. Res.* **2017,** *56* (13), pp 3713–3725.
[17] *MIL-DTL-64159: Coating, Water Dispersible Aliphatic Polyurethane, Chemical Agent Resistant*; U.S. Army Research Laboratory, ATTN: AMSRL-WM-MA: Aberdeen Proving Ground, MD, 30 January 2002.
[18] Cooley, K.A.; Pearl, T.P.; Varady, M.J.; Mantooth, B.A.; Willis, M.P. Direct Measurement of Chemical Distributions in Heterogeneous Coatings. *ACS Appl. Mater. Interfaces.* **2014,** *6* (18), pp 16289–16296.
[19] Coleman, M.M.; Lee, K.H.; Skrovanek, D.J.; Painter, P.C. Hydrogen-Bonding in Polymers .4. Infrared Temperature Studies of a Simple Polyurethane. *Macromolecules.* **1986,** *19* (8), pp 2149–2157.
[20] Coleman, M.M.; Skrovanek, D.J.; Hu, J.B.; Painter, P.C. Hydrogen-Bonding in Polymer Blends .1. Ftir Studies of Urethane Ether Blends. *Macromolecules.* **1988,** *21* (1), pp 59–65.
[21] Huheey, J.E. Electronegativity of Multiply Bonded Groups. *J. Phys. Chem.* **1966,** *70* (7), pp 2086–2092.

SEEDLING PROJECTS

Effect of organophosphates on the regulation of endothelial barrier function

Daniel J. Angelini*, Christopher S. Phillips, Jennifer R. Horsmon, Amber M. Prugh
U.S. Army Edgewood Chemical Biological Center, Research & Technology Directorate,
5183 Blackhawk Rd, Aberdeen Proving Ground, MD 21010

ABSTRACT

Organophosphate compounds have been shown to have numerous toxic effects on the body. In addition to being extremely toxic, these chemicals are known to have profound effects on cells and tissues at levels that are not lethal. Recent evidence has demonstrated that non-lethal exposures to these compounds can disrupt endothelial cells and induce edema in several organs. To better understand these toxic mechanisms, we examined the effects of the organophosphate compound, malathion, and its metabolite, malaoxon, on the human endothelial cell line HMEC-1. In initial experiments, a 24-hour exposure to malathion or malaoxon produced a dose-dependent decrease in cellular viability. Additional experiments demonstrated that malathion or malaoxon can alter cellular impedance and the flow of macromolecules in a time-dependent manner in the absence of cellular death. Overall, these data suggest that both malathion and malaoxon are capable of disrupting endothelial cells in the absence of cellular death.

Keywords: endothelial cells, malaoxon, malathion, organophosphates, paracellular pathway

1. INTRODUCTION

Understanding the mechanisms and pathways utilized by new and emerging chemical threats and their association to adverse health outcomes will provide a path towards better protection, decontamination techniques, pretreatment, and/or therapy associated with exposure. Recent evidence has suggested that sub-lethal exposures to several chemical warfare agents (CWA) and biological toxins can disrupt endothelial barriers and induce edema in several different organs including lung, skin, and brain.[1,2] These low-level exposures could occur from contaminated environments or through the ingestion of contaminated food or water supplies, and could potentially lead to endothelial toxicities in various organ systems. The effect of CWAs on the endothelium is widely unexplored and further studies in this area could provide significant insights on a new set of possible toxic effects. In this study, we hypothesized that an organophosphate CWA simulant will disrupt the endothelial barrier resulting in the opening of the endothelial paracellular pathway.

1.1 Endothelial barrier function

Endothelial cells (EC) lining the vasculature play a crucial role in maintaining homeostasis; these cells have the responsibility of tightly regulating the passage of fluid, nutrients, and immune cells to tissues throughout the body.[3] The passage of molecules through this barrier can be regulated through either the paracellular pathway (through cell-cell gaps) or the transcellular pathway (transcytosis or vesicular transport). Edema formation or the accumulations of fluid within tissues typically occurs through the paracellular pathway. This pathway is regulated at the cell-cell level by three different groups of junctional proteins—adherens junctions (AJ), tight junctions (TJ), and gap junctions. The amount of these different junctions in an EC is dependent on its location within the vascular tree. For example, brain microvascular ECs contain many more TJs than ECs from any other vessel.[3] Both AJs and TJs are tethered to the actin cytoskeleton, but AJs play a prominent role in the regulation of endothelial barrier function in almost all of the vascular tree. AJs consist of several proteins, including vascular endothelial (VE)-cadherin, α-catenin, β-catenin, γ-catenin, and p120.[3] VE-cadherin is responsible for calcium-dependent homotypic cell-cell adhesion and is linked to the actin cytoskeleton through the catenin proteins. Both rapidly acting (e.g., thrombin or histamine) and late-acting (e.g., tumor necrosis factor-α) regulators of endothelial barrier function have been shown to induce tyrosine phosphorylation of VE-cadherin; this tyrosine phosphorylation induces a loss of cell-cell adhesion and actin depolymerization, leading to intercellular gap formation and vascular leak.[3–5]

1.2 CWAs and vascular injury

Several CWAs, including V-/G-series nerve agents as well as vesicants (e.g., HD), have been shown to disrupt the endothelium and induce edema following exposures in experimental animals.[1,2] Choking agents, such as chlorine and phosgene, have been also shown to disrupt the endothelial barrier, particularly within the lungs.[6] It is interesting to note that biological toxins of military importance have also been shown to disrupt the endothelial barrier, including ricin,[7] staphylococcal enterotoxin B,[8] and anthrax lethal toxin.[9] In many of these cases (either with CWAs or biological toxins), it is unknown whether these alterations in endothelial barrier function are due to necrosis/apoptosis or alterations of the EC cytoskeleton. Additional studies in this research area are necessary to address the knowledge gap that exists concerning the mechanisms of action of toxins on the endothelium.

2. METHODOLOGY

2.1 Human EC culture

The human microvascular EC line HMEC-1[10] was obtained from ATCC® (Manassas, VA) and cultured in MCDB131 culture media (ATCC®) supplemented with 10 ng/mL epidermal growth factor, 1 µg/mL hydrocortisone, 10 mM glutamine, and 10% fetal bovine serum (all supplements from Fisher Scientific™; Waltham, MA). Even though HMEC-1 cells are an immortalized cell line, we only examined the cells within a 10-passage window. This cell line was chosen due to its EC origin and its usefulness as a generalized microvascular EC. These ECs have been shown to express all of the typical EC markers, have EC morphology, and form consistent endothelial barriers.[10] Also, these ECs have been shown to be responsive to classical regulators of endothelial barrier function (e.g., histamine).[10]

2.2 Preparation of the OP chemicals

Stock solutions of the organophosphate pesticide malathion (ULTRA® Scientific; N. Kingstown, RI) and its metabolite, malaoxon (Sigma-Aldrich®; St. Louis, MO), were prepared in 100% ethanol (EtOH) and stored at 4 °C.[11]

2.3 Evaluation of EC viability

HMEC-1 cells were plated in 96-well tissue culture plates at a cellular density of 5.0×10^4 cells/well and allowed to attach for 24 hours. The cells were then treated for 24 hours with increasing concentrations of malathion or malaoxon (1 µM, 3 µM, 10 µM, 30 µM, 100 µM, 300 µM, 1,000 µM, 3000 µM, or 10000 µM), equivalent amounts of vehicle control (EtOH), or media alone. Following each 24-hour exposure, an MTT Cell Viability Assay (Roche Applied Science; Indianapolis, IN) was performed according to the manufacturer's instructions.[11] Results were read on a SpectraMax® plate reader (Molecular Devices; Sunnyvale, CA) and expressed as Relative Viability.

2.4 Evaluation of cellular impedance

Cellular impedance measurements were performed using the xCELLigence® Real-Time Cell Analyzer (RTCA™) DP system (ACEA Biosciences, Inc.; San Diego, CA).[12,13] All experiments were performed using E-Plate® 16s according to the manufacturer's recommended instructions. Briefly, background readings only containing cell culture media were taken before the HMEC-1 cells were plated in the wells. Following the background readings, 5×10^4 cells were plated in each well of the E-Plate® 16s. Baseline impedance measurements were taken every 30 minutes for 24 hours. Following this, the HMEC-1 cells were exposed to media alone, vehicle (EtOH), malathion (100 µM, 300 µM, 1,000 µM), or malaoxon (100 µM, 300 µM, 1,000 µM) for 24 hours. During the exposures, impedance readings were taken every 30 minutes and reported as normalized cell index (CI), which was calculated in accordance with the xCELLigence® system manufacturer's recommendations.[12,13]

2.5 Macromolecular tracer assay

We performed this assay as described.[14] Briefly, HMEC-1 cells (1.25×10^5) were cultured for 72 hours on tissue culture-treated Transwell® filter inserts (pore size 0.4 µm, 12 mm diameter, polyester membrane; Corning, NY). There was 0.5 mL media in the upper chamber and 1.5 mL in the lower chamber to eliminate any hydrostatic or osmotic pressure gradients that may occur between the two chambers. The HMEC-1 cells were then exposed to media, vehicle (EtOH), malathion, or malaoxon in the presence of fluorescein isothiocyanate (FITC)-bovine serum albumin (66.5 kDa; Fisher Scientific™; total of 100 µg) in the apical chamber. Samples were taken (20 µL) at 4 hours and

24 hours following exposure. This volume was replaced after each individual sampling. The amount of fluorescence in the collected samples was measured using a fluorescence plate reader (ex: 485 nm; em: 535 nm). The results were expressed as albumin flux relative to media control.

2.6 Statistical analysis

All data was expressed as the mean ± standard error of the mean. Statistical analysis was performed using GraphPad Prism 7 software (GraphPad Software, Inc.; La Jolla, CA). A one-way analysis of variance (ANOVA) was used to compare the mean responses among the experimental and control groups. The Dunnett's multiple comparisons test was used to determine whether significant differences between groups existed. A p value of less than 0.05 was considered significant.

3. RESULTS

3.1 Human EC culture

HMEC-1 cells were grown to confluency on tissue-culture plastic in MCDB131. Once confluent, these cells display a cobblestone-like morphology. Figure 1 is a phase-contrast photomicrograph of HMEC-1 cells cultured in our laboratory.

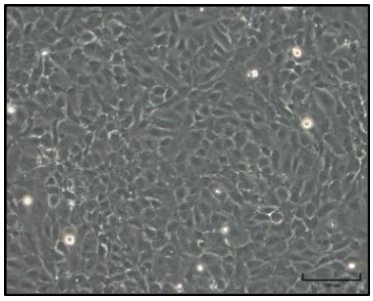

Figure 1. A representative phase-contrast image of cultured HMEC-1 cells. Bar = 100 µm.

3.2 Effect of malathion/malaoxon on EC viability

HMEC-1 cells were plated at a density of 5.0×10^4 cells/well in 96-well tissue culture plates and allowed to attach for 24 hours. The cells were then exposed to media, vehicle (EtOH), or increasing concentrations of malathion or malaoxon (1–1,000 µM) for 24 hours. The exposures were evaluated using the MTT Viability Assay (Figure 2). Following exposure to malathion, significant reductions in viability were observed from treatment with concentrations ≥ 1,000 µM (Figure 2A). Treatments with the metabolite of malathion, malaoxon, induced reductions in viability at concentrations ≥ 3000 µM (Figure 2B).

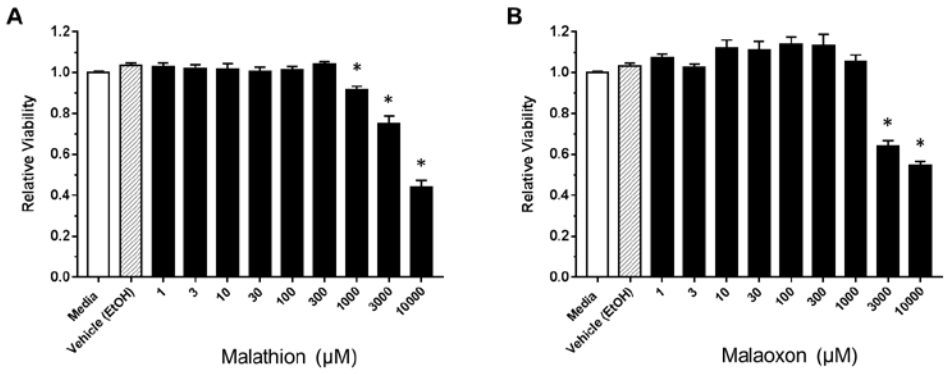

Figure 2. Effects of malathion and malaoxon on HMEC-1 viability. HMEC-1 cells were exposed to increasing concentrations (1–1,000 µM) of malathion (A) or malaoxon (B) (closed bars), media alone (open bars), or vehicle (cross-hatched bars) for 24 hours. Following exposure, the cells were assayed for viability using the MTT Viability Assay. The results are reported as mean ± standard error of the mean as Relative Viability; $n \geq 16$ for each condition tested. *$p < 0.05$ compared to media control.

3.3 Effect of malathion/malaoxon on cellular impedance

The HMEC-1 cells were grown to confluence on E-Plate® 16s for 72 hours, and then exposed to increasing concentrations of malathion (100 µM, 300 µM, and 1,000 µM), malaoxon (100 µM, 300 µM, and 1,000 µM), vehicle (EtOH), or media alone for 24 hours. Cellular impedance was measured every 30 minutes following the exposures (Figure 3). Reductions in normalized CI were observed with malathion (1,000 µM) between 5–6 hours post-exposure (Figure 3A). These reductions stabilized and then returned to baseline at approximately 22 hours post-exposure. Treatments with the lower concentrations of malathion (100 µM, 300 µM) did not alter the normalized CI. With malaoxon treatment, there was a dose-dependent decrease in normalized CI (Figure 3B). The greatest reductions were observed following the 1,000 µM treatment with malaoxon. At this concentration, the normalized CI continued to decrease throughout the duration of the experiments. The other concentrations examined 100 µM and 300 µM displayed slight decreases in normalized CI throughout the experimental timeframe. With all malaoxon exposures, the effect on normalized CI was time-dependent and decreases were observed 3–4 hours post-exposure.

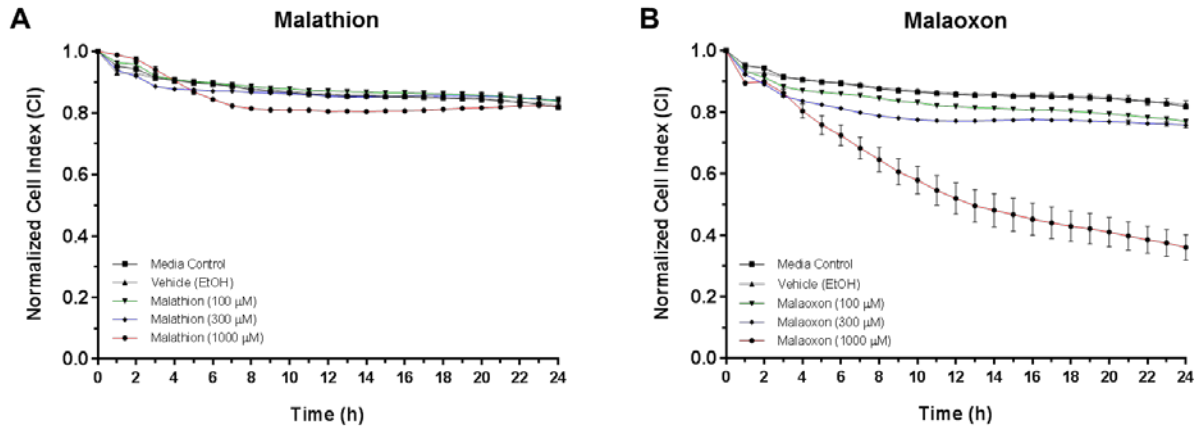

Figure 3. Cellular impedance changes in cultured HMEC-1 following malathion/malaoxon exposure. HMEC-1 cells were exposed to increasing concentrations (100 µM, 300 µM, and 1,000 µM) of malathion (A) or malaoxon (B), media alone, or vehicle (EtOH) for 24 hours. The results are expressed as mean ± standard error of the mean of the normalized CI ($n \geq 5$ for each experimental condition). ■ (black) media control; ▲ (gray) vehicle; ▼ (green) 100 µM malathion/malaoxon; ♦ (blue) 300 µM malathion/malaoxon; ● (red) 1,000 µM malathion/malaoxon.

3.4 Effect of malathion/malaoxon on albumin flux

The HMEC-1 cells were plated on 12-well Transwell® filter inserts at a concentration of 1.25×10^5 cells/well and allowed to grow to confluence for 72 hours. The cells were then treated with media, vehicle (EtOH), malathion (1,000 µM), or malaoxon (1,000 µM) along with FITC-albumin (100 µg) in the upper chamber for 24 hours (Figure 4). Samples were taken from the lower chamber at 4 hours and 24 hours post-exposure and fluorescence was measured. The concentrations of malathion and malaoxon were based on both the results from the viability and impedance assays. Results observed at 4 hours post-exposure showed increases in albumin flux with malathion (~10%) and malaoxon (~12%) compared to media control (Figure 4A), but these results were not statistically significant ($p > 0.05$). At 24 hours, malathion exposure induced an approximate 10% increase in albumin flux and malaoxon exposure induced an approximate 15 % increase in albumin flux (Figure 4B). Both of these changes were considered to be statistically significant ($p < 0.05$).

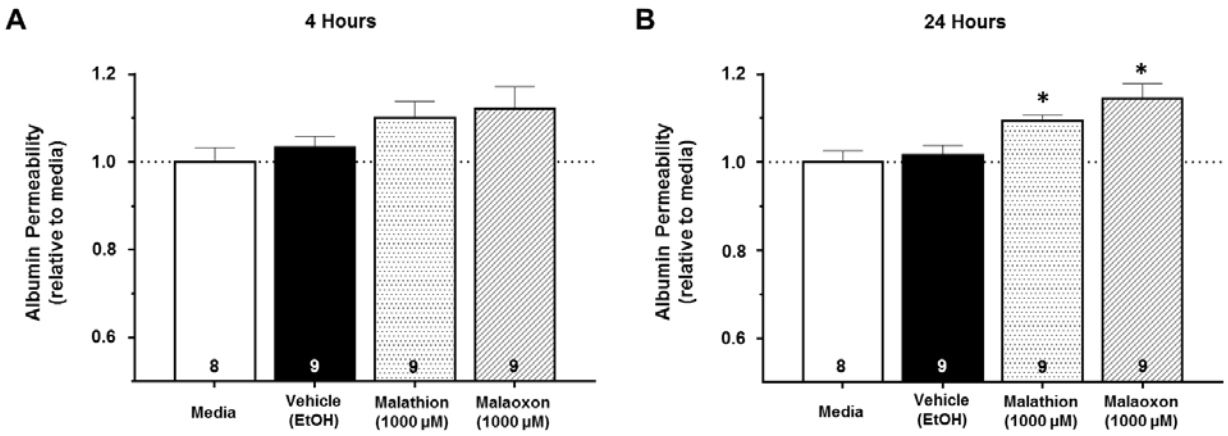

Figure 4. Effect of malathion and malaoxon on the endothelial barrier. Albumin permeability (relative to media) was measured at 4 hours (A) and 24 hours (B) following exposure to media, vehicle (EtOH), malathion (1,000 µM), or malaoxon (1,000 µM). The vertical bars represent the mean ± standard error of the mean of albumin permeability (relative to media). The experimental n is indicated within each bar. *$p < 0.05$ compared to media control.

4. CONCLUSIONS

In the current study, we have demonstrated that the OP compound, malathion, and its metabolite, malaoxon, can alter endothelial barrier function in a time-dependent manner. These changes in barrier function were shown by two different methods: measurements of cellular impedance and the flow of macromolecules through the barrier. Cellular impedance measurements are more sensitive to alterations in the endothelial barrier than changes in albumin permeability, but measuring the flow of albumin through the endothelial barrier demonstrates that the changes observed could lead to edema formation *in vivo*. In addition to the effects on barrier function, we demonstrated that malathion and malaoxon induce cellular toxicity at concentrations > 1,000 µM. Overall, these results suggest that the compounds malathion and malaoxon are able to affect the ability of endothelial cells to form a tight barrier.

ACKNOWLEDGMENTS

Support for this research was provided by the U.S. Army Edgewood Chemical Biological Center Research & Technology Directorate's Seedling Program. The authors would also like to thank Dr. Augustus W. Fountain, Ms. Rebecca Braun, and Ms. Stacey Broomall for continued scientific and administrative support.

REFERENCES

[1] Angelini, D.J.; Dorsey, R.M.; Willis, K.L.; Hong, C.; Moyer, R.A.; Oyler, J.; Jensen, N.S.; Salem, H. Chemical warfare agent and biological toxin-induced pulmonary toxicity: could stem cells provide potential therapies? *Inhal. Toxicol.* **2013,** *25* (1), pp 37–62.

[2] Testylier, G.; Lahrech, H.; Montigon, O.; Foquin, A.; Delacour, C.; Bernabe, D.; Segebarth, C.; Dorandeu, F.; Carpentier, P. Cerebral edema induced in mice by a convulsive dose of soman. Evaluation through diffusion-weighted magnetic resonance imaging and histology. *Toxicol. Appl. Pharmacol.* **2007,** *220* (2), pp 125–37.

[3] Sukriti, S.; Tauseef, M.; Yazbeck, P.; Mehta, D. Mechanisms regulating endothelial permeability. *Pulm. Circ.* **2014,** *4* (4), pp 535–551.

[4] Angelini, D.J.; Hasday, J.D.; Goldblum, S.E.; Bannerman, D.D. Tumor Necrosis Factor-α-Mediated Pulmonary Endothelial Barrier Dysfunction. *Curr. Respir. Med. Rev.* **2005,** *1* (3), p 14.

[5] Angelini, D.J.; Hyun, S.W.; Grigoryev, D.N.; Garg, P.; Gong, P.; Singh, I.S.; Passaniti, A.; Hasday, J.D.; Goldblum, S.E. TNF-alpha increases tyrosine phosphorylation of vascular endothelial cadherin and opens the paracellular pathway through fyn activation in human lung endothelia. *Am. J. Physiol. Lung Cell. Mol. Physiol.* **2006,** *291* (6), pp L1232–L1245.

[6] Werrlein, R.J.; Madren-Whalley, J.S.; Kirby, S.D. Phosgene effects on F-actin organization and concentration in cells cultured from sheep and rat lung. *Cell. Biol. Toxicol.* **1994,** *10* (1), pp 45–58.

[7] Lindstrom, A.L.; Erlandsen, S.L.; Kersey, J.H.; Pennell, C.A. An in vitro model for toxin-mediated vascular leak syndrome: ricin toxin A chain increases the permeability of human endothelial cell monolayers. *Blood.* **1997,** *90* (6), pp 2323–2334.

[8] Campbell, W.N.; Fitzpatrick, M.; Ding, X.; Jett, M.; Gemski, P.; Goldblum, S.E. SEB is cytotoxic and alters EC barrier function through protein tyrosine phosphorylation in vitro. *Am. J. Physiol.* **1997,** *273* (1 Pt 1), pp L31–L39.

[9] Warfel, J.M.; Steele, A.D.; D'Agnillo, F. Anthrax lethal toxin induces endothelial barrier dysfunction. *Am. J. Pathol.* **2005,** *166* (6), pp 1871–1881.

[10] Ades, E.W.; Candal, F.J.; Swerlick, R.A.; George, V.G.; Summers, S.; Bosse, D.C.; Lawley, T.J. HMEC-1: establishment of an immortalized human microvascular endothelial cell line. *J. Invest. Dermatol.* **1992,** *99* (6), pp 683–690.

[11] Angelini, D.J.; Moyer, R.A.; Cole, S.; Willis, K.L.; Oyler, J.; Dorsey, R.M.; Salem, H. The Pesticide Metabolites Paraoxon and Malaoxon Induce Cellular Death by Different Mechanisms in Cultured Human Pulmonary Cells. *Int. J. Toxicol.* **2015,** *34* (5), pp 433–441.

[12] Bischoff, I.; Hornburger, M.C.; Mayer, B.A.; Beyerle, A.; Wegener, J.; Furst, R. Pitfalls in assessing microvascular endothelial barrier function: impedance-based devices versus the classic macromolecular tracer assay. *Sci. Rep.* **2016,** *6*, p 23671.

[13] Ke, N.; Wang, X.; Xu, X.; Abassi, Y.A. The xCELLigence system for real-time and label-free monitoring of cell viability. *Methods Mol. Biol.* **2011,** *740*, pp 33–43.

[14] Warfel, J.M.; D'Agnillo, F. Anthrax lethal toxin-mediated disruption of endothelial VE-cadherin is attenuated by inhibition of the Rho-associated kinase pathway. *Toxins (Basel).* **2011,** *3* (10), pp 1278–1293.

Interaction of water with hygroscopic crystals studied by low-frequency Raman spectroscopy

Erik D. Emmons*, Ashish Tripathi
U.S. Army Edgewood Chemical Biological Center, Research & Technology Directorate,
5183 Blackhawk Rd, Aberdeen Proving Ground, MD 21010

ABSTRACT

Time-resolved Raman chemical imaging microscopy was used to study the interaction of water vapor with hygroscopic crystals of ammonium nitrate and ammonium nitrate/potassium nitrate mixtures. The Raman spectroscopy measurements covered both the low-frequency structural modes that are indicative of the solid-state lattice structure, as well as the high-frequency internal modes that are present in both solution and solid phases. The low-frequency lattice bands are distinct indicators of the crystalline phase, which is helpful for distinguishing between the multiple phases in which ammonium nitrate and mixed ammonium/potassium nitrate crystals can be present. As initially dry crystals of ammonium/potassium nitrate absorb water and begin to dissolve, the intensity of the low-frequency Raman bands decreases relative to the internal modes, allowing for a sensitive method for determining crystalline/solution phase. This can be done in a time-resolved manner by repeatedly imaging the same area of a sample. Time-resolved Raman chemical imaging reveals new information that could not previously be obtained and is made possible by advances in Raman chemical imaging technology. Measurements of this type are useful in areas including characterization of inkjet-printed surface-detection standards as well as transport of water and other liquids through filter and decontamination materials.

Keywords: Raman chemical imaging, time-resolved spectroscopy, lattice vibrations, polymorphism, hygroscopic

1. INTRODUCTION

Many materials absorb ambient water from the atmosphere, leading to important changes in their properties. Ammonium nitrate (AN), a common material used in explosives, is particularly hygroscopic and, in a sufficiently humid environment, will absorb enough water that it will dissolve and form a solution.[1] This has important consequences for the production of surface detection standards for testing of standoff explosive detection systems. These standards are typically produced by inkjet printing of solutions of AN and allowing the solutions to dry on a heated substrate.[2] After production, the samples consist of dried crystalline AN, and they can be stored and maintained in this form by vacuum packaging. However, if the detector testing is performed in a humid environment, the samples can quickly be rendered unsuitable by absorbing water and dissolving the crystals. In addition, the crystalline phase that is produced via inkjet printing may not necessarily be the most stable phase, but may instead be a metastable phase, since AN is known to exist in several phases depending on temperature, pressure, and humidity.[2–4] Temperature cycling may also lead to repeated transitions between these phases, which can be influenced by humidity. These transitions can lead to shattering of crystals, which changes the average particle size of the crystals.[3,4]

Raman chemical imaging is a useful technique for characterizing inkjet-printed surface coverage standards. The crystal structure of AN consists of ammonium (NH_4^+) and nitrate (NO_3^-) ions in the lattice structure. In molecular ionic crystals such as AN, there are, in general, two types of modes that can be observed in the Raman spectra. First, there are low-frequency external lattice modes in which the ions as a whole translate or rotate relative to their lattice positions. These are known as translational or librational modes, the latter sometimes called hindered rotations. These low-frequency external modes are indicative of the stolid state lattice structure of the material, and are strongly dependent on the crystalline phase. They occur at low frequencies since these types of vibrations involve weak bonds such as Van der Waals, hydrogen bonding, or electrostatic interactions. Second, there are high-frequency internal modes in which the internal bonds of the molecular ions undergo changes, such as stretching or bending motions. These types of modes are often only weakly modified by the phase of the material (i.e., whether it is a crystalline or amorphous solid, solution, liquid, or gas). For example, Hudson et al. measured the high frequency modes of nitrate

ions in concentrated aqueous solutions and found only small, but measurable frequency shifts.[5] Measurement of the low-frequency region of the Raman spectrum is a strong indicator of crystallinity, and a lack of sharp peaks in this region indicates that the material is in a non-crystalline phase. By contrast, the higher frequency internal modes are indicative of intramolecular covalent bonding and give chemical identity information. Although there is no strict dividing line, generally the external modes are found at frequencies < 300 cm^{-1}.

The Raman spectra of both the internal and external modes of AN are described in several references.[6–8] AN has several crystalline phases that occur at different temperatures. At room temperature, the ambient pressure phase is denoted as phase IV.[9] This phase is orthorhombic and is thermodynamically stable in the temperature range of -16 °C to 32 °C. From 32 °C to 84 °C, the stable phase is denoted as phase III, which is also orthorhombic.[9] Between 84 °C and 125 °C the tetragonal phase II is stable. The appearance of phase III has been shown to be highly dependent on moisture content, and in some cases with very dry samples, transitions between phase IV and phase II have occurred directly without the phase III intermediary.[3,7,9] Potassium nitrate (KN) is a closely related material used in fertilizers and is a component of black powder. KN, however, is much less hygroscopic than AN.[1] KN can form solid solutions with AN, where potassium cations randomly substitute in the positions occupied by ammonium cations.[10,11] This occurs since potassium cations are only slightly smaller than ammonium ions and can easily substitute for them in the AN lattice. [10,11] With mass fractions of KN ranging from a few wt% up to ∼40 wt%, formation of the solid solution leads to the AN phase III form becoming the stable phase at room temperature. [10,11] At higher KN concentrations, the mixtures tend to adopt the KN II phase.[10] Since KN is much less hygroscopic than AN but forms solid solutions with it, it makes a good control for showing the effects of humidity on nitrate salts.

In this study, mixtures of AN and potassium were exposed to humid environments in order to determine the effects of humidity on the structure, as observed via Raman spectroscopy. Raman chemical imaging was used in a time-resolved manner in order to show the absorption of water and the resulting dissolution of crystals. Measurements of both the low-frequency lattice modes and high-frequency internal modes were performed in order to spatially and temporally determine the distributions of crystalline and solution phases. The low-frequency modes are intense and vary significantly depending on the crystalline/solution phase present. Therefore, they give a very good diagnostic for imaging absorption and dissolution.

2. METHODOLOGY

The Raman chemical imaging microscopy experiments were performed using a WItec alpha300 R confocal Raman microscopy system with 532 nm excitation. A 10X microscope objective (Zeiss EC Epiplan-Neofluar, N.A. = 0.25) was used both to focus light on the sample and to collect the Raman-scattered return light. The laser light was coupled into the microscopic via optical fiber. A WItec RayShield Coupler was used to filter out the intense Rayleigh scattered light to prevent it from entering the spectrometer. The filter has a cutoff of ∼10 cm^{-1}, which allows for measurement of low-frequency lattice modes of materials simultaneous with the higher frequency internal modes. Approximately 20 mW of laser power was incident on the samples in these measurements. Typically, approximately 0.1–0.2 second integration was used per point, and a grid of 20 x 20 points was measured in each image. The sample was raster scanned under the laser beam with a precision stepper motor controlled stage in order to perform the mapping. The Raman-scattered light was coupled into the spectrometer using an additional optical fiber. A 300-mm focal length spectrometer in combination with a 600 grooves/mm grating was used to spectrally disperse the Raman-scattered light. The spectral range covered was from approximately -600 cm^{-1} to 3500 cm^{-1}, allowing for measurements ranging from the anti-Stokes regions of the low-frequency modes through to the N–H stretching modes. A thermoelectrically cooled (-60 °C) back-illuminated charge-coupled device from Andor was used to detect the Raman-scattered light with a quantum efficiency of greater than 90%.

The samples were prepared by first dissolving mixtures of AN and KN in ultrapure water (resistivity 18.2 MΩ.cm) in molar percentages from 0 mol% to 37 mol% KN with the remainder being AN. These solutions were then dried to precipitate out solid material and stored in a vacuum oven at 60 °C prior to measurement to ensure that they remained dry. A small amount of powder was placed on an aluminum-coated microscope slide which was then placed in a covered polystyrene petri dish with 10 μL of ultrapure water, creating a local environment of saturated water vapor during the measurements. Brightfield microscopy images of the regions that were measured with Raman chemical imaging were obtained before and after the chemical imaging. Typically, an area of 500 μm x 500 μm was measured during chemical imaging. In order to determine the change in the sample as a function of time, the same region of the sample was imaged repeatedly. In this manner, a video showing chemical images at successive times can be

constructed. These types of measurements have recently become possible due to advances in Raman chemical imaging technologies and data acquisition systems.

3. RESULTS AND DISCUSSION

In order to illustrate the discrimination ability of the low-frequency Raman modes, the Raman spectra of AN are shown in Figure 1 for both AN in the ambient crystalline phase IV as well as in solution. Note that these are spatially averaged measured, which was done to obtain high signal-to-noise spectra for illustrative purposes. These measurements are normalized so that the totally symmetric nitrate stretching mode near 1045 cm^{-1} has an intensity of 1. The most intense modes are the low-frequency lattice modes at < 200 cm^{-1} at the nitrate stretching mode at 1045 cm^{-1}. Note that the intense scattering at 0 cm^{-1} is elastic Rayleigh scattering, and the modes with negative Raman shift values are the anti-Stokes counterparts of the positive shift modes. In the solution phase, the sharp low-frequency lattice modes completely disappear and are replaced by broad amorphous scattering. The changes in the higher frequency internal modes are subtler. The nitrate stretching mode near 1045 cm^{-1} shifts to a slightly higher frequency when the crystals dissolve to form a solution. The other high-frequency modes undergo more significant changes, particularly those within the range of 1200–1700 cm^{-1}, but they are significantly less intense, making them more difficult to detect in Raman chemical imaging measurements where the signal-to-noise ratio in individual pixels is not as high as in the spatially averaged measurements shown. When time-dependent Raman chemical imaging is performed, the analysis typically centers on the most intense modes out of necessity.

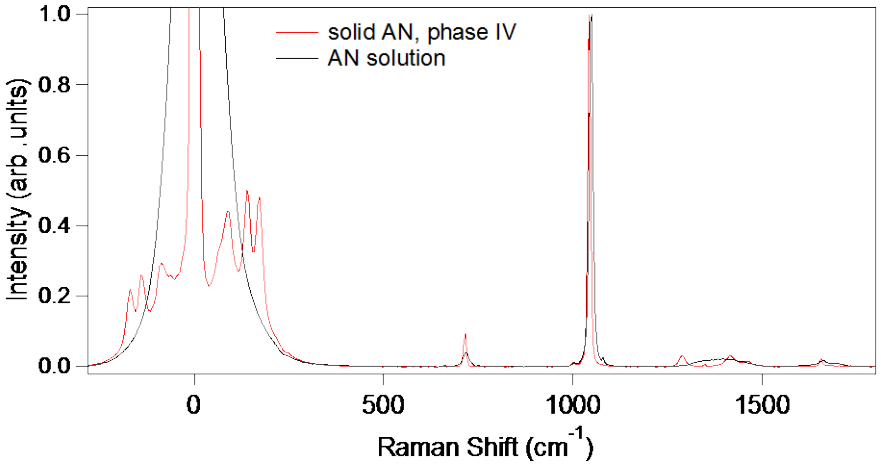

Figure 1. Raman spectra of AN in both the crystalline phase IV (red) and in solution (black). The measurements are normalized so that the totally symmetric nitrate stretching mode near 1045 cm^{-1} has a normalized intensity of 1.

Figure 2 illustrates these points in more detail. Figure 2a shows the low-frequency modes for AN in the solution phase, AN in the ambient phase IV, and a crystalline sample of AN with 11% by mass KN. The mode identifications for the lattice modes are shown as given in the literature.[7,8,11] Here, T denotes a translational-type mode, while L denotes a librational mode for the ions indicated. The spectrum for pure crystalline AN closely matches that in the literature for the ambient phase IV, with band positions that are consistent with those previously observed. As mentioned previously, mixtures of AN/KN with mass fractions of KN less than 40 % typically adopt the AN phase III lattice structure. The spectrum of the 11 % KN sample shown is similar to that of AN phase III, with frequency shifts of the modes to slightly higher frequencies.[11] Figure 2b shows mode identifications for the high-frequency internal vibrational modes for the same samples. The labels of the different modes are taken from Tang and Torrie[8], and follow Herzberg's notation. The unprimed symbols indicate the nitrate mode, with ν_1 the symmetric stretch, ν_2 the out-of-plane deformation, ν_3 the antisymmetric stretch and ν_4 the in-plane deformation. The primed symbols refer to the ammonium ion modes, with ν_2' indicating symmetric deformation and ν_4' indicating asymmetric deformation. Again, differences are observable in the high-frequency internal modes, but they are mainly small frequency shifts or changes in the weaker modes. The changes in the lattice modes are much less subtle and are useful for Raman chemical imaging measurements where single pixel measurements have lower signal-to-noise ratios.

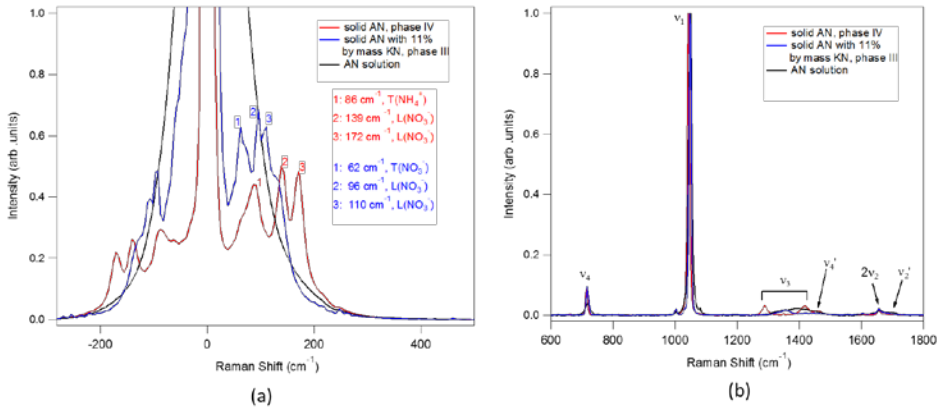

Figure 2. (a) Low-frequency Raman modes of AN and AN/KN mixtures in different phases. Mode identifications of the lattice modes of the crystalline phases are numbered. (b) High-frequency Raman modes of AN and AN/KN mixtures in different phases, with mode labels as described in the text shown.

As mentioned in the Methods section, experiments were performed where samples of the crystalline materials were exposed to saturated humidity environments and the absorption process was observed over time with Raman chemical imaging. Figure 3 shows a brightfield image of a sample of AN with 11 % KN by mass. Figure 3a shows the sample before exposure to the humid air, while Figure 3b shows the sample after it has been dissolved and a droplet of water has been formed. Figure 4 shows the same sample using time-resolved Raman chemical imaging microscopy. The images shown in Figure 4 show 20 x 20-pixel Raman chemical images at different advancing times. Each pixel in the Raman chemical images was measured with an integration time of 0.1 seconds. The area mapped with Raman chemical imaging is indicated in Figure 3 by the red box, and has dimensions of approximately 630 μm x 570 μm. Returning to Figure 4, the red frames at the top of the figure were created by integrating the nitrate symmetric stretching mode near 1045 cm^{-1}. Since this mode is not very sensitive to the material phase, it is indicative of total nitrate content regardless of phase. The green frames at the bottom of Figure 4 were obtained by integrating the total intensity of the low-frequency modes as labelled 1–3 in the blue trace in Figure 2a. Therefore, they are indicative only of the presence of crystalline materials. As can be seen by the green frames in Figure 4, the crystalline material is gradually disappearing as time goes by due to dissolution. By contrast, as indicated by the red frames, tracking total nitrate content shows a spatial redistribution from jagged crystals into spherical droplets. Note that not every frame measured is shown in Figure 4 due to limited space. Videos showing the entire data set have been created and are available from the authors upon request. Technically, the ability to perform time-resolved Raman chemical imaging is an important step forward and should have great general scientific utility.

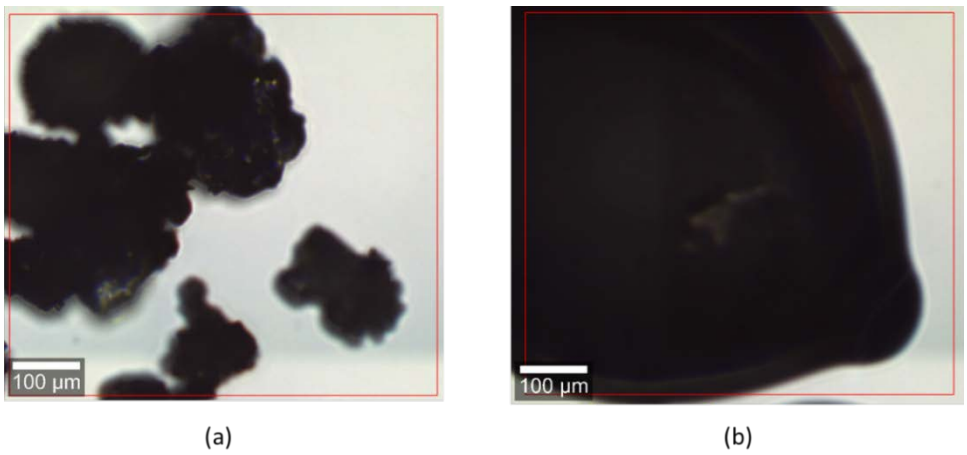

Figure 3. (a) Brightfield image of an AN sample with 11% KN by mass before exposure to saturated water vapor. (b) Image of the same area after crystal dissolution.

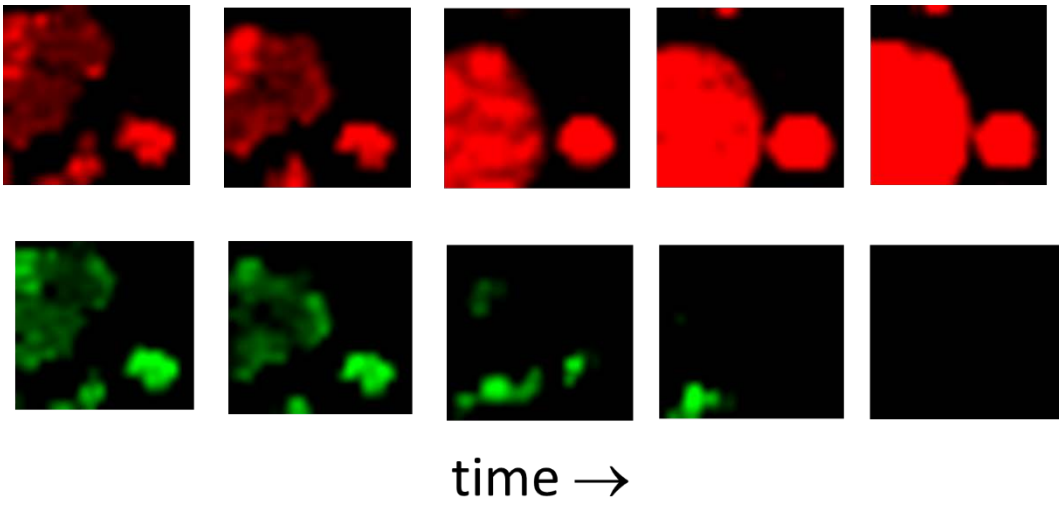

Figure 4. Raman chemical images obtained at successive times for the sample shown in Figure 3. The red frames show the integrated intensity of the nitrate stretching mode near 1045 cm^{-1} and is indicative of total nitrate content. The green frames show the integrated intensity of the low-frequency lattice modes and are indicative of crystalline content.

Additional time-resolved chemical imaging experiments were performed with different AN/KN ratios. Detailed analysis of these results is in progress. Figure 5 shows averaged spectra from the crystalline samples prior to exposure to saturated water vapor. The spectra from pure AN and pure KN are significantly different from the other samples. As mentioned, the AN/KN mixtures adopt the crystalline structure of AN phase III, which pure AN only adopts at temperatures > 32 °C. There are subtle differences between the low-frequency spectra of the different AN/KN mixtures, with the centroid of group of modes shifting to higher frequencies as the KN content increases. Initial analysis shows that the kinetics of the dissolution of the crystals does not greatly change as the KN concentration is increased to 37 % by mass. For pure KN, the kinetics are much slower, and over the course of a few hours during the experiment the crystals still were undissolved. These results seem consistent with the discussion of the critical relative humidity values given in Adams and Merz.[1] The critical relative humidity is the relative humidity above which humidity is absorbed from the atmosphere. For AN, this value is given as 59 %, while for KN the value is 90 %. Adams and Merz also discuss how, for mixtures of materials, the critical relative humidity is often close to, or even below that, of the component with the lowest critical relative humidity.[1]

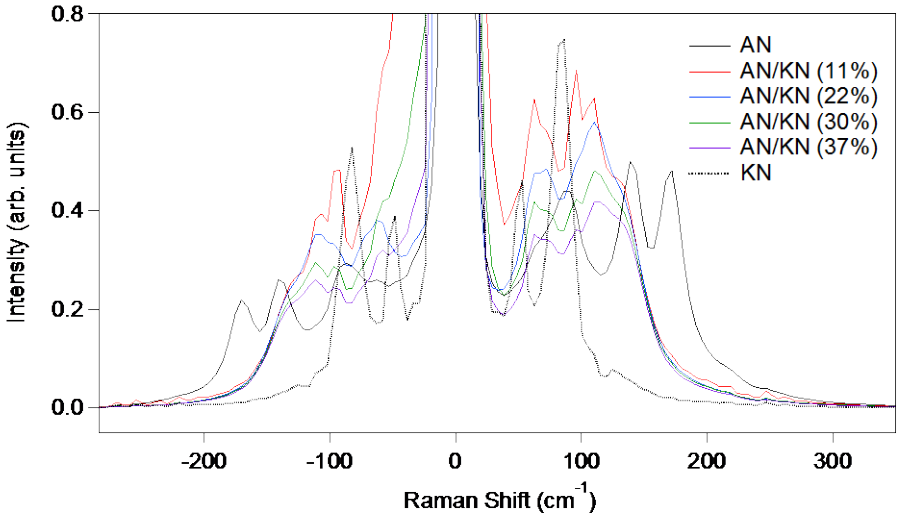

Figure 5. Low-frequency Raman spectra of different AN/KN mixtures. The relative fractions of the different compounds are indicated.

4. CONCLUSIONS

Time-resolved Raman chemical imaging has been used to study absorption of water vapor by AN/KN mixtures. Inclusion of the low-frequency region of the spectra allows for a much more sensitive discrimination between crystalline and non-crystalline nitrate content. This allows for a large number of pixels to be measured with short integration times while maintaining sufficient signal-to-noise ratios to spatially and temporally resolve the material phase. As the crystals absorb water, the low-frequency lattice modes become relatively less intense compared to the higher-frequency modes. Videos of the Raman chemical images obtained in a series of successive time frames can be obtained. Additional analysis is in progress to quantify the kinetics of the dissolution process. Future measurements will use a temperature-controlled cell that can be mounted on the microscope stage to measure the effect of humidity on different phases that the mixtures are present in at different temperatures. These measurements have relevance for production of inkjet produced surface detection standards. In addition, these types of time-resolved measurements may be useful for describing transport and reactions of water and other liquids into filter and protection materials.

ACKNOWLEDGMENTS

The authors would like to acknowledge U.S. Army funding provided through the Edgewood Chemical Biological Center's Seedling program.

REFERENCES

[1] Adams, J.R.; Merz, A.R. Hygroscopicity of Fertilizer Materials and Mixtures. *Ind. Eng. Chem.* **1929,** *21* (4), pp 305–307.

[2] Farrell, M.E.; Holthoff, E.L.; Pellegrino, P.M. Surface-Enhanced Raman Scattering Detection of Ammonium Nitrate Samples Fabricated Using Drop-on-Demand Inkjet Technology. *Appl. Spectrosc.* **2014,** *68* (3), pp 287–296.

[3] Brown, R.N.; McLaren, A.C. On the Mechanism of the Thermal Transformations in Solid Ammonium Nitrate. *Proc. Roy. Soc. A.* **1962,** *266* (1326), pp 329–343.

[4] European Fertilizer Manufacturers' Association (EFMA). *Guidance for Compatibility of Fertilizer Blending Materials* [Online]; Edition 2006, Issue 2014; Fertilizers Europe: Brussels, Belgium, 2014; http://www.productstewardship.eu/fileadmin/user_upload/user_upload_prodstew/documents/Guidance_for_compatibility2.pdf.

[5] Hudson, P.K.; Schwarz, J.; Baltrusaitis, J.; Gibson, E.R.; Grassian, V.H. A Spectroscopic Study of Atmospherically Relevant Concentrated Aqueous Nitrate Solutions. *J. Phys. Chem. A.* **2007,** *111* (4), pp 544–548.

[6] Iqbal, Z. Raman Scattering Study of the Low Temperature Phase Transitions in Ammonium Nitrate. *Chem. Phys. Lett.* **1976,** *40* (1), pp 41–44.

[7] Kenji, A.; Yoshiyuki, M.; Ichiro, N. Raman Scattering and Phase Transition of Ammonium Nitrates. *Bull. Chem. Soc. Japan.* **1981,** *54* (6), pp 1662–1666.

[8] Tang, H.C.; Torrie, B.H. Raman Study of NH_4NO_3 and ND_4NO_3—250–420K. *J. Phys. Chem. Solids.* **1977,** *38* (2), pp 125–138.

[9] Kim, J.-K.; Choi, S.-I.; Kim, E.J.; Kim, J.H.; Koo, K.-K. Preparation of Spherical Ammonium Nitrate Particles by Melt Spray. *Ind. Eng. Chem. Res.* **2010,** *49* (24), pp 12632–12637.

[10] Holden, J.R.; Dickinson, C.W. Crystal Structures of Three Solid Solution Phases of Ammonium Nitrate and Potassium Nitrate. *J. Phys. Chem.* **1975,** *79* (3), pp 249–256.

[11] Kenji, A.; Yoshiyuki, M.; Ichiro, N. Raman Scattering and Phase Transition of NH_4NO_3–KNO_3 Mixed Crystals. *Bull. Chem. Soc. Japan.* **1981,** *54* (6), pp 1667–1670.

In vitro screening of opioid antagonist effectiveness

Michael G. Feasel*, Theodore S. Moran
U.S. Army Edgewood Chemical Biological Center, Research & Technology Directorate,
5183 Blackhawk Rd, Aberdeen Proving Ground, MD 21010

ABSTRACT

Opioid agonists, such as fentanyl and its congeners, are health risks to both the Department of Defense and the general public. Traditionally, opioid overdoses are reversed with the opioid antagonist naloxone (Narcan®). However, naloxone is reported to be less and less effective at treating overdoses to more potent and new psychoactive substances. One such substance, acrylfentanyl, has been reported to be an "irreversible binder" of the opioid receptor, and thus "Narcan®-resistant." This study utilized *in vitro* methods to test/confirm the nature of the ligand/receptor interaction by competing the mu-opioid receptor with a co-administration of acrylfentanyl and naloxone. Reversibility of the acrylfentanyl was achieved at naloxone concentrations comparable to that of the control compound.

Keywords: acrylfentanyl, naloxone, opioid, new psychoactive substances, overdose

1. INTRODUCTION

Opioid overdoses have increased from 2010–2016 at a rising rate. In 2016 alone, deaths related to fentanyl increased 540 % over the number seen in 2013.[1] Illicit drug overdoses and deaths have increased as well, but not to the same degree. In Maryland, a 67 % increase in drug overdoses is second only to that of Delaware (71 %).[2] What is perhaps most concerning, is the increase in deaths due to overdose of synthetic opioids (excluding methadone). Synthetic opioids, like fentanyl, are becoming more popular, and illicit drug suppliers have been incorporating more and more potent and toxic analogues into these supplies. Carfentanil, the ultra-potent large animal tranquilizer, has been reported to be responsible for deaths in Ohio, Maryland, and Philadelphia.[3] As attention is focused on limiting the number of pharmaceuticals in circulation, illicit drug manufacturers are able to skirt federal drug scheduling by synthesizing fentanyl analogues that are not listed under any controlled substances laws. These compounds, termed "new psychoactive substances" (NPS), have little-to-no pharmacological or toxicological data, and nearly always no human use data. This makes attributing drug overdoses very difficult for forensic toxicologists when these NPS evade the standard toxicological screens used for attribution. NPS also make clinicians' and emergency medical personnel's jobs difficult in that traditional therapeutics for opioid overdose do not work as efficaciously as they have with known psychoactive compounds, like heroin.

This study aimed to assess the ability of an *in vitro* method to assess the binding interactions of opioid compounds and one novel NPS to test whether reported irreversible opioid receptor binders were truly irreversible, or were resistant to the effects of naloxone through other means, i.e., potency, distribution, or other pharmacological properties. Fentanyl (Figure 1A) was used in this study as the benchmark compound for reference, and an experimental NPS, acrylfentanyl, (Figure 1B) was used as it has been reported to be an irreversible opioid agonist and "Narcan®-resistant." Acrylfentanyl was first synthesized in 1982 as part of an effort to synthesize an affinity label of the opioid receptor macromolecular complex.[4] It was hoped that one or more of the structures generated as part of this study would achieve irreversible binding to the receptor for use in pharmacological studies *in vivo*. In the radio-ligand-binding study performed as part of the same study, acrylfentanyl demonstrated higher potency to fentanyl, from which the authors concluded that it would be suitable for affinity-labeling studies. However, during binding affinity studies, it was concluded that it did not exhibit irreversible binding to the opioid receptor. With this information, it is not at all curious why illicit drug manufacturers would include it in their inventories, but why reports of the irreversible nature of this drug compound has ever circulated as rumor.

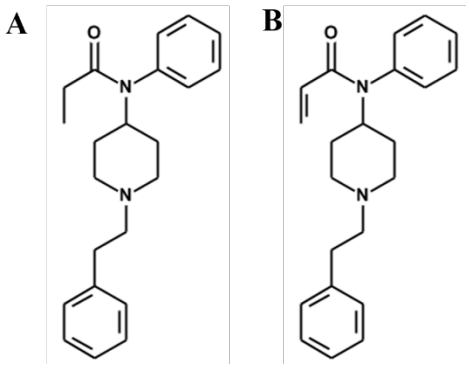

Figure 1. Chemical structures of A) fentanyl, and B) acrylfentanyl.

The current study, nevertheless, worked to confirm the reversible nature of acrylfentanyl, and validated the slightly higher potency of acrylfentanyl compared to fentanyl. Ultimately, however, this study worked toward standing up a capability at the Edgewood Chemical Biological Center that previously did not exist—to be able to not only assess potency of a pharmaceutical at its target receptor, but to assess the binding interaction of the compound which has major implications in pharmacology, symptomology, and toxicology.

2. METHODOLOGY

2.1 Chemicals

The LANCE® cAMP 10,000 assay point kit and ProxiPlate™-384s were purchased from PerkinElmer® (Shelton, CT). The LANCE® kit consisted of cAMP standard, 50 µM; Eu-cAMP tracer, ULight™-anti-cAMP; cAMP detection buffer; and bovine serum albumin stabilizer. Fentanyl citrate was procured from Mallinckrodt Pharmaceuticals (St. Louis, MO). Acrylfentanyl HCl was procured from Cayman Chemical (Ann Arbor, MI). µ-opioid receptor selective agonist [D-Ala2, NMe-Phe4, Gly-ol5]-enkephalin (DAMGO) was purchased from Tocris Bioscience (Park Ellisville, MO). HBSS 1X, HEPES 1M, Versene® solution, and Geneticin® were procured from Life Technologies™ (Grand Island, NY). DMSO, IBMX (3-isobutyl-1-methylxanthine), forskolin, and naloxone were procured from Sigma-Aldrich® (St. Louis, MO). DPBS/modified buffer and Ham's F-12 media were procured from HyClone™ Laboratories, Inc. (Logan, UT). Fetal Bovine Serum (FBS) was procured from Mediatech, Inc. (Manassas, VA).

2.2 Cell lines

ValiScreen® CHO-K1 cells expressing human µ-opioid receptors (ES-542-C) were purchased from PerkinElmer® (Waltham, MA). Cells were kept frozen in liquid nitrogen storage (vapor phase) until they were cultured. Cells were grown per PerkinElmer® product literature. Cell cultures were split when they reached ~60–80% confluency and no cells were used past passage 10. Cells were used for opioid assay when they met requirements described in the product literature, i.e., 60–80% confluency. Cellular solutions used in plating were counted on a Beckman Coulter® Vi-CELL™ XR hemocytometer prior to use. Cells were plated at a concentration of 2.0×10^5 cells/mL as optimized in previous studies.

2.3 Incubation and standard solutions

10 mM standard solutions of fentanyl, acrylfentanyl, and naloxone were made in DMSO and stored until use in a freezer at 4° F. A 1.95 mM standard solution of DAMGO was made in sterile water. 500 µM working solutions of fentanyl, acrylfentanyl, naloxone, and DAMGO were prepared immediately prior to performing the assay in fresh stimulation buffer. Stimulation buffer, forskolin dilutions, and cAMP standards were all made as needed as described by the LANCE® Ultra cAMP assay protocol immediately before performing the assay.

2.4 Assay protocol

Assay development followed the protocols set out in PerkinElmer® LANCE® Ultra cAMP assay development guidelines.[5] PerkinElmer® ProxiPlate™-384s were used for all assays with the following dimensions: Plate Height 14.4 mm, Well Diameter 3.15 mm, Well Volume 25 µL. All plates were read on a Molecular Devices SpectraMax® i3 plate reader with HTRF cartridge installed in TR-FRET endpoint mode with the following exposure parameters—Measurement 1: excitation 340 nm, emission 615 nm. Measurement 2: Excitation 340 nm, emission 665 nm. Plate type: 384 well ProxiPlate Plus White, height 14.4 mm. Shake: off. Read Order: row. Read height optimizer: on. Integration time: 0.5 ms. Excitation time: 0.05 ms. Number of pulses: 5. Meas. Delay: 0.03 ms. Read from: top. Read height: 7.04 mm. Data was acquired and analyzed in Molecular Devices' SoftMax Pro v.6.5.1.

For the competition assay, the EC_{90} was calculated using GraphPad Prism v7.0.2 (GraphPad Software, Inc., La Jolla, CA) for each agonist and this single concentration was co-administered to each well with log-dosing of the antagonist (Figure 2).

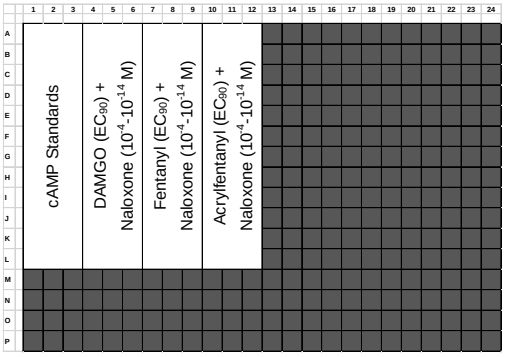

Figure 2. Plate layout of agonists, all at their respective EC_{90} molar concentration, and antagonist at log-dosing from 10^{-4}–10^{-14} M.

3. RESULTS

3.1 Acrylfentanyl dose-response

In order to properly conduct the competition assay performed with naloxone, a full dose-response curve had to be generated for each test agent. In this case, fentanyl was completed under a predecessor program,[6] but acrylfentanyl needed a full study performed. Potency was assessed for acrylfentanyl, and EC_{50}, EC_{90}, and efficacy were calculated (Figure 3). These values were compared to those of fentanyl (Table 1).

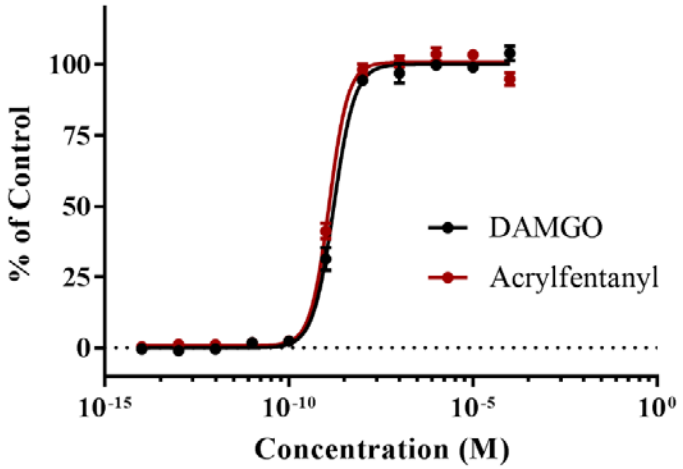

Figure 3. Dose-response curve for acrylfentanyl with control compound DAMGO for reference. Data points plotted as mean ± standard error of the mean.

Table 1. EC_{50}, EC_{90}, and efficacy values for opioid agonist compounds.

Drug	EC_{50} (M)	EC_{90} (M)	Efficacy (%)
Fentanyl*	5.11E-10	2.89 E -09	100
Acrylfentanyl	1.26 E -09	4.58 E -09	101
DAMGO	1.66 E -09	6.98 E -09	100

*Dose-response data not shown

Based on the EC_{50} calculation as a reflection of potency, it is calculated that acrylfentanyl is 0.41 times as potent as fentanyl in regard to its ability to not only bind, but cause a cAMP response in the cells. This is contradictory to the radio-ligand binding study performed in 1982, which indicated acrylfentanyl was 1.14 times more potent than fentanyl based on receptor binding alone. This study demonstrates that receptor binding is not always indicative of potency, and that functional assays may be advantageous.

3.2 Competition assay

With the EC_{50}s and EC_{90}s calculated for fentanyl and acrylfentanyl, the competition assay was then performed. Cells were incubated with both the EC_{90} of fentanyl or acrylfentanyl and log-dosing of naloxone. All other assay steps remained the same. This experimental design is dictated by the LANCE® cAMP development guidelines and reflects how much antagonist is required to reverse the EC_{90} of an agonist. From the resulting backwards-S dose-response curves, median inhibitory concentrations (IC_{50}) were calculated for naloxone against the respective agonist challenge compounds fentanyl and acrylfentanyl (Figure 4 and Table 2).

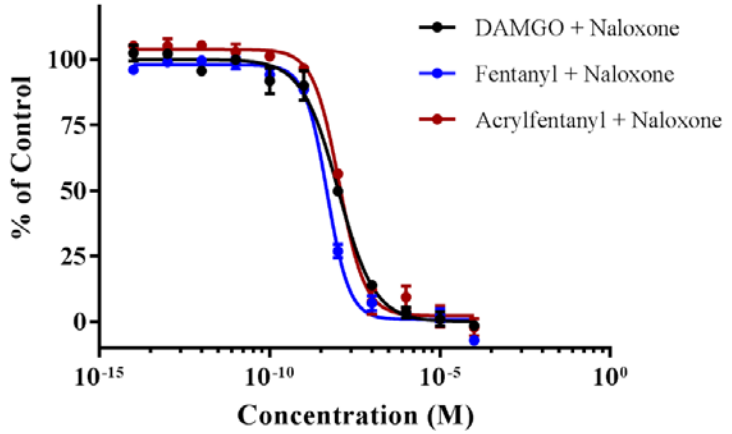

Figure 4. Inhibition dose-response curves for DAMGO (black), fentanyl (blue), and acrylfentanyl (red) with naloxone antagonism. Data points plotted as mean ± standard error of the mean.

Table 2. IC_{50} values for naloxone when challenged with EC_{90} of DAMGO, fentanyl, and acrylfentanyl

Drug	IC_{50} (M)	Efficacy (%)
Fentanyl	$4.85E^{-09}$	98
Acrylfentanyl	$1.09\,E^{-08}$	104
DAMGO	$1.04\,E^{-08}$	100

Based on the IC_{50} values of fentanyl and acrylfentanyl, 2.25 times more naloxone is required to reverse the cAMP inhibition caused by acrylfentanyl binding and receptor agonism.

4. DISCUSSION

NPS and illicit drug acrylfentanyl has been reported to be both more potent than fentanyl and Narcan®-resistant by means of irreversibly binding the opioid receptor. This has been a cause of great concern for law enforcement and public health officials, as well as clinicians. The Edgewood Chemical Biological Center, through this study, was able to respond to these reports by standing up new capabilities—to test the nature of the receptor-ligand interaction; to assess whether or not a poorly studied opioid compound was in fact more potent; and further, to observe and measure the reversibility (i.e., affinity) of the interaction at the receptor binding site. This paradigm of experiments assessed acrylfentanyl to be less than half (0.41) as potent as fentanyl, but calculated an antagonist load of 2.25 times that of fentanyl in order to reverse the effects.

These results demonstrate that potency isn't, or shouldn't be, the single descriptor when describing a threat compound. Inhibition/reversal data, such as that generated from the competition assay here, also indicates severity of toxicity from compound to compound. Had acrylfentanyl only been assessed for potency, one may have shrugged it off as a less-harmful opioid congener. However, that information combined with the amount of antagonist needed to reverse agonism renders acrylfentanyl perhaps more hazardous than initially thought. What this also indicates is that, while not entirely irreversible when bound to the opioid receptor, acrylfentanyl may require more naloxone, or other reversal agent, if an overdose with this compound is suspected.

Further, what this study also confirms is that data gathered from historical publications that are radio-ligand-binding assays may differ in their conclusions from data gathered from functional assays such as this. According to the 1982 publication on acrylfentanyl, acrylfentanyl is 1.4 times more potent than fentanyl, yet we observed a functional EC_{50} response less than half as potent as fentanyl. This indicates a substantial difference between binding a receptor and activating a receptor. This caveat can indicate even more substantial differences when looking at physiological responses. For *in vivo* studies, it may be more useful to have functional data than binding data since these higher order responses will only manifest when the receptor is activated, not merely bound.

5. CONCLUSIONS

The work performed under this Seedling program helped the Edgewood Chemical Biological Center, the U.S. Army, and the Department of Defense gain more insight into the opioid epidemic, and the chemical weapons threat opioids pose. The capabilities gained under this funded effort are able to be applied to current toxicological assessment programs, as well as be used to bring more projects and programs to the Edgewood Chemical Biological Center that will help the warfighter when faced with an opioid threat compound, both in the field and domestically.

Future studies can help further examine the problem of opioid toxicity treatment by measuring metabolism of the drug compound(s) of interest, and compare it to the metabolic rate of the reversal agent itself. Metabolic clearance data, when combined with a potency and competition assay, would not only indicate how much more (or less) reversal agent would be required initially, but how frequently it would have to be re-administered.

ACKNOWLEDGMENTS

Support for this research was provided by the U.S. Army Edgewood Chemical Biological Center Research and Technology Directorate's Seedling program. The author would like to acknowledge all those who support this opportunity for executing programs that can push the cutting edge of science and technology, and better equip the Edgewood Chemical Biological Center to provide the answers vital to the warfighter in the chemical/biological defense arena. The authors would also like to acknowledge the U.S. Army Public Health Command, specifically Drs. Valerie Adams and Emily Reinke, for the use of their multi-mode plate reader during the repairs of ours.

REFERENCES

[1] Katz, J. The First Count of Fentanyl Deaths in 2016: Up 540% in Three Years. *The New York Times*, Sep 2, 2017. Accessed 10 October 2017.

[2] *Provisional Counts of Drug Overdose Deaths, as of 8/6/2017*; The Centers for Disease Control and Prevention, National Center for Health Statistics, National Vital Statistics System: Atlanta, GA, 2017.

[3] Davis, P. Carfentanil linked to 6 deaths in 6 weeks in Anne Arundel. *Maryland Gazette*, Jun 6, 2017. Accessed 10 October 2017.

[4] Maryanoff B.E., Simon E.J., Gioannini T., Gorissen H. Potential Affinity Labels for the Opiate Receptor Based on Fentanyl and Related Compounds. *J. Med. Chem.* **1982,** *25* (8), pp 913–919.

[5] PerkinElmer®. *LANCE® Ultra cAMP Assay Development Guidelines*, version 2; Perkin Elmer, Inc.: Waltham, MA, 2010.

[6] Feasel M.G., Moran T.S., Walz A.J. *In Vitro Approach to Evaluating Opioid Receptor Subtype Specificity*, ECBC-TR-1440; U.S. Army Edgewood Chemical Biological Center: Aberdeen Proving Ground, MD, **2017;** UNCLASSIFIED Report.

Mass spectrometric identification of *Yersinia pestis* antigens specific to the select agent polyclonal antibodies

E. Randal Hofmann[a,b], Bao Q. Tran[a,b], Katherine A. Rhea[a,b], Gabrielle M. Boyd[a,b], Trevor G. Glaros[a*]
[a]U.S. Army Edgewood Chemical Biological Center, Research & Technology Directorate, 5183 Blackhawk Rd, Aberdeen Proving Ground, MD 21010
[b]Excet Inc., 6225 Brandon Ave, Suite 360, Springfield, VA 22150

ABSTRACT

Immunoprecipitation is widely used as an effective technique to capture and purify protein (antigens). By integrating this technique with liquid chromatography-mass spectrometry, we successfully developed a sensitive and selective method which resulted in several potential *Yersinia pestis* antigens to a goat anti-*Y. pestis* polyclonal antibody and a rabbit anti-*Y. pestis* polyclonal antibody. Determination of these antigen candidates is essential for the development of a suitable monoclonal antibody replacement which can be incorporated into a next-generation *Y. pestis* detection assay. Additionally, a comprehensive characterization of these polyclonal antibodies results in a deeper understanding the host-immune response which will aid in the development of new vaccines.

Keywords: *Yersinia pestis*, antigens, antibody, immunoprecipitation, mass spectrometry

1. INTRODUCTION

Detection of *Yersinia pestis*, a virulent and potential bioweapon Tier 1 Select Agent bacterium, is normally performed by an immunological detection platform provided by the Joint Program Executive Office for Chemical and Biological Defense. Our current understanding of the antigens detected on the surface of the bacteria is lacking. *Y. pestis* is known to have temperature-regulated surface proteins that may, or may not, be expressed under different growth and production conditions. Both naturally occurring and genetically engineered bacterial variants lacking these proteins may still be pathogenic, but are undetectable if the antibodies used in these assays are directed toward them. Understanding what surface antigens are primarily recognized by these antibodies would aid in the development of a new assay able to detect all pathogenic variants.

Under the support of the Defense Threat Reduction Agency and the Defense Biological Product Assurance Office, researchers in the Edgewood Chemical Biological Center BioSciences Division worked to develop a new, quick, and cost-effective assay that can recognize all the pathogenic variants of *Y. pestis*. The principal concept of the assay is to create *Y. pestis* antibodies by grafting a single-chain variable fragment (scFv) that specifically binds to the bacterial antigens in a thermal IgG acceptor scaffold. Among the existing anti-*Y. pestis* antibodies currently used in detection platforms provided by the Defense Biological Product Assurance Office are two polyclonal antibodies, AB-G-YERS (goat anti-*Y. pestis*) and AB-R-YERS (rabbit anti-*Y. pestis*), which are targeted for additional development and integration into the next generation *Y. pestis* detection assay. However, the bacterial antigens to these antibodies, which play a critical role in the assay development, have not been well characterized at the molecular level. High-throughput discovery of antigens is normally done by employment of protein or peptide arrays. The peptide array assay provides information on the immunogenic peptide epitopes that can be used to predict the structure and properties of the *Y. pestis* protein antigens; however, it cannot directly identify the immunogenic proteins. On the other hand, the Nucleic Acid-Programmable Protein Array (NAPPA)[1] allows for thousands of proteins to be synthetized and captured in high spatial density on a pre-printed DNA array by incubation with *Y. pestis* cell extract. This array provides a simple platform that is capable of specific and sensitive screening for antigens that induces a strong immune response. However, the NAPPA is limited only to the translated proteins present in the array. In addition, both the technologies are quite expensive and time consuming; especially when the peptide or DNA libraries need to be generated *de novo*.

To overcome the limitations of NAPPA and other peptide array assays, we employed an accurate and sensitive approach that integrated immunoprecipitation (IP) and liquid chromatography-mass spectrometry (LC-MS)[2] to determine globally the *Y. pestis* antigen's immune response to the polyclonal antibodies. IP is widely used as an effective technique based on antibody-antigen interaction to capture and purify protein targets which are bound onto an antibody immobilized on solid-supporting material. Eluent of purified/enriched protein targets were then reduced, alkylated, and cleaved into peptides prior to analysis on an LC-MS system. LC-MS is a powerful, high throughput, and sensitive technique capable of simultaneous identification of thousands of proteins in a single analysis via determination of generated peptides. With the described advantages, the combination of IP and LC-MS for determination of antigens is cost effective, particularly for organisms that don't have an available cDNA library for NAPPA.

To fulfill the gap of identification of targets that may not be recognized by NAPPA, as well as to offer a cross-reference approach to support and validate the technique, we developed an advance application of IP and LC-MS to determine accurately and sensitively the protein target's immune-response to the polyclonal anti-*Y. pestis* antibody. This work resulted in the identification of several potential *Y. pestis* antigens recognized by two different anti-*Y. pestis* polyclonal antibodies. Interestingly, these targets do not overlap with the data generated using the NAPPA approach. Additional, work is needed to confirm these antigens using different *Y. pestis* strains and alternative methods to generate bacterial lysates.

2. EXPERIMENTAL AND METHODOLOGY

2.1 Bacterial growth and lysate preparation

The *Y. pestis* strain EV76 was grown in brain heart infusion (BHI) broth by inoculating a 1-mL culture with a single colony picked from a plate streaked from a frozen glycerol stock. Cultures were scaled up to 10 mL using the 1-mL starter culture, and then 100 mL using the 10-mL culture. Cultures were incubated at 28 °C overnight (16–20 hrs) with shaking. Cultures were harvested by centrifugation at 4,000 x g for 10 minutes. The cell pellet was washed once with 20 mL of a 20 % sucrose solution and pelleted again by centrifugation. Cells were re-suspended in 20 % sucrose to a final volume of 7 mL. Cells were then lysed by passage through an M-110P Microfluidizer® (Microfluidics™; Westwood, MA) at 20,000 psi. The lysate was then centrifuged at 700 x g for 10 minutes to remove large cell debris before loading onto the gradient. A sucrose gradient was generated in a 30-mL ultracentrifuge tube by layering 16 mL of 50 % sucrose over 6 mL of 60 % sucrose. The 7-mL lysate was then layered on top of the gradient. This gradient was centrifuged at 73,000 x g at 4 °C for 16 hours in an ultracentrifuge (Beckman Coulter®; Brea, CA). The outer membrane (OM) fraction, which is found at the 50–60 % sucrose interface, was extracted using a 3-mL syringe. The OM fraction was transferred to a new ultracentrifuge tube and mixed with 5 mL of distilled deionized (pure) water. This mix was then centrifuged for 6 hours at 73,000 x g at 4 °C. The supernatant was then decanted, and the OM pellet was washed once and resuspended in pure water.

2.2 Immunoprecipitation antigen enrichment

The SCIEX BioBA high capacity sample enrichment kit (SCIEX; Framingham, MA) was selected for use in our immunoprecipitation experiment since the beads are less susceptible to degradation and have a higher binding capacity than magnetic bead-based systems. The IP experiments were performed following the manufacturer's protocol with a few slight modifications. Briefly, all antibodies were diluted to 1 mg/mL before binding to the beads.

Immunoprecipitations were carried out overnight at 4 °C using 200 µL of *Y. pestis* outer membrane material. A negative control sample was prepared identically using an anti-Shigella polyclonal antibody. The IP eluent was neutralized with 5 µL of BioBA neutralization buffer (500 mM ammonium bicarbonate, pH 8). One 4-µL portion of IP eluent was run on a Bio-Rad Experion™ automated electrophoresis system (Bio-Rad; Hercules, California) gel to visualize total protein content following manufacturer's protocol.

2.3 Sample preparation and LC-MS analysis

The rest of the IP eluent was reduced with 5 µL of reducing agent (100 mM tris(2-carboxyethyl)phosphine solution) for 60 minutes at 50 °C. The reduced sample was alkylated with 5 µL of cysteine blocking solution (100 mM iodoacetamide) at room temperature for 30 minutes. Proteins were digested overnight at 37 °C by addition of 10 µL of 30 µg/mL of Trypsin/Lys-C and 5 µL of 0.4 % SCIEX mass spectroscopy-compatible surfactant. The tryptic digest

was acidified with 20 µL of 10 % formic acid and dried to ~5 µL in a Savant™ SpeedVac™ (Thermo Scientific™; Waltham, MA). 12 µL of loading buffer (5 % acetonitrile/0.1 % formic acid) was added, and a 4-µL sample was injected for LC-MS analysis.

LC-MS analysis was performed using a Dionex™ UltiMate™ 3000 RSLCnano system coupled with a Q Exactive™ Plus mass spectrometer (Thermo Scientific™; Waltham, MA). Peptides were separated on an EASY-Spray™ 75 µm x 50 cm C18 column over a 182-minute LC gradient using a mobile phase A (5 % acetonitrile/95 % water/0.1 % formic acid) and a mobile phase B (80 % acetonitrile/20 % water/0.1 % formic acid). Peptides were analyzed using a Top-12 data-dependent acquisition method. The LC-MS data was processed using MaxQuant software, and searched against a UniProtKB protein sequence database of *Y. pestis* UP000000815 plus sequences of *Oryctolagus cuniculus* (rabbit, taxonomy ID 9986) and *Capra hircus* (goat, taxonomy ID 9925) immunoglobulins. Peptide and protein identifications were filtered at a minimum false discovery rate of 0.01%. Only proteins identified with a minimum of 2 peptides were considered for analysis.

3. RESULTS

In this study, 812 proteins were identified in the anti-Shigella negative control monoclonal antibody. These proteins were considered non-specific targets, and were not considered as potential *Y. pestis* antigens. The anti-*Y. pestis* goat and rabbit polyclonal antibodies pulled down a total of 94 protein targets from the *Y. pestis* outer membrane extract; 58 from the goat polyclonal antibody, and 80 from the rabbit polyclonal antibody. The top 50 proteins based upon abundance are presented in Table 1. Among these, 44 proteins (46.8 %) were recognized by both antibodies, while another 14 and 36 proteins were specific to goat Ab and rabbit Ab, respectively (Figure 1).

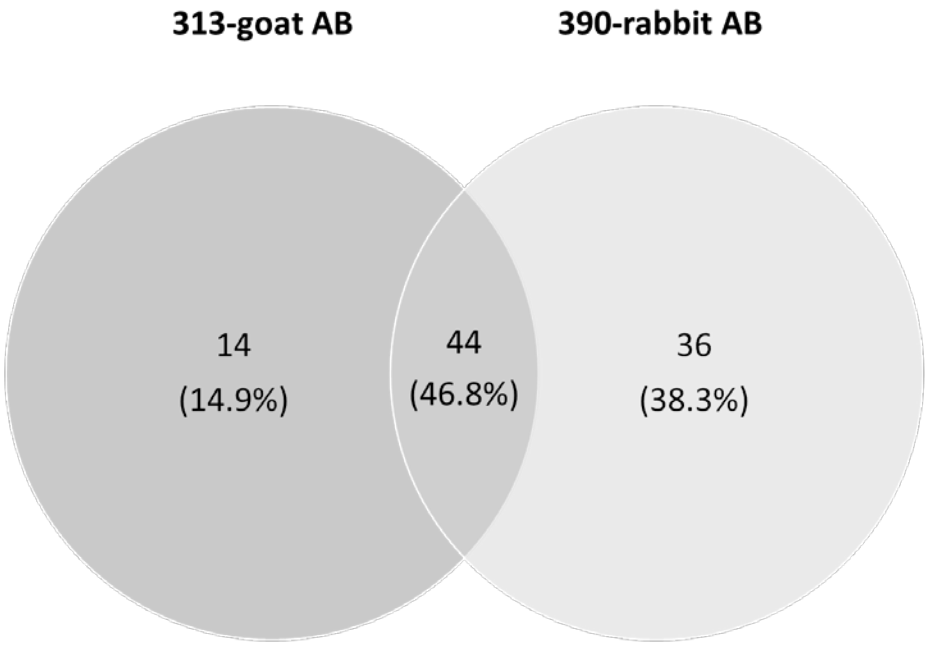

Figure 1. Venn diagram illustrating the distribution of *Y. pestis* proteins determined by IP LC-MS analysis as antigens to goat and rabbit antibodies.

We observed that a majority of the protein targets determined in the rabbit and goat antibody's IP eluent had molecular weights ranging roughly from 29–90 kDa as shown in Table 1. A similar result was also observed in the protein gel analysis (Figure 2). Unlike the IP eluent of rabbit polyclonal antibody, the goat polyclonal antibody had fewer overall proteins; however, these proteins span a broader range of molecular weights, from 28–110 kDa as determined by LC-MS.

Table 1. Top 50 *Y. pestis* protein targets recognized by goat and rabbit polyclonal antibodies using an IP LC-MS approach. The proteins are listed in order of highest to lowest relative abundance.

Recognized by Ab 313	Recognized by Ab	Protein description	Gene names	Peptides	Peptides 313YPM	Peptides 390YPM	Mol. weight [kDa]
+	+	Urease subunit gamma	ureA	7	7	2	11.05
+	+	Putative exported protein	YPO2336	13	13	5	36.96
+	+	Chaperone protein caf1M	caf1M	9	8	8	28.75
+	+	6,7-dimethyl-8-ribityllumazine synthase	ribH	5	5	4	16.20
+		Carbon storage regulator homolog	csrA	2	2	0	6.85
+	+	Transketolase	tkt	19	13	18	71.87
	+	Carbonic anhydrase	YPO0819	7	0	7	26.81
	+	Exported sulfate-binding protein	sbp1	8	0	8	36.39
	+	Putative glutathione S-transferase	yghU	7	0	7	32.13
+	+	Ferritin	ftn	4	3	4	19.21
	+	Inorganic pyrophosphatase	ppa	4	0	4	19.61
+	+	N utilization substance protein B homolog	nusB	3	2	1	15.51
+	+	Secreted chorismate mutase	pheA2	4	2	4	20.75
	+	Phosphoheptose isomerase	gmhA	4	0	4	20.99
	+	Putative shikimate dehydrogenase	YPO1610	6	0	6	31.72
+	+	Uncharacterized protein	YPO1362	12	8	10	63.49
	+	Superoxide dismutase	sodB	4	0	4	21.47
	+	Glucose-6-phosphate isomerase	pgi	11	0	11	61.16
	+	Aminoacyl-histidine dipeptidase	pepD	9	0	9	52.99
	+	Glucosamine-6-phosphate deaminase	nagB	5	0	4	29.67
	+	Sugar-binding periplasmic protein	YPO4037	6	0	6	35.91
+	+	Met repressor	metJ	2	1	1	12.15
	+	Periplasmic oligopeptide-binding protein	oppA	10	0	10	61.62
+	+	Putative glutamine-binding periplasmic protein	glnH	4	3	3	26.95
	+	Putative sugar binding protein	YPO3472	7	0	7	48.19
	+	Probable soluble cytochrome b562 1	cybC1	2	0	2	14.19
+	+	FAD:protein FMN transferase	apbE	5	2	5	37.48
+		Uncharacterized protein	YPO0665	2	2	0	16.38
+	+	Orotidine 5-phosphate decarboxylase	pyrF	3	1	2	26.21
+		Lipopolysaccharide heptosyltransferase-1	rfa-2	4	3	0	36.12
	+	Peptidyl-prolyl cis-trans isomerase	ppiB	2	0	1	18.15
	+	3-hydroxydecanoyl-[acyl-carrier-protein] dehydratase	fabA	2	0	1	18.81
	+	Protein SprT	sprT	2	0	2	19.92
+		1,4-dihydroxy-2-naphthoyl-CoA synthase	menB	3	1	0	31.60
+	+	Lipid-A-disaccharide synthase	lpxB	4	3	2	43.26
+	+	TetR-family transcriptional regulatory protein	YPO2378	2	2	1	21.80
+	+	Putative iron transport protein	YPO4022	3	2	1	34.13
+		Uncharacterized protein	YPO2401	4	1	0	45.63
+	+	Bifunctional uridylyltransferase/uridylyl-removing enzyme	glnD	9	8	3	103.16
+	+	Metallo-beta-lactamase superfamily protein	YPO1409	2	2	1	23.52
+		Endonuclease III	nth	2	2	0	23.86
	+	Putative sugar-binding protein	YPO1719	4	0	4	48.67
	+	Ribulose-phosphate 3-epimerase	rpe	2	0	2	24.43
+	+	Uncharacterized protein	YPO0864	2	2	1	24.94
+	+	L-seryl-tRNA(Sec) selenium transferase	selA	4	3	2	50.21
+	+	Thiosulfate-binding protein	cysP	3	1	3	38.51
	+	Probable short-chain dehydrogenase	ybbO	2	0	1	27.94
+	+	Deoxyribose-phosphate aldolase 2	deoC2	2	1	1	28.274
	+	Uncharacterized protein	YPO3242	2	0	2	28.976
+	+	Maltose-binding periplasmic protein	malE	3	3	3	43.828

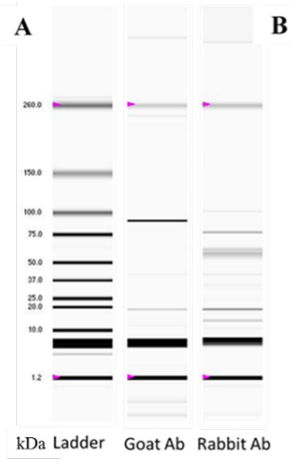

B

Sample	Mol. Wt. (kDa)	% Total
Goat Ab	90.0	68
Goat Ab	18.9	13
Goat Ab	41.2	3
Goat Ab	243.4	2
Goat Ab	208.4	2
Rabbit Ab	57.9	26
Rabbit Ab	19.0	18
Rabbit Ab	14.2	15
Rabbit Ab	77.6	11
Rabbit Ab	61.6	8
Rabbit Ab	11.0	6
Rabbit Ab	41.1	3
Rabbit Ab	34.1	3
Rabbit Ab	32.6	3

Figure 2. Molecular weight ranges of the IP eluents as determined by (A) Bio-Rad Experion™ gel and (B) molecular weights and relative abundance of the most abundant gel bands (minimum 2 %).

4. CONCLUSIONS

None of the LC-MS-determined proteins in both IP eluents matched to the clones list of 281 outer membrane proteins selected by the bioinformatics team from Arizona State University for the NAPPA assay development. Some possible explanations for why there was no overlap between the two lists are that the techniques used to extract the membrane fraction were compromised by alterations made to the protocol due to safety concerns that resulted in a less accurate extraction technique, or that the incubation time for the IP was too long—resulting in inference from non-specific binding of highly abundant proteins. Whole cell extracts may be suitable for these experiments without the need to extract the membrane, given the specificity of the antibodies.

By applying the IP LC-MS strategy, we successfully identified *Y. pestis* strain EV76 proteins targeted by the two polyclonal antibodies AB-G-YERS and AB-R-YERS; although, additional work is needed to confirm these potential antigens. Moving forward, this approach should be applied to other strains of *Y. pestis* to determine the common antigens among the different strains. These results will be incorporated with NAPPA data to finalize the best antigen candidates for developing *Y. pestis* detection assay. In addition, this data will be made available to researchers in the U.S. Army Medical Command, and will hopefully be valuable for the development of a safe vaccine, which is not currently available in the United States.

ACKNOWLEDGMENTS

The authors would like to thank Dr. Way Fountain and Ms. Rebecca Braun for their scientific and administrative support. Support for this research was provided by the U.S. Army Edgewood Chemical Biological Center Research and Technology Directorate's Seedling program.

REFERENCES

[1] Ramachandran, N.; Raphael, J.V.; Hainsworth, E.; Demirkan, G.; Fuentes, M.G.; Rolfs, A.; Hu, Y.; LaBaer, J. Next-generation high-density self-assembling functional protein arrays. *Nat. Methods.* **2008,** *5* (6), pp 535–538.

[2] ten Have, S.; Boulon, S.; Ahmad, Y.; Lamond, A.I. Mass spectrometry-based immuno-precipitation proteomics–The user's guide. *Proteomics.* **2011,** *11* (6), pp 1153–1159.

Raman chemical imaging based cell cytometry: differentiation and quantification of viable and gamma-deactivated *B. anthracis* Sterne spore

Jason Guicheteau*, Ashish Tripathi, Erik D. Emmons, Michael H. Kim, Jerry W. Pfarr
U.S. Army Edgewood Chemical and Biological Center, Research & Technology Directorate,
5183 Blackhawk Rd, Aberdeen Proving Ground, MD 21010

ABSTRACT

In 2015, viable *Bacillus anthracis* spores were inadvertently shipped outside of Department of Defense-controlled laboratories. Since that time, ongoing studies have been attempting to establish more robust and quantitative inactivation methodologies to eliminate future occurrences. One particular study is focusing on gamma irradiation inactivation of *Bacillus anthracis* Sterne spores. We believe, with Raman chemical imaging microscopy, individual spores can be analyzed rapidly to obtain spectral differences between viable and gamma-irradiated spores, isolating unique spectral differences and enhancing discrimination capability.

Keywords: *Bacillus anthracis*, Raman chemical imaging, gamma inactivation

1. INTRODUCTION

On May 22, 2015, a private company notified the Centers for Disease Control and Prevention that inactivated *Bacillus anthracis* (BA) spores in their possession were viable. Unfortunately, upon an exhaustive review of the situation it was determined that the material in question originated from a Department of Defense lab and was further distributed to other areas around the country and the world.[1] Since that incident, the Centers for Disease Control and Prevention and the Department of Defense has focused on re-assessing and better characterizing all inactivation procedures currently being performed across all capable laboratories. The Edgewood Chemical Biological Center (ECBC) has been a crucial part of this process and has been tasked to provide the Chemical Biological Defense Program with a methodology to properly inactivate *B. anthracis* spores, while maintaining molecular and immunological targets for assay development, performance verification, and proficiency testing. To that end, along with more robust inactivation methods needing to be developed, analysis techniques to rapidly detect and determine viable and non-viable biological material is a priority.

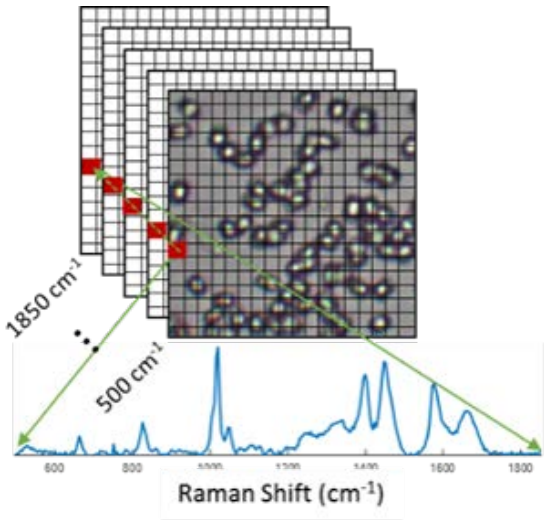

Figure 1. Raman hyperspectral cube.

Through the work being led by Dr. Sandy Gibbons at ECBC in coordination of the "*Bacillus anthracis* (Ba) Gamma Inactivation Study" sponsored by the Office of the Secretary of Defense, the ECBC Spectroscopy Branch was able to secure a small sample set of viable and non-viable gamma irradiated *B. anthracis* Sterne spores (BASP) currently being investigated. Utilizing Raman chemical imaging we were able to ascertain several key spectral differences between the viable BASP samples and gamma irradiation deactivated spore samples. Raman chemical imaging allows for spatially resolved Raman spectral information to be obtained through Raman hyperspectral cubes in which every pixel or binned group of pixels is treated as an independent Raman spectrograph (Figure 1). This allows for the probing of a field of view (FOV), resulting in chemical analysis of individual spores as well as chemical discrimination of heterogenous type mixtures. Our work presents a study of Raman spectral features to specific biological sources to identify chemical components that give rise to the spectral features responsible for viable, non-viable discrimination. The goal of this work was to determine if a spectral analysis method be can developed to rapidly verify the difference between viable and non-viable bacteria, including determination of inactivation method.

2. EXPERIMENTAL METHODS

2.1 Materials

Multiple aliquots at 1–2 × 10^{10} BASP/mL were produced by the Naval Surface Warfare Center Dahlgren Division Chemical, Biological, and Radiological Defense Division using a standard spore preparation method and were received by ECBC for this irradiation study. This sample was diluted 1,000 times, and multiple 2-µl aliquots of the suspension were deposited on an aluminum-coated microscopy slide. The water was allowed to dry, leaving a residue of BASP on the slide.

2.2 Gamma irradiation

The JL Shepherd & Associates Model 484R-2 is a self-contained Category I Co^{60} gamma irradiator with 3 Co^{60} sources, each at 6,500 curie, for a total of 19,500 curie at time of source replacement in September 2016. A full width door provides access to the entire irradiation chamber, where samples can be rotated on turntables to receive an integrated dose, equivalent to cylindrical source geometry, for exposure over 1 minute. Source operation is via pneumatic cable cylinders; the source travels from the fully shielded off position to the irradiation chamber in less than 2 seconds, and returns in less than 2 seconds. Sample dose is determined by turntable position and irradiation time. The door and source drive systems are fully interlocked so that the source is fully shielded. Irradiation was performed at 40 kGy.

2.3 Raman microscopy

The Raman chemical imaging microscopy experiments were performed using a WItec alpha300 R confocal Raman microscopy system with 532 nm excitation. A 100X microscope objective (Zeiss EC Epiplan-Neofluar, N.A. = 0.9) was used both to focus light on the sample and collect the Raman scattered return light. The laser light was coupled into the microscopic via optical fiber. A WItec RayShield Coupler was used to filter out the intense Rayleigh scattered light to prevent it from entering the spectrometer. The filter has a cutoff of ~10 cm^{-1}, which allows for measurement of low-frequency lattice modes of materials simultaneous with the higher frequency internal modes. Approximately 4 mW of laser power was incident on the samples in these measurements. Typically, 6-second integration was used per point and a spectrum was acquired from a 0.5 µm x 0.5 µm area. The sample was raster scanned under the laser beam with a precision stepper motor controlled stage in order to perform the mapping. The Raman scattered light was coupled into the spectrometer using an additional optical fiber. A 300-mm focal length spectrometer in combination with a 600 grooves/mm grating was used to spectrally disperse the Raman-scattered light. The spectral range covered was from approximately 600 cm^{-1} to 3500 cm^{-1}, allowing for measurements ranging from the anti-Stokes regions of the low-frequency modes through to the N–H stretching modes.

2.4 Biological Raman library acquisition

Raman chemical imaging from a few selected FOVs of BASP deposited on an aluminum-coated microscopy slide was acquired. The locations of these FOVs were recorded. The aluminum slide containing the spore was exposed to a gamma radiation dosage of 1 kGy. The Raman chemical images from the same FOVs were acquired using the same instrument settings. Additionally, 20 µL of 0.01% Tween 80 solution was added to one of the many BASP-containing

spots on the microscopy slide. The droplet was stirred and deposited on a tryptic soy agar plate for determination of growth. The above steps were repeated until no growth was observed. The BASP spectra before and after 40 kGy of gamma radiation were used as library spectra of viable and deactivated spores, respectively.

3. RESULTS AND DISCUSSION

The primary goal of this effort was to determine and identify spectral differences between viable and gamma-irradiated spores of *B. anthracis* Δ Sterne, and determine if gamma exposure time differences could be used to monitor and identify levels of inactivation due to irradiation. Due to technical issues with the JL Shepherd Co^{60} Irradiator, the exposure amounts and time experiments are still currently being performed. The results below are from an initial exposure of 40 kGy used as a baseline for the follow-up experiments.

Upon receipt of BASP samples, a visual examination via the brightfield imaging component of the microscope determined that no readily identifiable differences between irradiated and viable cells existed at the 20X magnification level (Figure 2A and B). However, upon Raman interrogation, unique spectral features associated with the interrogated biological material were observed. Figure 2C, shows the average spectrum obtained from 300 single viable spores with several bands of interest, 1017 cm^{-1} and 1395 cm^{-1} observed. These bands are known to be associated with calcium dipicolinic acid (Ca-DPA), a common marker for presence of certain types of bacterial spores. More specifically, the 1017 cm^{-1} band is associated with a symmetric ring breathing mode and the 1395 cm^{-1} to the O–C–O symmetric stretch.[2] Upon examination of the obtained average Raman chemical imaging spectrum (200 spores) of the gamma-irradiated spores (Figure 2D), the two previously mentioned vibrational bands are noticeably absent along with other diminished bands (amide peaks at 1243 cm^{-1} and 1335 cm^{-1}, respectively). The band observed at 1004 cm^{-1} is, again, a ring breathing mode, but associated with the amino acid phenylalanine.[2] Concentrating on this initial difference, we explored whether using the Ca-DPA maker may lead to discrimination between viable and gamma-irradiated (deactivated) BASP.

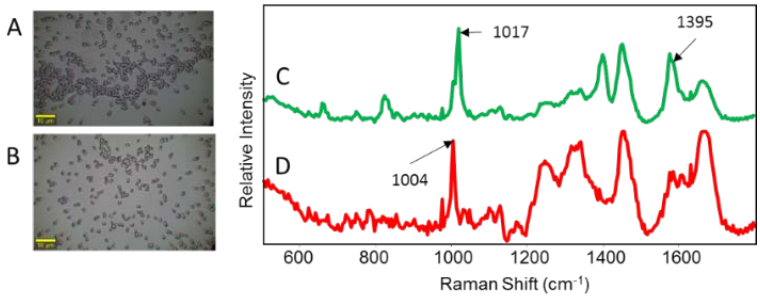

Figure 2. Brightfield image of A) viable and B) gamma irradiated spores. Raman library spectrum of C) viable BASP and D) gamma-irridated BASP.

Initially, library data, as described above, was used to determine if Raman chemical imaging analysis could identify viable spores in the field of view. Figure 3A, is the brightfield image of a FOV with approximately 144 viable BASP. Spectral data acquisition was performed as described above, followed by Pearson's cross correlation analysis (CCR) to perform a direct one-to-one spectral match between the library BASP spectrum with the experimental spectra collected in the FOV. Using a threshold of $r > 0.80$, a false-color image (Figure 3B) superimposed on the brightfield image clearly shows that, from the spectral data in Figure 3C, only viable spores of *B. anthracis* Sterne are observed. Each collected spectrum was also compared with the library spectrum of the gamma-irradiated spores with no identifications made.

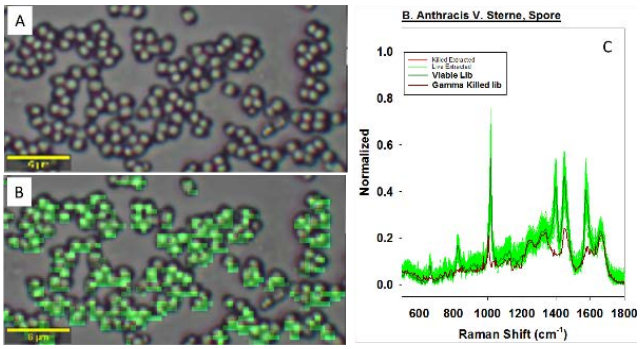

Figure 3. A) 144 viable spores in FOV. B) False color image of A, from CCR using $r > 0.80$ identifying only viable BASP. C) Comparison of collected spectra of individual spores against library spectrum of viable (green) and gamma-irradiated (red) spores used for data analysis.

Upon completion of this first set of experiments, the viable BASP used for analysis were gamma irradiated with 40 kGy following the current protocols being developed by ECBC to ensure full deactivation of the spores. Again, a sample was deposited onto an aluminum-coated slide, and Raman chemical imaging performed. Following the same procedures as above, this clearly shows that only non-viable (gamma-irradiated) spores were observed in the investigated FOV (Figure 4).

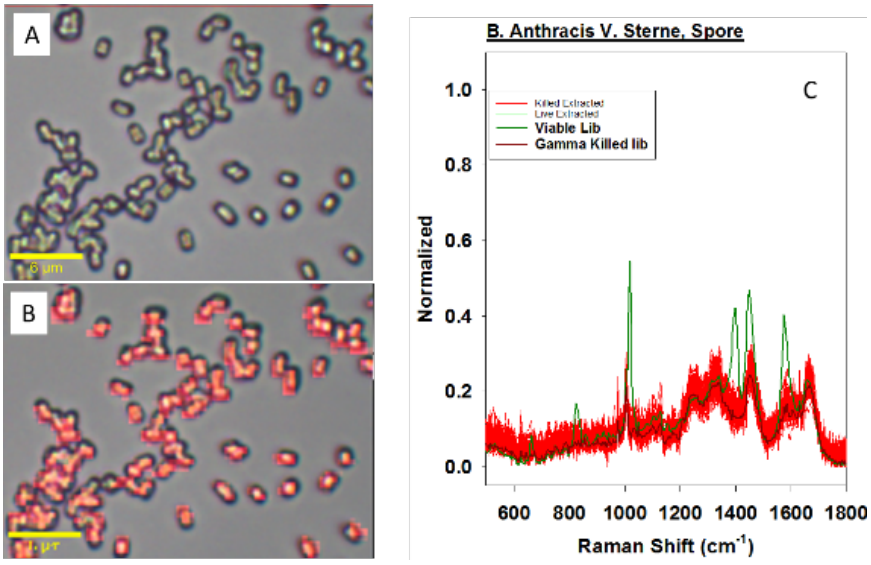

Figure 4. A) 101 viable spores in FOV. B) False-color image of A, from CCR using $r > 0.80$ identifying only non-viable (gamma irradiated) BASPs. C) Comparison of collected spectra of individual spores against library spectrum of viable (green) and gamma irradiated (red) spores used for data analysis.

Following determination that viable and non-viable (gamma irradiated) BASP contained significant spectral differences, a 50:50 mixture of viable and non-viable spores was prepared and assessed with Raman chemical imaging. In Figure 5, the brightfield image (Figure 5A) is shown to visually demonstrate there are no distinguishable differences between a mixture of viable and gamma irradiated deactivated spores. However, upon performing Raman chemical imaging and utilizing a threshold of $r > 0.80$ to spectrally match each individual spore in the FOV, a clear determination of viable versus gamma-irradiated spores is observed. In this mixture, a total of 174 spores were counted, of which 70 were determined to be viable, and 104 determined to be gamma-irradiated (non-viable) spores.

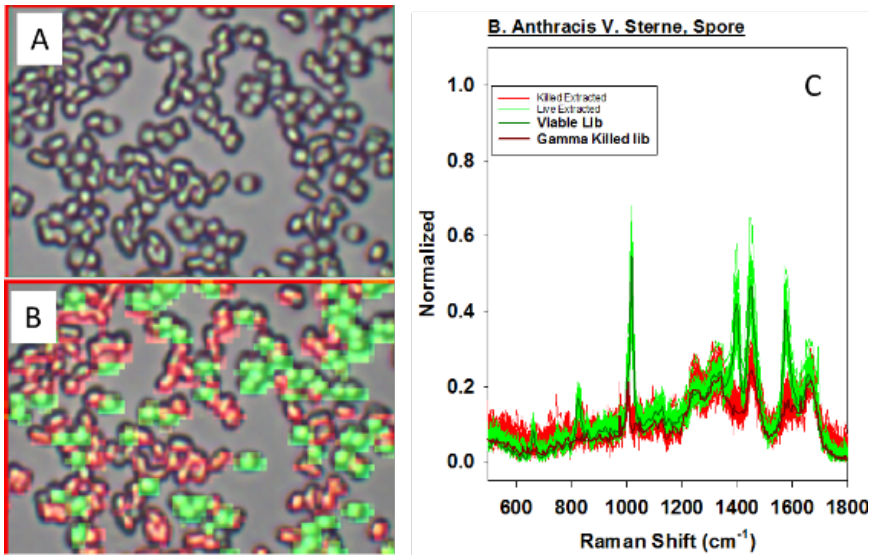

Figure 5. A) 174 spores in FOV. B) False color image of A, from CCR using r>0.80 idenfiying both viable and non-viable spores. C) Comparison of collected spectra of indidual spores against library specrtrum of viable (green) and gamma irradiated (red) spores used for data anlysis

To further our hypothesis that the presence or absence of Ca-DPA-specific vibrational bands could be used as indicators of gamma irradiated spores, the spectral data acquired in the above mixture in Figure 5 was re-processed. In Figures 3–5, the CCR was performed using the spectral information between 500–1800 cm^{-1}, which accounts for all vibrational bands in the fingerprint region. Figure 6 shows the same analysis, but only using the spectral bands 1017 cm^{-1} (Ca-DPA from viable spore library) and 1004 cm^{-1} (phenylanine vibration, gamma-irradiated BASP) for analysis. As can be seen, the discrimination between the spores is visible, and the exact 70 viable and 104 gamma-irradiated spores were identified.

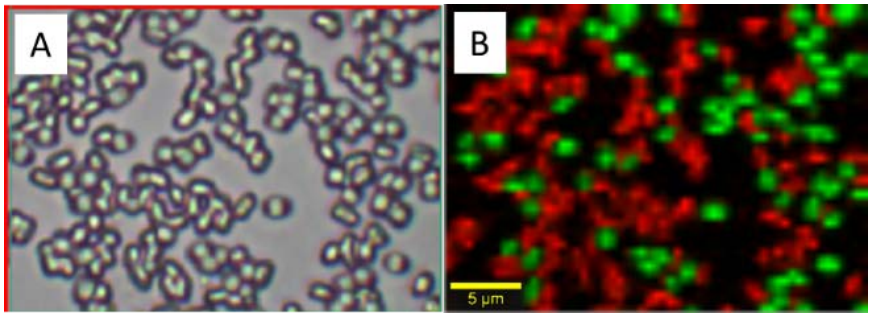

Figure 6. A) Brightfield image of a 50:50 mixture of viable and gamma-irradiated BASP. B) False-color image after CCR processing with 1017 cm^{-1} and 1004 cm^{-1} vibrational bands.

Principal component analysis was performed on the above data set and is shown in Figure 7. Figure 7A shows the first three principal components, clearly demonstrating separation between the viable and non-viable (gamma-irradiated) spores—showing that the majority of discrimination is due to the disappearance of the Ca-DPA spectral components.

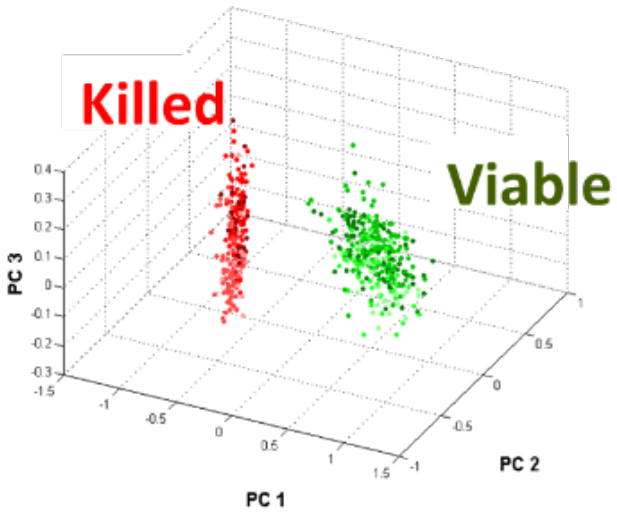

Figure 7. Principal component analysis of a mixture of viable and non-viable (gamma-irradiated) BASP.

4. CONCLUSION

The work described above demonstrated that high-throughput Raman chemical imaging can be used to differentiate and quantify viable and gamma-irradiated (deactivated) gram-positive BASP. The disappearance of the Ca-DPA contribution from the irradiated spores appears to be the main source of spectral discrimination. At the time of submission of this report, the work is still continuing to determine if Raman can be used to monitor various levels of inactivation upon different gamma radiation exposure times by monitoring the decomposition of the Ca-DPA spectral features. The resulting data from the successful completion of this work may have significant implications in providing increased discrimination of biological threats in more varied environments. The comparative simplicity of a system based on exploiting optical signatures may also decrease the overall logistical burden when compared to competing, reagent-heavy techniques.

ACKNOWLEDGMENTS

The authors acknowledge financial support from ECBC's Surface Science Initiative Program. We thank all the personnel from the Naval Surface Warfare Center Dahlgren Division, the ECBC Bioscences Division and Directorate of Program Integration, as well as team members from the U.S. Army Medical Research Institute of Infectious Diseases Bacteriology Division and Statistics Diagnostics Systems.

REFERENCES

[1] *Review Committee Report: Inadvertent Shipment of Live Bacillus anthracis Spores by DoD*; The Committee for Comprehensive Review of DoD Laboratory Procedures, Processes, and Protocols Associated with Inactivating Bacillus anthracis Spores: Washington, DC, 2015. https://www.defense.gov/Portals/1/features/2015/0615_lab-stats/Review-Committee-Report-Final.pdf.

[2] Huang, S.S.; Chen, D.; Pelczar, P.L.; Vepachedu, R.V.; Setlow, P.; Li, Yong-qing, L. Levels of Ca2+ Dipocolinic Acid in Individual Bacillus Spores Determined using Microfluidic Raman Tweezer. *J. Bacteri.* **2007,** *189* (13), pp 4681–4687.

Reducing false positives via capture/recapture modeling for early-warning

Thomas E. Ingersoll*
U.S. Army Edgewood Chemical Biological Center, Research & Technology Directorate,
5183 Blackhawk Rd, Aberdeen Proving Ground, MD 21010

ABSTRACT

Capture/recapture modeling is a method for removing bias from population estimates when underreporting occurs; that is, when the population is imperfectly observed and not all individuals can be counted. Another common problem in population counts is false positives, which occurs when individuals other than those sought are counted, as when a species is misidentified, or a disease misdiagnosed. Recently, capture-recapture methods have been extended to correct bias due to false positives. Further model extensions include modeling of spatial distribution, modeling of states other than population sizes, and modeling from binary presence/absence data, as opposed to counts, which is called occupancy modeling. This project applied occupancy modeling of threat probability to simulated chemical/biological warfare agent alarm data—binary data which typically include both false positives and underreporting. Estimated threat probability was compared to true values used to generate the simulation in order to evaluate model accuracy. Accuracy was compared between the occupancy model and two other methods for estimating threats. A full model was fit, giving location-specific probability of contamination by agents, local probability of false positives, and local probability of underreporting. Occupancy modeling was found to be highly reliable and accurate under conditions where underreporting and false positives could be modeled independently.

Keywords: false positives, capture/recapture model, occupancy model, hierarchical model, state-space model, chemical/biological early warning

1. INTRODUCTION

Capture/recapture modeling (CRM) is an emerging analytic capability for evaluation of surveillance data. CRM was originally developed for estimating the size of incompletely observed bird populations.[1,2] A repeated-measures design distinguishes CRM from other population sampling methods. Bird populations are sampled repeatedly across time. Individual birds are marked with uniquely numbered bands. These numbers allow individuals to be recognized, that is, distinguished from other individuals during subsequent sample repetitions. CRM has since been extended to population estimation where individuals are not marked with bands, and for models of spatial distribution (occupancy modeling).[3] Additionally, CRM has been extended beyond bird studies to include estimating incidence of imperfectly reported diseases,[4] distribution of biological agents,[5] and other examples of imperfectly observed states. Such CRM extensions are commonly referred to as state-space models,[6] or hierarchical models.[7] All these various extensions have the repeated-measures design in common, and a probabilistic estimation method that exploits supplemental information inherent to the detection history provided by the repeated-measures series. Presented here is a study that used simulated repeated-measures for chemical/biological (CB) agent alarm data, resulting in an occupancy model giving CB threat distribution.

As well as estimating population size, density, or distribution, CRM is used to estimate the magnitude of two operationally relevant observation errors—the detection probability and the probability of false positives.[6] The detection probability is the probability that a state is observed, given that it is present on a sample-site; in this case, the probability that contamination with a CB agent is detected. Thus, the compliment of the detection probability is an observation error—the probability that a state exists on the site but is unobserved (underreporting). The false-positive probability is the probability that a state is recorded as observed even though it is absent from a site. False positives are errors that cause overestimation of population size, density, or distribution. Examples are when a species is misidentified when surveying for birds, or a disease is misdiagnosed during disease surveillance. Experts are in disagreement regarding validity of capture/recapture models for disease surveillance when false positives occur.[8] However, recent work suggests that false positives can be corrected using occupancy models for bird and amphibian

distribution,[9] and when estimating densities of imperfectly counted birds.[10] Thus, CRM might be used to correct two common observation errors that complicate CB agent surveillance data—false positives and underreporting.

Sensors for CB agents usually fall into one of two categories, standoff or point. Standoff sensors include such devices as radar, lidar, and a variety of optical sensors capable of sensing threat agents at distances up to many kilometers. Such devices collect data surfaces across areas, or volumes. Standoff sensors, such as lidar, tend to be non-specific, so they produce a high proportion of false positives where harmless substances are reported as threats. Point detectors typically must be in contact with an agent, so can be more specific to particular agents than standoff detectors. Stationary point sensors collect data on points, rather than areas or volumes. Moving point sensors can collect data along transects. Because of the contact requirement, point surveillance devices tend to produce data that have a high proportion of false negatives, thus threats may be underreported; that is, threats may be present but undetected. Data fusion of point and standoff sensor data is complicated by unequal false negative and false positive error rates (heterogeneous rates) between the two types of devices.

Standoff data are frequently augmented by confirmatory point samples, where a more specific detection technology is applied at particular locations. For example, an aerosol plume observed using lidar may be a biological agent, or may be smoke or dust. In order to distinguish between a biological agent and harmless substances in the plume, a reconnaissance may be deployed to collect samples for lab analysis, or to apply a more discriminating point sensor at locations within the plume. Because sample collection and point detectors can have high rates of underreporting, a large number of samples may need to be collected. When CB agent is not detected in any of the point samples, it might be concluded that agent is absent from the area, and that the alarm from the standoff device was a false positive. We will call this the method of confirmatory sampling (CS). A shortcoming of CS is that detection probability is not explicitly estimated, thus the number of samples needed to reduce underreporting to an acceptable level is unknown. The CRM method of occupancy modeling with false positives (OccFP) could correct this shortcoming by explicitly estimating the detection probability, thus estimating the number of confirmatory samples required to reduce underreporting below an acceptable level. Additionally, OccFP provides a direct estimate of the probability that the initial alarm was false, and can correct the estimate that a threat agent is present on the site for bias caused by imperfect observation.

A likelihood function for the occupancy model with underreporting and false positive observation errors[9] can be written as

$$L(p,\psi \mid y) \propto \prod_{i=1}^{R} \left\{ \left[p_{11}^{y_i} (1-p_{11})^{T-y_i} \right] \psi + \left[p_{10}^{y_i} (1-p_{10})^{T-y_i} \right] (1-\psi) \right\}, \quad (1)$$

where R is the number of sampled locations (sites), p is the classification probability, ψ is the probability that a threat agent is present on the site (occupancy probability), y are the data, and T is the number of times the measurements are repeated.

The classification probability includes the probability that a site is occupied and a threat detected (p_{11}), occupied and a threat not detected (p_{01}), not occupied and a threat falsely detected (p_{10}), or not occupied and a threat not detected (p_{00}), where the sum of all alternative classification probabilities is equal to one.

Given the data, the number of sites, and the number of repeated-measures, the parameters p and ψ can be adjusted numerically until the highest likelihood value is reached by using a computational optimization algorithm.[10] The maximum-likelihood estimates for the detection probability (p_{11}), the false positive probability (p_{10}), and the probability that a threat is present on the site (ψ) are estimated in this manner, along with confidence intervals.

Heterogeneous values for p_{11}, p_{10}, and ψ can be included in the model by adding a logistic regression describing the relationship between these parameters and a set of covariates[9] by

$$logit(\psi_i) = \sum_{0:n} \beta_n x_n \quad (2)$$

and

$$logit(p_i) = \sum_{0:m} \alpha_m w_m \quad , \quad (3)$$

where β and α are coefficients, and x and w are the measured covariates. For example, a categorical covariate of both p_{11} and p_{10} is sensor type. Other covariates can include environmental conditions such as weather measurements, or source terms such as distance from suspected release locations.

This methodology was extended for estimates of threat distribution when alarm data contain both underreporting and false alarms; estimates were compared to true values and other methods of threat assessment. A full model giving site-specific threat probabilities, underreporting, and false-alarm rates was fit. Conditions were identified where CRM methods were insufficient for site-specific threat assessment, and conditions where CRM was superior to other methods.

2. METHODS

Functions were written for the computational language R[11,12] to generate data-simulating sites where threat agents were present (occupied) and not present. A vector containing true values for site occupancy was prepared, with a value of 1 if occupied, or 0 if not. An equal number of occupied and unoccupied sites were simulated for each sample, so that the true occupied status of sites was known *a priori*. Thirty sites in each occupancy category were generated (for a total of 60) per iteration during hypothesis testing and sensitivity analyses. For the power analysis, site numbers varied between 10 and 100 (20–200 total).

For each site, a set of six repeated observations (y_i) was simulated. For occupied sites, underreporting was simulated and added to a matrix of observation values by generating a random binomial value according to the equation

$$y_i \sim \text{Binomial}\,(1, p_{01}), \tag{4}$$

where p_{01} was the detection probability. Thus, occupancy values of 1 were transformed to 0 at a rate complementary to the detection probability ($1 - p_{01}$). False positives were generated within data from unoccupied sites in a similar fashion, so that 0s were converted to 1s at the false positive rate (p_{10}). High detection probability with high false positives was used to represent a standoff detector, and five repetitions of lower detection and low false positive probability were generated to represent point detectors or samples. Specific detection and false positive probabilities were functions of simulated covariates (below), and varied across ranges for sensitivity analyses (below).

Two sets of detection and false positive covariate vectors were compared. A first set used the detector type exclusively, standoff versus point, as a categorical covariate for both detection and false positives. A second set scaled the false positive covariates by a random number, so that detection covariates and false positive covariates were independent within sensor categories, while differing in expected value between sensor categories.

Once the simulated imperfect observations and covariates were generated, they were subject to three types of analysis to estimate the proportion of sites with threat agent present (occupied). A generalized linear model (LM) was fit using logistic regression, using the R library *lme4*.[13] The method of confirmatory samples (CS: above) was applied. Finally, an OccFP was applied using the method of Royle and Link,[7] and executed within the R library *unmarked*.[14] Estimates of proportion of sites occupied via the three methods were compared to the true proportion occupied (known because the data were simulated) using the mean absolute deviance (MAD), which inversely measures accuracy (low MAD scores close to 0 indicate high accuracy of estimates). The standard deviation of MAD scores was used to inversely measure precision.

A formal test of hypothesis was executed using analysis of variance within the base library in R. Additionally, sensitivity of MAD scores and their confidence intervals to changes in false positives was compared between the three estimation methods graphically. Sensitivity of MAD scores and their confidence intervals to changes in detection probability were compared between the three estimation methods graphically for the case where detection and false positive covariate were independent. Sensitivity of MAD scores and their confidence intervals to detection probability when detection and false positive covariates are not independent was demonstrated for OccFP. MAD scores were also compared between estimation methods for differing sample sizes (power analysis).

A fully heterogeneous OccFP model was applied, giving estimates for and including covariates of, site-specific occupancy, underreporting, and false positive probabilities.

3. RESULTS

A null hypothesis that LM, CS, and OccFP produce equivalent MAD scores was rejected at a highly significant level with analysis of variance (Table 1). The alternative hypothesis was that the methods produce different MAD scores.

Table 1. Analysis of variance.

Response: Mean Absolute Deviance					
	Df	Sum Sq	Mean Sq	F value	Pr(>F)
Factor: Mode type	2	780.8	390.39	6501.1	< 2.2e-16 ***
Residuals	59997	3602.8	0.06		
Signif. codes: 0 '***' 0.001 '**' 0.01 '*' 0.05 '.' 0.1 ' ' 1					

Low MAD scores and low MAD standard deviations indicated that OccFP was both more precise and more accurate than other methods (Table 2). CS produced estimating errors 5.108434 times that of OccFP, LM produced estimation errors 31.37349 times those of OccFP. Independent P:FP.

Table 2. Normalized coefficients.

Model Type	Normalized Mean Absolute Deviance
OccFP	1
CS	5.108434
LM	31.37349

Site specific occupancy, underreporting and false positive probabilities were estimated (example in Table 3).

Table 3. Estimates for Site 1.

Probability of contamination with CB agent	
0.9999676	
False positive probability	
Standoff device	0.00000289
Point device	0.00000159
Detection probability	
Standoff device	0.8318786
Point device	0.2772788

Sensitivity analysis indicated that MAD in OccFP is less sensitive to a range of false positive probabilities than either LM or CS (Figure 1) when tested for Type 2 devices. This means that OccFP maintained a level of precision greater than other methods across a broad range of false positive error intensities.

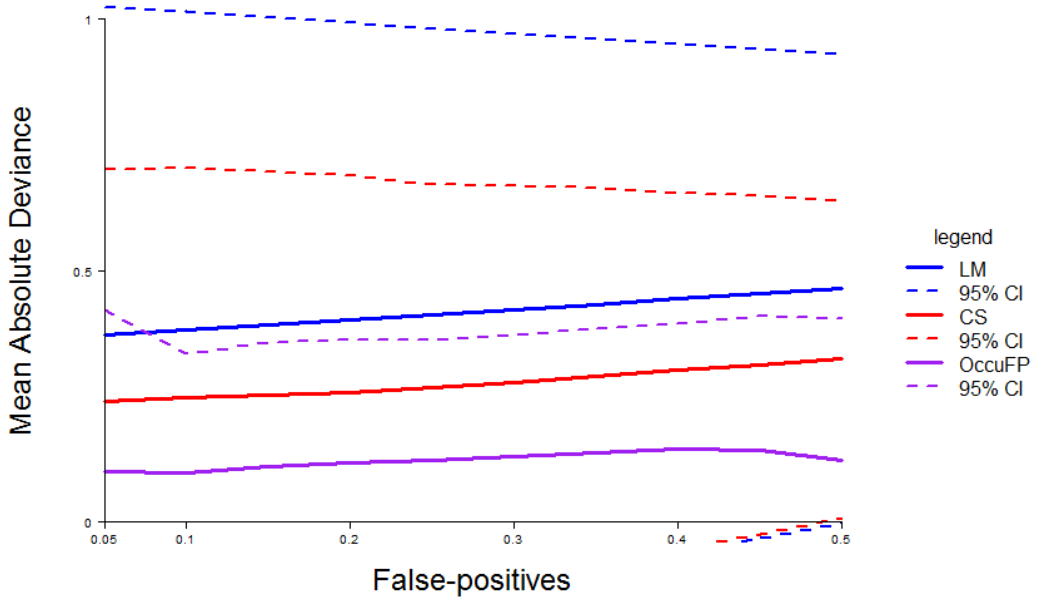

Figure 1. Sensitivity analysis comparing estimation errors produced by three methods in response to false positive probability. LM produced the highest errors, CS produced intermediate levels of error, while OccFP produced the lowest levels of errors. LM and CS showed a steady increase in errors with increasing false positives. 10,000 iterations, sample size of 30, detection probabilities at 0.8 and 0.2 for standoff and point respectively.

Sensitivity analysis indicated that MAD in OccFP was lower across a range of detection probabilities than either LM or CS (Figure 2) as long as detection probability and false positive probability were independent. This means that OccFP maintained a level of accuracy greater than other methods across a range of false negative error intensities.

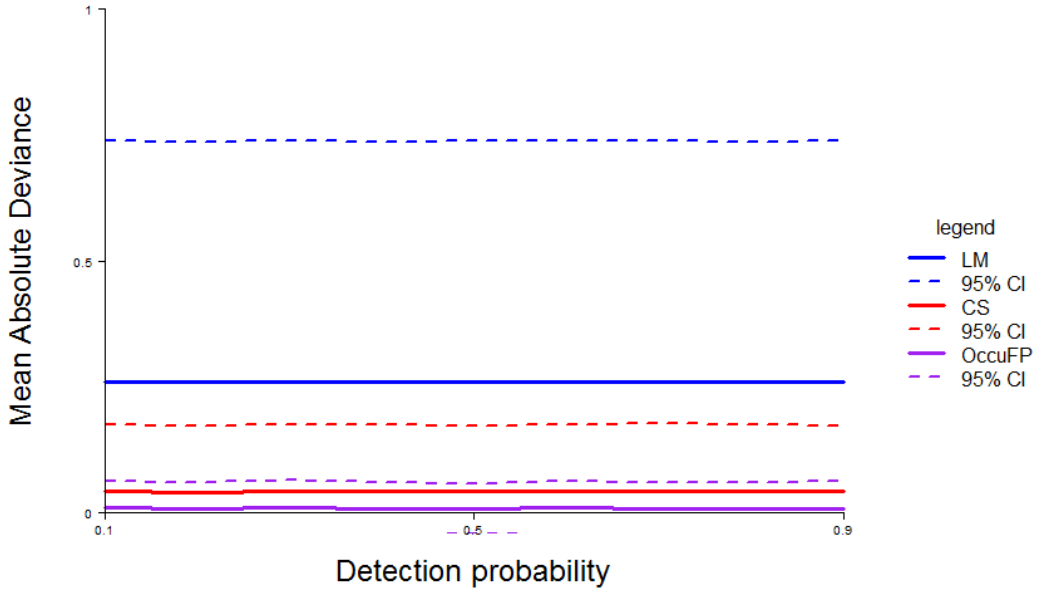

Figure 2. Sensitivity analysis comparing estimation errors produced by three methods in response to detection probability when detection and false positives modeled independently. LM produced the most errors, followed by CS. OccFP produced the lowest errors, near 0.

Sensitivity analysis indicated that MAD in OccFP is highly sensitive to a range of detection probabilities when detection probability and false positive probability were fully correlated (confounded: Figure 3).

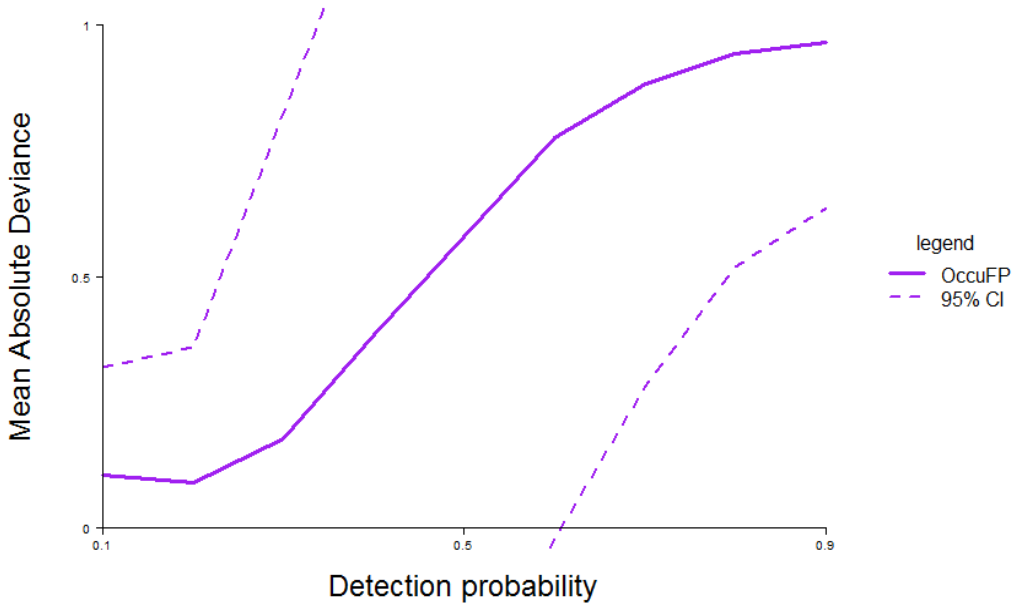

Figure 3. Sensitivity analysis showing estimation errors produced by OccFP in response to detection probability when detection and false positives are not independent. Confounding causes increased errors at higher detection probability when false positives cannot be modeled separately.

Power analysis indicated that MAD in OccFP responds dramatically to sample size, more so than either LM or CS (Figure 4). Deviation in OccFP approaches a level close to zero asymptotically when sample size increases.

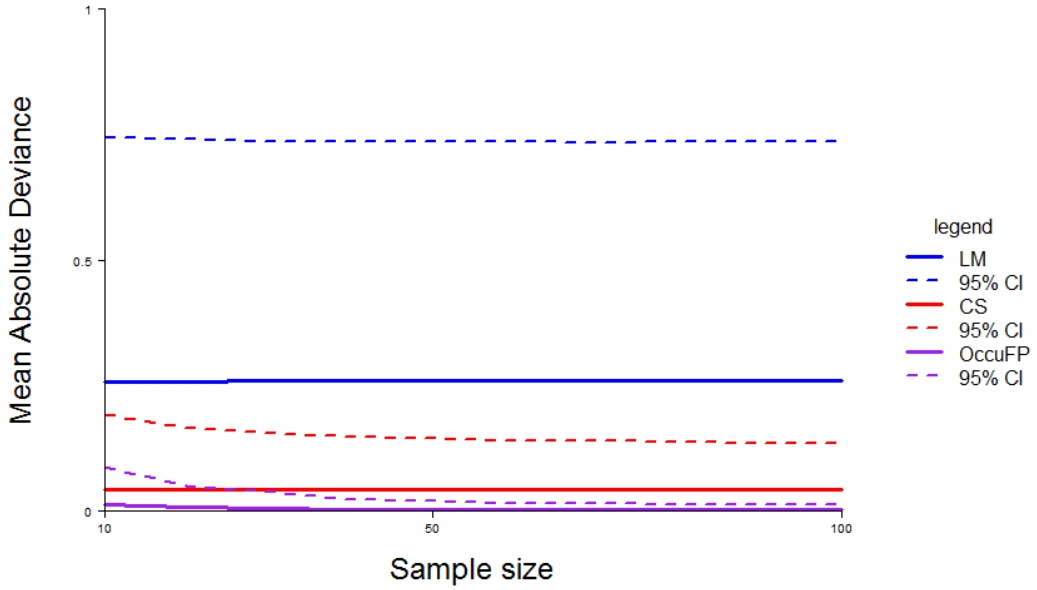

Figure 4. Comparing estimating errors for three methods in response to sample size. OccFP demonstrated a dramatic increase in accuracy with increasing sample size. Errors in other models insensitive to sample size.

4. CONCLUSIONS

Reducing false positives in CB early-warning data is a priority task identified within the Defense Threat Reduction Agency Research and Development Directorate (J9) Science and Technology plan.[15] An alternative to developing new sensor technology is to estimate the probability of false positives, based on sensor configuration, environmental conditions, and other relevant information. Underreporting is a similar problem, creating bias and uncertainty in threat estimates. Underreporting can also be estimated using CRM methods, as long as independent covariates for false positives and underreporting can be collected. CRM methods may be used to fuse data from a variety of unequal sensing devices or other sources of information by adjusting for differences in observation errors. False positive and underreporting probability estimates can be used to reduce bias caused by observation errors, correct estimates of threat intensity and distribution, identify and measure sources of uncertainty, and provide commanders with objective and defensible intelligence.

CS may be the most intuitive method for reducing the effect of false positives. However, underreporting may require that a large number of samples be taken, and that samples be collected from carefully selected locations. Current selection of sampling locations may be haphazard, or at best, directed at locations where the signal from standoff devices is highest. Such a sampling system does not account for an uneven spatial distribution of false positive errors in standoff data. Furthermore, CS methods do not indicate how many confirmatory samples are needed, or objectively estimate the best locations for their collection. No current method is employed for evaluating confidence in negative results from CS. CS methods might warn us that a threat is present, but cannot explicitly tell us the likelihood that threats are absent. An optimized method would combine the strengths of standoff and confirmatory sensing devices, reduce bias and errors, reduce the prevalence of false-alarms, and quantify confidence in the assessment that particular threats are absent from the field.

No one would argue that a generalized LM is an appropriate method for estimating parameters from data that are contaminated with the multiple pathologies encountered here. However, LM provides a suitable comparison for a model that is appropriate for these pathologies and demonstrates the estimation errors that occur when underreporting and false positives aren't estimated and corrected.

The substantial increase in accuracy for OccFP with increasing sample size that was observed by the author suggests avenues for further research. While point sensors tend to generate small data sets, standoff and remote sensing data produce large data sets. Spatial replicates within the data could be considered as small in area as the resolution of the instruments, thus the number of individually observed sites can be quite large. Typically, these data sets are reduced from surfaces to points when attempting to fuse standoff data with those from point sensors, resulting in a loss of information. An interpolative geospatial method might be applied to the point data instead, to produce a data surface to match that of the standoff device. CRM methods might be appropriate to see that uncertainty is properly propagated during the interpolative and fusion processes. Such a method might also allow data from predictive models to be combined with sensor data (data assimilation).

Binomial alarm data contain less information than count data or continuous data. However, CRM methods exist for these latter data types. Development of these models to accommodate false positives is less complete than the occupancy model examined by the author, for which a library of computational codes exists in publication.[13] Further research could be used to develop these models and produce a library of computational functions for their execution. Alternatively, Shelly et al.[5] used a density-dependent occupancy model to estimate densities of biological agents from binomial data; this model could be developed and extended to accommodate false positives.

While an OccFP model without site-specific heterogeneity would reduce the need to collect covariate data, thus relaxing the necessity of independence in these data, such a model produces a mean estimate of threat prevalence, rather than site-specific values. Such a model is less useful than the full model with heterogeneity, which gives a probability of contamination at each location, along with expected observation errors. Such specific information is far more informative to decision makers who are required to balance risks.

CRM methods are powerful, and under-used tools for evaluating a wide variety of surveillance data, which is typified by underreporting and false positive errors. These include CB early-warning data, but could be used for many other types of information, whenever cryptic states or populations must be assessed. The ability to distinguish underreporting and false positive probability is critical to controlling these sources of error, and can be informative to decision-making, particularly when determining the deployment of surveillance resources. The author recommends that a study of CRM methodology be embraced to enhance defense intelligence.

ACKNOWLEDGMENTS

The author would like to acknowledge U.S. Army funding provided through the Edgewood Chemical Biological Center's Seedling Research program.

REFERENCES

[1] Seber, G.A.F. A note on the multiple-recapture census. *Biometrika*. **1965,** *52*, pp 249–259.
[2] Jolly, G.M. Explicit estimates from capture-recapture data with both death and immigration - Stochastic model. *Biometrika*. **1965,** *52*, pp 225–247.
[3] MacKenzie, D.I.; Nichols, J.D.; Lachman, G.B.; Droege, S.; Royle, J.A.; Langtimm, C.A. Estimating site occupancy rates when detection probabilities are less than 1. *Ecology*. **2002,** *83*, pp 2248–2255.
[4] Buenconsejo, J.; Fish, D.; Childs, J.E.; Holford, T.R. A Bayesian hierarchical model for estimation of two incomplete surveillance data sets. *Statist. Med.* **2008,** *27*, pp 3269–3285.
[5] Shelly, E.E.; Narayanan, F.E.; Kierzewski, M.O.; Ingersoll, T.E. Estimating threat agent concentration through state-space analysis. *Proceedings of the ECBC In-House Laboratory Independent Research and Surface Science Initiative Programs FY15.* **2016,** pp 135–143.
[6] de Valpine, P.; Hastings, A. Fitting population models incorporating process noise and observation error. *Ecol. Monogr*. **2002,** *72*, pp 57–76.
[7] Royle, J.A.; Dorazio, R.M. *Hierarchical Modeling and Inference in Ecology, The Analysis of Data from Populations, Metapopulations and Communities*, 1st ed.; Academic Press, Elsevier: London, 2008.
[8] Abubakar, I.; Bassili, A.; Bierrenbach, A.; Bloss, E.; Floyd, K.; Glaziou, P.; Harris, R.; Lonnroth, K.; Mecatti, F., Pavli, A.; Sismanidis, C.; Timimi, H.; Uplekar, M.; van Hest, R.; Glaziou, P.; Floyd, K. *Assessing tuberculosis under-reporting through inventory studies*; World Health Organization Press: Geneva, 2010.
[9] Royle, J.A., Link, W.A. Generalized site occupancy models allowing for false positive and false negative errors. *Ecology.* **2006,** *87*, pp 835–841.
[10] Kery, M.; Royle, J.A.; Schmid, H. Modeling avian abundance from replicated counts using binomial mixture models. *Ecol. Appl.* **2005,** *15*, pp 1450–1461.
[11] R Development Core Team. *R: A language and environment for statistical computing*; The R Foundation for
[12] Statistical Computing, Vienna, Austria, 2011. http://www.R-project.org/
[13] Bates, D.; Maechler, M.; Bolker, B. lme4: Linear mixed-effects models using S4 classes. R package version 0.999999-2. http://CRAN.R-project.org/package=lme4
[14] Fiske, I.; Chandler, R. unmarked: An R Package for Fitting Hierarchical Models of Wildlife Occurrence and Abundance. *J. Stat. Softw.* **2011,** *43* (10), pp 1–23. http://www.jstatsoft.org/v43/i10/
[15] Defense Threat Reduction Agency. *Research and Development Directorate (J9) Chemical and Biological Technologies Department Science and Technology Plan*. **2016.**

Oxidative decomposition of fentanyl by immobilized peroxide catalysts—a biomimetic perspective

Li Kong[a], Jason Navin[b], Alex Balboa[a], John Landers[b], Monica McEntee[c], Christopher J. Karwacki[a*]
[a]U.S. Army Edgewood Chemical Biological Center, Research & Technology Directorate, 5183 Blackhawk Rd, Aberdeen Proving Ground, MD 21010
[b]Oak Ridge Institute for Science and Education, P.O. Box 117, Oak Ridge, TN 37831
[c]The National Academies of Sciences, Engineering, and Medicine, 500 Fifth St NW, Washington, DC 20001

ABSTRACT

This work demonstrates for the first time the oxidative decomposition of fentanyl using a solid form of oxy complexes on nanocrystalline metal substrates. Specifically, the interaction of fentanyl citrate with zinc peroxide, cerium peroxide, and iron (III) oxide was investigated using liquid chromatography-mass spectrometry and compared to oxidation solely by hydrogen peroxide. Reaction of fentanyl citrate with both hydrogen peroxide and a metal peroxide or oxide quickly yielded detectable amounts of products during contact times of 5 minutes and 24 hours. In the absence of hydrogen peroxide, little-to-no product formation was detected for zinc peroxide, but products were detected for cerium peroxide and iron (III) oxide. The objective of this work is to develop a foundational understanding of surface interactions and possible decomposition mechanisms of fentanyl with the aim to establish design strategies that will facilitate rapid development of active materials for protection and decontamination applications.

Keywords: catalyst, fentanyl, peroxide, oxidation, decomposition

1. INTRODUCTION

Fentanyl and its derivatives are powerful opioids which exhibit narcotic effects many times more powerful and addictive than heroin, and have garnered considerable attention with respect to their health impact to the general population. However, compared to heroin, fentanyl-based compounds are relatively easy to obtain, since the latter can be readily synthesized. It is this combination of potency and availability that renders fentanyl so dangerous, which drives the need to develop advanced protective measures against it.[1] The severity of this issue has extended itself to first responders, who may be affected by accidental dermal contact. Approaches to alleviate exposure will thus require strategies that are reliant on heterogeneous chemistries through, for instance, the incorporation of catalytic active components into self-decontaminating protective materials.

Inspired by the heme enzyme catalytic cycle, we report measured data on the degradation of fentanyl using surface-bound peroxides to a metal center (e.g., M–OOH). Numerous studies centered on fentanyl metabolism in the context of pharmacokinetics have shed light on its uptake, potency, duration, and decomposition mechanisms (Figure 1a).[2,3] *In vivo* studies have shown that fentanyl undergoes catalyzed oxidation by cytochrome P450 enzymes, specifically via CYP3A4.[4,5] The P450 (oxygenase) is one of many metalloporphyrins containing heme active centers that have been optimized (naturaliter) to shuttle electrons between proteins, and is responsible for virtually all *in vivo* reductive and oxidative chemistries involving decomposition of exogenous compounds. Oxidation of fentanyl is known to occur at five primary locations (Figure 1a) involving a series of processes described by the heme enzyme catalytic cycle.[6–9] The key active surface groups (Figure 1b) consist of oxy complexes, such as Fe(III)–O–O, enabling formation of peroxo (Fe(III)–O–O^-), hydroperoxo (Fe(III)–O–OH), and oxo (Fe(V)=O) groups.[10–12] The oxy complexes are regarded as the most powerful surface groups for oxidation of chemicals, particularly towards compounds containing nitrogen, sulfur, and carbon compounds. Although P450 is not amenable to functions external to natural metabolic environments, we view the metabolic fate of fentanyl as an instructive tool to design surfaces that mimic the oxidative properties of P450. Therefore, based on these known biological pathways, our research hypothesis is centered on the oxidative coupling and decomposition of fentanyl by use of surface-bound oxy-peroxides to active

metal nanoparticles. In this work, we studied the activity of oxy complexes on nanocrystalline metal substrates with the aim of designing highly efficient chemistries for the oxidative decomposition of fentanyl (Figure 1c).[13–15] Specifically, the oxy metal structures will consist of undercoordinated forms of ceria, zinc, and titania, which form bridged and terminal peroxo species similar to the groups formed on heme enzymes (Figure 1b). In this work, liquid chromatography-mass spectrometry (LC-MS) was employed to monitor the degradation of fentanyl, and density functional theory (DFT) methods were pursued in order to identify different vibrational modes, correlate these modes with experiments, and map the reaction coordinate of solvated reaction conditions.

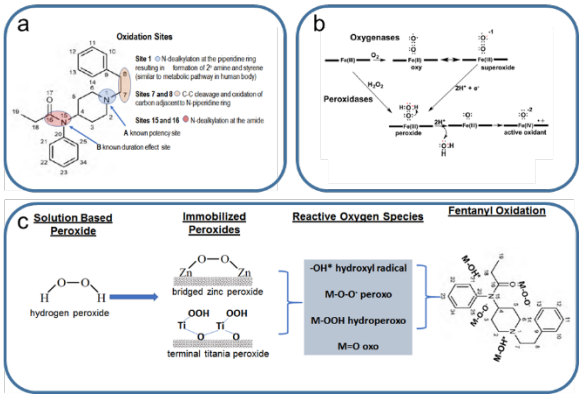

Figure 1. a) Active sites on fentanyl (a), oxygen and peroxide activation by heme enzymes (b), and formation of reactive oxygen species on immobilized peroxides (c).

2. METHODOLOGY

2.1 Experimental methods

2.1.1 H_2O_2 and fentanyl citrate

All fentanyl citrate experiments were conducted in aqueous phase, at room temperature, under constant stirring. An aliquot of fentanyl citrate stock solution was first added to a reaction vial, followed by the addition of either H_2O_2 or water, depending on the desired experiment. After 24 hours of stirring, an aliquot of sodium sulfite was added to the reaction vial in order to scavenge any remaining oxidant and halt the reaction. The initial reaction measurements were conducted in the exact same manner, but the reaction was terminated soon after the reaction was initiated. After the reaction was halted, an aliquot of fentanyl-D5 was added to the reaction mixture as an internal standard. The reaction mixture was then centrifuged to remove any sodium sulfate that precipitated, and the liquid was removed for LC-MS analysis.

2.1.2 H_2O_2, metal peroxide or oxide, and fentanyl citrate

An amount of metal peroxide or oxide was first added to a reaction vial, followed by an addition of either H_2O_2 or water, depending on the desired experiment. Next, an aliquot of fentanyl citrate stock solution was added to the reaction vial and the mixture was stirred for 24 hours. After 24 hours of stirring, an aliquot of sodium sulfite was added to the reaction vial in order to scavenge any remaining oxidant and stop the reaction. The initial reaction measurements were conducted in the exact same manner, but the reaction was terminated soon after the reaction was initiated. After the reaction was halted, an aliquot of fentanyl-D5 was added to the reaction mixture as an internal standard. The reaction vial was then centrifuged to separate the sodium sulfate and metal peroxide from the liquid. The liquid was then removed and analyzed using LC-MS analysis.

2.2 Materials synthesis and characterization

2.2.1 Zinc peroxide (ZnO_2) synthesis

Approximately 1 g of zinc acetate dihydrate was added to 12 mL of 5 M ammonium hydroxide to form a solvated mixture of zinc hydroxide. 100 mL of 30 % w/w H_2O_2 was added to the zinc hydroxide dropwise to yield ZnO_2 nanoparticles. The ZnO_2 nanoparticles were then triply rinsed in deionized water and dried at ~ 60 °C overnight.

2.2.2 Cerium peroxide synthesis

A 450-mL stock solution of 0.035 M (5.73 g) cerium chloride salt solution was prepared. The pH of the solution was adjusted dropwise to 1.90 by the addition of 18 M HCl in order to prevent the rapid precipitation upon the addition of H_2O_2. A 10:1 molar ratio of H_2O_2:Ce ion was added, and the solution was allowed to sit for 30 minutes in order to ensure efficient ligand exchange with the Ce ion. After 30 minutes, 20 mL of 1 M NaOH was titrated into 100 mL of the freshly prepared H_2O_2-Ce stock solution over the course of 2 hours at low stir rates. Once titrated, the precipitate was filtered and washed with deionized water, and then placed in the oven at 70 °C overnight. The subsequent powder was ground, then sieved in order to make a slurry.

2.2.3 Fe_2O_3 synthesis

A 1-L solution of 1 M NaOH was poured into a 1-L solution of 0.05 M $Fe(NO3)_3$. Afterward, the solution was placed in the oven at 60 °C for 6 hours, then filtered and washed extensively with deionized water. The resultant powder was dried for 24 hours at 100 °C, then ground with a mortar and pestle and sieved.

2.3 Theoretical modeling

All calculations were performed with the software package Gaussian09. This research used high performance computing resources from the National Synchrotron Light Source, a U.S. Department of Energy Office of Science User Facility operated for the Department of Energy Office of Science by Brookhaven National Laboratory under Contract No. DE-AC02-98CH10886. Geometrical optimization of the fentanyl and its derivatives were performed with the B3LYP functional with the 6-31G(d,p) basis set. All calculations were finished when convergence was reached when the maximum force was less than 0.00450 hartrees and the root means square force was less than 0.00300 hartrees. Raman spectra for each molecule were calculated using the keyword = XX, and displayed in the software package GaussSum. True energetic minimums were confirmed with harmonic frequencies calculations. The converged structures were used as input geometries for SCRF = PCM calculations, which apply an implicit solvent model.

3. DATA AND RESULTS

3.1 Experimental

3.1.1 H_2O_2 and fentanyl citrate

In order to test the baseline reactivity of fentanyl citrate toward oxidation, initial experiments were conducted that tested the ability of H_2O_2 to oxidize fentanyl citrate. The initial reactivity, at less than 5 minutes contact time, showed the generation of small amounts of products, as shown in Figure 2a. After a reaction time of 24 hours, substantial amounts of products were formed, as seen in Figure 2b.

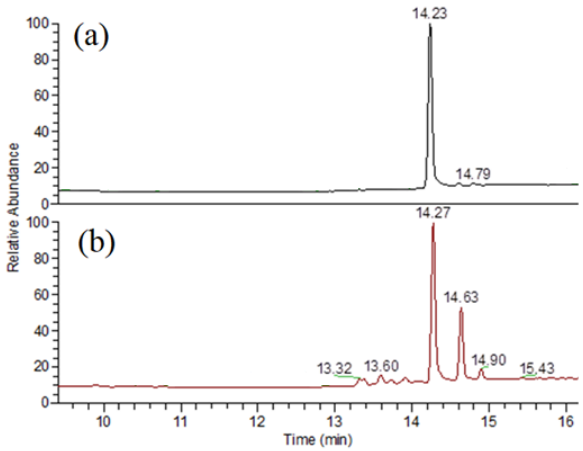

Figure 2. LC-MS spectra of the reaction of fentanyl citrate and H_2O_2 at initial reaction (a) and after 24 hours (b). The parent peak at ~ 14.25 corresponds to fentanyl citrate, and all other peaks are products.

3.1.2 ZnO_2 and fentanyl citrate

The reaction of ZnO_2 with fentanyl citrate in the absence of H_2O_2 yielded little to no products and the overall concentration of fentanyl citrate did not decrease substantially. However, when H_2O_2 was introduced to the reaction, products were formed after 24 hours as shown in Figure 3.

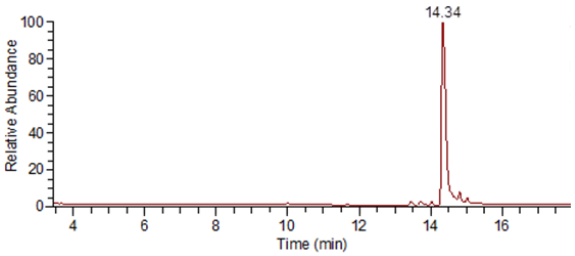

Figure 3. LC-MS spectrum of the reaction of fentanyl citrate, H_2O_2, and ZnO_2 after 24 hours. The parent peak at 14.34 corresponds to fentanyl citrate, and all other peaks are products.

3.1.3 Cerium peroxide and fentanyl citrate

The reaction of cerium peroxide with fentanyl citrate in the absence of H_2O_2 yielded a small amount of product during the initial reaction. After 24 hours, more products were measured, and the fentanyl citrate concentration was reduced by a modest amount (Figure 4). The addition of H_2O_2 to the reaction yielded interesting results. During the initial reaction, products were seen at relatively high amounts, as shown in Figure 5a. However, after 24 hours, the product peaks decreased in size, while the amount of fentanyl citrate continued to decrease.

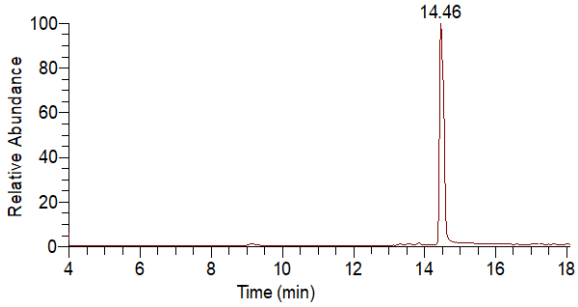

Figure 4. LC-MS spectrum of the reaction of fentanyl citrate and cerium peroxide after 24 hours. The parent peak at 14.46 corresponds to fentanyl citrate, and all other peaks are products.

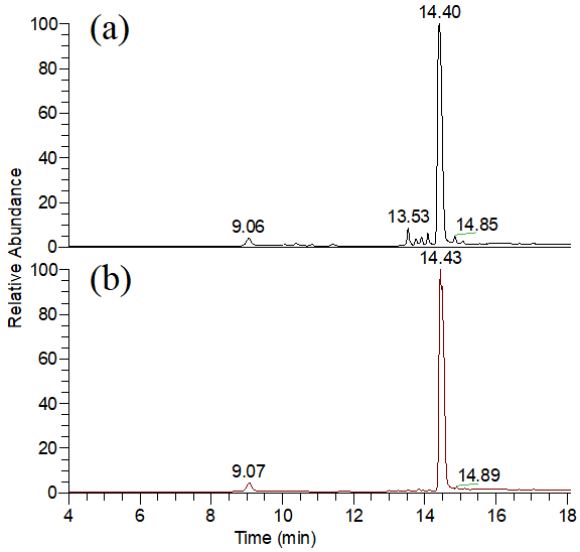

Figure 5. LC-MS spectra of the reaction of fentanyl citrate, cerium peroxide, and H_2O_2 at initial reaction (a) and 24 hours (b). The parent peak at ~14.4 corresponds to fentanyl citrate, and all other peaks are products.

3.1.4 Iron (III) oxide (Fe_2O_3) and fentanyl citrate

Due to a lack of material, only the initial reaction of Fe_2O_3 and fentanyl citrate was probed. As with cerium peroxide, reaction of Fe_2O_3 with fentanyl citrate, whether in the presence or absence of H_2O_2, yielded products during the initial reaction as shown in Figure 6.

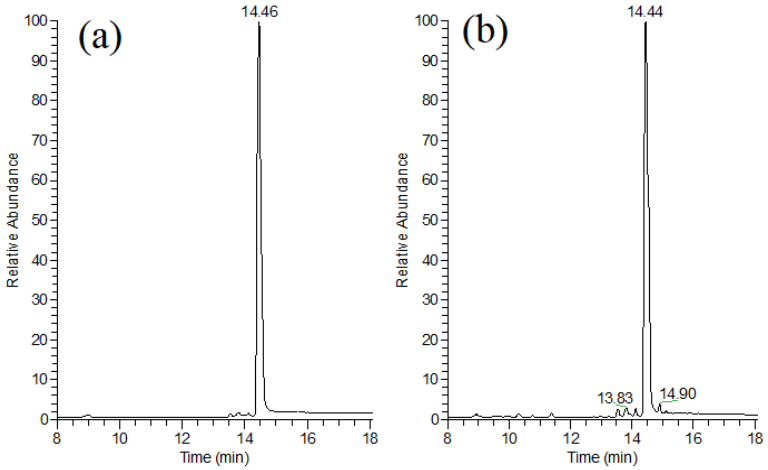

Figure 6. LC-MS spectra of the reaction of fentanyl citrate and Fe_2O_3 at initial reaction without (a) and with (b) H_2O_2. The parent peak at ~ 14.45 corresponds to fentanyl citrate, and all other peaks are products.

3.2 Experimental results

Fentanyl citrate has been shown to react with H_2O_2, as well as with cerium oxide, Fe_2O_3, and ZnO_2. In the case of cerium oxide and Fe_2O_3, it appears that H_2O_2 enhances reactivity, but is not required, whereas ZnO_2 appears to require H_2O_2, though more investigation is necessary. A wide array of products is formed upon reaction with fentanyl citrate and Table 1 summarizes the proposed structures of products.

Table 1. Proposed oxidation products of fentanyl citrate with (a) H_2O_2, (b) cerium peroxide, (c) cerium peroxide and H_2O_2, (d) Fe_2O_3, and (e) Fe_2O_3 and H_2O_2, where OP denotes the oxidation product.

Fentanyl and oxidation products		RT (min)	*Matrix	Exact Mass	Accurate Mass	Mass error (ppm)	Proposed Structure
Fentanyl		14.37-14.46		337.22744	337.22760	0.47	
OP1		8.35-9.08	a,b,c,d,e	233.16484	233.16473	-0.47	
OP2	OP2A	10.02-10.10	a, c,d,e	371.23292	371.23280	-0.32	
	OP2B	10.35-10.44	a, c,d,e		371.23276	-0.43	
	OP2C	10.82-10.83	a, c,d,e		371.23274	-0.48	
	OP2D	11.43-11.49	a, c,d,e		371.23277	-0.40	
OP3	OP3A	13.54-13.60	a,b,c,d,e	353.22235	353.22257	0.62	
	OP3B	13.80-13.88	a,b,c,d,e		353.22243	0.23	
	OP3C	13.97-13.98	c,d,e		353.22247	0.34	
	OP3D	14.10-14.15	a,b,c,d,e		353.22241	0.17	
	OP3E	14.86-14.94	a,b,c,d,e		353.22217	-0.51	
	OP3F	15.08-15.13	a,b,c,d,e		353.22192	-1.22	

3.3 Theoretical modeling

A molecular dynamics conformer search was performed using the MMFF94 force field with the 10 energetically lowest conformers chosen for candidates for DFT calculations. The lowest conformer, defined by an open and extended structure (see Figure 7) was taken as the parent structure for all subsequent functionalization. The calculated ground state energies indicate that the conversion of fentanyl to its oxide is an exothermic process, with the oxide having a higher stability by 10.77 kcal/mol. The calculated infrared frequencies are in good agreement with experimental findings (compare Figure 7 to Figure 8), and demonstrates that the peak occurring at 2820 cm^{-1} inherent to the fentanyl structure, disappears when the nitrogen on the ring is oxidized. This result paves the way to experimentally distinguish between the oxidized product and the unreacted parent structure of fentanyl.

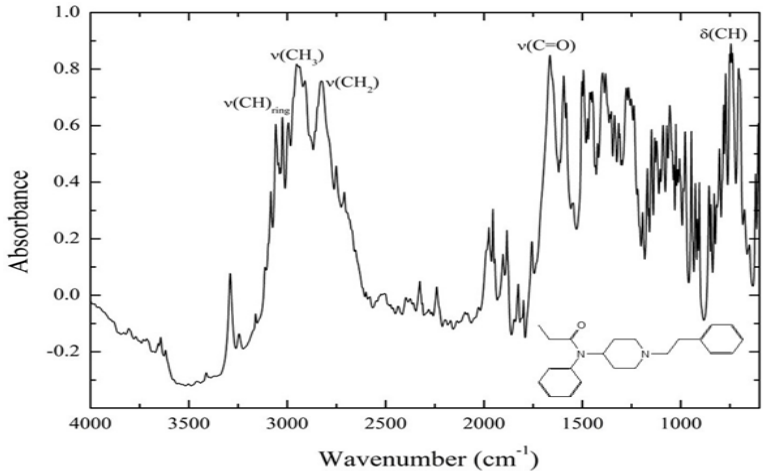

Figure 7. DRIFTS spectra of neat fentanyl.

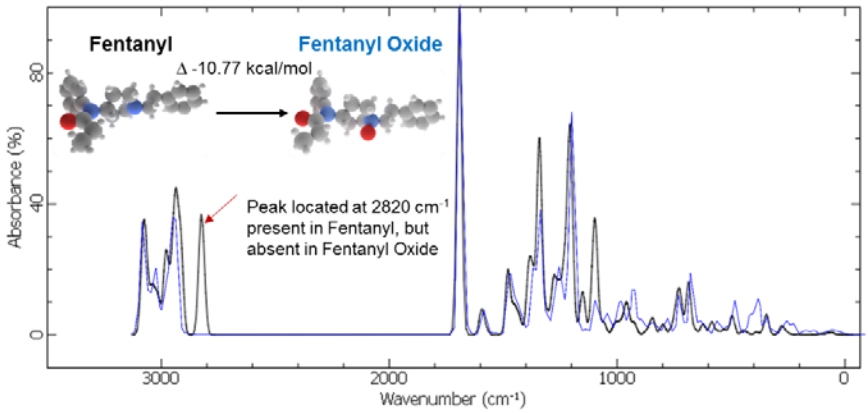

Figure 8. Calculated IR spectra from DFT calculations for fentanyl and fentanyl oxide.

In order to determine the most likely site of oxidation, DFT calculations were performed on the OP2 and OP3 products by placing a hydroxyl group at various sites on the molecule, which accounts for the increase in molecular weight. The ground state energies were compared to the parent fentanyl structure, as shown in Figure 9, and demonstrates that both the OP2 and OP3 products are more stable than fentanyl, indicating that the reaction is exothermic. The most stable OP2 configuration occurs when the carbon adjacent to the amine is hydroxylated, with a structure that is higher in stability by 91.21 kcal/mol. Meanwhile, the most stable structure for oxidation is the carbon adjacent to the nitrogen within the ring structure, with an increase in stability by 83.16 kcal/mol. Sites where there are two values represent the axial and equatorial hydrogens. It should be noted that the relative energies to hydroxylate the ortho, meta, and para positions on either of the rings is quite low compared to the energetically most favorable structure, and that a mixture of experimental products could be expected.

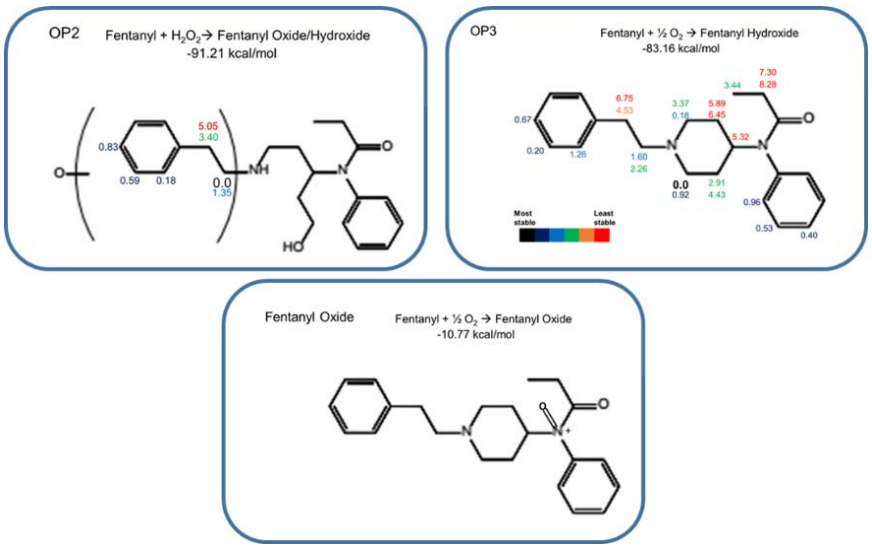

Figure 9. DFT calculations for the oxidation of fentanyl as determined by LC-MS measurements. Colored values represent the relative change in energies with respect to the lowest configuration (noted as 0.0 in black) in kcal/mol.

4. CONCLUSIONS

Although further refinement of the studied materials is required, it has been shown that H_2O_2, metal peroxides, and metal oxides readily react with fentanyl citrate. Additionally, LC-MS has been shown to be a capable tool in determining the products of reaction. Further studies will investigate solid-state degradation of fentanyl with the catalysts investigated within this study. Work is ongoing to develop a foundational understanding of surface interactions and possible decomposition mechanisms of fentanyl with the aim to establish design strategies that will facilitate rapid development of active materials for protection and decontamination applications. Since these sorbents are known to be easily incorporated into textiles, fabrics, and breathable membranes, it is anticipated that the research presented here will be the first step toward self-decontaminating protective clothing for first responders against the current opioid epidemic.

ACKNOWLEDGMENTS

Support for this research was provided by the U.S. Army Edgewood Chemical Biological Center Research and Technology Directorate's Seedling program.

REFERENCES

[1] Hedegaard, H.; Warner M.; Miniño, A.M. *NCHS Data Brief, No. 273: Drug Overdose Deaths in the United States, 1999–2015*, U.S. Department of Health and Human Services, Centers for Disease Control and Prevention, National Center for Health Statistics: Hyattsville, MD, 2017.

[2] Feasel, M.G.; Wohlfarth, A.; Nilles; J.M.; Pang, S.; Kristovich, R.L.; Huestis, M.A. Metabolism of Carfentanil, an Ultra-Potent Opioid, in Human Liver Microsomes and Human Hepatocytes by High-Resolution Mass Spectrometry. *AAPS J*. **2016,** *18* (6), pp 1489–1499.

[3] Smith, S.S. Opioid Metabolism. *Mayo Clin. Proc*. **2009,** *84* (7), pp 613–624.

[4] Van Nimmen, N.F.; Veulemans, H.A. Development and validation of a highly sensitive gas chromatographic-mass spectrometric screening method for the simultaneous determination of nanogram levels of fentanyl, sufentanil and alfentanil in air and surface contamination wipes. *J. Chromatogr. A.* **2004,** *1035* (2), pp 249–259.

[5] Dosen-Micovic, L.; Roglic, G.; Micovic, I.V.; Ivanovic, M. Conformational study of fentanyl and its analogs 1. Conformational space of the N-phenethyl substituent. *Electron. J. Theor. Chem*. **1996,** *1* (1), pp 199–210.

[6] Labroo R.B., Paine M.F.; Thummel K.E.; Kharasch; E.D. Fentanyl Metabolism by Human Hepatic and Intestinal Cytochrome P450 3A4: Implications for Interindividual Variability in Disposition, Efficacy, and Drug Interactions. *Drug Metab. Dispos.* **1997,** *25* (9), pp 1072–1080.
[7] Garg, A., Solas, D.W.; Takahashi, L.H.; Cassella, J.V. Forced degradation of fentanyl: identification and analysis of impurities and degradants. *J. Pharm. Biomed. Anal.* **2010,** *53* (3), pp 325–334.
[8] Qi, L.; Cheng, Z.; Zou, G.; Fan, Q. Oxidative Degradation of Fentanyl in Aqueous Solutions of Peroxides and Hypochlorites. *Def. Sci. J.* **2011,** *61* (1), pp 30–35.
[9] Xu, L. Oxidative treatment of fentanyl compounds in water by sodium bromate combined with sodium sulphite. *Water Sci. Technol.* **2015,** *72* (1), pp 38–44.
[10] Poulos, T.L. Heme Enzyme Structure and Function. *Chem. Rev.* **2014,** *114* (7), pp 3919−3962.
[11] Meunier, B.; de Visser, S.P.; Shaik, S. Mechanism of Oxidation Reactions Catalyzed by Cytochrome P450 Enzymes. *Chem. Rev.* **2004,** *104* (9), pp 3947–3980.
[12] Sono, M.; Roach, M.P.; Coulter, E.D.; Dawson, J.H. Heme-Containing Oxygenases. *Chem. Rev*. **1996**, *96* (7), pp 2841–2888.
[13] Polarz, S.; Strunk, J.; Ischenko, V.; van den Berg, M.W.E.; Hinrichsen, O.; Muhler, M.; Driess, M. On the Role of Oxygen Defects in the Catalytic Performance of Zinc Oxide. *Angew. Chem. Int. Ed.* **2006,** *45* (18), pp 2965–2969.
[14] Damatov, D.; Mayer, J.M. (Hydro)peroxide ligands on colloidal cerium oxide nanoparticles. *Chem. Commun.* **2016,** ***52*** (67), pp 10281–10284.
[15] Conte, V.; Coletti, A.; Floris, B.; Licini, G.; Zonta, C. Mechanistic aspects of vanadium catalysed oxidations with peroxides. *Coord. Chem. Rev.* **2011,** *255* (19–20), pp 2165– 2177.

Obscurant bispectral smoke

Danielle L. Kuhn[a,b], Amee L. Polk[a*], Zach B. Zander[a],
[a]U.S. Army Edgewood Chemical Biological Center, Research & Technology Directorate,
5183 Blackhawk Rd, Aberdeen Proving Ground, MD 21010
[b]The National Academies of Sciences, Engineering, and Medicine, 500 Fifth St NW,
Washington, DC 20001

ABSTRACT

Bispectral screening smokes are of interest to the U.S. Army due to the proliferation of thermal imaging, night vision, and thermal-guided threats. Metal-organic frameworks are compounds consisting of metal ions coordinated to organic ligands. This coordination results in a stable porous structure. It is hypothesized that metal-organic frameworks can be used to replace, supplement, or enhance components of pyrotechnic formulations in order to produce a visible/IR blocking smoke. To date, no work has been done to explore using metal-organic frameworks in obscuration. The structural components of metal-organic frameworks are uniquely suited to smoke production, since metal-organic frameworks consist of a self-contained pyrotechnic mix, including a fuel (metal node) and oxidizer (ligand). UiO–66, a zirconium-based metal-organic framework containing terephthalic acid ligands has been identified as a potential high performer for this study, as it is composed of metal oxides and organic linkers whose visual obscuration properties are well-characterized. Preliminary studies conducted using UiO–66 as a replacement for terepthalic acid in the smoke formulation provided successful smoke production. It is surmised that functionalization of the metal-organic framework may result in binding to infrared-producing particles, influence formation of metal rods in the porous space, or decrease agglomeration. UV-Vis spectroscopy and other analytical aerosol techniques are used to quantify the obscuring properties of a metal-organic framework and composites.

Keywords: metal-organic frameworks, obscuration, bispectral, aerosol

1. INTRODUCTION

Bispectral (visible through far infrared (IR) electromagnetic radiation) screening smokes are of increased interest to the U.S. Army and its allies due to the proliferation of thermal imaging, night vision, and other thermal-guided threats. Recent work conducted under Project Arrangement Number A-PA-UK-2011-0317, an agreement between the United States and United Kingdom, resulted in initial development of a bispectral grenade. That technology increases the warfighter's level of protection against emerging threats and methods of detection, while combining technologies to reduce logistical load. There is, however, no known high-efficiency bispectral obscurant smoke or continuously burning grenade. Ideally, the warfighter would have a pyrotechnic smoke grenade that can provide a high-performance bispectral obscuration with continuous cloud production. The purpose of this effort is to investigate an emerging, novel technology as a novel manner to increase the effectiveness and efficiency of bispectral smoke technologies.

Metal-organic frameworks (MOF) are compounds consisting of metal ions coordinated to organic ligands. This coordination network results in a stable porous structure usable for the storage of small molecules. In this work, MOFs will be used to replace, supplement, or enhance components of pyrotechnic smoke formulations in order to produce a visible- and IR-blocking smoke. Specifically, MOFs will be combined or reacted with metals to create an IR-obscuring component. Furthermore, MOFs may increase the packing density of the visible/IR smoke components of mix, thus allowing the standard hand grenade to hold a higher volume of smoke producing material, or for the production of a smaller, more efficient grenade, thereby reducing the logistical load of the warfighter.

MOFs possess appealing characteristics, which in turn have made them successful in applications such as gas purification and separation, catalysis, and sensors. To date, no work has been done to explore the use of MOFs in obscurant chemistry. The structural components of MOFs are uniquely suited to smoke production. In particular, MOFs consist of a self-contained pyrotechnic mix, including a fuel (metal node) and oxidizer (ligand). Understanding MOFs and their application in obscurant technologies would be uniquely a U.S. Army effort.

This research aims to examine if MOFs are a suitable candidate for use in pyrotechnic applications based on their composition. Subsequently, the research strives to gain a better understanding whether MOFs, with the appropriate pyrotechnic characteristics, will be successful as an obscurant. Both solution and aerosol analyses were performed to establish if MOFs exhibit visual obscuring properties that can be modified or added to an existing material to create a composite material with higher-performing bispectral properties.

2. BACKGROUND AND OBJECTIVES

MOFs are made up of two tunable components—metal oxide clusters, known as secondary building units (SBU), and organic linkers that connect the SBUs to form porous, reticular structures. Each of these components are highly tunable to achieve desired properties and structures. For example, many MOFs are made from SBUs that contain metal oxides pertinent to IR obscurance, such as zirconium oxide, zinc oxide, copper oxide, and titania. Organic linkers can also be tuned to have visual obscurance properties. For example, terephthalic acid is one of the most common linkers, and is currently used for white obscurant smoke. Adding an amine moiety to the linker (aminoterephthalic acid) can result in enhanced reactivity. These linkers can be mixed within the structure, allowing for multiple functionalities. Additional traditional linkers are shown in Figure 1, but any number of organic species can be used to develop new MOFs and spectral obscurant capabilities.

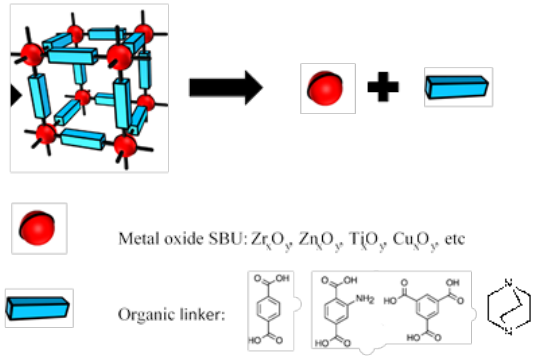

Figure 1. Concept of operations and typical metal oxides and organic linkers used. Burning MOFs, or treating them with an acid or base, results in structural breakdown.

Effective obscuration is based on extinction efficiency; in order to design the most effective MOF, the extinction efficiency of the individual materials used for the linkers and metals was determined. To generate equal performance in both IR and visual, the packing density of each material was multiplied by the efficiency to get the mass of each material. This was used to determine the proper ratio of linkers to metal nodes.

UiO–66 was identified as a potential high performer for this study as it is composed of metal oxides and organic linkers whose visual obscuration properties are already well characterized. UiO–66 is composed of $[Zr_6O_4(OH)_4]$ clusters with 1,4-benzodicarboxylic acid struts, the SBU is connected to a 12-bidentate terephthalic acid ligand.[1,4–7] UiO–66 possess a pore size of 6 Å, which is conducive for the reduction of a metal rod within the pore possessing the appropriate dimensions for an IR obscurant. In addition, preliminary studies conducted using UiO–66 as a replacement for TA in the smoke mix formulation provided successful white smoke production. Figure 2 shows the structure of UiO–66.

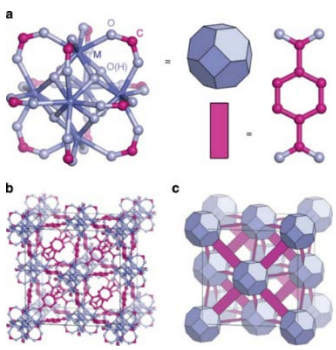

Figure 2. Structure of UiO–66.

After selection of the most compatible MOF for pyrotechnic applications, the focus of the investigation was the obscuration properties in solution. Extinction coefficients were calculated as a means of quantifying obscuration potential by utilizing UV-Vis spectroscopy. Extinction coefficients were calculated from equations (1), (2), and (3). In these equations, α (extinction coefficient) is calculated as a function of *T* (transmittance) through *l* (path length) at a given *c* (concentration).[2]

$$\mathrm{Abs} = \alpha c l \tag{1}$$

$$T = 10^{-\mathrm{Abs}} \tag{2}$$

$$\alpha = -\ln(T)/cl \tag{3}$$

Solutions of terepthalic acid (TA) and brass were used as controls for the spectral evaluation; TA was the control for visual, and brass the baseline for IR. A brass-with-TA solution was analyzed as a bispectral control. These experiments were achieved through mechanical sonication prior to analysis. As a baseline, the extinction of the MOFs was measured in solution to verify any visible obscuring properties. This was followed by a creating a mixture of the MOFs and brass in solution, and testing using UV-Vis. This data was compared to the extinction values obtained during control measurements of TA and brass.

Extinction coefficients were also evaluated using the aerosol chamber. Mixtures of the materials were pyrotechnically disseminated in the aerosol chamber and evaluated for extinction coefficient and yield.

In parallel, several composite MOFs were synthesized in which a potential IR obscurant was introduced to the pore and/or surface of the MOF, potentially creating covalent bonds between the two materials. Extinction coefficient measurements were repeated for the composite materials that possess alternative means of interaction other than mechanical sonication. These composite MOFs include NU 1000, a zirconium node-based MOF,[3] and Cu-MOF-74, a copper node-based MOF from the M-MOF-74 analogs.[4]

The particle size of any obscurant is a critical parameter associated with its effectiveness. Most effective scattering of electromagnetic radiation is directly related to the wavelength of the electromagnetic radiation and the physical size and shape of the particle. We assessed the physical characteristics of the samples using scanning electron microscopy (SEM) and energy dispersive X-Ray spectroscopy (EDX).

3. EXPERIMENTAL PROCEDURES

3.1 UV-Vis spectroscopy

3.1.1 UiO–66 samples

Two non-polar solvents, cyclohexane and toluene, were chosen for UV-Vis analysis. Selection was based on their low/no dipole moment, and ability to thoroughly suspend all materials evaluated. Samples of each material or mixture of interest listed in Table 1 were prepared at a concentration of 0.2 mg/mL in their respective solvent. Solutions were sonicated for 15–30 minutes and placed in quartz cuvettes for UV-Vis analysis on a JASCO V-670 Spectrometer.

Table 1. Materials of interest and mixture ratios for compositions tested.

Material	Percent Composition
TA	100
Brass	100
TA/Brass	25/75
TA/Brass	50/50
TA/Brass	75/25
UiO–66	100
Brass	100
UiO–66/Brass	25/75
UiO–66/Brass	50/50
UiO–66/Brass	75/25

A second set of samples identical to those listed in Table 1 were also prepared at 0.2 mg/mL in each solvent and allowed to stir magnetically for 24 hours. These samples were sonicated for 15–30 minutes to ensure proper mixing, then placed on a stir plate and allowed to stir undisturbed for 24 hours. Solutions were again sonicated for 15–30 minutes and placed in quartz cuvettes for UV-Vis analysis on a JASCO V-670 Spectrometer.

3.1.2 Composite materials

In addition to composite materials synthesized with UiO–66, other MOFs including NU1000 and Cu-MOF-74 were evaluated and used to synthesize composite materials for extinction using UV-Vis spectroscopy. All composite materials tested are listed in Table 2. Figures 3 and 4 depict the molecular structure of NU1000 and Cu-MOF-74, respectively.

Table 2. Composite materials tested.

Composite Materials
NU1000
Cu MOF 74
$Cu(OAc)_2$ + NU1000
$Cu(OAc)_2$ + Cu MOF 74
Ag + UiO–66
$Cu(OAc)_2$ + UiO–66

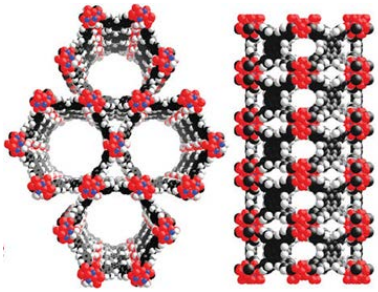

Figure 3. Structure of NU 1000.[3]

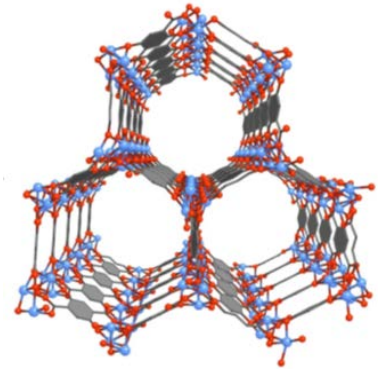

Figure 4. Structure of Cu-MOF-74.[4]

Cu was grown in the pores of the MOF by using copper acetate as a precursor to grow copper oxide, followed by reduction to Cu with $NaBH_4$ in a nitrogen atmosphere. The resulting materials were kept under ethanol to prevent oxidation of the Cu. Ag was grown in the pores using a polyol synthesis in which silver nitrate was reduced to Ag in a dimethylformamaide and polyvinylpyrrolidone solution that was refluxed at 160 °C for 2 hours.

3.2 Aerosol testing

3.2.1 Subscale grenade preparation

Subscale grenades were prepared using 10-g samples of pyrotechnically driven mixtures of each material of interest. Mixes were wet-blended in acetone by hand in small batches to ensure homogeneous mixing. All mixes were dried for a minimum of one hour in a friction air oven at 165 °F. Samples were pressed into subscale grenade bodies having an inner diameter of 1.136 inches and a height of 2.221 inches. 10 g of each mix with 0.5 g of first fire starter were pressed into the subscale grenade can using a Carver® press at 2,000 pounds dead load. Samples were ignited using visco cannon fuse in the pyrotechnic smoke box, and video was recorded for each trial. Two sets of each sample mixture were prepared—one for testing in the pyrotechnic smoke box, and one for testing in the aerosol chamber.

3.2.2 Aerosol chamber testing

All materials were disseminated in a cylindrical chamber with a volume of 190 m^3 (6-m diameter, 6.8-m height), as depicted in Figure 5. The chamber was equipped with a stirring fan to provide a homogeneous mixture throughout the volume. Transmission measurements in the visible region (0.3–0.9 µm) were achieved with a balanced deuterium halogen UV-Vis source (Model DH 2000-BAL, Mikropack GmBh) and a UV-Vis spectrometer (Model HR2000CG-UV-NIR, Ocean Optics). Transmission in the IR region (0.9–2.5 µm and 2.5–20 µm) was determined using two Fourier transform IR spectrometers (Model FT/IR-6100, JASCO). A path length of 6 m was used in all calculations for extinction, since the sources and detectors for the spectrometers were on opposite sides of the 6 m-diameter chamber. The spectrometers were placed at a height of 3.4 m. The concentration of material within the chamber was determined by taking an aliquot of air from the chamber. This was done by drawing a vacuum from the chamber onto a filter for 30 seconds, to obtain a yield factor, and 120 seconds, for concentration measurements. The volume of air passed through the filter was measured using a flow meter (Model FMA-1618A, OMEGA® Engineering). The mass accumulated on the filter was weighed using a microbalance (Model MX5, Mettler Toledo®). Inside the chamber, a mixing fan was operated at 97 rpm throughout the test. Using a 672-nm laser diode (Newport®; Mountain View, CA) throughout the test, laser transmission was observed. After the material is disseminated, the laser transmission has a decaying oscillation and will reach a steady state, and then homogeneity is presumed. At this time, spectrometers and filter measurements are started. The software Keysight (formerly Agilent) VEE was used to control and capture the data from the flow meter and laser diode instruments. All the data gathered from the various instruments were then processed with MathWorks MATLAB.

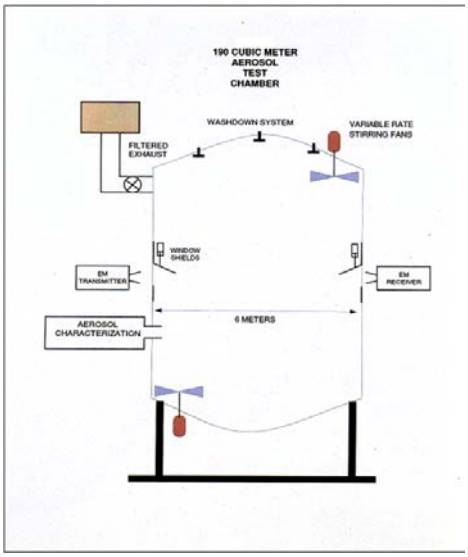

Figure 5. Aerosol test chamber.

For all tests, the item to be tested was placed in the center on the bottom of the chamber upon a 1.5-foot-high metal table. The chamber was sealed, and the mixing fan was turned on. Background measurements were taken on spectrometers. Device was initiated. Filter samples were taken to determine concentration. Spectrometer data was collected at this point. After the test, the chamber was completely exhausted and end measurements were taken with the spectrometers.

4. RESULTS AND DISCUSSION

4.1 UV-Vis spectroscopy results

UV-Vis spectroscopy was used as an analytical tool to measure extinction. The materials of interest were dispersed in a non-polar solvent that allowed for homogenous dispersion. Both toluene and cyclohexane were also chosen due to their limited interaction into the IR region. The concentration of each solution remained constant at 0.2 mg/mL. Once dispersed in solution, each vial was mechanically sonicated for 15–30 minutes to ensure homogeneity. Samples were immediately analyzed post-sonication.

Extinction was plotted versus wavelength for each material and mixture ratio that was examined. In toluene, the 25/75 TA/brass mixture showed the highest extinction over the entire range of wavelengths tested. In toluene, TA had the lowest values for extinction, followed by UiO–66. Samples showed some synergistic effects when toluene was used as a solvent for dispersion. However, values of extinction are much lower than ideal. It is common to see values of extinction at a much higher value when calculated in solution in comparison to aerosol. Figure 6 gives the plot of these values for the samples in toluene.

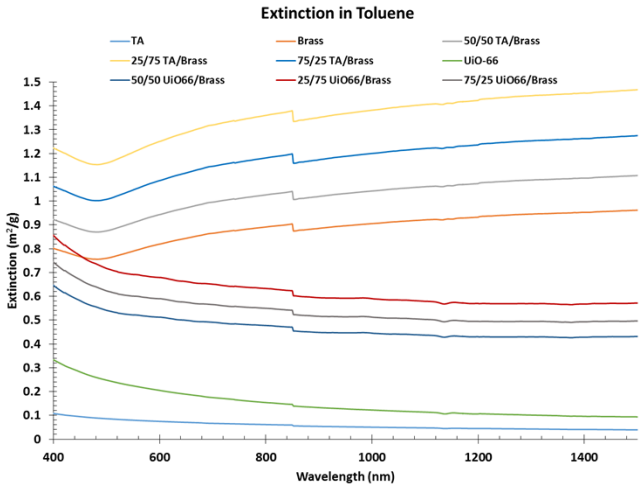

Figure 6. Extinction values versus wavelength for materials of interest and mixture ratios in toluene.

The extinction was calculated and plotted versus wavelength for all samples in which cyclohexane was used as the solvent. The 25/75 UiO–66/brass mix ratio possessed the highest values for extinction, followed by brass alone. Again, TA showed the lowest values for extinction. Samples containing UiO–66 were less consistent in the value of extinction versus wavelength. In the case of cyclohexane, there was no clear trend or synergistic affects apparent in the spectra. Figure 7 gives the plot of these values for the samples in cyclohexane.

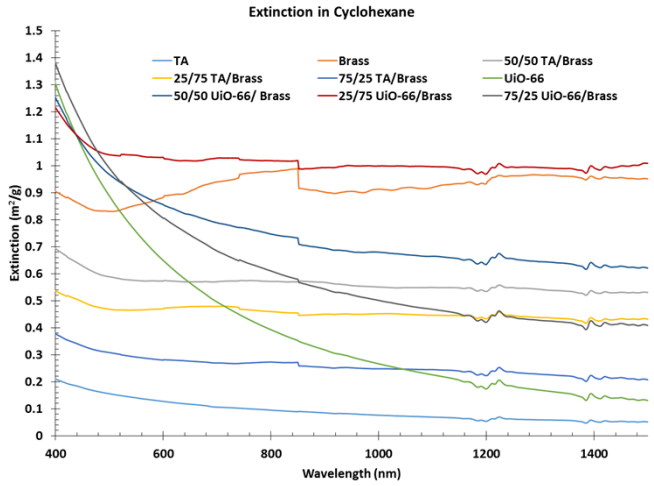

Figure 7. Extinction values versus wavelength for materials of interest and mixture ratios in cyclohexane.

The same set of experiments were repeated for the synthesized composite MOF samples under the same aforementioned conditions. The extinction was calculated and plotted versus wavelength to compare all composite samples. Samples of NU1000 showed a very high extinction in the shorter wavelengths, declining sharply and flattening out after 1200 nm. The high extinction around 410 nm was expected for this sample, due to its yellow color as a solid. NU1000 synthesized with reduced copper showed a similar trend, but maintained a little more consistency into the near IR region. UiO–66 containing silver produced a relatively consistent value of extinction over the wavelengths measured. Samples of Cu-MOF-74 had the lowest extinction values. There were no initial expectations for this MOF, it became of interest due to Cu being a suitable IR obscurant. Figure 8 shows the plot of extinction versus wavelengths for these samples in cyclohexane.

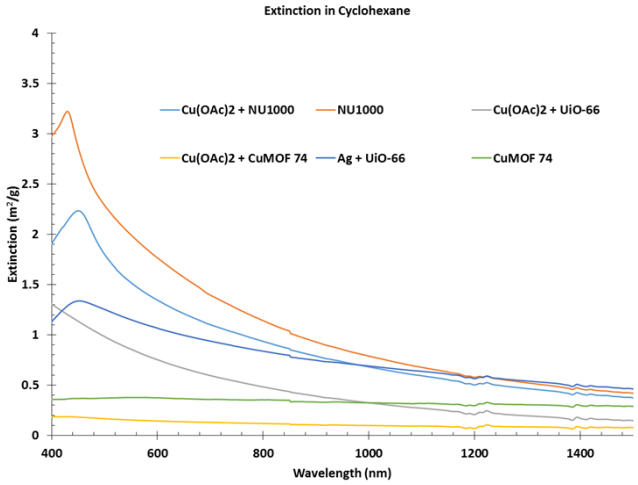

Figure 8. Extinction values versus wavelength for composite materials in cyclohexane.

All samples were analyzed under the same conditions, but in a toluene solution, for comparison. Values of extinction for the composite materials became significantly lower when the solvent was changed. However, the shape of the curves as well as the "best" performing materials remained the same. Both NU1000 and UiO–66 possessing Ag remained the highest extinction in the visible. In this experiment, the sample containing Cu-MOF-74 showed a more consistent trend over the wavelengths being measured. Figure 9 gives the values of extinction calculated versus wavelength for the composite materials in toluene.

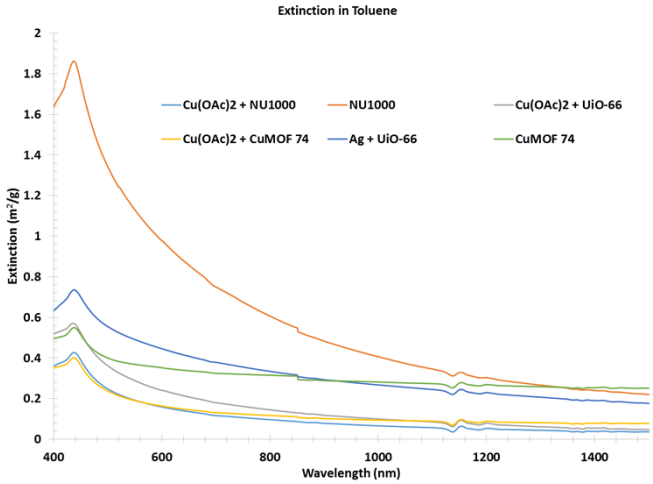

Figure 9. Extinction values versus wavelength for composite materials in toluene.

4.2 Aerosol testing results

After the inconsistency of extinction seen in the two different solvent matrices, it became apparent that aerosol testing was necessary to quantitatively determine the extinction for the materials of interest. The materials containing a blend

of TA and brass as well as UiO–66 and brass were incorporated with a fuel mix into a subscale grenade canister. All subscale grenade tests were tested in the pyrotechnic smoke box for qualitative analysis before sending a second set of samples to the aerosol chamber. All samples were successfully ignited, resulting in no duds or misfires in the pyrotechnic smoke box. Figure 10 shows still images captured of each material after cloud development.

Figure 10. Pyrotechnic smoke box still images. 1) TA only, 2) UiO–66 only, 3) brass only, 4) 25 TA/75 brass, 5) 50 TA/50 brass, 6) 75 TA/25 brass, 7) 25 UiO–66/75 brass, 8) 50 UiO–66/50 brass, 9) 75 UiO–66/25 brass.

After successful dissemination of the subscale grenades in the pyrotechnic smoke box, the second set of prepared samples were sent to the large aerosol chamber for UV-Vis far-IR spectroscopy testing to obtain quantitative extinction calculations. Figure 11 shows the results for the extinction plotted against wavelength for the samples containing TA, and Figure 12 shows the extinction plotted against wavelength for the samples containing UiO–66. Unfortunately, due to the small quantity of material used and the large volume of the chamber, the calculated extinction values fell into the noise region of the spectra, making them unreliable. Even with a mixing fan, the disseminated cloud was too small and not concentrated enough for the detectors to gain an adequate reading.

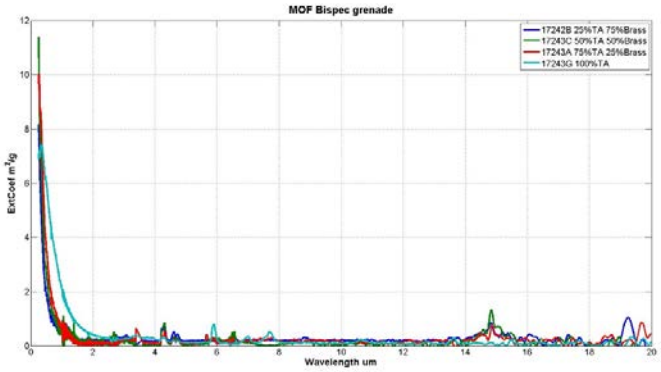

Figure 11. Extinction versus wavelength for TA-based samples.

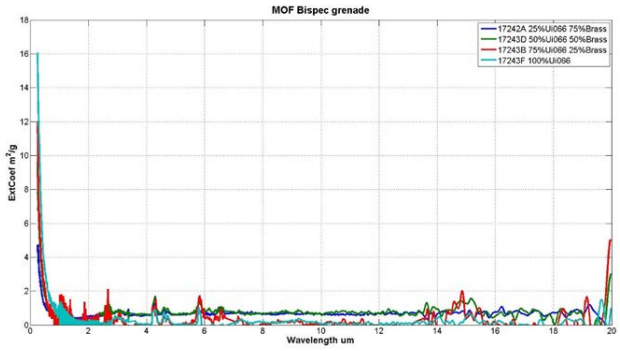

Figure 12. Extinction versus wavelength for UiO–66-based samples.

However, yield could be calculated from filters that were removed from the chamber after dissemination. Yield is calculated as the mass of the airborne material divided by the initial mass of material. Table 3 gives the calculated yield for each test sample. The objective was to eject as much material as possible in the cloud, which will increase the concentration, and in turn, increase the obscurance. For reference, most pyrotechnic-generated smoke has a yield of 40–50 %. In this situation, even the sample containing TA, which is under its ideal conditions, produced a lower-than-expected yield. However, despite the low values, it is promising to see that material is being ejected into the cloud upon dissemination, and future work will strive to create a mixture that is ideal for each material.

Table 3. Calculated yield for each subscale grenade tested in the aerosol chamber.

Material	Percent Composition	Yield (%)	Material	Percent Composition	Yield (%)
UiO-66	100	3.5	TA	100	26.7
Brass	100	8.6	Brass	100	8.6
UiO-66/Brass	25/75	7.6	TA/Brass	25/75	7.5
UiO-66/Brass	50/50	5.0	TA/Brass	50/50	7.4
UiO-66/Brass	75/25	3.0	TA/Brass	75/25	11.5

4.3 Discussion

Based on the data from the UV-Vis spectroscopy testing, values of extinction in the visible and IR wavelengths were seen for the UiO–66 samples. A strong dependency was seen on the choice of solvent. Samples containing UiO–66 showed higher extinctions compared to TA samples in cyclohexane, while TA samples showed higher extinction values in toluene. High extinction values were seen for NU1000 in both cyclohexane and toluene. This MOF had the highest extinction values for any sample tested; however, it showed a steep decrease once out of the yellow-absorbing region of the spectrum. The UiO–66 containing silver and the NU1000 containing copper both showed higher values for extinction than the mechanically sonicated mixture of TA/brass and UiO–66/brass samples. Subscale grenade samples showed indication of smoke production; however, the samples did not possess enough material. and dissipated too quickly in the large aerosol chamber to obtain reliable results. The large chamber values for extinction fell in the

noise range of the electromagnetic spectrum. Calculated values of yield were also low for all samples tested, once again, due to the small quantity disseminated.

5. CONCLUSIONS

As seen in the aforementioned results, the choice of solvent has a strong impact on the extinction values of the samples when dispersed in solution, despite choosing a solvent in which the properties would have little to no interaction in that region of the spectrum. Additional testing needs to be performed to determine the potential interaction the materials have with the solvent. Moving forward, composite MOFs possessing promising extinction values will be incorporated into a pyrotechnic subscale grenade for both quantitative and qualitative results. Prior to large chamber testing, a smaller aerosol chamber will be used to gain reliable extinction values using the smaller 10-g samples, as some of the composite materials will be more challenging to scale up at this time. UiO–66 did produce a white smoke cloud, indicative of TA, during pyrotechnic smoke box testing, and requires further investigation. Larger-sized grenades (approximately 100 g) will be needed to combat the quick dissipation of the smoke in the large aerosol chamber. This is feasible with the quantity of material possessed. The resulting yield of each subscale grenade was significantly lower than desired. This is likely attributed to the low burning temperature of the pyrotechnic fuel mix to effectively eject the material from the grenade body into the cloud, and therefore, preventing liberation of the TA from the UiO–66. Without decomposing the UiO–66, the TA ligands cannot sublime and recondense to produce the desired white smoke cloud. A hotter-burning fuel mixture is needed to increase yield, and therefore increase cloud production. Current efforts are underway examining a fuel with a temperature closer to the decomposition temperature of UiO–66 (500 °C).

ACKNOWLEDGMENTS

Support for this research was provided by the U.S. Army Edgewood Chemical Biological Center Research and Technology Directorate's Seedling program. The authors would like to acknowledge Mr. Greg Peterson and Dr. Jared DeCoste from the Edgewood Chemical Biological Center CBR Filtration Branch for providing intellectual support and MOF test materials, Ms. Diane Wylie for technical writing support, and Mr. Ernest Black for large-scale aerosol chamber testing data and report assistance.

REFERENCES

[1] Cavka, J.H.; Jakobsen, S.; Olsbye, U.; Guillou, N.; Lamberti, C.; Bordiga, S.; Lillerud K.P. A New Zirconium Inorganic Building Brick Forming Metal Organic Frameworks with Exceptional Stability. *J. Am. Chem. Soc.* **2008,** *130* (42), pp 13850–13851.

[2] Hughes, H.K. Beer's Law and the Optimum Transmittance in Absorption Measurements. *Appl. Opt*. **1963,** *2* (9), pp 937–945.

[3] Mondloch, J.E.; Katz, M.J.; Isley III, W.C.; Ghosh, P.; Liao, P.; Bury, W.; Wagner, G.W.; Hall, M.G.; DeCoste, J.B.; Peterson, G.W.; Snurr, R.Q.; Cramer, C.J.; Hupp, J.T.; Farha, O.K. Destruction of Chemical Warfare Agents Using Metal Organic Frameworks. *Nat. Mater.* **2015,** *14* (5), pp 512–516.

[4] Glover, T.G.; Peterson, G.W.; Schindler, B.J.; Britt, D.; Yaghi, O. MOF-74 Bulding Unit has a Direct Impact on Toxic Gas Adsorption. *Chem. Eng. Sci.* **2011,** *66* (2), pp 163–170.

[5] DeCoste, J.B.; Peterson, G.W.; Schindler, B.J.; Killops, K.L.; Browe, M.A.; Mahle, J.J. The effect of water adsorption on the structure of the carboxylate containing metal–organic frameworks Cu-BTC, Mg-MOF-74, and UiO-66. *J. Mater. Chem. A.* **2013,** *1*, pp 11922–11932.

[6] DeCoste, J.B.; Peterson, G.W.; Jasuja, H.; Glover, T.G.; Huang, Y.-g.; Walton, K.S. Stability and degradation mechanisms of metal–organic frameworks containing the Zr6O4(OH)4 secondary building unit. *J. Mater. Chem. A.* **2013,** *1*, pp 5642–5650.

[7] Cavka, J.H.; Jakobsen, S.; Olsbye, U.; Guillou, N.; Lamberti, C.; Bordiga, S.; Lillerud, K.P. A new zirconium inorganic building brick forming metal organic frameworks with exceptional stability. *J. Am. Chem. Soc.* **2008,** *130* (42), pp 13850–13851.